

## TESIS DOCTORAL

ANÁLISIS ÓPTICO-TÉRMICO DE RECUBRIMIENTOS ABSORBENTES SOLARES TÉRMICOS  
BAJO CONDICIONES DE RADIACION SOLAR CONCENTRADA  
BASADO EN MEDIDAS ESPECTRALES

### PhD THESIS

OPTO-THERMAL ANALYSIS OF SOLAR THERMAL ABSORBER COATINGS UNDER  
CONCENTRATED SOLAR RADIATION BASED ON SPECTRAL MEASUREMENT TECHNIQUES



Escuela Internacional de  
**DOCTORADO**  
Universidad de Almería



UNIVERSIDAD  
DE ALMERÍA

AUTOR

SIMON CARON HELLER

DIRECTORES

PROF. FRANCISCO MANZANO AGUGLIARO

DR. MARC RÖGER

UNIVERSIDAD DE ALMERÍA

Escuela de Doctorado de la Universidad de Almería

Almería 2024



## **Título de la Tesis en español**

Análisis óptico-térmico de recubrimientos absorbentes solares térmicos bajo condiciones de radiación solar concentrada basado en medidas espectrales

## **Título de la Tesis en inglés**

Opto-thermal analysis of solar thermal absorber coatings under concentrated solar radiation based on spectral measurement techniques

## **Nombres y apellidos del autor**

Simon Caron Heller

## **Nombres y apellidos de los directores**

Prof. Francisco Manzano Agugliaro (Director)

Dr. Marc Röger (Codirector)

## **Programa de doctorado**

Doctorado en Tecnología de Invernaderos e Ingeniería Industrial y Ambiental (RD99/11)



*To my beloved grandmother  
Isolde Heller, born Hoffmann  
(01.12.1924-01.12.2013)*

*Fiat lux et facta est lux.*



## Acknowledgements

*Life is what happens to you while  
you are busy making other plans.*

“Beautiful Boy” (1980)- John Lennon

It has been a long ride since I started researching in the field of Concentrated Solar Power, at Plataforma Solar de Almería, back in 2011. The renewable energy landscape has changed considerably since then.

I first began as a master student at CIEMAT. Since 2012, I worked as a research scientist for the German Aerospace Center (DLR) in Almería, Spain. I took the decision to start a PhD thesis at Universidad Almería (UAL) in September 2019, a few months before the COVID pandemic spread over the world.

This scientific journey has been filled with its lot of good and bad times, with moments of creativity, but also moments of sheer doubts and loneliness. I would like to express here my gratitude to all the persons who have contributed, directly or indirectly, to the completion of this scientific journey.

First, I am sincerely grateful to my thesis directors, Prof. Francisco Manzano Agugliaro and Dr. Marc Röger for their unwavering guidance, support, and mentorship throughout this research.

I am thankful to all OPAC members: Arantxa Fernández García, Florian Sutter, Ricardo Sanchez, Florian Wiesinger, Johannes Wette, Alejandro García Segura, Francisco Buendía Martínez, Tomas Reche Navarro, Lucia Martinez Arcos and Carmen Amador Cortes, for fostering a pleasant work atmosphere in the laboratory.

I extend my sincere thanks to my colleagues at CIEMAT and DLR. I am thankful to all the international students I had the opportunity to supervise since 2013: David, Henning, Marcos, Leslie, Nils, Lars, Juan, Luca, Eduardo, Albin and Romain.

To my close colleagues and friends: Ricardo, Jorge, Eneko, Jose, Guillaume and Sahar for engaging in passionate scientific and technical discussions.

To David Muruve and Jose Galindo, for their cheerfulness and their precious help in crafting scientific ideas into real life experiments.

Last but not least, I am wholeheartedly thankful to my parents, sisters, close family and friends, for their unconditional emotional support through all the obstacles that came along the way.





## Table of Contents

Resumen .....	1
Abstract .....	3
1 Introduction.....	7
1.1 Context.....	7
1.1.1 A civilisational challenge .....	7
1.1.2 The relevance of solar energy .....	8
1.1.3 The role of CSP in the energy transition .....	10
1.2 CSP technology overview.....	13
1.2.1 Operating principles .....	13
1.2.2 CSP system costs.....	15
1.2.3 System reliability .....	16
1.3 Thermal receivers and absorber coatings.....	17
1.3.1 Design of solar thermal receivers .....	17
1.3.2 Solar thermal absorber coatings.....	19
1.3.3 Durability of solar thermal absorber coatings .....	20
1.4 Opto-thermal characterisation.....	21
1.4.1 Figures of merit.....	21
1.4.2 Spectral characterisation at ambient temperature.....	23
1.4.3 Spectral characterisation at operating temperature.....	26
1.5 Infrared thermometry .....	28
1.5.1 Radiometric chain .....	28
1.5.2 Blackbody calibration .....	30
1.5.3 Single band IR thermometry.....	31
1.5.4 State of the art in CSP .....	33
1.6 References: Chapter 1.....	35
2 Investigation plan.....	49
2.1 Hypotheses.....	49
2.2 Objectives.....	49
2.3 Methodology .....	50
3 A comparative analysis of opto-thermal figures of merit for high temperature solar thermal absorber coatings.....	55
3.0 Abstract.....	55
3.1 Introduction.....	55
3.2 Materials and methods .....	59
3.2.1 System definition .....	59
3.2.2 Modelling assumptions .....	60
3.2.3 Reference coatings.....	61
3.2.4 Inventory of FoMs.....	63
3.3 Figures of Merits (FoMs).....	64
3.3.1 FoMs : Level 1 .....	64
3.3.2 FoMs: Level 2 .....	68
3.3.3 FoMs: Level 3 .....	70
3.4 Results and discussion.....	73

3.4.1	FoMs: Level 1 .....	73
3.4.2	FoMs: Level 2 .....	76
3.4.3	FoMs: Level 3 .....	79
3.4.4	Summary and discussion.....	82
3.5	Conclusion and outlook.....	84
3.6	References: Chapter 3.....	85
4	Laboratory intercomparison of solar absorptance and thermal emittance measurements at room temperature.....	97
4.0	Abstract.....	97
4.1	Introduction.....	97
4.2	Materials and methods .....	98
4.2.1	Organization and participants.....	98
4.2.2	Instrumentation .....	99
4.2.3	Reference and calibration samples .....	103
4.2.4	Optical characterization.....	105
4.3	Results and discussion.....	109
4.3.1	Spectral processing .....	109
4.3.2	Spectral weighting.....	111
4.3.3	Opto-thermal efficiency.....	114
4.4	Conclusion and outlook.....	115
4.5	References: Chapter 4.....	116
5	Intercomparison of opto-thermal spectral measurements for concentrating solar thermal receiver materials from room temperature up to 800 °C.....	123
5.0	Abstract.....	123
5.1	Introduction.....	123
5.2	Materials and methods .....	124
5.2.1	Organization and participants.....	124
5.2.2	Reference samples.....	125
5.2.3	Instrumentation .....	126
5.2.4	Data processing .....	130
5.3	Results and discussion.....	134
5.3.1	Room temperature .....	134
5.3.2	Operating temperature.....	140
5.3.3	Comparison .....	143
5.4	Conclusion and outlook.....	144
5.5	References: Chapter 5.....	145
6	Simulation of shortwave infrared ratio thermometers for the remote opto-thermal characterisation of central external cylindrical receivers .....	151
6.0	Abstract.....	151
6.1	Introduction.....	151
6.2	State of the art .....	152
6.2.1	Measurement instruments.....	152
6.2.2	Measurement techniques .....	155
6.3	Measurement principle .....	157
6.3.1	Radiometric chain .....	157

6.3.2	Ratio thermometry .....	159
6.3.3	Camera configuration.....	161
6.4	Modelling approach.....	163
6.4.1	Forward problem.....	163
6.4.2	Inverse problem.....	165
6.4.3	Batch simulation setup.....	165
6.5	Results and discussion.....	166
6.5.1	First SWIR ratio thermometer.....	166
6.5.2	Second SWIR ratio thermometer .....	169
6.6	Conclusion and outlook.....	171
6.7	References: Chapter 6.....	172
7	Conclusion and outlook.....	179
7.1	Publication n°1: A comparative analysis of opto-thermal figures of merit for high temperature solar thermal absorber coatings .....	179
7.2	Publication n°2: Laboratory intercomparison of solar absorptance and thermal emittance measurements at room temperature.....	179
7.3	Publication n°3: Intercomparison of opto-thermal spectral measurements for concentrating solar thermal receiver materials from room temperature up to 800 °C .....	181
7.4	Publication n°4: Simulation of shortwave infrared ratio thermometers for the remote opto-thermal characterization of central external cylindrical receivers.....	182
7.5	General conclusion and outlook.....	183
Appendix.	Publications derived from this thesis.....	185
	Publication n°1: A comparative analysis of opto-thermal figures of merit for high temperature solar thermal absorber coatings.....	187
	Publication n°2: Laboratory intercomparison of solar absorptance and thermal emittance measurements at room temperature .....	189
	Publication n°3: Intercomparison of opto-thermal spectral measurements for concentrating solar thermal receiver materials from room temperature up to 800 °C .....	191
	Publication n°4: Simulation of shortwave infrared ratio thermometers for the remote opto-thermal characterization of central external cylindrical receivers.....	193

## List of figures

Figure 1.1: 2023 status of control variables for all nine planetary boundaries [2].....	7
Figure 1.2: Sustainable Development Goals defined by the UN in 2015 [4].....	8
Figure 1.3: Recoverable energy reserves of renewable and finite energy resources over the next 30 years in comparison to the estimated total demand over the same period [5].....	8
Figure 1.4: Levelised Cost of Electricity (LCOE) of renewable power systems [6].....	9
Figure 1.5: Electricity capacity and generation trends for Solar Energy since 2011 [7]. PV (yellow), CSP (orange). a) Power capacity in MW. b) Energy Generation in GWh. ....	9
Figure 1.6: Global deployment of CSP projects in 2022 [8].....	9
Figure 1.7: Deployment of CSP plants from 2009 to 2019 [10]. Red: United States of America (U.S.A.). Yellow: Spain. Grey: Other countries.....	10
Figure 1.8: U.S. SunShot initiative 2030 Goals [11]. a) Solar PV b) CSP.....	11
Figure 1.9: Total final energy consumption 2018: 382 EJ (IEA/IRENA) [28]. ....	12
Figure 1.10: Worldwide distribution of Direct Normal Irradiation (DNI) [34]. ....	13
Figure 1.11: Overview of main CSP configurations. Illustrations extracted from [14]. ....	14
Figure 1.12: Schematic diagram of a CSP power plant. ....	15
Figure 1.13: Evolution of the cost breakdown of installed CSP plants by technology from 2010-2011 to 2019-2020 [6]. a) Parabolic Troughs. b) Central Receiver Systems.....	15
Figure 1.14: PTC issues ranked by priority and frequency of perceived occurrence [65].....	16
Figure 1.15: CRS issues ranked by priority and frequency of perceived occurrence [65]. ....	16
Figure 1.16: Schematic of a parabolic trough HCE [87]. ....	17
Figure 1.17: Schematic of external tubular receiver (left) and cavity receiver (right) design configurations [39].....	18
Figure 1.18: Volumetric receivers a) close up view of the absorber structure. b) Individual absorber modules. c) Main receiver mounted at a Solar Tower in Jülich, Germany [107]. ....	18
Figure 1.19: Heat transfer diagram for a solar thermal absorber coating. ....	19
Figure 1.20: Pictures of tubular metal substrates (T91) and STACs. a) Polished metal substrate and SSC. b) Sand blasted metal substrate and HSA coating. ....	19
Figure 1.21: Illustration of SSC architecture. a) Multilayer interference stack. b) Double layer CERMET [110,113,114].....	20
Figure 1.22: Spectral distributions a) reference solar spectrum (direct+circumsolar) as a function of relative optical AM. b) Blackbody spectral exitance as a function of temperature.....	22
Figure 1.23: Reference solar spectrum (ASTM G173-03; AM1.5, direct) and blackbody radiation (25 °C, 750 °C).....	23
Figure 1.24: SDHR data for calibrated reference samples.....	24
Figure 1.25: Benchtop spectrophotometers available at OPAC laboratory. a) Perkin Elmer Lambda 1050 b) Perkin Elmer Frontier FTIR with Pike integrating sphere. c) Diagram of Lambda 1050 integrating sphere. d) Diagram of Frontier FTIR Pike integrating sphere.....	25
Figure 1.26: Surface Optics Corporation 410-Vis-IR portable instrument. a) Instrumentation, including portable unit, measurement heads and reference calibration coupons. b) Integrating sphere. The red arrow is the illuminating beam. The purple arrow is the reflected beam, green arrows correspond to scattered light.....	25
Figure 1.27: Spectral response of portable instrument measurement heads in arbitrary units. a) 410 Solar reflectometer (0.33 – 2.5 μm). b) ET100 emissometer (1.5 – 21 μm). ....	26

Figure 1.28: Schematic view of the optical path for an experimental setup including a FTIR instrument [158].	27
Figure 1.29: MEDIASE setup mounted at the focus of the 1 MW solar furnace in Odeillo, France [156,157].	27
Figure 1.30: Schematic radiometric chain for a CRS configuration.	29
Figure 1.31: Exemplary blackbody calibration function (Eq.1.28-1.29). $R=366545$ ; $B=1428$ ; $F=1$ ; $O=342$ a) function $BF$ b) reciprocal function $BF^{-1}$ .	31
Figure 1.32: Example of reference blackbodies for temperature calibration. a) Mikron M305 cavity blackbody [176]. b) ECN100 extended area blackbody [177].	31
Figure 1.33: Measurement setup for the experimental characterization of effective directional emittance [178].	32
Figure 1.34: Simulation of atmospheric spectral transmissivity for two horizontal paths with MODTRAN6 software. $T_{amb}$ : 25 °C; RH: 50%. $CO_2$ : 400 ppm.	33
Figure 1.35: Airborne LWIR monitoring of parabolic trough receivers glass envelope [95].	34
Figure 1.36: Commercial LWIR system for CRS applications [181].	34
Figure 3.1: Illustration of PTC and CRS technologies. a) Parabolic Trough Concentrator (Andasol 3, Spain) [80]. b) Central Receiver System (Gemasolar, Spain) [81].	57
Figure 3.2: Heat flux diagram for a high temperature STAC.	59
Figure 3.3: Spectral directional hemispherical reflectivity (SDHR) data for reference STAC. a) SDHR for reference STAC plotted from 0.28 $\mu m$ to 20 $\mu m$ . b) Spectral overlap from 1.6 $\mu m$ to 2.5 $\mu m$ between UV-VIS-NIR and FTIR spectrophotometers.	62
Figure 3.4: Pictures of absorber coatings applied on T91 flat and tubular metal substrates. a) Flat reference sample coated with the ref. SSC b) Flat reference sample coated with the ref. HSA black coating. c) Tubular samples, bare polished substrate and coated with the ref. SSC. d) Tubular samples, bare sand blasted substrate and coated with the ref. HSA black coating.	62
Figure 3.5: Synoptical diagram of STAC opto-thermal FoMs	63
Figure 3.6: Reference data for Solar Spectral Irradiance. a) SSI plotted for different AM values. b) Cumulative SSI fraction normalised by 1000 $W/m^2$ for different AM values.	65
Figure 3.7: Blackbody spectral irradiance. a) Planck's law of blackbody radiation for a temperature ranging from 25 °C to 1000 °C b) Cumulative fraction of Stefan-Boltzmann law.	66
Figure 3.8: Comparison of solar and blackbody spectral irradiances. a) Spectral irradiances normalised by their maximum value. b) Normalised cumulative spectral irradiances. The solar spectral irradiance is normalised by the integral value computed at AM1.5d from 0.28 $\mu m$ to 4 $\mu m$ , while the blackbody spectral irradiance is normalised with respect to Stefan Boltzmann law ( $\sigma T^4$ ).	67
Figure 3.9: Calculation of $\alpha_{sol}$ (Eq.3.6) from 0.28 $\mu m$ to 2.5 $\mu m$ a) as a function of AM for reference coatings. b) Cumulative solar absorptance according to (Eq.3.7) considering the coating SDHR.	73
Figure 3.10: Calculation of thermal emittance $\epsilon_{th}$ (Eq.3.8-3.9) a) as a function of $T_{abs}$ for reference coatings. b) Cumulative thermal emittance at 600 °C according to (Eq.3.10) considering the coating SDHR.	74
Figure 3.11: Spectral curve fitting of reference SSC with parameterised spectral models. a) Comparison of spectral models. b) Residuals for logistic models derived from (Eq.3.12).	76

Figure 3.12: Selectivity indices as a function of absorber temperature  $T_{abs}$  a) Selectivity ratio  $S_i$   
 b) normalised selectivity ratio  $S_i^*$ ..... 76

Figure 3.13: Comparison of the reference black coating and SSC as a function of  $C_x$  and  $T_{abs}$ . a)  
 Marginal useful heat flux difference  $\Delta q_{use}$  b) Marginal opto-thermal efficiency  $\Delta \eta_{opt-th}$  ..... 77

Figure 3.14: Spectral analysis of STAC opto-thermal efficiency. a)  $C_x = 250$ ,  $T_{abs} = 600$  °C. b)  $C_x =$   
 $850$ ,  $T_{abs} = 300$  °C..... 78

Figure 3.15: Contour map of trade-off factor as a function of  $C_x$  and  $T_{abs}$ . ..... 79

Figure 3.16: Calculation of  $T_{SST,max}$  a) as a function of  $C_x$  for all reference coatings. b) Calculation  
 at  $C_x = 1000$  for reference STACs, sweeping the  $T_{abs}$  parameter beyond the reference coating  
 operating temperature range. .... 80

Figure 3.17: Calculation of solar reflectance indices as a function of  $C_x$ . a) SRI b) SRI\*..... 80

Figure 3.18: a)  $S_i^*$  as a function of  $\alpha_{sol}$  and  $\epsilon_{th}$ . b)  $T_{SST,max}$  as a function of  $\alpha_{sol}$  and  $\epsilon_{th}$  ( $C_x = 1000$ )  
 ..... 81

Figure 3.19: Thermal efficiency  $\eta_{thermal}$  for STAC with  $f_{Carnot} = 70\%$  a)  $C_x = 100$  b)  $C_x = 1000$ ..... 81

Figure 3.20: Peak efficiency temperature  $T_{peak,opt}$  as a function of  $C_x$  for reference STAC..... 82

Figure 4.1: Laboratory intercomparison – location of participants..... 99

Figure 4.2: Comparison of spectral ranges. a) Global overview b) SOC portable devices. .... 101

Figure 4.3: Comparison of spectral ranges for benchtop spectrophotometers. .... 101

Figure 4.4: Benchtop spectrophotometers a) Perkin Elmer Lambda 1050 b) Perkin Elmer Frontier  
 FTIR with Pike Ltd integrating sphere (upward sample positioning). c) Bruker Vertex 80 with  
 both integrating spheres. .... 102

Figure 4.5: Portable reflectometers and emissometers. a) SOC 410-Vis-IR portable solar  
 reflectometer and emissometer. b) D&S AE1/RD1 c) AZ Technology Temp 2000A..... 103

Figure 4.6: Flat coated samples a) Black coating b) SSC..... 103

Figure 4.7: Spectral directional hemispherical reflectivity (SDHR) of calibrated reference  
 samples, including  $2\sigma$  spectral uncertainty bands in the infrared range for black and SSC  
 calibrated reference samples. .... 104

Figure 4.8: Spectral weighting functions. a) ASTM G173-03 reference solar spectra. b) ASTM  
 G173-03 AM1.5d and blackbody spectra at 25 °C and 750 °C. c) Fraction of Stefan Boltzmann  
 law ( $\sigma T^4$ ) as a function of blackbody temperature for benchtop spectrophotometers d) Fraction  
 of  $\sigma T^4$  for portable emissometers..... 107

Figure 4.9: Opto-thermal efficiency a) trade-off factor  $Z$  b) weighting coefficient for  $\epsilon_{th}$   
 uncertainty. .... 109

Figure 4.10: UV-VIS-NIR spectral datasets. a) Black coating, b) Solar selective coating. .... 110

Figure 4.11: Infrared spectral datasets. a) Black coating, b) Solar selective coating..... 110

Figure 4.12: Concatenated spectral datasets from 0.3  $\mu m$  to 16  $\mu m$ . a) Black coating, b) Solar  
 selective coating. .... 110

Figure 4.13: Spectral deviation between UV-VIS-NIR and FTIR spectrophotometers. a) Spectral  
 deviation, black coating b) Spectral deviation, solar selective coating. c) Average mismatch (2  
 – 2.5  $\mu m$ ), black coating. d) Average mismatch (2 – 2.5  $\mu m$ ), solar selective coating..... 111

Figure 4.14: Solar absorptance calculations according to ASTM G173-03 a) Black coating,  
 direct+circumsolar, b) Solar selective coating, direct+circumsolar, c) HSA Black coating,  
 AM0/AM1.5g/AM1.5d d) Solar selective coating, AM0/AM1.5g/AM1.5d..... 112

Figure 4.15: Thermal emittance calculations. For benchtop spectrophotometers, the integration  
 interval spans here from 0.3  $\mu m$  to 16  $\mu m$ . a) Black coating b) Solar selective coating..... 113

Figure 4.16: Deviation in $\epsilon_{th}$ calculations after adjusting the integration interval from 16 $\mu\text{m}$ toward 50 $\mu\text{m}$ .....	114
Figure 4.17: Opto-thermal efficiency $\eta_{opt-th}$ a) Black coating b) Solar selective coating. ....	115
Figure 4.18: Propagation of uncertainty on the opto-thermal efficiency.....	115
Figure 5.1: a) H230 sample coupons submitted for RT and OT measurements. Samples are shown upon return after both RT and OT test campaigns. b) SiC samples submitted for RT and OT measurements. Top: original samples. Bottom: Square inch samples cut by PROMES-CNRS for OT measurements up to 500 °C.....	125
Figure 5.2: a) Perkin Elmer Lambda 1050 spectrophotometer. b) Perkin Elmer Frontier FTIR with Pike Ltd Mid-IR downward looking integrating sphere. c) Geometrical configuration for the Lambda 950/1050 integrating sphere. d) Geometrical configuration for the Pike Ltd mid-IR integrating sphere.....	126
Figure 5.3: Spectral directional hemispherical reflectivity (SDHR) of flat baseline coupons...	128
Figure 5.4: CEA laboratory setup for spectral emissivity measurements at operating temperature. a) Benchtop optical assembly. b) Sample holder overview.....	129
Figure 5.5: MEDIASE setup mounted at the 1 MW solar furnace in Odeillo, France. ....	130
Figure 5.6: a) Reference solar spectrum [31] and blackbody spectra at 25 °C and 800 °C. b) Fraction of Stefan-Boltzmann law ( $f\sigma T^4$ ) as a function of blackbody temperature for different spectral ranges. ....	133
Figure 5.7: Solar absorptance $\alpha_{sol}$ results for H230 sample coupons (RT measurements). a) oxidised H230, absolute values. b) oxidised H230, Z-score. c) Pyromark 2500, absolute values. d) Pyromark 2500, Z-score. e) Industrial black coating, absolute values. f) Industrial black coating, Z-score. g) SiC samples, absolute values. h) SiC samples, Z-score.....	136
Figure 5.8: Thermal emittance $\epsilon_{th,calc}(T)$ for H230 and SiC sample coupons (RT measurements). a) oxidised H230, b) Pyromark 2500, c) Industrial black coating. d) SiC sample coupons. ....	137
Figure 5.9: Thermal emittance $\epsilon_{th,calc}(800\text{ °C})$ for H230 and SiC samples measured at RT. a) oxidised H230, absolute values. b) oxidised H230, Z-score. c) Pyromark 2500, absolute values. d) Pyromark 2500, Z-score. e) Industrial black coating, absolute values. f) Industrial black coating, Z-score. f) SiC, absolute values. g) SiC, Z-score.....	139
Figure 5.10: Spectral measurements recorded for H230 samples coupons from 220 °C to 760 °C by CEA laboratory.....	140
Figure 5.11: Spectral measurements recorded for H230 sample coupons from 25 °C to 500 °C by PROMES-CNRS laboratory with the InGaAs detector (1-2 $\mu\text{m}$ ).....	141
Figure 5.12: Spectral measurements recorded for H230 sample coupons from 25 °C to 500 °C by PROMES-CNRS laboratory with the DTGS detector (>2 $\mu\text{m}$ ).....	141
Figure 5.13: Spectral measurements recorded for SiC sample coupons from 25 °C to 500 °C by PROMES-CNRS laboratory with the InGaAs detector (1-1.5 $\mu\text{m}$ ).....	142
Figure 5.14: Spectral measurements recorded for SiC sample coupons from 25 °C to 500 °C by PROMES-CNRS laboratory with the DTGS detector (>1.5 $\mu\text{m}$ ).....	142
Figure 5.15: Spectral measurement datasets recorded at OT from 618 °C to 805 °C by PROMES-CNRS with MEDIASE setup. Samples investigated: D01A, D01B, D02A, D02B, S3, S4. ....	143
Figure 5.16: Influence of incidence angle on thermal emittance $\epsilon_{th,meas}(T)$ for measurements recorded at OT from 618 °C up to 805 °C by PROMES-CNRS with MEDIASE setup. ....	143

Figure 5.17: Comparison of thermal emittance  $\epsilon_{th}(T)$  for H230 and SiC sample coupons obtained from RT and OT measurements. a) oxidised H230, b) Pyromark 2500, c) Industrial grade black coating, d) SiC sample coupons..... 144

Figure 6.1: Field Instrumentation for CRS monitoring a) Thermographic Monitoring (LWIR) of Solar Power Tower (Infratec SPTC) [35] b) Surface Optics (SOC) portable 410-Vis-IR solar reflectometer and emissometer [36]..... 153

Figure 6.2: Spectral response of portable instrument measurement heads in arbitrary units. a) 410 Solar reflectometer (0.33 -2.5  $\mu\text{m}$ ). b) ET100 emissometer (1.5 – 21  $\mu\text{m}$ )..... 154

Figure 6.3: Radiometric chain for ground-based thermography of central receiver systems. 158

Figure 6.4: SWIR spectral measurements of reference materials from ambient temperature up to 500 °C. a) H230, pre-oxidised at 800 °C for 100 hours. b) Pyromark 2500 applied on H230 substrate..... 161

Figure 6.5: Spectral response of camera system components..... 162

Figure 6.6: Camera system response. a) Virtual blackbody calibration for each NB filter [200-1000] °C. b) Virtual greybody calibration for each ratio thermometer [200-1000] °C..... 162

Figure 6.7: Spectral simulation of atmospheric paths. Simulation parameters: SZA= 60° (AM2),  $d_2= 500\text{ m}$ ,  $d_3= 350\text{ m}$ ,  $p_{atm}= 960\text{ mbar}$ ,  $T_{amb}= 30\text{ °C}$ , RH= 30%. a) Atmospheric transmissivity  $\tau_{atm}$ , for each path. b) Atmospheric transmissivity; path product and path 3..... 163

Figure 6.8: Surface emittance and atmospheric transmittance. Simulation parameters: Pyromark 2500, SZA= 60° (AM2),  $d_2= 500\text{ m}$ ,  $d_3= 350\text{ m}$ ,  $p_{atm}= 960\text{ mbar}$ ,  $T_{amb}= 30\text{ °C}$ , RH= 30%. a) Spectral emissivity  $\epsilon_{surf}(\lambda)$  for Pyromark 2500 and atmospheric transmissivity for path 3  $\tau_{atm,path3}(\lambda)$ . b) Surface band emittance  $\epsilon_{surf}(\text{filter})$  and atmospheric band transmittance  $\tau_{atm,path3}(\text{filter})$  for each NB filter..... 164

Figure 6.9: Spectral radiometric balance. Simulation parameters: Pyromark 2500:  $T_{surf}= 600\text{ °C}$ ,  $C_x= 300$ , SZA= 60° (AM2),  $d_2= 500\text{ m}$ ,  $d_3= 350\text{ m}$ ,  $p_{atm}= 960\text{ mbar}$ ,  $T_{amb}= 30\text{ °C}$ , RH= 30%. a) Spectral irradiance, absolute values [ $\text{W}\cdot\text{m}^{-2}\cdot\mu\text{m}^{-1}$ ]. b) Relative values [%]..... 164

Figure 6.10: Band radiometric balance. Simulation parameters: Pyromark 2500;  $T_{surf}= 600\text{ °C}$ ,  $C_x= 300$ , SZA= 60° (AM2),  $d_2= 500\text{ m}$ ,  $d_3= 350\text{ m}$ ,  $p_{atm}= 960\text{ mbar}$ ,  $T_{amb}= 30\text{ °C}$ , RH= 30%). a) Radiometric signal, absolute values [ $\text{W}\cdot\text{m}^{-2}$ ]. b) Relative values [%]..... 165

Figure 6.11: Contour plot of  $OD_{path1}$  as a function AH and SZA. a) NB1386-10 b) NB1912-10 ..... 167

Figure 6.12: Contour plot of  $\tau_{atm,path3}$  as a function of AH and  $d_3$ . a) NB1386-10 b) NB1912-10 ..... 167

Figure 6.13: Analysis of  $\Delta T/T$  as a function of SZA, AH,  $T_{surf}$  and  $C_x$ . Boundary conditions:  $d_3=350\text{ m}$ , Pyromark 2500.  $p_{atm}=960\text{ mbar}$ ,  $T_{amb}=30\text{ °C}$ , RH: (20...50) % ..... 168

Figure 6.14. Correlation of  $\Delta\epsilon$  and  $\Delta T/T$  for the first SWIR ratio thermometer. Boundary conditions:  $\Delta T/T < 2\%$ ;  $d_3=350\text{ m}$ . a) Pyromark 2500. b) Oxidised H230..... 169

Figure 6.15: Contour plot of  $\tau_{atm,path3}$  as a function of AH and  $d_3$ . a) NB1640-25 b) NB2090-25 ..... 169

Figure 6.16: Analysis of relative temperature error  $\Delta T/T$  as a function of  $T_{surf}$ . Boundary conditions:  $d_3=350\text{ m}$ ,  $C_x=0$ . a) Pyromark 2500. b) oxidised H230..... 170

Figure 6.17: Correlation of  $\Delta\epsilon$  and  $\Delta T/T$  for the second SWIR ratio thermometer. Boundary conditions:  $C_x=0$ ,  $d_3=350\text{ m}$ . a) Pyromark 2500. b) Oxidised H230..... 171



## List of tables

Table 3.1: Summary of boundary conditions for PTC and CRS applications relevant for STAC selection.....	58
Table 3.2: Validity and limitations of modelling assumptions for PTC and CRS applications...61	61
Table 3.3: Inventory of selected STAC opto-thermal FoMs.....	64
Table 3.4: Summary of SSC model parameterization.....	68
Table 3.5: Sensitivity of opto-thermal efficiency $\eta_{\text{opt-th}}$ ; $G_{\text{sol}}(\text{AM1.5d})= 900 \text{ W/m}^2$ ; $T_{\text{abs}}= 600 \text{ }^\circ\text{C}$ , $T_{\text{sky}}= 25 \text{ }^\circ\text{C}$ .....	70
Table 3.6: Results of SSC spectral model curve fitting applying ordinary least squares.....	75
Table 3.7: Comparison of reference STACs for different opto-thermal FoMs.....	83
Table 4.1: List of participants.....	99
Table 4.2: Inventory of measurement instruments.....	100
Table 4.3: Comparison of spectral ranges reported in raw spectral datasets.....	101
Table 4.4: UV-VIS-NIR instrument specifications.....	102
Table 4.5: Infrared instrument specifications.....	102
Table 4.6: Inventory of measurement datasets.....	104
Table 4.7: Calibrated reference samples for baseline measurements.....	105
Table 4.8: Spectral mismatch statistics.....	111
Table 4.9: Solar absorptance calculations according to ASTM G173-03.....	113
Table 4.10: Thermal emittance calculations. Integration interval for spectrophotometers: from $0.3 \text{ }\mu\text{m}$ to $16 \text{ }\mu\text{m}$ . (*) The outlying value reported for the SSC by the D&S AE1/RD1 is omitted in the standard deviation calculation.....	113
Table 5.1: Test campaign participants and roles.....	124
Table 5.2: H230 flat sample coupons for RT and OT campaigns. Sample thickness: 2 mm... 125	125
Table 5.3: Inventory of spectrophotometer for RT measurements.....	127
Table 5.4: Overview of spectrophotometer characteristics.....	127
Table 5.5: Spectral ranges and sampling resolutions of raw datasets.....	127
Table 5.6: Baseline flat reference coupons used for calibration.....	128
Table 5.7: Temperature and spectral ranges for OT measurements.....	129
Table 5.8: Summary of solar absorptance $\alpha_{\text{sol}}$ results for H230 and SiC samples at RT.....	135
Table 5.9: Thermal emittance $\varepsilon_{\text{th,calc}}$ ( $800 \text{ }^\circ\text{C}$ ) results for H230 sample coupons (RT measurements).....	138
Table 6.1: Key instrumentation specifications for CRS monitoring.....	153
Table 6.2: Specifications of NB filters for SWIR ratio thermography.....	161
Table 6.3: Sakuma Hattori fit coefficients for virtual blackbody calibration (Eq.6.18).....	162
Table 6.4: Fit coefficients for virtual greybody calibration (Eq.6.19).....	163
Table 6.5: Inventory of simulation parameters.....	166
Table 6.6: First SWIR ratio thermometer. Reference values $\varepsilon_{\text{surf}}(\text{filter})$ values for Pyromark 2500 and oxidised H230.....	169
Table 6.7: Second SWIR ratio thermometer. Reference $\varepsilon_{\text{surf}}(\text{filter})$ values for Pyromark 2500 and oxidised H230.....	170

## Nomenclature

### Abbreviations

A.U.	Arbitrary Units
AFD	Allowable Flux Density
AM	Air Mass
ARC	Anti-Reflective Coating
ASTM	American Society for Testing and Materials
BoP	Balance of Plant
BSI	Blackbody Spectral Irradiance
CEA	Commissariat à l'énergie atomique et aux énergies alternatives
CERMET	Ceramic Metallic
CIEMAT	Centro de Investigaciones Energéticas, Medioambientales y Tecnológicas
CNRS	Centre National de la Recherche Scientifique
CNT	Carbon Nanotube
COTS	Commercial of the Shelf
CPC	Compound Parabolic Collector
CPV	Concentrated Photovoltaics
CRS	Central Receiver System
CSP	Concentrating Solar Power
CST	Concentrating Solar Thermal
CVD	Chemical Vapor Deposition
D&S	Devices and Services
DLR	German Aerospace Center
DMP	Double Modulation Pyrometry
DNI	Direct Normal Irradiance
DOE	Design of Experiments
DTGS	Deuterated Triglycine Sulfate
EPC	Engineering, Procurement and Construction
FAMP	Flash Assisted Multiwavelength Pyrometry
FoM	Figure of Merit
FT	Fourier Transform
GHG	Greenhouse Gases
HCE	Heat Collection Element
HSA	High Solar Absorptance
HTF	Heat Transfer Fluid
HUJI	Hebrew University of Jerusalem
ICE	Internal Combustion Engine
IEA	International Energy Agency
INTA	Instituto Nacional de Técnica Aeroespacial
IPCC	Intergovernmental Panel on Climate Change
IPH	Industrial Process Heat
IR	Infrared
IRENA	International Renewable Energy Agency
ISE	Fraunhofer Institute for Solar Energy Systems
ISO	International Organization for Standardization
JCR	Journal Citation Reports
JIF	Journal Impact Factor

LCOC	Levelised Cost of Coating
LCOE	Levelised Cost of Electricity
LF	Line Focusing
LNEG	Laboratório Nacional de Energia e Geologia
LWIR	Longwave Infrared (8 - 14 $\mu\text{m}$ )
m.a.s.l.	Meters above sea level
MCT	Mercuric Cadmium Telluride
MEDIASE	Moyens d'Essais et de Diagnostic pour l'Espace et l'Energie
MLS	Mid Latitude Summer
MODTRAN	MODerate resolution atmospheric TRANsmission
MWIR	Midwave Infrared (3 -5 $\mu\text{m}$ )
NB	Narrow Bandpass
NIR	Near Infrared
NIST	U.S. National Institute of Standards and Technology
NPL	U.K. National Physical Laboratory
NREL	National Renewable Energy Laboratory
NUC	Non-Uniformity Correction
O&M	Operation and Maintenance
OPAC	Optical and Ageing Characterization
OT	Operating Temperature
PF	Point Focusing
PROMES	Procédés et Matériaux pour l'Energie Solaire
PSA	Plataforma Solar de Almería
PTC	Parabolic Trough Concentrator, Parabolic Trough Collector
PTFE	Polytetrafluoroethylene
PTR	Parabolic Trough Receiver
PV	Photovoltaics
PVD	Physical Vapor Deposition
RMSE	Root Mean Square Error
RT	Room Temperature
SDG	Sustainable Development Goal
SDHR	Spectral Directional Hemispherical Reflectivity
SEGS	Solar Electricity Generation Systems
SETO	Solar Energy Technologies Office
SGS	Steam Generation System
SH	Sakuma-Hattori
SMARTS	Simple Model of the Atmospheric Radiative Transfer of Sunshine
SOC	Surface Optics Corporation
SPTC	Solar Power Tower Check
SRF	Spectral Response Function
SSC	Spectral Selective Coating, Solar Selective Coating
SSI	Solar Spectral Irradiance
SST	Steady-State Temperature
STAC	Solar Thermal Absorber Coating
STE	Solar Thermal Electricity
STEG	Solar Thermal Electric Generator
SWIR	Shortwave Infrared (0.9 -2.5 $\mu\text{m}$ )
TBC	Thermal Barrier Coating

TES	Thermal Energy Storage
TNO	Netherlands Organization for Applied Scientific Research
U.S.A.	United States of America
UAL	Universidad de Almería
UHI	Urban Heat Island
UN	United Nations
UV	Ultraviolet
VIS	Visible

## **Greek symbols**

<b>Symbol</b>	<b>Description</b>	<b>Unit</b>
$\alpha$	Absorptivity, Absorptance	[%]
$\Delta$	Difference	[-]
$\varepsilon$	Emissivity, Emittance	[%]
$\eta$	Efficiency	[%]
$\theta$	Incidence angle	[°]
$\lambda$	Wavelength	[ $\mu\text{m}$ , nm]
$\rho$	Reflectivity, Reflectance	[%]
$\tau$	Transmissivity, Transmittance	[%]
$\phi$	Radiometric signal	[ $\text{W}\cdot\text{m}^{-2}$ ]

## **Universal Physical Constants**

$c$	Speed of light in vacuum	299792458	[ $\text{m}\cdot\text{s}^{-1}$ ]
$h$	Planck constant	$6.62607015 \cdot 10^{-34}$	[J.s]
$k$	Boltzmann constant	$1.380649 \cdot 10^{-23}$	[J.K <sup>-1</sup> ]
$\sigma$	Stefan-Boltzmann constant	$5.670374419 \cdot 10^{-8}$	[ $\text{W}\cdot\text{m}^2\cdot\text{K}^{-4}$ ]

Values retrieved from (NIST, CODATA): <https://physics.nist.gov/cuu/Constants/index.html>

## English symbols

<b>Symbol</b>	<b>Description</b>	<b>Unit</b>
$A_1$	Sakuma Hattori fit coefficient	$[\text{W.m}^{-2}]$
$A_2$	Sakuma Hattori fit coefficient	$[\text{K}^{-1}]$
$A_a$	Mirror aperture area	$[\text{m}^2]$
$A_r$	Receiver aperture area	$[\text{m}^2]$
$AH$	Absolute Humidity	$[\text{g.m}^{-3}]$
$B_1$	Greybody ratio fit coefficient	$[\text{K}^{-1}]$
$B_2$	Greybody ratio fit intercept	$[-]$
$BF$	Blackbody function	$[-]$
$Cr$	Adimensional number	$(-)$
$CV$	Coefficient of variation	$[-]$
$CWL$	Central wavelength	$[\mu\text{m}]$
$C_x$	Concentration factor	$[-]$
$d$	Distance	$[\text{m}]$
	Direct+circumsolar	$[-]$
$E$	Spectral radiant exitance	$[\text{W.m}^{-2}.\mu\text{m}^{-1}]$
$f$	Fraction, factor	$[\%], [-]$
$f_{Carnot}$	Fraction of Carnot efficiency	$[\%]$
$f_{shape}$	Spectral shape factor	$[-]$
$f_{SSC}$	Spectral selective coating model	$[-]$
$f_{\sigma T^4}$	Blackbody fraction	$[\%]$
$F_{view}$	View factor	$[-]$
$FWHM$	Full Width at Half Maximum	$[\mu\text{m}]$
$G$	Spectral irradiance	$[\text{W.m}^{-2}.\mu\text{m}^{-1}]$
$h$	Heat transfer coefficient	$[\text{W.m}^{-2}.\text{K}^{-1}]$
$I$	Spectral intensity	$[\text{W.m}^{-2}.\mu\text{m}^{-1}]$
$I$	Intensity	$[-]$
$k$	Thermal conductivity	$[\text{W.m}^{-1}.\text{K}^{-1}]$
$L$	Spectral radiance	$[\text{W.m}^{-2}.\mu\text{m}^{-1}.\text{sr}^{-1}]$
$NGCF$	Non-Grey Compensation Factor	$[-]$
$OD$	Optical Depth	$[-]$
$p$	Pressure	$[\text{mbar}]$
$\dot{q}''$	Heat flux	$[\text{W.m}^{-2}]$
$QE$	Quantum Efficiency	$[\%]$
$RH$	Relative Humidity	$[\%]$
$S$	Radiometric signal	$[\text{W.m}^{-2}]$
$S_i$	Selectivity index	$[-]$
$S_i^*$	Normalized Selectivity index	$[-]$
$SR$	Signal Ratio	$[-]$
$SRI$	Solar Reflectance Index	$[-]$
$SRI^*$	Normalized Solar Reflectance Index	$[\%]$
$SZA$	Solar Zenith Angle	$[\circ]$
$T$	Temperature	$[\circ\text{C}, \text{K}]$
$Z$	Trade-off factor, Z-score	$[-]$

## **Subscripts**

<i>abs</i>	Absorber
<i>amb</i>	Ambient
<i>atm</i>	Atmosphere
<i>band</i>	Bandpass filter
<i>base</i>	Baseline
<i>BB</i>	Blackbody
<i>calib</i>	Calibration
<i>cam</i>	Camera
<i>Carnot</i>	Carnot
<i>coating</i>	Coating
<i>cold</i>	Cold sink
<i>cond</i>	Conduction
<i>conv</i>	Convection
<i>cut-off</i>	Cut-off
<i>detector</i>	Detector
<i>env</i>	Ambient environment
<i>filter</i>	Filter
<i>g</i>	Global
<i>hot</i>	Hot sink
<i>HTF</i>	Heat Transfer Fluid
<i>IR</i>	Infrared
<i>lens</i>	Objective lens
<i>max</i>	Maximum
<i>meas</i>	Measurement
<i>metal</i>	Metal substrate
<i>mirror</i>	Mirror
<i>opt</i>	Optical
<i>opt-th</i>	Opto-thermal
<i>path,i</i>	Atmospheric path (1,2,3)
<i>peak</i>	Peak
<i>rad</i>	Radiation
<i>ref</i>	Reference
<i>sample</i>	Sample
<i>sensor</i>	Sensor
<i>sky</i>	Sky
<i>sol</i>	Solar
<i>SST</i>	Steady-State Temperature
<i>sun</i>	Sun
<i>surf</i>	Receiver surface
<i>th, thermal</i>	Thermal
<i>trade-off</i>	Trade-Off
<i>use</i>	Useful
<i>window</i>	Protective window
<i>{x,y}</i>	Pixel
<i>z</i>	Zenith
<i>zero</i>	Zeroline

## Resumen

El cambio climático es uno de los principales retos a los que se enfrenta la humanidad en el siglo XXI. Es imprescindible aprovechar la energía solar para descarbonizar el sistema energético mundial. Se espera que la tecnología de concentración solar térmica (CST) desempeñe un papel decisivo en el suministro de calor para procesos industriales de media y alta temperatura. Los receptores térmicos y los recubrimientos absorbentes solares térmicos son componentes claves de los sistemas CST. La monitorización de las características opto-térmicas de dichos recubrimientos, tales como la absorbancia solar, la emitancia térmica y la temperatura de superficie, es crítica para el funcionamiento eficiente y durable de dichos sistemas.

El objetivo principal de esta tesis doctoral es desarrollar un marco para el análisis óptico-térmico de los recubrimientos absorbentes solares térmicos para CST. El análisis óptico-térmico se basa principalmente en técnicas de medición infrarroja, como la espectrofotometría y la radiometría multiespectral. El análisis se desarrolla para materiales relevantes, primero en condiciones de laboratorio, tanto a temperatura ambiente como de funcionamiento, hasta 800 °C. Se introduce una nueva técnica de medición para la caracterización opto-térmica in situ de recubrimientos absorbentes solares térmicos en sistemas de receptor central.

El rendimiento óptico-térmico de un recubrimiento absorbente solar térmico para aplicaciones CSP es sensible al factor de concentración  $C_x$  y a la temperatura de la superficie  $T$ . Mientras que los recubrimientos solares selectivos son definitivamente relevantes para los colectores cilindro-parabólicos, los recubrimientos negros con una alta absorbancia solar son más relevantes para los sistemas de receptor central, debido al mayor factor de concentración.

Las campañas de medición de intercomparación han demostrado que los valores de absorbancia solar derivados de las mediciones espectrales a temperatura ambiente son reproducibles con una desviación estándar por debajo del 1%, para los recubrimientos selectivos solares, los recubrimientos negros, el Haynes 230 (H230) oxidado y el carburo de silicio (SiC). Para los mismos materiales, se observó una desviación estándar superior de ~ 3% para los valores de emitancia térmica derivados de mediciones espectrales a temperatura ambiente. La comparación de los valores de emitancia térmica derivados de la temperatura ambiente y de funcionamiento hasta 800 °C demuestran un acuerdo bastante coherente para H230 oxidado, los recubrimientos negros y SiC.

La caracterización opto-térmica a distancia de materiales grises como el H230 oxidado y los recubrimientos negros es factible en un Sistema Receptor Central utilizando termografía infrarroja de onda corta. Se analizaron respectivamente dos configuraciones para condiciones de funcionamiento con y sin radiación solar concentrada.

### **Palabras clave:**

Energía solar concentrada; Energía solar térmica; Recubrimiento absorbente; Absorbancia solar; Emitancia térmica; Espectrofotometría; Termografía infrarroja





## Abstract

Climate change is one of the major challenge faced by mankind in the 21<sup>st</sup> century. Solar energy must be harnessed for decarbonising the global energy system. Concentrated Solar Thermal (CST) technology is expected to play a decisive role in supplying heat for medium to high temperature industrial processes. Thermal receivers and solar thermal absorber coatings are key components in CST systems. The monitoring of coating opto-thermal characteristics, such as solar absorptance, thermal emittance and surface temperature, is critical for the efficient and durable operation of such systems.

The main objective of this doctoral thesis is to develop a framework for the opto-thermal analysis of solar thermal absorber coatings for CST. The opto-thermal analysis is mostly based on infrared measurement techniques, such as spectrophotometry and multispectral radiometry. The analysis is developed for relevant materials, first under laboratory conditions, both at ambient and operating temperature, up to 800 °C. A new measurement technique is introduced for the in-situ opto-thermal characterisation of solar thermal absorber coatings in Central Receiver Systems (CRS).

The opto-thermal performance of a solar thermal absorber coating for CSP applications is sensitive to the concentration factor  $C_x$  and the surface temperature  $T$ . While solar selective coatings are definitely relevant for parabolic trough collectors, high solar absorptance black coatings are more relevant for central receiver systems, due to the higher concentration factor.

Intercomparison measurement campaigns have shown that solar absorptance values derived from room temperature spectral measurements are reproducible with a low standard deviation of 1%, for solar selective coatings, black coatings, oxidized Haynes 230 (H230) and silicon carbide (SiC). For the same materials, a higher standard deviation of ~ 3% was observed for thermal emittance values derived from room temperature spectral measurements. The comparison of thermal emittance values derived from room and operating temperature up to 800 °C show a rather consistent agreement for oxidised H 230, black coatings and SiC.

The remote opto-thermal characterization of grey materials such as oxidised H230 and black coatings is feasible in a Central Receiver System using shortwave infrared thermography. Two configurations were respectively analysed for on-sun and off-sun operating conditions.

### **Keywords:**

Concentrated Solar Power; Solar thermal; Absorber coating;  
Solar absorptance; Thermal emittance; Spectrophotometry; Infrared thermography



## **Chapter 1. Introduction**



# 1 Introduction

## 1.1 Context

### 1.1.1 A civilisational challenge

According to the Bulletin of Atomic Scientists, the Doomsday Clock ticks at 90 seconds to mid-night in 2023. Mankind lives in "a time of unprecedented danger" [1]. Beside the nuclear risk, inherited from World War II, Human activities have been impacting the stability and resilience of Earth ecosystems, threatening the welfare of our future generations. According to a team of international scientists [2], six out of nine planetary boundaries have been already crossed as of 2023 (Figure 1.1).

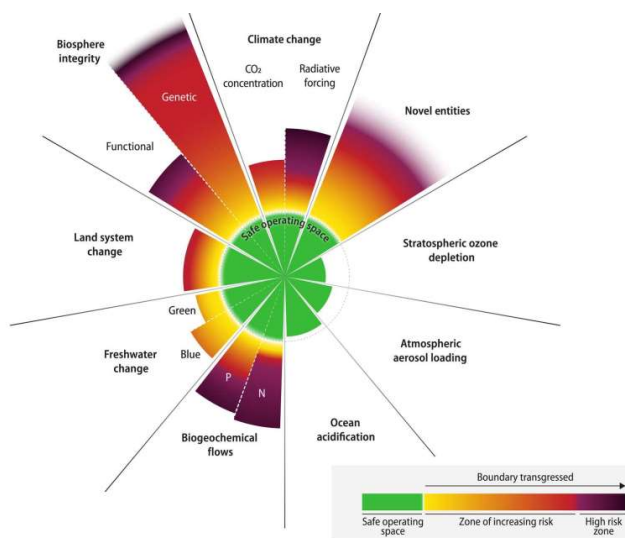


Figure 1.1: 2023 status of control variables for all nine planetary boundaries [2].

Climate change has become one of the major threats for our modern civilization. According to the Intergovernmental Panel on Climate Change (IPCC), "Human activities, principally through emissions of greenhouse gases, have **unequivocally** caused global warming, with global surface temperature reaching 1.1 °C above 1850-1900 in 2011-2020" (A1) [3]. Mitigation pathways have been defined to contain global warming within 1.5 ... 2 °C above pre-industrial levels. These mitigation pathways "involve rapid and deep and, in most cases, immediate greenhouse gas emissions reductions in all sectors this decade" (B6) [3].

Reducing drastically our greenhouse gas (GHG) emissions, not exclusively carbon dioxide CO<sub>2</sub>, requires a structural transformation of the global energy sector, involving a worldwide transition from fossil fuels to renewable energies, energy efficiency, electrification as well as energy storage, at multiple time scales. The UN Agenda 2030 defines a set of 17 Sustainable Development Goals (SDGs) (Figure 1.2), among which stands **Goal 7: Ensure access to affordable, reliable, sustainable and modern energy for all**. According to the UN SDG 2023 report [4], "Modern renewables power nearly 30% of electricity, but remain low in heating and transport".

**Goal 7** is further declined in five targets for 2030: 7.1) Universal access to modern energy, 7.2) Increase global percentage of renewable energy, 7.3) Double the improvement in energy efficiency, 7.4) Promote access to research, technology and investments in clean energy, 7.5) Expand and upgrade energy services for developing countries.



Figure 1.2: Sustainable Development Goals defined by the UN in 2015 [4].

### 1.1.2 The relevance of solar energy

A look at supply side energy reserves for the planet [5] (Figure 1.3) shows that solar energy is by far the largest resource available on Earth, "even after accounting for reasonable deployment restrictions and presently achievable conversion efficiencies". As an order of magnitude, solar energy could supply about twelve times the world energy primary demand over a thirty years period. This order of magnitude tends to shift further upwards (~x27), assuming a full electrification of end usages. The combustion of fossil fuels in Internal Combustion Engines (ICEs) or building heating is indeed about three times less efficient than using directly electric motors in transportation or electrical heat pumps for space heating and cooling.

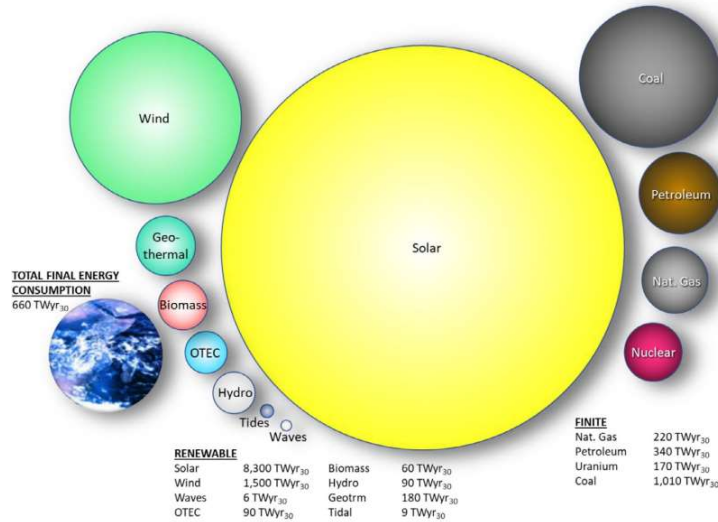


Figure 1.3: Recoverable energy reserves of renewable and finite energy resources over the next 30 years in comparison to the estimated total demand over the same period [5].

Since 2010, a dramatic reduction in renewable power generation costs has been observed, as documented by the International Renewable Energy Agency (IRENA) [6] (Figure 1.4). Today, renewable power systems have already achieved a lower Levelised Cost of Electricity (LCOE) than fossil fuels and are thus more cost-efficient. The LCOE of Solar Photovoltaics (PV) has plummeted by a factor x10 from 2010 until 2022, down to ~0.05 USD/kWh, while the LCOE of Concentrating Solar Power (CSP) has dropped by a factor x3, down to ~0.12 USD/kWh.

Electricity capacity and generations trends are shown below for Solar PV and CSP since 2011 in Figure 1.5 [7]. In 2022, the global PV installed capacity exceeded the 1 TW<sub>p</sub> landmark, while CSP reached 6.6 GW<sub>e</sub> (x150). As of 2021, the generation of solar PV reached ~1 PWh, while CSP reached nearly 14 TWh (x75). Solar PV experienced a steady global exponential growth, while CSP is currently deployed in approximately 20 countries (Figure 1.6), with an intermittent deployment since 1980s.

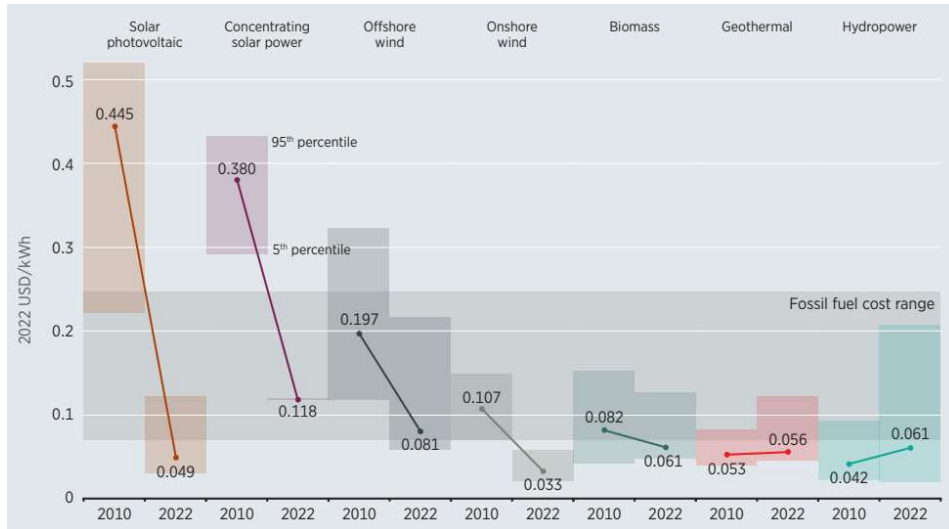


Figure 1.4: Levelised Cost of Electricity (LCOE) of renewable power systems [6].

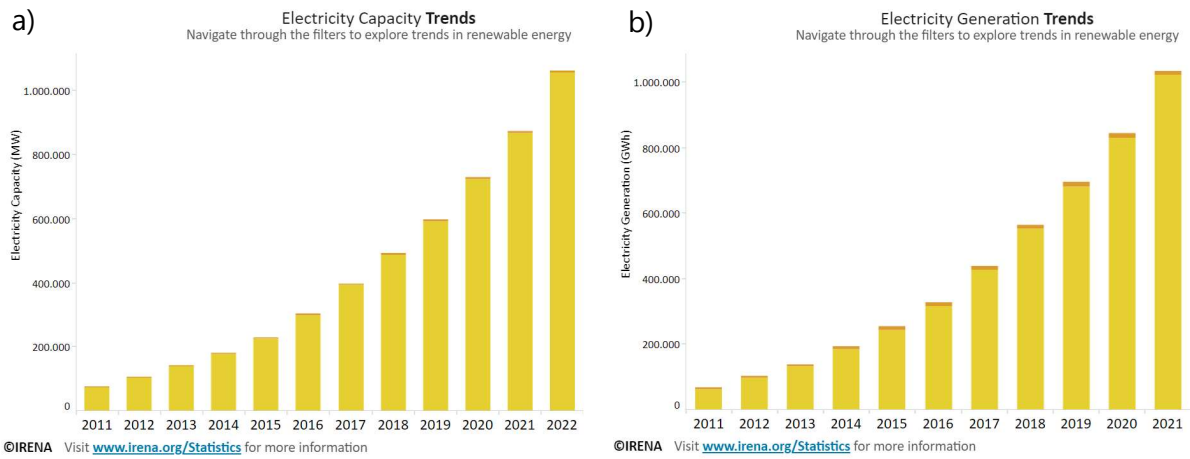


Figure 1.5: Electricity capacity and generation trends for Solar Energy since 2011 [7]. PV (yellow), CSP (orange). a) Power capacity in MW. b) Energy Generation in GWh.

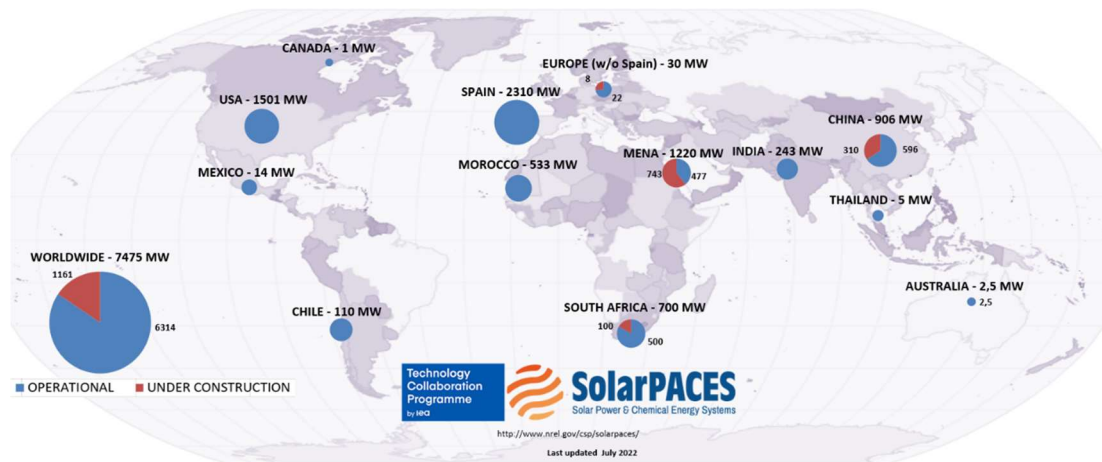


Figure 1.6: Global deployment of CSP projects in 2022 [8].

### 1.1.3 The role of CSP in the energy transition

The first commercial utility-scale CSP systems were built and commissioned in California, U.S.A from 1984 to 1990. These systems, known as Solar Electricity Generation Systems (SEGS) [9], had the architecture of a traditional thermal power plant, using solar Direct Normal Irradiance (DNI) as a “fuel” for Parabolic Trough Collectors (PTCs), generating steam. A steam turbine coupled a generator converted the steam to electricity, referred to as Solar Thermal Electricity (STE). Most of the SEGS, except SEGS IX, have been progressively decommissioned since 2015, as SEGS I-VIII power plants reached the end of their 30 years’ service lifetime.

Spain was the second country to develop a market for CSP systems. The former German company Solar Millennium GmbH developed the Andasol complex in the province of Granada, Spain. Three 50 MW<sub>e</sub> CSP plants using PTCs to generate STE, each with a molten salt thermal storage capacity of 7.5 hours, were built from 2006 to 2008 and started operation between 2008 and 2011. Several other projects were built and commissioned in Spain until 2014.

The deployment of CSP plants is shown in Figure 1.7. The construction of new utility-scale CSP plants has stalled in the U.S.A. and Spain since 2014, while new plants have been built and commissioned in emerging countries such as Chile, Morocco, South Africa, Middle East, India. In the recent years, most of utility-scale CSP projects are developed in China, while Australia is considered as an emerging market.

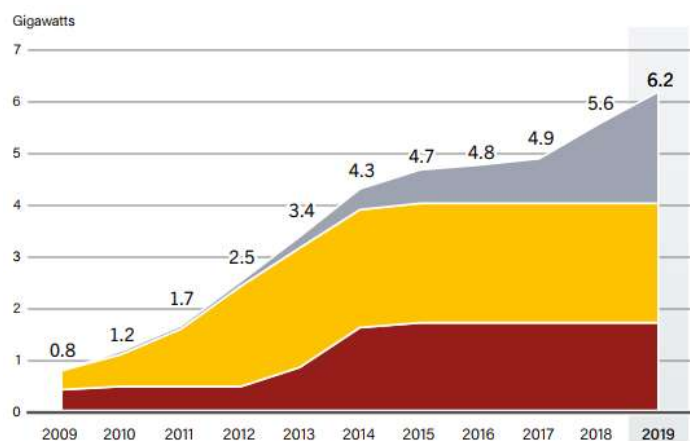


Figure 1.7: Deployment of CSP plants from 2009 to 2019 [10]. Red: United States of America (U.S.A.). Yellow: Spain. Grey: Other countries.

In the power market, CSP technology was directly competitive in terms of LCOE with Solar PV in the early 2010s (Figure 1.4). According to the U.S. SunShot Initiative [11] (Figure 1.8), The LCOE of utility-scale Solar PV in 2010 was 0.28 USD/kWh, while the value was CSP without storage was 0.21 USD/kWh. However, the price of PV modules plummeted due to significant economies of scale, as the cost of PV modules declined by at least 20% for each doubling of cumulative installed capacity [12]. This significant cost reduction, as well as the steady improvement of solar PV efficiency [13], fostered the widespread adoption of PV technology.

While solar PV is becoming a mainstream technology, CSP technology is yet at an early stage of commercial deployment. The U.S. Solar Energy Technologies Office (SETO) set ambitious cost reduction targets for CSP (Figure 1.8.b): 0.05 USD/kWh for baseload generation with at least 12 hours of storage and 0.10 USD/kWh for peaker plants with less than 6 hours of storage.



Meanwhile, the 2030 cost target for solar PV spans from 0.03 USD/kWh for utility-scale solar PV to 0.05 USD/kWh for residential solar PV (Figure 1.8.a). At the current rate of deployment, SunShot cost targets for solar PV are expected to be met before 2030, while the pipeline of commercial utility-scale CSP plants is yet restricted, despite recent constructions in China [14].



Figure 1.8: U.S. SunShot initiative 2030 Goals [11]. a) Solar PV b) CSP.

There is an ongoing debate regarding the respective roles and values of CSP and solar PV for the energy transition, while recent project developments actually combine PV and CSP in hybrid systems [15,16]. A discussion solely centered around LCOE is probably blind and biased, although it is currently the most popular metrics. The time-varying value of energy [17], the capacity factor of renewable power [18], the curtailment of excess renewable energy, the addition of storage capacity at different timescale [19] are further arguments to consider for a complex system analysis.

CSP technology, combined with Thermal Energy Storage (TES) [14,20,21] offers in principle baseload, dispatchable power around the clock. This is a serious alternative in sunny regions to traditional fossil fuel thermal power plants using coal, natural gas or uranium. In reality, TES technology has not been added systematically with CSP plants. Looking at the 44 Spanish 50 MW<sub>e</sub> CSP plants using PTCs built between 2006 and 2011, 45% include molten salt TES with a storage capacity of 7.5 hours while 55% did not include any TES.

Recent studies [22,23] indicate that the cost decline of Lithium-ion (Li-ion) battery technology is similar to PV technology, i.e. a cost reduction, or learning rate, of at least 20% is observed for each doubling of installed capacity. Li-ion battery technology is employed to electrify transportation and for stationary electricity storage, compatible with solar PV and wind power.

A comparison of CSP-TES versus PV with Li-ion battery storage [24] shows that the latter option is today more attractive economically than CSP-TES for a storage duration shorter than 4 hours. This tipping point may be pushed upwards, depending on future cost developments [25]. Despite a fast learning rate, CSP technology has expanded slower than other renewable technologies [26-28].

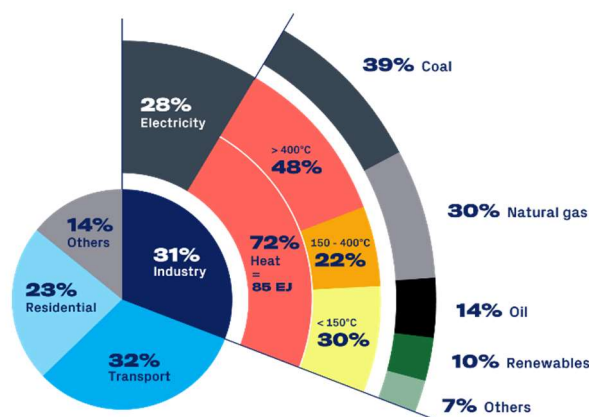
While CSP technology may play a marginal but critical role in decarbonizing electrical power supply, there are other sectors to consider, in particular Industrial Process Heat (IPH) or synthetic fuels [20,21,29,30]. According to the International Energy Agency (IEA), "Heat is the largest energy end-use. Providing heating for homes, industry and other applications accounts for around half of total energy consumption."

A distribution of total final energy consumption is shown in Figure 1.9 [31]. In 2018, Industry (Food and beverage, Chemicals, Textile, Machinery, Mining, etc.) accounted for 31% of the total final energy consumption. 28% of this consumption is electrified, while 72% is heat. 10% of this heat demand was supplied by renewable energy.

The heat demand can be segmented in three temperature ranges:

- <150 °C (*Low*): Boiling, pasteurising, sterilising, cleaning, drying, steaming, cooking, etc.
- 150 – 400 °C (*Medium*): Distilling, nitrate melting, dyeing, compression.
- >400 °C (*High*): Material transformation processes, synthetic fuels.

One possible pathway to decarbonize IPHs would be to increase the share of electrification and take advantage of available renewable energy power [32]. Alternatively, solar thermal technologies are also relevant to directly generate IPH [33]. For low temperature applications, direct electrification or stationary solar thermal collectors are the first choice. Stationary solar thermal collectors include flat plate, vacuum tube and compound parabolic collectors (CPC). Concentrating Solar Thermal (CST) technology is relevant for a temperature above 150 °C, i.e. line focusing (LF) concentrator for medium temperature applications (150-400 °C), and point focusing (PF) concentrators for high temperature processes above 400 °C.



Total final energy consumption 2018: 382 EJ. Source: IEA / IRENA.

Figure 1.9: Total final energy consumption 2018: 382 EJ (IEA/IRENA) [28].

## 1.2 CSP technology overview

### 1.2.1 Operating principles

While PV technology directly convert solar radiation into direct electric current, CSP technology converts DNI into useful heat, using a tracking mirror field to concentrates sunlight on a thermal receiver. A Heat Transfer Fluid (HTF) is pumped through the thermal receiver. This heat can be stored and supplied to a thermodynamic cycle, producing electrical power, for instance with a steam turbine. It can also be used for any IPH.

A world map of long-term average DNI is shown in Figure 1.10. A comparison with the map of deployed CSP projects (Figure 1.6) shows that desert areas, with a yearly total DNI above 2000 kWh/m<sup>2</sup>, are most favorable in terms of LCOE for generating STE, although CSP technology can still work at lower values [6].

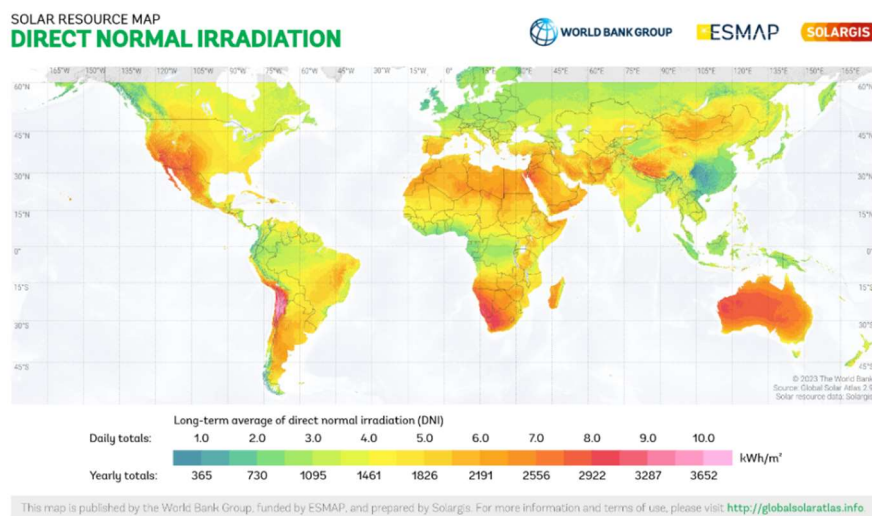


*Figure 1.10: Worldwide distribution of Direct Normal Irradiation (DNI) [34].*

There are four main CSP configurations for mirror fields and thermal receivers, shown in Figure 1.11. One can distinguish between line focusing (LF) and point focusing (PF) systems. On the one hand, LF systems concentrate sunlight on a linear receiver. The mirror field is coupled to a one-axis tracking system. LF systems include PTCs [9,35,36] and Linear Fresnel [37,38]. On the other hand, PF systems concentrate sunlight on a compact receiver surface. The mirror field is coupled to a two-axis tracking system. PF systems include Central Receiver Systems (CRS), also known as Solar Towers [39,40] and parabolic dishes [41,42].

Some variations of the four main CSP configurations can be found in the literature. Mirror fields can be substituted both in LF and PF systems by Fresnel lenses [43,44]. Beam-down solar concentrating systems are also found [45], which use secondary optics to bring the thermal receiver closer to the ground and allow more compact systems.

According to the project database CSP.guru [46], the global operational capacity of CSP plants accounts 6.34 GW<sub>e</sub> as of July 1<sup>st</sup> 2023, while 1.76 GW<sub>e</sub> is currently under construction. Parabolic troughs represent 74% of the operational CSP capacity, Solar towers 22% and Linear Fresnel 4%. Meanwhile, Solar Towers represent 52% of CSP projects under construction, Parabolic Trough 37% and Linear Fresnel 12%.

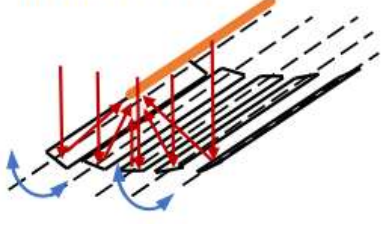
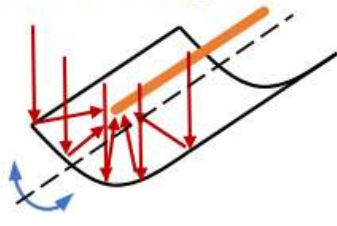
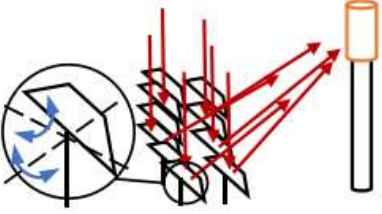

	Stationary receiver	Mobile receiver
Line Focusing (One-axis tracking)	<p><b>Linear Fresnel</b></p> 	<p><b>Parabolic trough</b></p> 
Point Focusing (Two-axis tracking)	<p><b>Central receiver</b></p> 	<p><b>Parabolic dish</b></p> 

Figure 1.11: Overview of main CSP configurations. Illustrations extracted from [14].

The geometric concentration ratio  $C_x$  of a CSP system is defined, in first approximation, as the ratio of the mirror aperture area to the receiver area (Eq.1.1).

$$C_x \sim \frac{A_a}{A_r} \quad (1.1)$$

PF mirror systems can achieve a higher geometric concentration ratio in comparison to LF mirror systems. Theoretical limits are respectively  $\times 212$  for LF mirror systems and  $\times 45000$  for PF mirror systems. In practice, LF systems such as PTCs can achieve a  $C_x$  value lower than  $\times 100$ , while PF systems such as CRS can reach an upper  $C_x$  value of approx.  $\times 1500$ . Higher  $C_x$  values allow reaching higher operating temperature levels, however this require more precise optics, both for the concentrator and tracking systems [47,48].

Reaching higher operating temperature levels allows achieving a higher efficiency for the thermodynamic cycle, which is theoretically limited by Carnot efficiency (Eq.1.2), where  $T_{cold}$  and  $T_{hot}$  would respectively correspond to the inlet and outlet HTF temperature in Kelvins.

$$\eta_{CSP} < \eta_{carnot} = 1 - \frac{T_{cold}}{T_{hot}} \quad (1.2)$$

PTC systems have traditionally used diphenyl oxide/biphenyl based thermal oils, operating from 290 °C to 390 °C [49,50]. Silicon based HTFs can operate up to 425 °C [51]. Next generation PTC systems consider molten salts as HTF, pushing the maximum operating temperature towards 550 °C [52]. This shift allows simplifying the CSP power plant architecture, as molten salts were already used for TES. In the case of CRS, molten salt based HTF are already state of the art, however the maximum operating temperature could be pushed beyond 600 °C with new salt formulations [53-55], one critical issue being metal corrosion at higher temperatures [56]. Next generation CRS plants also consider liquid sodium HTF [57,58] or solid particles [59-62] in order to push the upper operating temperature towards 1000 °C. A temperature level of 1500 °C is achievable with air as an HTF, using porous volumetric receivers made of silicon carbide (SiC) [63,64].

### 1.2.2 CSP system costs

The simplified schematic of a CSP power plant architecture is shown in Figure 1.12. The system consists of three subsystems: i) Solar field, ii) Thermal storage and iii) Power block (IPH). A primary HTF loop connects the solar field to the TES unit, the secondary HTF loop connects the TES unit to the power block. The third HTF loop includes the steam turbine, connected to the tower generator. The primary and secondary HTF loops could be operated with the same fluid (molten salts) to spare one heat exchanger, while the power block may be substituted with any other IPH. This simplified diagram does not include auxiliary heating sources for hybridization.

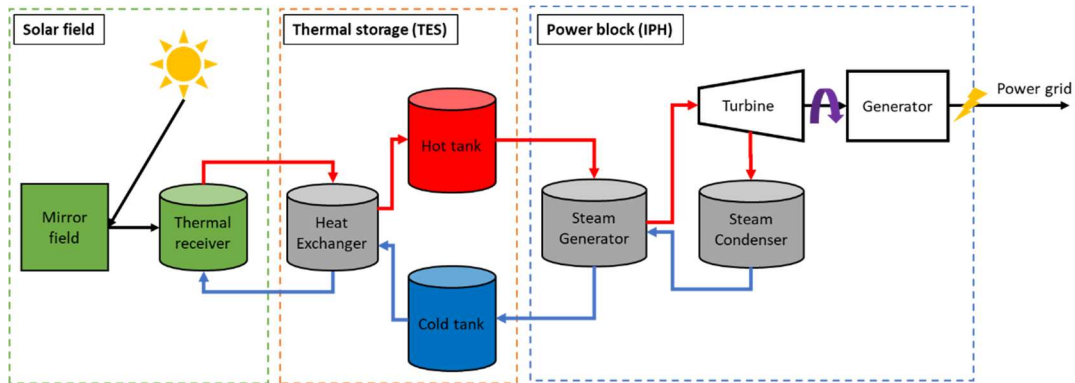


Figure 1.12: Schematic diagram of a CSP power plant.

The evolution of the cost breakdown of installed CSP plants is illustratively shown below in Figure 1.13 for PTCs and CRS between 2010 and 2020 [6]. Installed costs are shown in USD/kW, including a typical TES unit. Between 2010 and 2020, The cost of PTC technology has decreased by 55%, while the cost of CRS technology has dropped by 66%.

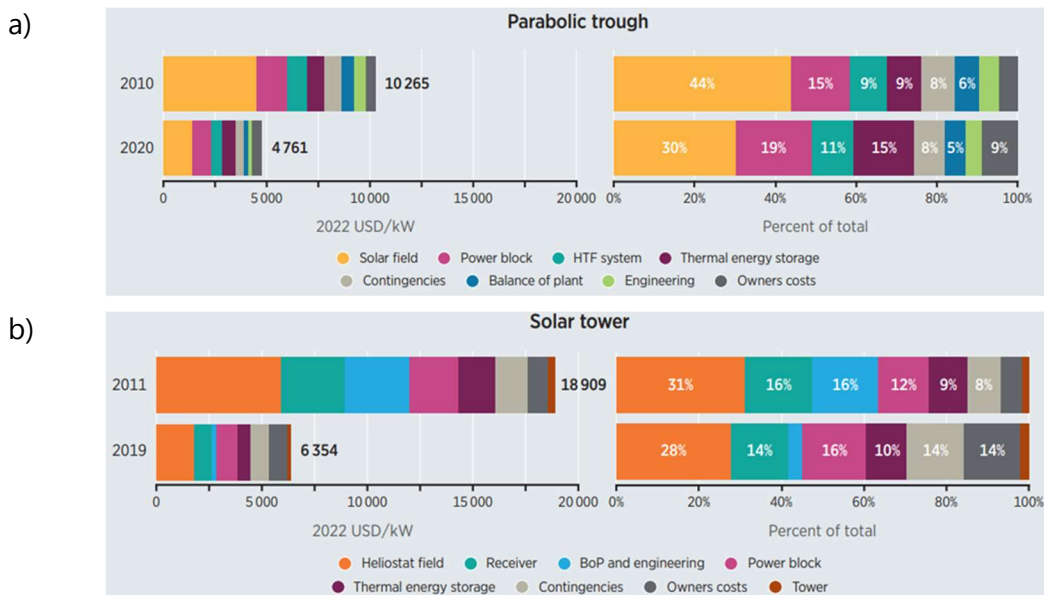


Figure 1.13: Evolution of the cost breakdown of installed CSP plants by technology from 2010-2011 to 2019-2020 [6]. a) Parabolic Troughs. b) Central Receiver Systems.

The cost of installed PTC technology is dominated by the solar field, followed by the power block, the HTF system and the TES unit. Significant cost reductions have been achieved from 2010 until 2020: -68% for the solar field, -40% for the power block, -47% for the HTF system and -19% for the TES unit.

The cost of installed CRS technology is dominated by the heliostat field, followed by the receiver, the power block, the TES unit and balance of plant (BoP) and engineering. Significant cost reductions were achieved from 2011 until 2019: -70% for the heliostat field and the receiver, -55% for the power block, -63% for the TES unit. BoP and engineering costs dropped by -93%, becoming a marginal cost, thanks to learning effects.

### 1.2.3 System reliability

In 2020, NREL released a technical report on CSP best practices [65], analysing the feedback of CSP stakeholders to identify and rank issues related to CSP technology, project development, Engineering, Procurement and Construction (EPC) as well as Operation and Maintenance (O&M). These issues were collected over multiple interviews and ranked according to the frequency of perceived occurrences and their perceived priority, which is defined as the product of impact and risk. Ranking of technology related issues are shown below in Figure 1.14 for PTC technology and in Figure 1.15 for CRS technology.

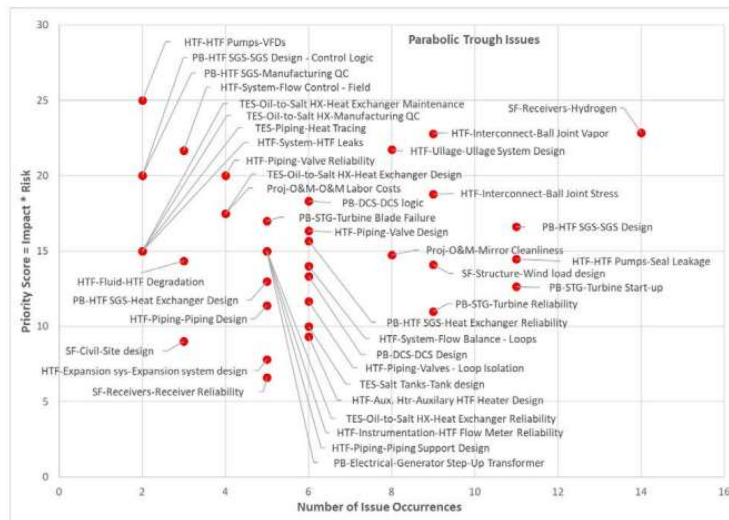


Figure 1.14: PTC issues ranked by priority and frequency of perceived occurrence [65].

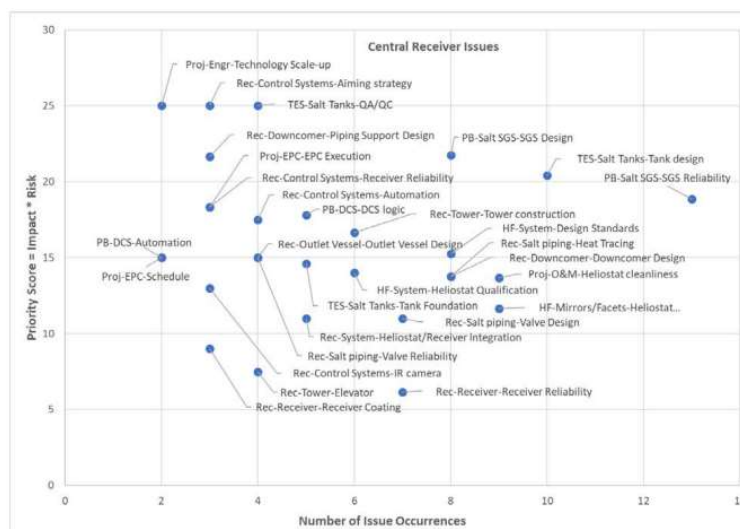


Figure 1.15: CRS issues ranked by priority and frequency of perceived occurrence [65].

PTC technology is today perceived as a mature technology, with improvement needed in the performance and reliability of some systems and components. Most PTC plants appear to

achieve high availability of the solar field, with most problems occurring in conventional equipment or systems such as heat exchangers, pumps, and valves. The dominant issue is the permeation of hydrogen in thermal receivers [50,51,66]. The next tier includes: ullage system design, HTF pump seal issues, ball-joint and flex hoses stress and leakage [67], Steam Generator System (SGS) design and reliability [68-70].

CRS technology is at an earlier stage of commercial maturity in comparison to PTC technology. The key issues identified for CRS technology are the design and reliability of the SGS and the hot tank foundation, in particular molten salt leakages due to corrosion [56,71]. Secondary issues include: i) the accurate measurement of atmospheric attenuation [72-77], ii) differences between actual and expected flux distributions on the receiver [78-84], leading to spillage and reduced receiver lifetime, iii) molten salt heat tracing capacity and insulation quality, leading to high parasitic losses to avoid molten salt freezing [85,86]. Other related issues of less importance related to the thermal receiver include periodical re-coating and Infrared (IR) temperature monitoring, further discussed in the next chapters.

### 1.3 Thermal receivers and absorber coatings

#### 1.3.1 Design of solar thermal receivers

Thermal receivers are critical components in CSP systems, as they receive concentrated solar radiation and transfer thermal energy to the circulating HTF. This subsection provides a brief overview of existing designs for PTC and CRS technologies.

Given the commercial maturity of PTC technology, the design of thermal receivers, also referred as Heat Collection Elements (HCEs), has been standardized for mass production. The design of HCEs is shown in Figure 1.16 [87]. An HCE consists of two concentric tubes, i.e. a steel absorber tube inserted in a tubular glass envelope. The steel absorber tube is coated with a spectrally selective coating (SSC) to maximise the absorption of solar radiation and minimise radiative thermal losses. The annulus ring between both tubes is evacuated to minimise thermal losses due to gas conduction [88,89]. The steel absorber tube and the glass envelope are connected on both ends with glass metal seals and bellows. Bellows compensate for the thermal dilatation of the absorber tubes and are shielded from concentrated solar radiation.

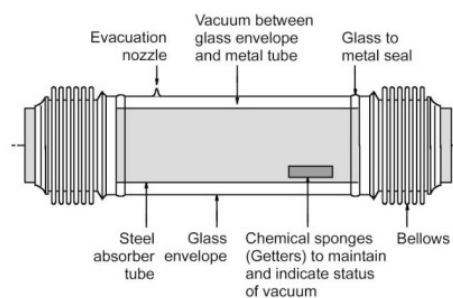


*Figure 1.16: Schematic of a parabolic trough HCE [87].*

The optical and thermal performance as well as the durability of single HCEs can be tested under laboratory conditions [87, 90-93]. The permeation of hydrogen in the annulus ring is a known issue mentioned in subsection 1.2.3. This phenomenon has been modelled [94] and investigated under field conditions, using IR thermography to monitor the glass envelope tem-

perature [95-97]. The replacement or repair of defect HCE items has also been analysed from a techno-economical perspective [98].

As already mentioned, CRS technology has not yet reached the same commercial maturity as PTC technology. Consequently, different receiver designs can be found in existing commercial power plants. Tubular receivers are dominant, although there is no standard geometry. Most of CRS power plants include an external tubular receiver design with a cylindrical shape, while cavity receivers are also found. Both design configurations are shown in Figure 1.17.

Tubular receiver design configurations consist of several receiver panels, made of metal tubes, coated with a black paint such as Pyromark 2500 [99]. The receiver is mounted on top of a tower, which height can exceed 200 meters for the largest CRS power plants. The receiver design configuration is the result of complex simulation work, taking multiple factors into account [100]: allowable flux density, aiming strategy and molten salt induced corrosion [78-80], thermo-hydraulic design and yield optimization for a given HTF [101-103], thermal stress and fatigues due to non-uniform flux and temperature profiles [104-106].

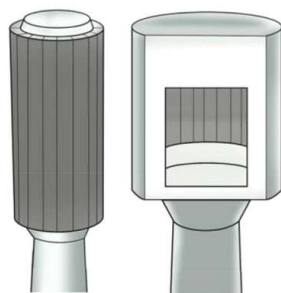


*Figure 1.17: Schematic of external tubular receiver (left) and cavity receiver (right) design configurations [39].*

An alternative design considers porous volumetric receivers [63,64], made of ceramic materials, such as SiC, using air at atmospheric pressure as an HTF. This design consists of multiple receiver cups [107] (Figure 1.18), which can be independently replaced for maintenance. Porous volumetric receivers would allow reaching an operating temperature above 1000 °C but require further optimization of material properties and absorber structure, in particular the porous mesh design [108,109].

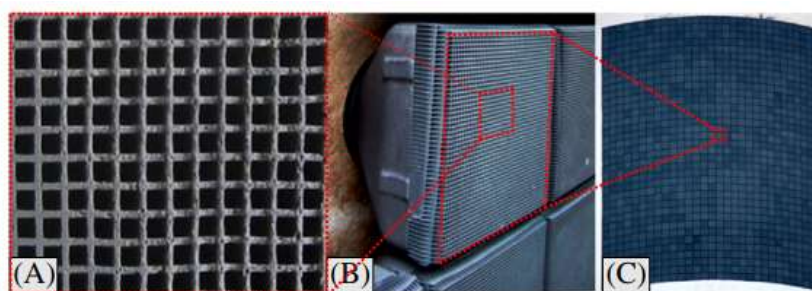


*Figure 1.18: Volumetric receivers a) close up view of the absorber structure. b) Individual absorber modules. c) Main receiver mounted at a Solar Tower in Jülich, Germany [107].*

In the case of solid particles, multiple receiver designs are being investigated [60]. Solid particles can be heated directly by concentrated solar radiation, for instance in free-falling, obstructed, centrifugal or fluidized bed receiver designs. Indirect receiver designs include gravity-driven flow in enclosures or fluidized flow in metal tubes.



### 1.3.2 Solar thermal absorber coatings

Solar thermal absorber coatings (STACs) play a major role in the opto-thermal performance of thermal receivers. For commercial receiver designs, STACs are applied on a metal substrate. A simple heat transfer diagram is shown for a thermal receiver section in Figure 1.19. The STAC absorbs a fraction  $\alpha_{sol}$  of the concentrated solar flux  $\dot{q}''_{sol}$  and heats up to a temperature  $T_{abs}$ . The STAC loses heat to the ambient by thermal radiation  $\dot{q}''_{rad,sky}$  and convection  $\dot{q}''_{conv,amb}$ . Radiative losses primarily depend on the STAC thermal emittance  $\epsilon_{th}$  and its temperature  $T_{abs}$ . The absorbed heat is transferred by conduction, first through the coating  $\dot{q}''_{cond,coating}$ , then through metal substrate  $\dot{q}''_{cond,metal}$  to the HTF. Thermal conduction is a function of the thermal conductivity  $k_{coating}$  and  $k_{substrate}$ , temperature gradients are induced across the coating ( $\Delta T_{coating}$ ) and the metal substrate ( $\Delta T_{metal}$ ).

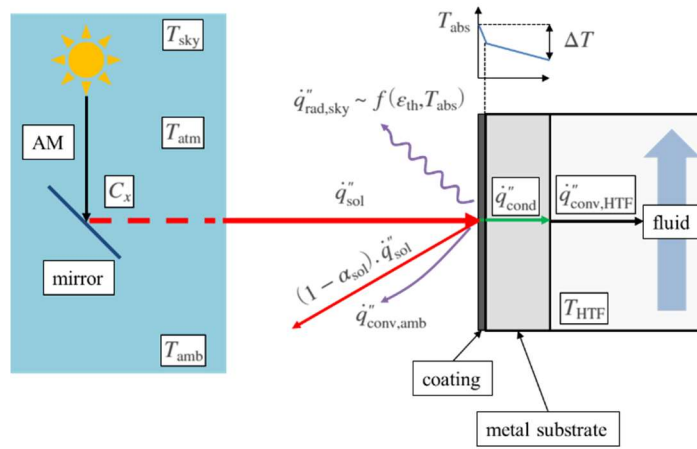


Figure 1.19: Heat transfer diagram for a solar thermal absorber coating.

There are two main categories of STACs, i.e. Spectrally Selective Coatings (SSCs) and High Solar Absorptance (HSA) [110]. The principle of SSC formulations is to maximise solar absorptance  $\alpha_{sol}$  while minimizing thermal emittance  $\epsilon_{th}$ . On the other hand, HSA coating formulations prioritise maximising solar  $\alpha_{sol}$ . The relative weights of  $\alpha_{sol}$  and  $\epsilon_{th}$  are determined by the coating opto-thermal efficiency  $\eta_{opt-th}$  (Eq.1.3).

$$\eta_{opt-th} \approx \frac{\alpha_{sol} \dot{q}''_{sol} - \epsilon_{th} \sigma T_{abs}^4}{\dot{q}''_{sol}} = \alpha_{sol} - \frac{\epsilon_{th} \sigma T_{abs}^4}{\dot{q}''_{sol}} \quad (1.3)$$

Depending on the operating conditions, i.e. concentration ratio  $C_x$  and absorber temperature  $T_{abs}$ , it may be beneficial to select either a SSC or a HSA coating formulation, or also fine tune a SSC [111,112]. SSC formulations are today relevant for PTC, while HSA formulations are preferred for CRS, in particular external tubular receiver designs [113]. Pictures of both coating formulations are shown in Figure 1.20.



Figure 1.20: Pictures of tubular metal substrates (T91) and STACs. a) Polished metal substrate and SSC. b) Sand blasted metal substrate and HSA coating.

The development of SSC formulations is an active research field, multiple SSC types have been identified in review studies [110,114,115], such as intrinsic SSC, semi-conductor metal tandems, multilayer interference stacks, Ceramic Metallic (CERMET) or textured surfaces.

The generic architecture of multilayer interference stacks and CERMET coatings is illustrated in Figure 1.21. The typical SSC thickness lies in the sub-micrometer range. Different manufacturing processes are relevant for the deposition of thin film SSCs, such as Physical Vapor Deposition (PVD), Chemical Vapor Deposition (CVD) atomic layer deposition, spray coating, sol-gel dip coating or spin coating

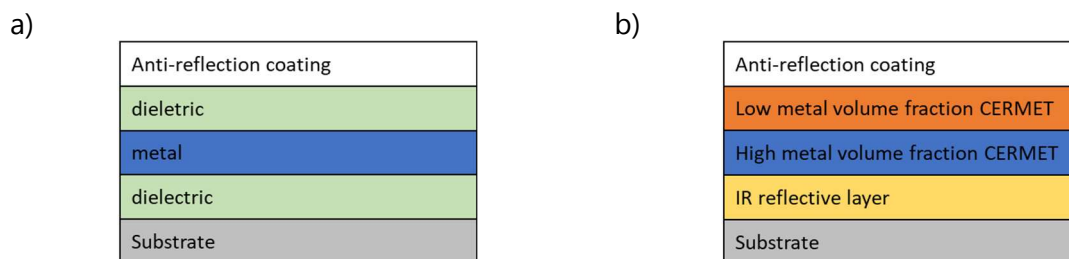


Figure 1.21: Illustration of SSC architecture. a) Multilayer interference stack. b) Double layer CERMET [110,113,114]

The optimization of HSA coatings is also an active research field. Pyromark 2500 [100], a silicon-based coating, has long been considered as a reference. Application parameters, such as surface preparation, spraying method, coating thickness, curing procedure have been recently investigated for optimization [116,117]. Alternative coating formulations have been developed and tested for performance and durability [118-121].

For CRS applications, nickel-chrome based superalloys, such as Inconel 617 or Haynes 230 are selected as relevant metal substrates, due to their excellent thermomechanical properties at high temperature. The typical coating thickness is about 20-30  $\mu\text{m}$ . Spraying is the most common deposition technique, as it is also applicable for re-coating on top of tower. The HSA coating typically consists of a single layer matrix of black spinel pigments and a silicon binder. Organic compounds evaporate during the first exposition to concentrated solar flux (curing), while a protective oxide layer grows [115,122,123] between the substrate and the HSA coating after several hours of exposition in air. Differences in thermal expansion of the substrate, oxide layer and coating may lead to micro-cracks in the coating structure, which are compromising the optical and mechanical durability of the HSA coating. While the HSA coating typically achieves a  $\alpha_{sol}$  values above 97%, the oxidised substrate may reach an  $\alpha_{sol}$  value above 93%.

### 1.3.3 Durability of solar thermal absorber coatings

CSP plants are typically designed for a service lifetime up to 30 years. The long-term durability of STACs is important for the efficient operation of these power plants, minimizing downtime and potential maintenance costs.

Different boundary constraints apply for STACs in PTC and CRS applications. Parabolic trough HCEs are sealed, the STAC is protected from the ambient by an evacuated glass envelope. The concentration ratio is less than x100 and the maximum temperature lies by 550  $^{\circ}\text{C}$  for a molten salt HTF. Defect HCEs can be individually replaced [98], the most critical failure mode being hydrogen permeation. External tubular receivers are exposed outdoor at the height of the tower, STACs are thus subject to multiple environmental factors, such as oxidation, humidity,

corrosion or sand erosion. Furthermore, the thermal receiver is exposed to higher fluxes ( $\times 1000$ ) and temperature levels above  $600\text{ }^\circ\text{C}$ , with frequent thermal cycling.

Although the STAC could be re-coated on tower, this operation remains tedious. The re-coating period is thus optimised, considering the Levelised Cost of Coating (LCOC) [124,125], which relies on the coating opto-thermal efficiency  $\eta_{opt-th}$  (Eq.1.3). The LCOC metric is defined as the ratio of the total annualised coating costs in monetary units, to the net annual thermal energy absorbed by the coating, expressed in  $\text{MWh}_{th}$ . Total annualised coating costs include initial coating costs annualised over the plant service lifetime and recoating costs annualised over the recoating interval. The net annual thermal energy balance includes the annualised energy losses due to coating degradation and due to down time for re-coating.

Durability testing of STACs involve a comprehensive test program, which is not standardised for CSP applications [126,127]. The test program includes isothermal and thermal cycling, at different operating temperatures and ramp rates. Accelerated ageing can be performed both in laboratory furnaces [120,121] or in solar furnaces [128-130]. The influence of different thermal processes on the optical and mechanical degradation of Pyromark 2500 has been investigated in the literature [131-133]. Thermal processes included muffle furnace isothermal testing, rapid cycling, cycling and hold as well as solar cycling. The analysis of optical degradation focused mostly on solar absorptance  $\alpha_{sol}$  and also the thermal emittance  $\varepsilon_{th}$ , while the analysis of mechanical degradation focused on coating morphology, i.e. crystal growth, oxide layer formation, micro-cracks and adhesion loss

## 1.4 Opto-thermal characterisation

### 1.4.1 Figures of merit

Two key figures of merit (FoMs) define a STAC opto-thermal efficiency  $\eta_{opt-th}$  of (Eq.1.3), namely its solar absorptance  $\alpha_{sol}$  and its thermal emittance  $\varepsilon_{th}$ . Both FoMs can be derived from measurements of spectral reflectivity  $\rho(\lambda, \theta)$  at a given incidence angle  $\theta$ .

For opaque material samples, the sample spectral transmissivity  $\tau(\lambda, \theta)$  is null. According to energy conversion, the sum of the sample spectral absorptivity  $\alpha(\lambda, \theta)$  and reflectivity  $\rho(\lambda, \theta)$  thus equal 100% (Eq.1.4). According to Kirchhoff's law of thermal radiation, spectral absorptivity and spectral emissivity are equal (Eq.1.5).

$$\rho(\lambda, \theta) + \alpha(\lambda, \theta) = 1 \quad (1.4)$$

$$\alpha(\lambda, \theta) = \varepsilon(\lambda, \theta) \quad (1.5)$$

Solar absorptance  $\alpha_{sol}$  is calculated according to (Eq.1.6). The sample spectral absorptivity  $\alpha(\lambda, \theta)$  measured at a given sample temperature  $T_{sample}$ , is weighted with a reference solar spectrum  $G_{sol}(\lambda, AM)$ , defined for a given Air Mass ( $AM$ ). For CSP applications, the standard solar spectrum is ASTM G173-03 [134], derived with the software SMARTS v2.9.2 [135]. The default  $AM$  value is set to 1.5, representative for mid-latitudes, while direct and circumsolar components of solar irradiance are selected ( $AM1.5d$ ). For integral calculations, the wavelength interval  $[\lambda_1; \lambda_2]$  spans from  $0.3\text{ }\mu\text{m}$  to  $2.5\text{ }\mu\text{m}$ , corresponding to 99% of the total solar irradiance  $G_{sol}$ , which reaches  $900\text{ W/m}^2$  at  $AM1.5d$ .

$$\alpha_{sol}(AM, T_{sample}) = \frac{\int_{\lambda_1}^{\lambda_2} [1 - \rho_{sample}(\lambda, T_{sample})] G_{sol}(\lambda, AM) d\lambda}{\int_{\lambda_1}^{\lambda_2} G_{sol}(\lambda, AM) d\lambda} \quad (1.6)$$

The distribution of the reference solar spectrum is shown in Figure 1.22.a for different AM values, considering the direct+circumsolar contribution.  $AM0$  corresponds to the extraterrestrial solar spectral irradiance, the total irradiance is  $1361 \text{ W.m}^{-2}$  [136,137]. The  $AM$  value corresponds to the relative optical length of the atmosphere at sea level and thus varies with the sun position. In first approximation,  $AM$  is defined as the inverse of the sun zenith angle cosine (Eq.1.7). This equation is reasonably accurate for a zenith angle up to  $75^\circ$  but diverges at the horizon, requiring further geometrical refinements [138].

$$AM \approx \frac{1}{\cos(\theta_z)} \quad (1.7)$$

Thermal emittance  $\epsilon_{th}$  is calculated according to (Eq.1.8). The sample spectral absorptivity  $\alpha(\lambda, \theta)$  measured at a given sample temperature  $T_{sample}$ , is weighted with a blackbody spectral exitance  $E_{bb}(\lambda, T_{sample})$  over a wavelength interval  $[\lambda_3; \lambda_4]$ . The blackbody spectral exitance is defined according to Planck's radiation law in (Eq.1.9) and plotted in Figure 1.22.b for temperatures ranging from  $25^\circ\text{C}$  to  $1000^\circ\text{C}$ .

$$\epsilon_{th}(T_{sample}) = \frac{\int_{\lambda_3}^{\lambda_4} [1 - \rho_{sample}(\lambda, T_{sample})] E_{bb}(\lambda, T_{sample}) d\lambda}{\int_{\lambda_3}^{\lambda_4} E_{bb}(\lambda, T_{sample}) d\lambda} \quad (1.8)$$

$$E_{bb}(\lambda, T_{sample}) = \frac{2\pi hc^2}{\lambda^5 [\exp\left(\frac{hc}{\lambda k T_{sample}}\right) - 1]} \quad (1.9)$$

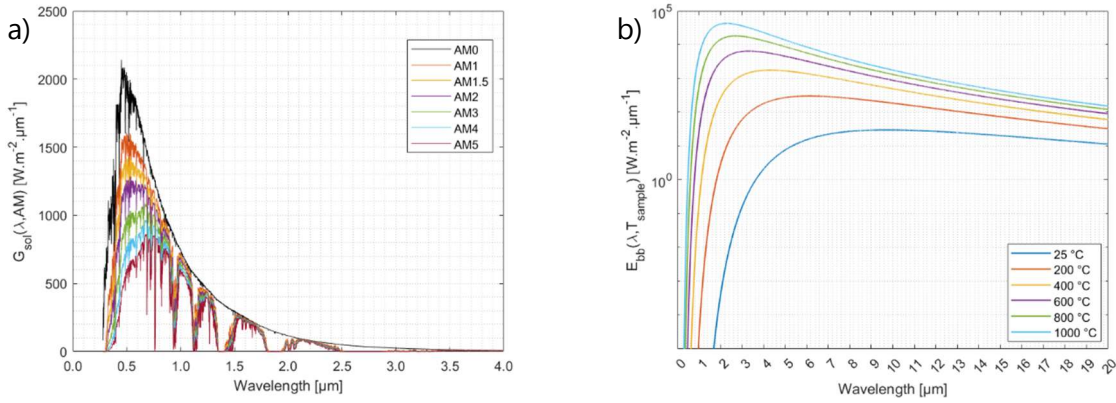


*Figure 1.22: Spectral distributions a) reference solar spectrum (direct+circumsolar) as a function of relative optical AM. b) Blackbody spectral exitance as a function of temperature.*

The thermal emittance  $\epsilon_{th}$  should be calculated over the broadest possible wavelength range, which is limited by the available instrumentation. The integration of Planck's law (Eq.9) over the interval  $[0; \infty[$  yields Stefan-Boltzmann law (Eq.1.10). In practice, any spectral instrument covers a fraction  $f_{\sigma T^4}$  of Stefan-Boltzmann law (Eq.1.11), which is a function of temperature. This fraction should be specified for any  $\epsilon_{th}$  calculation.

$$\int_0^{\infty} E_{bb}(\lambda, T_{sample}) d\lambda = \sigma T_{sample}^4 \quad (1.10)$$

$$f_{\sigma T^4} = \frac{\int_{\lambda_3}^{\lambda_4} E_{bb}(\lambda, T_{sample}) d\lambda}{\sigma T_{sample}^4} \quad (1.11)$$

The overlap of the solar spectrum and blackbody radiation is shown in Figure 1.23. Spectra are respectively normalised according to their maximum value. According to Wien's displacement law, the peak of blackbody radiation shifts towards shorter wavelengths at higher temperature. The spectral overlap between solar and blackbody radiation is thus more significant at higher temperature. Solar absorptance  $\alpha_{sol}$  and thermal emittance  $\varepsilon_{th}$  are not independent FoMs [111], design trade-offs have to be defined for optimization, depending on operating conditions.

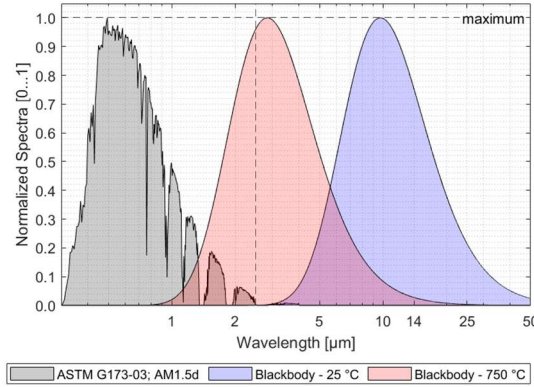


Figure 1.23: Reference solar spectrum (ASTM G173-03; AM1.5, direct) and blackbody radiation (25 °C, 750 °C).

## 1.4.2 Spectral characterisation at ambient temperature

The spectral directional hemispherical reflectivity (SDHR) or  $\rho_{sample}(\lambda, \theta, T)$  can be measured for opaque material samples, such as STACs applied on metal substrates, at room temperature under laboratory conditions. The SDHR is measured either with benchtop spectrophotometers or with portable reflectometers, both equipped with an integrating sphere. The measurement principle and relevant instruments are briefly explained in the next paragraphs.

### 1.4.2.1 Measurement principle

The SDHR of a sample is measured in different steps. First, the sample port of the instrument integrating sphere is left empty and the background light or zeroline ( $I_{zero, meas}$ ) is measured. A reference baseline coupon is selected, for which the calibrated reflectivity data ( $\rho_{ref, calib}$ ) is available. This baseline coupon is positioned on the integrating sphere sample port for measurement ( $I_{base, meas}$ ). Finally, the sample of interest is measured ( $I_{sample, meas}$ ). The sample reflectivity  $\rho_{sample}(\lambda, \theta, T)$  is calculated according to (Eq.1.12).

$$\rho_{sample}(\lambda, \theta, T_{amb}) = \frac{I_{sample, meas} - I_{zero, meas}}{I_{base, meas} - I_{zero, meas}} \rho_{ref, calib} \quad (1.12)$$

The measured  $\rho_{sample}(\lambda, \theta, T_{amb})$  is weighted with reference spectra for  $\alpha_{sol}$  and  $\varepsilon_{th}$  calculations, as previously outlined in the subsection 1.3.1. For  $\varepsilon_{th}$  calculations at higher temperature (Eq.1.8),  $\rho_{sample}(\lambda, \theta, T_{amb})$  is considered, assuming a stable spectrum for the material (Eq.1.13). This is valid if the material surface does not degrade after exposure (oxidation, overheating) and if no reversible spectral shift occurs.

$$\frac{d\rho_{sample}(\lambda, \theta, T)}{dT} \sim 0 \quad (1.13)$$

The relevant spectral range for  $\alpha_{sol}$  spans from 0.3  $\mu\text{m}$  to 2.5  $\mu\text{m}$ , i.e. from Ultraviolet (UV) to Shortwave IR (SWIR), For  $\varepsilon_{th}$  calculations, further IR spectral data is required, at least up to 14  $\mu\text{m}$ , ideally also in the Far IR ( $> 14 \mu\text{m}$ ).

Different reference calibration coupons are used for each spectral range. White diffuse Spectralon<sup>®</sup>, with a  $\rho_{ref,calib}$  value of 99%, is commonly used as a reference baseline coupon for measurements in the UV-Visible (VIS)-SWIR spectral range. Gold diffuse Infragold<sup>®</sup>, with a  $\rho_{ref,calib}$  value above 94%, is commonly used as a reference baseline coupon for IR measurements, i.e. from 2  $\mu\text{m}$  to 20  $\mu\text{m}$  [139]. Their spectra are shown in Figure 1.24, along with exemplary spectra for a SSC and a HSA formulations, previously shown in Figure 1.20.

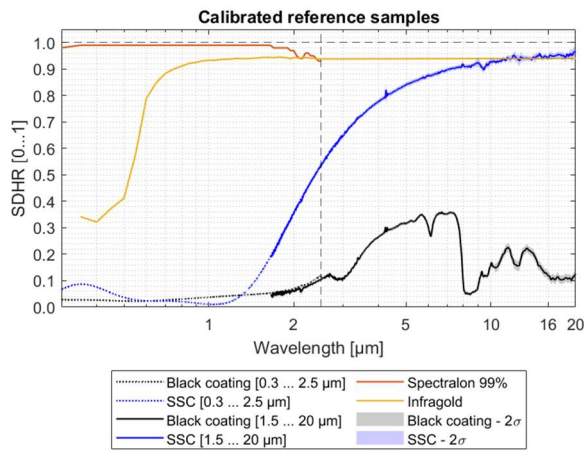


Figure 1.24: SDHR data for calibrated reference samples.

### 1.4.2.2 Benchtop spectrophotometers

Benchtop spectrophotometers are relevant for fine resolved spectral characterization of small material samples at room temperature, under laboratory conditions. Two complementary benchtop spectrophotometers are available at the optical laboratory OPAC, a joint CIEMAT-DLR facility located at the Plataforma Solar de Almería (PSA). These spectrophotometers are shown in Figure 1.25 with their respective integrating sphere diagram.

The Lambda 1050 (Figure 1.25.a) is suitable for SDHR measurements in the UV-VIS-SWIR spectral range [140]. This instrument is a scanning spectrophotometer. It combines two light sources, i.e. Deuterium for UV and Tungsten halogen for VIS-SWIR. Monochromators are used to scan the spectral range from 0.28  $\mu\text{m}$  to 2.5  $\mu\text{m}$ . Three detectors are combined, i.e. photomultipliers for the UV-VIS range, Peltier cooled InGaAs and PbS detectors for the SWIR range. The integrating sphere (Figure 1.25.c) is coated with a white diffuse  $\text{Ba}_2\text{SO}_4$  coating. Its diameter is 150 mm and the light incidence angle on the sample is near normal, i.e.  $\theta=8^\circ$ .

The Frontier FTIR (Figure 1.25.b) is suitable for SDHR measurements in the IR spectral range from 2  $\mu\text{m}$  to 14  $\mu\text{m}$ . This instrument is a Fourier Transform (FT) spectrophotometer. Its light source is an IR filament. An optical interferometer system is used to collect the spectrum. A HgCdTe detector cooled with liquid nitrogen collects the optical signal from the integrating sphere, from. The integrating sphere (Figure 1.25.d) is coated with a gold diffuse coating. Its diameter is 76.2 mm and the light incidence angle on the sample is near normal, i.e.  $\theta=12^\circ$ .

This integrating sphere includes a rotary mirror which can be tilted manually, toward the sphere for background measurements and toward the sample for sample measurements [141].

The Lambda 1050 spectrophotometer yields relevant measurements for  $\alpha_{SOI}$  calculations, while both spectrophotometers are required for  $\epsilon_{th}$  calculations, in particular for higher temperatures due to Wien's displacement law (Figure 1.23). There is a partial spectral overlap between both instruments, from 2  $\mu\text{m}$  to 2.5  $\mu\text{m}$ . Spectral mismatches can be observed in some cases, which should be ideally minimal.

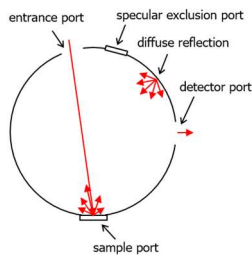
a)



b)



c)



d)

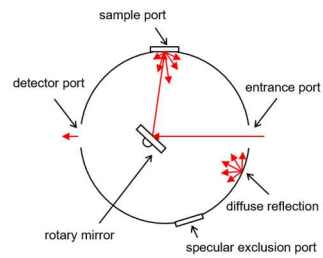


*Figure 1.25: Benchtop spectrophotometers available at OPAC laboratory. a) Perkin Elmer Lambda 1050 b) Perkin Elmer Frontier FTIR with Pike integrating sphere. c) Diagram of Lambda 1050 integrating sphere. d) Diagram of Frontier FTIR Pike integrating sphere.*

### 1.4.2.3 Portable instruments

Portable reflectometers are relevant for ambient temperature spectral characterization, in the laboratory or in the field. In comparison to benchtop spectrophotometers, these instruments have a coarser spectral and angular resolution. One reference instrument is the portable 410-Vis-IR solar reflectometer and emissometer, commercialised by Surface Optics Corporation (SOC) [142]. This instrument device is shown in Figure 1.26 with a diagram of its integrating sphere. The minimal incidence angle is  $\theta=20^\circ$ .

a)



b)

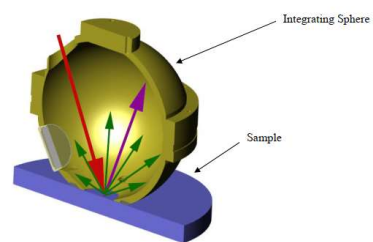


*Figure 1.26: Surface Optics Corporation 410-Vis-IR portable instrument. a) Instrumentation, including portable unit, measurement heads and reference calibration coupons. b) Integrating sphere. The red arrow is the illuminating beam. The purple arrow is the reflected beam, green arrows correspond to scattered light.*

The 410-Vis-IR device includes two modular measurement heads, i.e. 410 Solar and ET100. Their spectral bands are shown in Figure 1.27. The 410 Solar measurement head is used to characterise  $\alpha_{sol}$ . It has a tungsten filament light source and 7 spectral bands (Figure 1.27.a) spanning from 0.33  $\mu\text{m}$  to 2.5  $\mu\text{m}$ , with partial overlaps. The ET100 measurement head is used to characterise  $\varepsilon_{th}$ . It has an IR filament and 6 spectral bands (Figure 1.27.b), spanning from 1.5  $\mu\text{m}$  to 21  $\mu\text{m}$ . It includes a Peltier cooled PbSe detector (1.5-5  $\mu\text{m}$ ) and a Deuterated Triglycine Sulfate (DTGS) detector (5-21  $\mu\text{m}$ ).

For both measurement heads, reflectivity measurements are discretised in each spectral band and weighted with the corresponding reference spectrum fraction, i.e. solar spectrum or black-body radiation at a defined temperature  $T$ .

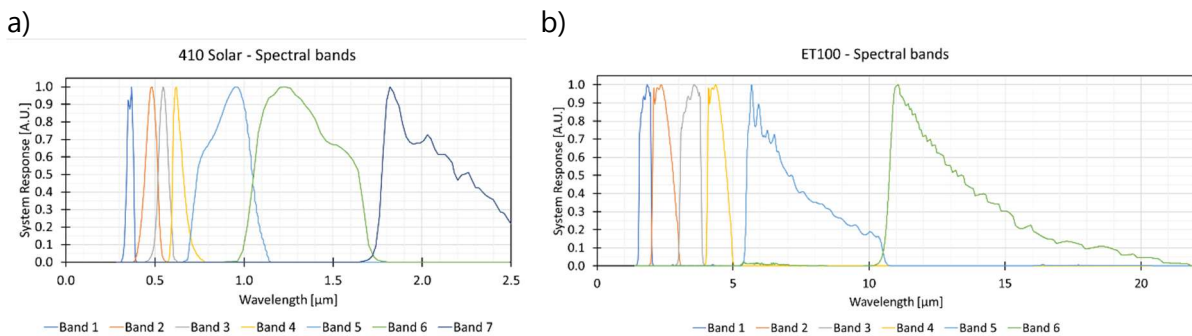


Figure 1.27: Spectral response of portable instrument measurement heads in arbitrary units. a) 410 Solar reflectometer (0.33 – 2.5  $\mu\text{m}$ ). b) ET100 emissometer (1.5 – 21  $\mu\text{m}$ ).

It is worth mentioning that SOC offers other similar portable devices, such as the ET-10 Emissometer [143], designed for the measurement of band IR emittance  $\varepsilon_{IR}$ , in two common bands for IR thermography, i.e. 3-5  $\mu\text{m}$  (MWIR) and 8-12  $\mu\text{m}$  (LWIR). Nonetheless, as of today, there is no available literature data published for this device in the field of CSP.

### 1.4.3 Spectral characterisation at operating temperature

For commercial CSP applications, the STAC operating temperature can raise up to 1000  $^{\circ}\text{C}$ . The calculation of  $\alpha_{sol}$  and  $\varepsilon_{th}$  (subsection 1.4.1) based on ambient temperature spectra may be inaccurate, potentially affecting the estimation of  $\eta_{opt-th}$ . Scientific instrumentation has been developed for spectral emissivity measurements at high temperature on materials and coatings [144-146], mainly in the IR range, i.e. above 1  $\mu\text{m}$ . A review of spectral emissivity measurements by radiometric methods is discussed in [147].

#### 1.4.3.1 Literature review

The IR spectral emissivity of different SSC formulations have been characterised up to 600  $^{\circ}\text{C}$  [148,149] and the importance of such measurements at operating temperatures has been discussed [150]. The IR spectral emissivity of black coatings, such as Pyromark 2500, has been characterised up to 800  $^{\circ}\text{C}$ , for incidence angles ranging from 10 $^{\circ}$  to 80 $^{\circ}$  [151]. The IR spectral emissivity of ceramic materials [152,153] and solid particles [154] has also been recently investigated. A first Round Robin was published for a few materials, i.e. SSCs, black paint and ceramics, with a comparison of spectral measurements performed from ambient temperature up to 560  $^{\circ}\text{C}$  [155]. High temperature measurements, above 800  $^{\circ}\text{C}$  and up to 1500  $^{\circ}\text{C}$  were performed on oxidised nickel-based superalloy [156] and SiC [157]. These later measurements



were performed at the MEDIASE test facility, located at the 1 MW solar furnace in Odeillo, France. To the best author's knowledge, there is little, if any scientific data available regarding the effect of high temperature on spectral measurements relevant for solar absorptance  $\alpha_{sol}$  (0.3  $\mu\text{m}$  – 2.5  $\mu\text{m}$ ).

### 1.4.3.2 Experimental setups

One of the most common experimental setups for high temperature IR spectral emissivity measurements is based on a FT-IR spectrometer. An extension is added to the original sample port. A typical optical path is shown in Figure 1.28 [158], while variations are discussed in [147]. The extension includes i) a controlled radiation source, i.e. a blackbody, ii) a system of sample heating and clamping, iii) a system for determining the sample surface temperature. The atmosphere may be optionally controlled to avoid oxidation. In this setup, a rotary parabolic mirror is alternatively rotated towards the heated sample and the reference blackbody.

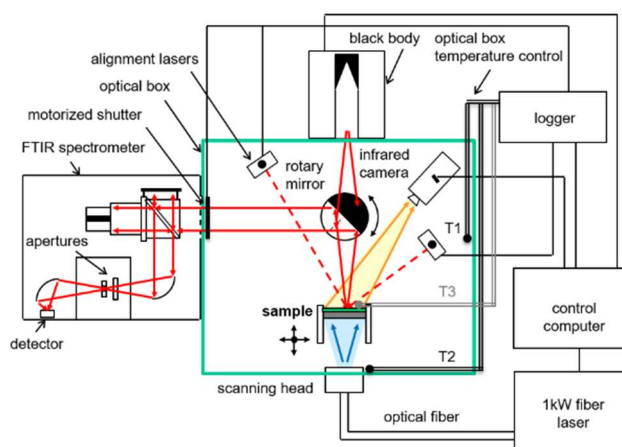


Figure 1.28: Schematic view of the optical path for an experimental setup including a FTIR instrument [158].

An alternative setup is shown in Figure 1.29. The disk-shaped sample is mounted at the focus of the solar furnace and heated on its backside with concentrated solar radiation through a hemispherical silica window. The sample is held onto a water-cooled sample holder. The sample front side surface temperature is measured with a two-colour pyroreflectometer [159]. The atmosphere can be controlled with a vacuum pump. Radiance measurements are performed with a SR-5000N spectroradiometer [160], from 1.34  $\mu\text{m}$  up to 14  $\mu\text{m}$ . The distance between the sample and the spectroradiometer is 1 meter. Spectral directional emissivity measurements can be obtained for different incidence angles using a custom goniometer. The spectroradiometer and the pyroreflectometer are calibrated with a blackbody.

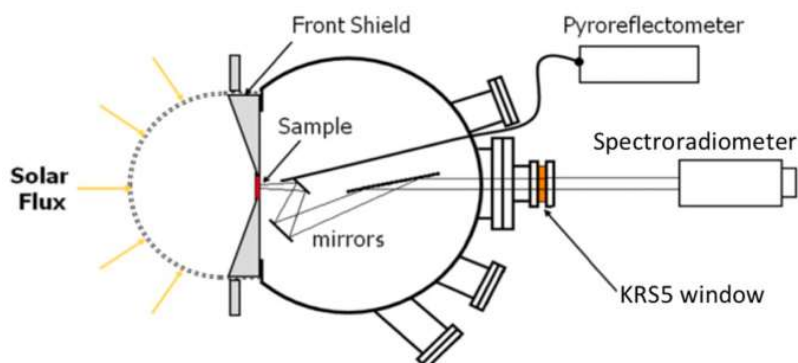


Figure 1.29: MEDIASE setup mounted at the focus of the 1 MW solar furnace in Odeillo, France [156,157].

### 1.4.3.3 Radiometric equations

For the previous radiometric experimental setups, the sample spectral radiance  $L_{sample}(\lambda, \theta, T)$  is measured instead of its spectral reflectivity  $\rho_{sample}(\lambda, \theta, T)$ . The radiance  $L_{BB}(\lambda, \theta, T)$  of a reference blackbody is required for comparison.

In the case of the FT-IR spectrophotometer, the detector measures the radiance emitted by the hot sample and the radiance reflected by the surrounding environment. The measured radiance signal  $L^*(\lambda, T)$  is thus the sum of two radiance terms (Eq.1.14).

$$L^*(\lambda, T) = \varepsilon(\lambda, \theta, T_{sample})L_{bb}(\lambda, T_{sample}) + [1 - \varepsilon(\lambda, \theta, T_{sample})]L_{bb}(\lambda, T_{env}) \quad (1.14)$$

The sample spectral emissivity  $\varepsilon(\lambda, T_{sample})$  is consequently extracted (Eq.1.15):

$$\varepsilon(\lambda, \theta, T_{sample}) = \frac{L^*(\lambda, T_{sample}) - L_{bb}(\lambda, T_{amb})}{L_{bb}(\lambda, T_{sample}) - L_{bb}(\lambda, T_{amb})} \quad (1.15)$$

In the case of the spectroradiometer, the measured signal is the spectral directional radiance of the heated sample  $L_{sample}(\lambda, \theta, T)$ . The spectral directional emissivity  $\varepsilon(\lambda, \theta, T_{sample})$  is calculated according to (Eq.1.16), assuming a sample temperature significantly higher than ambient.

$$\varepsilon(\lambda, \theta, T) = \frac{L_{sample}(\lambda, \theta, T)\tau_{atm, sample}(\lambda, d = 1 \text{ m})}{L_{bb}(\lambda, T)\tau_{atm, bb}(\lambda, d = 1 \text{ m})} \quad (1.16)$$

If the blackbody calibration and the sample measurements are performed in a short time interval, the effect of atmospheric spectral transmissivity would cancel out ( $\tau_{atm, sample}/\tau_{atm, bb} \sim 1$ ), although local atmospheric absorption effects can be observed at specific wavelengths, mainly due to water vapor (H<sub>2</sub>O) or carbon dioxide (CO<sub>2</sub>). The most visible absorption bands are located around 1.37, 1.87, 2.7, 4.2 and 5.5-7.3  $\mu\text{m}$ .

## 1.5 Infrared thermometry

### 1.5.1 Radiometric chain

Any surface with a temperature above 0 K emits thermal radiation over the electromagnetic spectrum according to Planck's law of blackbody radiation (Eq.1.9) (Figure 1.22.b). IR thermometry is a measurement technique that detects the infrared radiation emitted by a surface to determine its temperature [161-163]. The radiometric chain concept is used in IR thermometry to describe all the optical phenomena influencing the radiation detected by the IR sensor when observing a surface at a temperature  $T_{surf}$ .

A generic radiometric chain is sketched for a CRS configuration in Figure 1.30. This diagram is simplified for illustrative purposes, omitting additional optical components such as protective windows or mirrors.

The illustrated radiometric chain consists of three atmospheric paths: i) **Path 1**: Sun to mirror, ii) **Path 2**: Mirror to receiver surface, iii) **Path 3**: Receiver surface to IR sensor.

The IR sensor detects a radiometric signal  $\phi_{sensor}$  [ $\text{W}\cdot\text{m}^{-2}$ ], which is the sum of three terms: i) **Term A**: Thermal radiation emitted by the receiver surface ( $\phi_{surf}$ ), ii) **Term B**: Reflected concentrated solar radiation ( $\phi_{sun}$ ), iii) **Term C**: Thermal radiation emitted by the atmosphere ( $\phi_{atm}$ ).

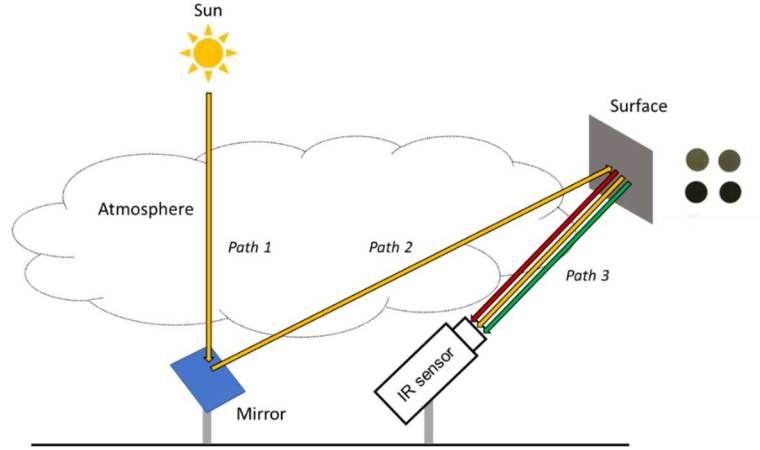


Figure 1.30: Schematic radiometric chain for a CRS configuration.

In Figure 1.30, terms A, B and C respectively correspond to the red, yellow and green arrows between the receiver surface and the IR sensor. Further terms could influence the radiometric balance inside the IR sensor, such as the IR sensor own thermal radiation and the reflections from the optical lens and/or filter [164].

A radiometric equation can be formulated for the spectral intensity  $I_{sensor}(\lambda)$  (Eq.1.17). This quantity can be further integrated bandwise over a defined spectral range  $[\lambda_{start}; \lambda_{stop}]$ , representative for the IR sensor spectral response (Eq.1.18).

$$I_{sensor}(\lambda) = I_{surf}(\lambda) + I_{sun}(\lambda) + I_{atm}(\lambda) \quad (1.17)$$

$$\phi_{sensor} = \int_{\lambda_{start}}^{\lambda_{stop}} I_{sensor}(\lambda) d\lambda = \phi_{surf} + \phi_{sun} + \phi_{atm} \quad (1.18)$$

$I_{surf}(\lambda)$ ,  $I_{sun}(\lambda)$  and  $I_{atm}(\lambda)$  are explicated further in (Eq.1.19-1.21):

$$I_{surf}(\lambda) = \varepsilon_{surf}(\lambda) \tau_{atm,path3}(\lambda) E_{bb}(\lambda, T_{surf}) SRF(\lambda, T_{sensor}) \quad (1.19)$$

$$I_{sun}(\lambda) = C_x [1 - \varepsilon_{surf}(\lambda)] \left[ \prod_{i=1}^3 \tau_{atm,path(i)}(\lambda) \right] \rho_{mirror}(\lambda) \cos(\theta) G_{sun}(\lambda, AM0) SRF(\lambda, T_{sensor}) \quad (1.20)$$

$$I_{atm}(\lambda) = [1 - \tau_{atm,path3}(\lambda)] E_{bb}(\lambda, T_{atm}) SRF(\lambda, T_{sensor}) \quad (1.21)$$

Blackbody spectral radiant exitance  $E_{bb}(\lambda, T)$  is defined in (Eq.1.9). The sensor spectral response function  $SRF(\lambda, T_{sensor})$  is defined in (Eq.1.22). It considers the IR sensor quantum efficiency  $QE(\lambda)$  and the spectral transmissivity of optical components, such as window, lens and filter.

$$SRF(\lambda, T_{sensor}) = \tau_{window}(\lambda) \tau_{lens}(\lambda) \tau_{filter}(\lambda) QE_{sensor}(\lambda, T_{sensor}) \quad (1.22)$$

The measurands of interest for opto-thermal characterization are respectively the surface spectral emissivity  $\varepsilon_{surf}(\lambda)$  and its temperature  $T_{surf}$ . The surface spectral emissivity  $\varepsilon_{surf}(\lambda)$  is embedded in (Eq.1.19-1.20), while  $T_{surf}$  is embedded in (Eq.1.19). Both measurands are accesible if term A, i.e.  $\phi_{surf}$  is dominant in the radiometric equation (Eq.1.18), while terms B ( $\phi_{sun}$ ) and C ( $\phi_{atm}$ ) can be deemed negligible. In this case, (Eq.1.18-1.19) simplify to (Eq.1.23):

$$\phi_{sensor} \approx \phi_{surf} = \int_{\lambda_{start}}^{\lambda_{stop}} \varepsilon_{surf}(\lambda) \tau_{atm,path3}(\lambda) E_{bb}(\lambda, T_{surf}) SRF(\lambda, T_{sensor}) d\lambda \quad (1.23)$$

Term B, i.e.  $\phi_{sun}$  (Integral of Eq.1.20) is negligible if so-called solar-blind conditions are met [165-169]. Different approaches can be adopted to achieve such conditions:

- i) Selecting a narrow bandpass (NB) filter centered on an atmospheric absorption band, such that solar irradiation is blocked, i.e.  $\tau_{atm,path1} \sim 0$ . However, atmospheric attenuation is expected on path 2 [72-77] and path 3 ( $\tau_{atm,path3} > 0$ ).
- ii) Selecting a spectral range where the mirror spectral reflectivity is minimal, i.e.  $\rho_{mirror}(\lambda) \sim 0$ .
- iii) Temporarily occulting concentrating solar radiation while maintaining the receiver surface isothermal ( $C_x = 0$ ).
- iv) Achieving near blackbody conditions for the receiver surface (i.e.  $\epsilon_{surf}(\lambda) \sim 1$ ).

Term C, i.e.  $\phi_{atm}$  (Integral of Eq.1.21) is generally considered negligible, as long as the atmosphere temperature  $T_{atm}$  is significantly lower than the receiver surface temperature  $T_{surf}$  ( $T_{atm} < T_{surf}$ ). Further internal contributions due to the reflection of the IR sensor thermal emission are a function of the sensor temperature  $T_{sensor}$  and the sensor spectral range of detection (SWIR, MWIR, LWIR). These contributions can be minimised if the IR optical system is athermalised (LWIR) or even cancelled if the IR sensor is cooled below ambient temperature.

## 1.5.2 Blackbody calibration

In practice, the detailed SRF of an IR sensor may not be directly accessible to the end user. The thermal radiation  $\phi_{surf}$  emitted by a surface (Eq.1.19) can be expressed in lumped form (Eq.1.24):

$$\phi_{surf} = \epsilon_{surf,band} \tau_{atm,band} BF(T_{surf}) \quad (24)$$

Where the band surface emittance  $\epsilon_{surf,band}$  and the band atmospheric transmittance  $\tau_{atm,band}$  are respectively defined in (Eq.1.25) and (Eq.1.26), while the blackbody calibration function  $BF(T_{surf})$  is defined in (Eq.1.27).

$$\epsilon_{surf,band} = \frac{\int_{\lambda_{start}}^{\lambda_{stop}} \epsilon_{surf}(\lambda) E_{bb}(\lambda, T_{surf}) SRF(\lambda, T_{sensor}) d\lambda}{bf(filter, T_{surf})} \quad (1.25)$$

$$\tau_{atm,band} = \frac{\int_{\lambda_{start}}^{\lambda_{stop}} \tau_{atm,path3}(\lambda) E_{bb}(\lambda, T_{surf}) SRF(\lambda, T_{sensor}) d\lambda}{BF(band, T_{surf})} \quad (1.26)$$

$$BF(T_{surf}) = \int_{\lambda_{start}}^{\lambda_{stop}} E_{bb}(\lambda, T_{surf}) SRF(\lambda, T_{sensor}) d\lambda \quad (1.27)$$

The function  $BF$  can be obtained under laboratory conditions for a given IR sensor with a reference blackbody ( $\epsilon_{surf,band} \rightarrow 1$ ), assuming the effect of atmospheric transmittance is either negligible for a short path, or corrected with a radiative transfer code, such as MODTRAN [170,171], monitoring laboratory parameters such as absolute humidity ( $g/m^3$ ) [172] and/or carbon dioxide ( $CO_2$ ) level (ppm).

Assuming the user has access to the IR sensor raw signal  $S$  in arbitrary units [A.U.] for a given blackbody temperature range, a mathematical model  $BF(T)$  can be fitted to the experimental data. Different equations have been proposed by Sakuma and Hattori [173]. One of the simplest mathematical models is expressed in (Eq.1.28). The reciprocal function  $BF^{-1}$  can be obtained analytically (Eq.1.29) to obtain the blackbody temperature  $T$  from a given signal  $S$ .

$$S = BF(T) = \frac{R}{\exp\left(\frac{B}{T}\right) - F} + O \quad (1.28)$$

$$T = BF^{-1}(S) = \frac{B}{\ln\left(\frac{R}{S-O} + F\right)} \quad (1.29)$$

One exemplary function  $BF$  and its reciprocal function  $BF^{-1}$  are shown for a LWIR camera in Figure 1.31. The calibration test method for IR sensor is defined in ASTM standards [174,175]. The IR sensor is positioned and aligned in front of a reference blackbody, which temperature is precisely controlled.

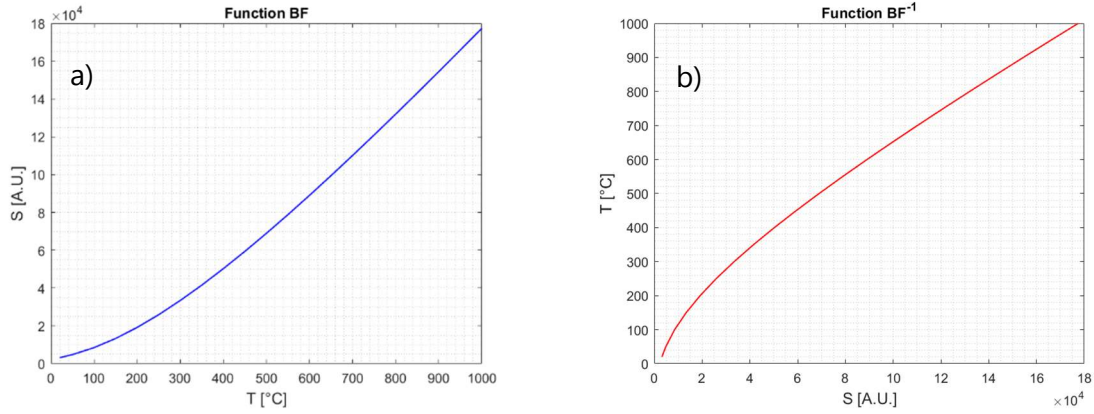


Figure 1.31: Exemplary blackbody calibration function (Eq.1.28-1.29).  $R=366545$ ;  $B=1428$ ;  $F=1$ ;  $O=342$  a) function  $BF$  b) reciprocal function  $BF^{-1}$ .

Reference blackbodies are available in different formats, for instance cavity and extended area blackbodies, as shown in Figure 1.32. Different cavity geometries exist, e.g. cylindrical or spherical, while the aperture diameter is typically 25.4 mm (one inch). In the case of IR thermography, cavity blackbodies allow calibrating a fraction of the image sensor, while extended blackbodies allow calibrating the full image sensor. Nonetheless, high temperature extended area blackbodies can only operate up to 600 °C because of electrical power consumption, while some cavity blackbodies can operate up to 3000 °C.



Figure 1.32: Example of reference blackbodies for temperature calibration. a) Mikron M305 cavity blackbody [176]. b) ECN100 extended area blackbody [177].

### 1.5.3 Single band IR thermometry

In the case of a single band IR sensor (Eq.1.24), a priori knowledge of  $\epsilon_{surf,band}$  (Eq.1.25) and  $\tau_{atm,band}$  (Eq.1.26) parameters is required to determine the surface temperature  $T_{surf}$ , according to (Eq.1.30). Both parameters  $\epsilon_{surf,band}$  and  $\tau_{atm,band}$  should be bound within ]0%;100%]. The determination of both parameters is briefly explained in the next paragraphs.

$$T_{surf} = BF^{-1}\left(\frac{\phi_{surf}}{\epsilon_{surf,band} \cdot \tau_{atm,band}}\right) \quad (1.30)$$

### 1.5.3.1 Surface band emittance

The surface band emittance  $\epsilon_{surf,band}$  is a material property, which is a function of several parameters: i) surface geometry, ii) surface structure (roughness), iii) view angle, iv) wavelength range and v) temperature. This material property may vary in time if the material degrades.

Laboratory methods for the measurement of spectral emissivity at ambient and operating temperature have already been introduced in subsections 1.4.2 and 1.4.3. In contrast to the thermal emittance  $\epsilon_{th}$  (Eq.1.8), the integration of spectral data requires this time the knowledge of the IR sensor spectral response  $SRF$  (Eq.1.22).

A laboratory measurement setup is shown in Figure 1.33 for the experimental characterization of effective directional emissivity, as a function of temperature, view angle for a given IR camera. A coated material sample is heated to a defined temperature. A reference coating of known band emittance  $\epsilon_{surf,band}$  is applied on a fraction of this sample surface to allow the temperature monitoring with a reference IR camera. Another IR camera is mounted on a metal frame, with an adjustable view angle. For this IR camera, the band emittance  $\epsilon_{surf,band}$  is adjusted for any viewing angle so that both IR cameras show the same temperature. This setup is applicable for small samples and short measurement ranges (approx. 1 meter), assuming atmospheric influences are negligible for the selected wavelength range.

Different practical methods exist in thermography for determining the effective value of  $\epsilon_{surf,band}$ , if laboratory measurements are not available. One may apply a tape or a paint for which  $\epsilon_{surf,band}$  is known and use a contact thermometer to have a reference area, assuming the adjacent area is isothermal. One may also directly use one or several contact thermometers in thermal equilibrium with the surface.

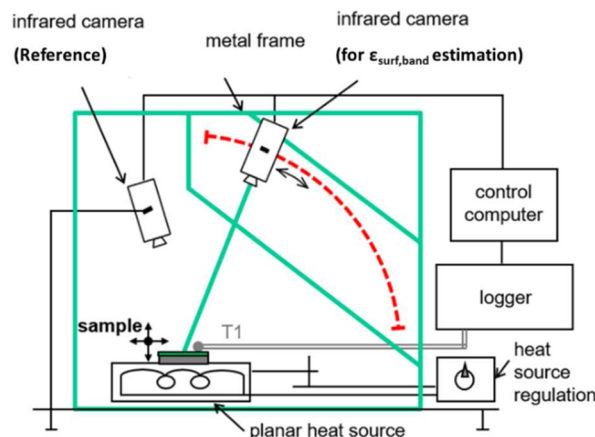


Figure 1.33: Measurement setup for the experimental characterization of effective directional emittance [178].

For solar thermal receivers used in CSP applications, the in-situ determination of  $\epsilon_{surf,band}$  is most often performed by using contact thermometers in thermal equilibrium with the surface. However, the contact thermometer cannot be exposed to concentrated solar radiation, otherwise the temperature reading would be biased. In practice, the HTF temperature is monitored with contact thermometers and the receiver is maintained isothermal without concentrated solar radiation, adjusting for instance the HTF mass flow.

### 1.5.3.2 Atmospheric band transmittance

The dry atmosphere is composed of several gases, i.e. 78% nitrogen (N<sub>2</sub>), 21% oxygen O<sub>2</sub> and various trace gases. In addition, there is a variable amount of water vapor (H<sub>2</sub>O). Molecules such as water vapor H<sub>2</sub>O, carbon dioxide CO<sub>2</sub>, ozone O<sub>3</sub> are able to absorb IR radiation. Aerosols also affect atmospheric attenuation [72-77]. The atmosphere consists of several layers: air composition, temperature and atmospheric pressure vary with the altitude.

Radiative transfer codes, such as SMARTS [135,136] or MODTRAN [170,171] allows simulating the atmospheric spectral transmissivity for different paths and wavelength ranges. An exemplary simulation performed with MODTRAN is shown in Figure 1.34 for two horizontal paths, respectively of 100 m and 1 km. The atmospheric spectral transmissivity is a function of the concentration of absorbing gas species and the distance between the object and camera.

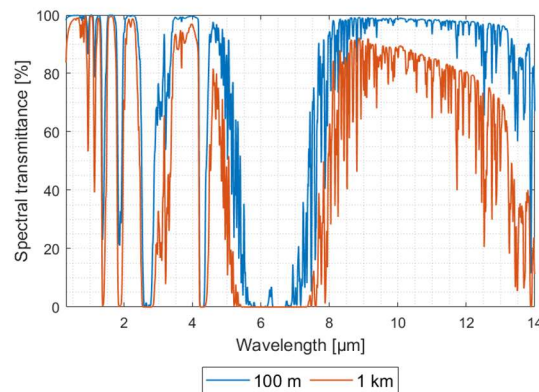


*Figure 1.34: Simulation of atmospheric spectral transmissivity for two horizontal paths with MODTRAN6 software.  $T_{amb}$ : 25 °C; RH: 50%. CO<sub>2</sub>: 400 ppm.*

Knowing the atmospheric spectral transmissivity and the camera SRF, one could calculate the atmospheric band transmittance  $\tau_{atm,band}$  using (Eq.1.26) and derive a correlation with respect to atmospheric parameters and the distance between the measurement object and the camera [179]. This correlation is however often embedded in the IR sensor software and may have to be adopted for different sites, while the atmospheric path may have an arbitrary tilt with respect to the ground.

While  $\tau_{atm,band}$  may not be critical for short ranges found in PTC application, it can affect IR measurements for CRS applications. There are some practical alternatives to a model-based correlation. One could for instance apply a similar method outline above for the determination of  $\epsilon_{surf,band}$ , but determine instead the product  $\epsilon_{surf,band}\tau_{atm,band}$  and monitor in parallel meteorological parameters such as absolute humidity (g/m<sup>3</sup>) [172] and/or CO<sub>2</sub> level (ppm). Alternatively, an electrically heated reference target with known  $\epsilon_{surf,band}$  or a cavity could be installed close to the central receiver. The temperature of this reference object being measured with a contact thermometer, one could determine in situ the value of  $\tau_{atm,band}$ , assuming an homogeneous atmosphere around the IR measurement object.

### 1.5.4 State of the art in CSP

IR thermography has been used for monitoring solar thermal receivers in CSP plants. For PTC applications, SWIR thermography can be used to measure the absorber tube temperature

through the glass envelope [169], while ground-based or airborne LWIR thermography is often used to measure the glass envelope temperature and draw an inference on the annulus vacuum quality [95-97]. In the case of PTC applications, IR thermography is used for predictive maintenance tasks to monitor the permeation of hydrogen or air infiltration [94,98]. The HTF inlet and outlet temperatures are measured and controlled in real time using contact temperature sensors. The concentration factor  $C_x$  is constant during operation due to collector geometry.

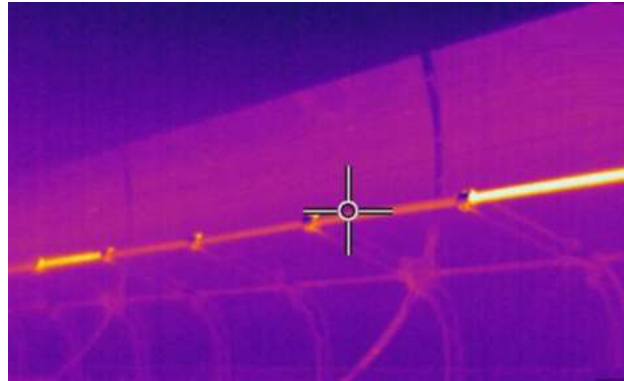


*Figure 1.35: Airborne LWIR monitoring of parabolic trough receivers glass envelope [95].*

For CRS applications with molten salts, the HTF loop temperature is also monitored in real time with contact thermometers. LWIR cameras monitor the receiver surface temperature in real time through all operation phases, in particular when molten salts are filled and drained in the central receivers. Pre-heating and cool-down are particularly critical as molten salt freeze below 250 °C. During operation, LWIR temperature maps can be used for indirect flux measurements inverting a thermodynamic model of the receiver [180]. The knowledge of flux maps [83,84] allows a dynamic control of the heliostat field aim point strategy [79,80].

One commercial LWIR system for CRS applications is shown in Figure 1.36. This system, known as Solar Power Tower Check (SPTC) is offered by Infratec GmbH. For external cylindrical receiver designs, multiple ground-based LWIR camera systems are located around the receiver circumference for redundant monitoring from different view angles. Each LWIR camera system uses an uncooled microbolometer with a high resolution as a detector, combined to a custom tele-objective made of Germanium with an anti-reflective coating (ARC). Each LWIR camera is mounted inside an athermalised protective housing, with a Ge protective window with ARC, to minimise the influence of outdoor conditions, such as solar radiation or ambient temperature, on the measurement accuracy.

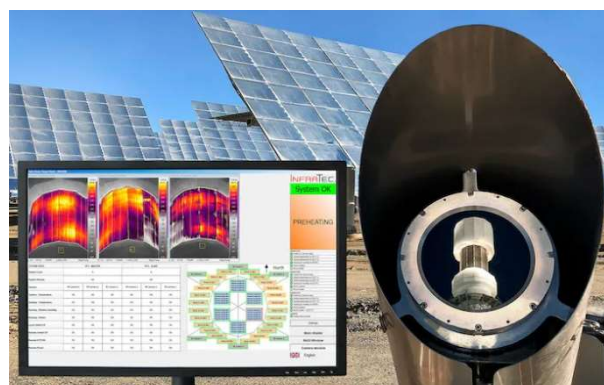


*Figure 1.36: Commercial LWIR system for CRS applications [181].*



## 1.6 References: Chapter 1

- [1] Bulletin of the Atomic Scientists, Current Time, available at: <https://thebulletin.org/doomsday-clock/current-time/>. Accessed: 15/12/2023.
- [2] K. Richardson et al., Earth beyond six of nine planetary boundaries. *Science Advances*, (37) (2023). DOI:10.1126/sciadv.adh2458
- [3] IPCC, Climate Change 2023, Synthesis Report, Summary for Policymakers, available at: [https://www.ipcc.ch/report/ar6/syr/downloads/report/IPCC\\_AR6\\_SYR\\_SPM.pdf](https://www.ipcc.ch/report/ar6/syr/downloads/report/IPCC_AR6_SYR_SPM.pdf). Accessed 15/12/2023.
- [4] UN, The Sustainable Development Goals Report, Special Edition (2023), available at: <https://unstats.un.org/sdgs/report/2023/The-Sustainable-Development-Goals-Report-2023.pdf>. Accessed: 15/12/2023.
- [5] M. Perez, R. Perez, A fundamental look at supply side energy reserves for the planet, *Solar Energy Advances*, 2 (2022), 100014. <https://doi.org/10.1016/j.seja.2022.100014>
- [6] IRENA, Renewable Power Generation Costs in 2022, available at <https://www.irena.org/Publications/2023/Aug/Renewable-Power-Generation-Costs-in-2022>. Accessed: 15/12/2023.
- [7] IRENA, Solar Energy, available at: <https://www.irena.org/Energy-Transition/Technology/Solar-energy>. Accessed: 15/12/2023.
- [8] SolarPACES, CSP Projects around the world, available at: <https://www.solarpaces.org/worldwide-csp/csp-projects-around-the-world/>. Accessed: 15/12/2023.
- [9] A. Fernandez-Garcia et al., Parabolic-trough solar collectors and their applications, *Renewable and Sustainable Energy Reviews*, 14 (2010), 1695–1721. <https://doi.org/10.1016/j.rser.2010.03.012>
- [10] REN 21, Renewables 2020 – Global Status Report, available at: [https://www.ren21.net/wp-content/uploads/2019/05/gsr\\_2020\\_full\\_report\\_en.pdf](https://www.ren21.net/wp-content/uploads/2019/05/gsr_2020_full_report_en.pdf). Accessed: 15/12/2023.
- [11] U.S. Solar Energy Technology Office, SunShot 2030, available at: <https://www.energy.gov/eere/solar/sunshot-2030>. Accessed: 15/12/2023.
- [12] I. Mauleón, Photovoltaic learning rate estimation: Issues and implications, *Renewable and Sustainable Energy Reviews*, 65 (2016), 507-524. <https://doi.org/10.1016/j.rser.2016.06.070>
- [13] NREL, Best Research-Cell Efficiency Chart, available at : <https://www.nrel.gov/pv/cell-efficiency.html>. Accessed: 15/12/2023.
- [14] P. Gauche et al., System value and progress of CSP, *Solar Energy*, 152 (2017), 106-139. <https://doi.org/10.1016/j.solener.2017.03.072>
- [15] X. Ju et al., A review on the development of photovoltaic/concentrated solar power (PVCSP) hybrid systems, *Solar Energy Materials and Solar Cells*, 161 (2017), 305-327. <https://doi.org/10.1016/j.solmat.2016.12.004>
- [16] A. Zurita et al., Techno-economic evaluation of a hybrid CSP + PV plant integrated with thermal energy storage and a large-scale battery energy storage system for base generation, *Solar Energy*, 173 (2018), 1262-1277. <https://doi.org/10.1016/j.solener.2018.08.061>
- [17] J. Simpson, E. Loth, K. Dykes, Cost of Valued Energy for design of renewable energy systems, *Renewable Energy*, 153 (2020),290-300. <https://doi.org/10.1016/j.renene.2020.01.131>
- [18] N. Bolso, P. Prieto, T. Patzek, Capacity factors for electrical power generation from renewable and nonrenewable sources, *Proceedings of the National Academy of Sciences*, 119 (52) (2022),1-6. <https://doi.org/10.1073/pnas.2205429119>

- [19] P. Denholm, T. Mai, Timescales of energy storage needed for reducing renewable energy curtailment, *Renewable Energy*, 130 (2019), 388-399. <https://doi.org/10.1016/j.renene.2018.06.079>
- [20] German Aerospace Center (DLR) Institute of Solar Research, Solar thermal power plants: heat, electricity and fuels from concentrated solar power, (2021), available at: [https://www.dlr.de/sf/en/PortalData/73/Resources/dokumente/publikationen\\_medien/dlr\\_und\\_sf/Study\\_Solar\\_thermal\\_power\\_plants\\_DLR\\_2021-05.pdf](https://www.dlr.de/sf/en/PortalData/73/Resources/dokumente/publikationen_medien/dlr_und_sf/Study_Solar_thermal_power_plants_DLR_2021-05.pdf). Accessed:15/12/2023.
- [21] DCSP, German Association for Concentrated Solar Power, Solar Power around the Clock, (2021), available at: [EN%20211116\\_DCSP\\_Kurzstudie\\_online\\_EN.pdf \(website-editor.net\)](EN%20211116_DCSP_Kurzstudie_online_EN.pdf_(website-editor.net)). Accessed: 15/12/2023.
- [22] M.S. Ziegler, J.E. Trancik, Re-examining rates of lithium-ion battery technology improvement and cost decline, *Energy & Environmental Science*, 14 (2021), 1635-1651. <https://doi.org/10.1039/D0EE02681F>
- [23] Lazard, 2023 Levelized Cost of Energy+, available at: <https://www.lazard.com/research-insights/2023-levelized-cost-of-energyplus/>. Accessed: 15/12/2023.
- [24] F. Schöninger et al., Making the sun shine at night: comparing the cost of dispatchable concentrating solar power and photovoltaics with storage, *Energy Sources, Part B: Economics, Planning and Policy*, 16(1) (2021), 55-74. <https://doi.org/10.1080/15567249.2020.1843565>
- [25] IRENA, Electricity Storage and Renewables: Costs and Market to 2030, available at: [Electricity storage and renewables: Costs and markets to 2030 \(irena.org\)](Electricity_storage_and_renewables:_Costs_and_markets_to_2030_(irena.org)). Accessed: 15/12/2023.
- [26] J. Lilliestam et al., Empirically observed learning rates for concentrating solar power and their responses to regime change, *Nature Energy*, 2 (2017), 17094. <https://doi.org/10.1038/nenergy.2017.94>
- [27] R. Pitz-Paal, Concentrating solar power: Still small but learning fast, *Nature Energy*, 2 (2017), 17095. <https://doi.org/10.1038/nenergy.2017.95>
- [28] J. Lilliestam et al., The near- to mid-term outlook for concentrating solar power: mostly cloudy, chance of sun, *Energy Sources, Part B: Economics, Planning, and Policy*, 16(1) (2021), 23-41. <https://doi.org/10.1080/15567249.2020.1773580>
- [29] Solar Payback, Solar Heat for Industry, (2017), available at: <https://www.solar-payback.com/download/solar-heat-for-industry-april-2017/>. Accessed: 15/12/2023.
- [30] R. Pitz-Paal et al., Decarbonizing the German industrial thermal energy use with solar, hydrogen, and other options—Recommendations for the world, *Solar Compass*, 3-4 (2022),100029. <https://doi.org/10.1016/j.solcom.2022.100029>
- [31] Absolicon, A smart transition towards solar thermal, available at: <https://www.absolicon.com/t160-production-line/heat-steam-and-cooling/>. Accessed: 15/12/2023.
- [32] M. We, C.A. McMillan, S. de la Rue du Can, Electrification of Industry: Potential, Challenges and Outlook, *Current Sustainable/Renewable Energy Reports*, 6 (2019), 140–148. <https://doi.org/10.1007/s40518-019-00136-1>
- [33] S.H. Farjana et al., Solar process heat in industrial systems – A global review, *Renewable and Sustainable Energy Reviews*, 82(3) (2018), 2270-2286. <https://doi.org/10.1016/j.rser.2017.08.065>
- [34] SolarGIS, Solar Resource Map : Direct Normal Irradiation, <https://solargis.com/maps-and-gis-data/download/world>. Accessed 15/12/2023.

- [35] J. Frederiksson et al., A comparison and evaluation of innovative parabolic trough collector concepts for large-scale application, *Solar Energy*, 215 (2021), 266-310. <https://doi.org/10.1016/j.solener.2020.12.017>
- [36] M. Wirz et al., Potential improvements in the optical and thermal efficiencies of parabolic trough concentrators, *Solar Energy*, 107 (2014), 398-414. <https://doi.org/10.1016/j.solener.2014.05.002>
- [37] G. Zhu et al., History, current state, and future of linear Fresnel concentrating solar collectors, *Solar Energy*, 103 (2014), 639-652. <https://doi.org/10.1016/j.solener.2013.05.021>
- [38] G. Morin et al., Comparison of Linear Fresnel and Parabolic Trough Collector power plants, *Solar Energy*, 86(1) (2012), 1-12. <https://doi.org/10.1016/j.solener.2013.05.021>
- [39] C.K. Ho, B.D. Iverson, Review of high-temperature central receiver designs for concentrating solar power, *Renewable and Sustainable Energy Reviews*, 29 (2014), 835-846. <https://doi.org/10.1016/j.rser.2013.08.099>
- [40] C.K. Ho, Advances in central receivers for concentrating solar applications, *Solar Energy*, 152 (2017), 38-56. <https://doi.org/10.1016/j.solener.2017.03.048>
- [41] J. Coventry, C. Andraka, Dish systems for CSP, *Solar Energy*, 152 (2017), 140-170. <https://doi.org/10.1016/j.solener.2017.02.056>
- [42] M.E. Zayed et al., A comprehensive review on Dish/Stirling concentrated solar power systems: Design, optical and geometrical analyses, thermal performance assessment, and applications, *Journal of Cleaner Energy Production*, 283 (2021), 124664. <https://doi.org/10.1016/j.jclepro.2020.124664>
- [43] W.T. Xie et al., Concentrated solar energy applications using Fresnel lenses: A review, *Renewable and Sustainable Energy Reviews*, 15(6) (2011), 2588-2606. <https://doi.org/10.1016/j.rser.2011.03.031>
- [44] A.R. Jensen et al., Thermal performance assessment of the world's first solar thermal Fresnel lens collector field, *Solar Energy*, 237 (2022), 447-455. <https://doi.org/10.1016/j.solener.2022.01.067>
- [45] E. Bellos, Progress in beam-down solar concentrating systems, *Progress in Energy and Combustion Science*, 97 (2023), 101085. <https://doi.org/10.1016/j.pecs.2023.101085>
- [46] R. Thonig, A. Gilmanova, J. Liliestam, CSP.guru 2023-07-01, dataset, available at: <https://doi.org/10.5281/zenodo.1318151>. Accessed: 15/12/2023.
- [47] J.A. Duffie, W.A. Beckman, *Solar Engineering of Thermal Processes, Photovoltaics and Wind*, Fifth edition, Wiley and Sons (2020). DOI:10.1002/9781119540328
- [48] K. Lovegrove, W. Stein, *Concentrating Solar Power Technology: Principles, Developments and Applications*, Second edition, Woodhead Publishing; (2020). <https://doi.org/10.1016/C2018-0-04978-6>
- [49] L. Moens, D.M. Blake, Advanced heat transfer and thermal storage fluids. In: *Proceedings of the ASME 2005 International Solar Energy Conference*, (2005), 791-793. <https://doi.org/10.1115/ISEC2005-76192>. ISEC2005-76192.
- [50] L. Moens, D.M. Blake, Mechanisms of hydrogen formation in solar parabolic trough receivers *Journal of Solar Energy Engineering*, 132(3) (2010), 0410006. <https://doi.org/10.1115/1.4001402>
- [51] C. Hilgert et al., Silicone-Based Heat Transfer Fluids (SiHTF) in Line Focusing Concentrating Solar Power Applications, *SolarPACES Guideline v1.0*, (2021), available at: [https://www.solarpaces.org/wp-content/uploads/Guideline\\_SiHTF\\_V1.0.pdf](https://www.solarpaces.org/wp-content/uploads/Guideline_SiHTF_V1.0.pdf). Accessed: 15/12/2023.

- [52] M. Wittmann et al., HPS2 – demonstration of molten-salt in parabolic trough plants – Design of plant, *AIP Conference Proceedings*, 2126 (2019), 120024. <https://doi.org/10.1063/1.5117642>
- [53] A. Bonk et al., Advanced heat transfer fluids for direct molten salt line-focusing CSP plants, *Progress in Energy and Combustion Science*, 67 (2018), 69-87. <https://doi.org/10.1016/j.pecs.2018.02.002>
- [54] A. Bonk et al., Solar Salt – Pushing an old material for energy storage to a new limit, *Applied Energy*, 262 (2020), 114535. <https://doi.org/10.1016/j.apenergy.2020.114535>
- [55] W. Ding, T. Bauer, Progress in Research and Development of Molten Chloride Salt Technology for Next Generation Concentrated Solar Power Plants, *Engineering*, 7(3) (2021), 334-347. <https://doi.org/10.1016/j.eng.2020.06.027>.
- [56] F. Sutter et al., Dynamic corrosion testing of metals in solar salt for concentrated solar power, *Solar Energy Materials and Solar Cells*, 232 (2021), 111331. <https://doi.org/10.1016/j.solmat.2021.111331>.
- [57] J. Coventry et al., A review of sodium receiver technologies for central receiver solar power plants, *Solar Energy*, 122 (2015), 749-762. <https://doi.org/10.1016/j.solener.2015.09.023>
- [58] N. Lorenzin, A. Abanades, A review on the application of liquid metals as heat transfer fluid in Concentrated Solar Power technologies, *International Journal of Hydrogen Energy*, 41(17) (2016), 6990-6995. <https://doi.org/10.1016/j.ijhydene.2016.01.030>
- [59] A. Calderon et al., Review of solid particle materials for heat transfer fluid and thermal energy storage in solar thermal power plants, *Energy Storage*, 1(4) (2020), 1-20. <https://doi.org/10.1002/est2.63>
- [60] C.K. Ho, A review of high-temperature particle receivers for concentrating solar power, *Applied Thermal Engineering*, 109(B) (2016), 958-969. <https://doi.org/10.1016/j.applthermaleng.2016.04.103>
- [61] T. Galiullin et al., High temperature oxidation and erosion of candidate materials for particle receivers of concentrated solar power tower systems, *Solar Energy*, 188 (2019), 883-889. <https://doi.org/10.1016/j.solener.2019.06.057>
- [62] B. Gobereit et al., Assessment and improvement of optical properties of particles for solid particle receiver, *Solar Energy*, 199 (2020), 844-851. <https://doi.org/10.1016/j.solener.2020.02.076>
- [63] A.L. Avila-Marin, Volumetric receivers in Solar Thermal Power Plants with Central Receiver System technology: A review, *Solar Energy*, 85(5) (2011), 891-910. <https://doi.org/10.1016/j.solener.2011.02.002>
- [64] Y.L. He, S. Du, S. Shen, Advances in porous volumetric solar receivers and enhancement of volumetric absorption, *Energy Reviews*, 2(3) (2023), 100035. <https://doi.org/10.1016/j.enrev.2023.100035>
- [65] M. Mehos et al., Concentrating Solar Power Best Practices Study, *NREL Technical report*, NREL/TP-5500-75763 (2020), available at: <https://www.nrel.gov/docs/fy20osti/75763.pdf>. Accessed: 15/12/2023.
- [66] G. Glatzmaier, Development of Hydrogen Mitigation for the Nevada Solar One Power Plant, *NREL Technical report*, NREL/TP-5500-75127 (2020), available at: <https://www.nrel.gov/docs/fy20osti/75127.pdf>. Accessed: 15/12/2023.
- [67] J. Leon et al., Test loop for inter-connections of parabolic trough collectors, *AIP Conference Proceedings*, 2033 (2018), 030008. <https://doi.org/10.1063/1.5067024>

- [68] M. Topel, B. Laumert, Improving concentrating solar power plant performance by increasing steam turbine flexibility at start-up, *Solar Energy*, 165 (2018), 10-18. <https://doi.org/10.1016/j.solener.2018.02.036>
- [69] D. Ferruzza et al., Impact of steam generator start-up limitations on the performance of a parabolic trough solar power plant, *Solar Energy*, 169 (2018), 255-263. <https://doi.org/10.1016/j.solener.2018.05.010>
- [70] A. Wang et al., Steam generation system operation optimization in parabolic trough concentrating solar power plants under cloudy conditions, *Applied Energy*, 265 (2020), 114790. <https://doi.org/10.1016/j.apenergy.2020.114790>
- [71] C. Prieto et al., Lessons learned from corrosion of materials with molten salts during molten salt tank preheating, *Solar Energy Materials and Solar Cells*, 247 (2022), 111943. <https://doi.org/10.1016/j.solmat.2022.111943>
- [72] J. Ballestin, A. Marzo, Solar radiation attenuation in solar tower plants, *Solar Energy*, 86(1) (2012), 388-392. <https://doi.org/10.1016/j.solener.2011.10.010>
- [73] J. Polo, J. Ballestrin, E. Carra, Sensitivity study for modelling atmospheric attenuation of solar radiation with radiative transfer models and the impact in solar tower plant production, *Solar Energy*, 134 (2016), 219-227. <https://doi.org/10.1016/j.solener.2016.04.050>
- [74] N. Hanrieder et al., Atmospheric extinction in solar tower plants – A review, *Solar Energy*, 152 (2017), 193-207. <https://doi.org/10.1016/j.solener.2017.01.013>
- [75] J. Polo et al., Analysis of solar tower plant performance influenced by atmospheric attenuation at different temporal resolutions related to aerosol optical depth, *Solar Energy*, 157 (2017), 803-810. <https://doi.org/10.1016/j.solener.2017.09.003>
- [76] J. Ballestrin et al., Solar extinction measurement system based on digital cameras. Application to solar tower plants, *Renewable Energy*, 125 (2018), 648-654. <https://doi.org/10.1016/j.renene.2018.03.004>
- [77] C. Heras et al., Atmospheric attenuation measurement system for commercial solar plants based on optical spectrum analysis, *Solar Energy*, 236 (2022), 782-789. <https://doi.org/10.1016/j.solener.2022.03.057>
- [78] L.L. Vant-Hull, The Role of "Allowable Flux Density" in the Design and Operation of Molten-Salt Solar Central Receivers, *Journal of Solar Energy Engineering*, 124(2) (2002), 165-169. <https://doi.org/10.1115/1.1464124>
- [79] R. Flesch et al., Towards an optimal aiming for molten salt power towers, *Solar Energy*, 155 (2017), 1273-1281. <https://doi.org/10.1016/j.solener.2017.07.067>
- [80] A. Sanchez-Gonzalez, M.R. Rodriguez-Sanchez, D. Santana, Aiming strategy model based on allowable flux densities for molten salt central receivers, *Solar Energy*, 157 (2017), 1130-1144. <https://doi.org/10.1016/j.solener.2015.12.055>
- [81] C.K. Ho, S.S. Khalsa, A Photographic Flux Mapping Method for Concentrating Solar Collectors and Receivers, *Journal of Solar Energy Engineering*, 134 (4) (2012), 041004. <https://doi.org/10.1115/1.4006892>
- [82] M. Röger et al., Techniques to Measure Solar Flux Density Distribution on Large-Scale Receivers, *Journal of Solar Energy Engineering*, 136(3) (2014), 031013. <https://doi.org/10.1115/1.4027261>
- [83] J. Ballestrin et al., Simplifying the measurement of high solar irradiance on receivers. Application to solar tower plants, *Renewable Energy*, 138 (2019), 551-561. <https://doi.org/10.1016/j.renene.2019.01.131>

- [84] M. Casanova et al., Improvements in the measurement of high solar irradiance on a 300 kWth volumetric receiver, *Renewable Energy*, 201(1) (2022), 441-449. <https://doi.org/10.1016/j.renene.2022.10.080>
- [85] M.M. Rodriguez-Garcia, M. Herrador-Moreno, E. Zarza Moya, Lessons learnt during the design, construction and start-up phase of a molten salt testing facility, *Applied Thermal Engineering*, 62(2) (2014), 520-528. <https://doi.org/10.1016/j.applthermaleng.2013.09.040>
- [86] A.M. Bonanos et al., Engineering aspects and thermal performance of molten salt transfer lines in solar power applications, *Applied Thermal Engineering*, 154 (2019), 294-301. <https://doi.org/10.1016/j.applthermaleng.2019.03.091>
- [87] F. Burkholder, C. Kutscher, Heat Loss Testing of Schott's 2008 PTR70 Parabolic Trough Receiver, *NREL Technical report*, NREL/TP-550-45633 (2009), available at : <https://www.nrel.gov/docs/fy09osti/45633.pdf>. Accessed: 15/12/2023.
- [88] R. Forristall, Heat Transfer Analysis and Modeling of a Parabolic Trough Solar Receiver Implemented in Engineering Equation Solver, *NREL Technical report*, NREL/TP-550-34169 (2003). <https://doi.org/10.2172/15004820>
- [89] S.A. Kalogirou, A detailed thermal model of a parabolic trough collector receiver, *Energy*, 48(1) (2012), 298-306. <https://doi.org/10.1016/j.energy.2012.06.023>
- [90] D. Lei et al., An experimental study of thermal characterization of parabolic trough receivers, *Energy Conversion and Management*, 69 (2013), 107-115. <https://doi.org/10.1016/j.enconman.2013.02.002>
- [91] J.L. Navarro-Hermoso et al., Parabolic trough solar receivers characterization using specific test bench for transmittance, absorptance and heat loss simultaneous measurement *Solar Energy*, 136 (2016), 268-277. <https://doi.org/10.1016/j.solener.2016.07.012>
- [92] J. Pernpeintner et al., Durability Testing of Parabolic Trough Receivers – Overheating, Thermal Cycling, bellow Fatigue and Antireflex-Coating Abrasion, *Energy Procedia*, 69 (2015), 1540-1550. <https://doi.org/10.1016/j.egypro.2015.03.105>
- [93] S. Caron, M. Röger, J. Pernpeintner, Heat flux and temperature measurements on glass envelope and bellows of parabolic trough receivers, *AIP Conference Proceedings*, 2033 (2018) 030004. <https://doi.org/10.1063/1.5067020>
- [94] J. Li et al., Hydrogen permeation model of parabolic trough receiver tube, *Solar Energy*, 86(5) (2012), 1187-1196. <https://doi.org/10.1016/j.solener.2012.01.011>
- [95] G. Espinosa-Rueda et al., Vacuum evaluation of parabolic trough receiver tubes in a 50 MW concentrated solar power plant, *Solar Energy*, 139 (2016),36-46. <https://doi.org/10.1016/j.solener.2016.09.017>
- [96] E. Setien, R. Lopez-Martin, L. Valenzuela, Methodology for partial vacuum pressure and heat losses analysis of parabolic troughs receivers by infrared radiometry, *Infrared Physics & Technology*, 98 (2019), 341-353. <https://doi.org/10.1016/j.infrared.2019.02.011>
- [97] M.E. Carra et al., Study of parameters influence on the measurement of vacuum level in parabolic trough collectors' receivers using infrared thermography, *Infrared Physics & Technology*, 131 (2023), 104657. <https://doi.org/10.1016/j.infrared.2023.104657>
- [98] M. Röger et al., Techno-economic analysis of receiver replacement scenarios in a parabolic trough field, *AIP Conference Proceedings*, 1734 (2016), 030030. <https://doi.org/10.1063/1.4949082>

- [99] S. Wang et al., Co-optimisation of the heliostat field and receiver for concentrated solar power plants, *Applied Energy*, 348 (2023), 121513. <https://doi.org/10.1016/j.apenergy.2023.121513>
- [100] C.K. Ho et al., Characterization of Pyromark 2500 paint for high-temperature solar receivers, *Journal of Solar Energy Engineering*, 136(1) (2014), 014502. <https://doi.org/10.1115/1.4024031>
- [101] P. Schöttl et al., Optimization of Solar Tower molten salt cavity receivers for maximum yield based on annual performance assessment, *Solar Energy*, 199 (2020), 278-294. <https://doi.org/10.1016/j.solener.2020.02.007>
- [102] M. Zheng et al., Analysis of tubular receivers for concentrating solar tower systems with a range of working fluids, in exergy-optimised flow-path configurations, *Solar Energy*, 211 (2020), 999-1016. <https://doi.org/10.1016/j.solener.2020.09.037>
- [103] C.A. Asselineau, J. Pye, J. Coventry, Exploring efficiency limits for molten-salt and sodium external cylindrical receivers for third-generation concentrating solar power, *Solar Energy*, 240 (2022), 354-375. <https://doi.org/10.1016/j.solener.2022.05.001>
- [104] R. Perez-Alvarez et al., Thermal stress and fatigue damage of central receiver tubes during their preheating, *Applied Thermal Engineering*, 195 (2021), 117115. <https://doi.org/10.1016/j.applthermaleng.2021.117115>
- [105] M. Laporte-Azcue et al., Deflection and stresses in solar central receivers, *Solar Energy*, 195 (2020), 355-368. <https://doi.org/10.1016/j.solener.2019.11.066>
- [106] D. Hering et al., Monitoring of service life consumption for tubular solar receivers: Review of contemporary thermomechanical and damage modeling approaches, *Solar Energy*, 226 (2021), 427-445. <https://doi.org/10.1016/j.solener.2021.08.022>
- [107] A. Tiddens et al., Air return ratio measurements at the solar tower Jülich using a tracer gas method, *Solar Energy*, 146 (2017), 351-358. <https://doi.org/10.1016/j.solener.2017.02.027>
- [108] A. Kribus et al., The promise and challenge of solar volumetric absorbers, *Solar Energy*, 110 (2014), 463-481. <https://doi.org/10.1016/j.solener.2014.09.035>
- [109] A.L. Avila-Marin et al., Experimental study of innovative periodic cellular structures as air volumetric absorbers, *Renewable Energy*, 184 (2022), 391-404. <https://doi.org/10.1016/j.renene.2021.11.021>
- [110] L. Noc, I. Jerman, Review of the spectrally selective (CSP) absorber coatings, suitable for use in SHIP, *Solar Energy Materials and Solar Cells*, 238 (2022), 111625. <https://doi.org/10.1016/j.solmat.2022.111625>
- [111] K. Burlafinger, A. Vetter, C.J. Brabec, Maximizing concentrated solar power (CSP) plant overall efficiencies by using spectral selective absorbers at optimal operation temperatures, *Solar Energy*, 120 (2015), 428-438. <https://doi.org/10.1016/j.solener.2015.07.023>
- [112] A. Grosjean, A. Soum-Glaude, L. Thomas, Influence of operating conditions on the optical optimization of solar selective absorber coatings, *Solar Energy Materials and Solar Cells*, 230 (2021), 111280. <https://doi.org/10.1016/j.solmat.2021.111280>
- [113] M. Lopez-Herraiz et al., Effect of the optical properties of the coating of a concentrated solar power central receiver on its thermal efficiency, *Solar Energy Materials and Solar Cells*, 159 (2017), 66-72. <https://doi.org/10.1016/j.solmat.2016.08.031>
- [114] C. Atkinson et al., Coatings for concentrating solar systems – A review, *Renewable and Sustainable Energy Reviews*, 45 (2015), 113-122. <https://doi.org/10.1016/j.rser.2015.01.015>

- [115] K. Xu et al., A review of high-temperature selective absorbing coatings for solar thermal applications, *Journal of Materiomics*, 6(1) (2020), 167-182 <https://doi.org/10.1016/j.jmat.2019.12.012>
- [116] J. Coventry, P. Burge, Optical properties of Pyromark 2500 coatings of variable thicknesses on a range of materials for concentrating solar thermal applications, *AIP Conference Proceedings*, 1850 (2017), 030012. <https://doi.org/10.1063/1.4984355>
- [117] A. Ambrosini et al., Influence of application parameters on stability of Pyromark® 2500 receiver coatings, *AIP Conference Proceedings*, 2126 (2019), 030002. <https://doi.org/10.1063/1.5117514>
- [118] L. Noc et al., High-temperature “ion baseball” for enhancing concentrated solar power efficiency, *Solar Energy Materials and Solar Cells*, 200 (2019), 109974. <https://doi.org/10.1016/j.solmat.2019.109974>
- [118] R. Harzallah et al., Development of high performances solar absorber coatings, *AIP Conference Proceedings*, 2126 (2019), 030026. <https://doi.org/10.1063/1.5117538>
- [120] L. Noc et al., High-solar-absorptance CSP coating characterization and reliability testing with isothermal and cyclic loads for service-life prediction, *Energy & Environmental Science*, 12 (2019), 1679-1694. <https://doi.org/10.1039/C8EE03536A>
- [121] J.F. Torres et al., Highly efficient and durable solar thermal energy harvesting via scalable hierarchical coatings inspired by stony corals, *Energy & Environmental Science*, 15 (2022), 1893-1906. <https://doi.org/10.1039/D1EE03028K>
- [122] L. Jian et al., Oxidation kinetics of Haynes 230 alloy in air at temperatures between 650 and 850 °C, *Journal of Power Source*, 159 (1) (2006), 641-645. <https://doi.org/10.1016/j.jpowsour.2005.09.065>
- [123] S. Caron et al., Forty shades of black: A benchmark of high temperature sprayable black coatings applied on Haynes 230, *AIP Conference Proceedings*, 2303 (2020), 150007. <https://doi.org/10.1063/5.0028773>
- [124] C.K. Ho, J. Pacheco, Levelized Cost of Coating (LCOC) for selective absorber materials, *Solar Energy*, 108 (2014), 315-321. <https://doi.org/10.1016/j.solener.2014.05.017>
- [125] A. Boubault et al., Levelized cost of energy (LCOE) metric to characterize solar absorber coatings for the CSP industry, *Renewable Energy*, 85 (2016), 472-483. <https://doi.org/10.1016/j.renene.2015.06.059>
- [126] K. Zhang et al., A review on thermal stability and high temperature induced ageing mechanisms of solar absorber coatings, *Renewable and Sustainable Energy Reviews*, 67 (2017), 1282-1299. <https://doi.org/10.1016/j.rser.2016.09.083>
- [127] A. Carling-Plaza. Accelerated aging and durability of selective materials for concentrating solar power plant receivers, PhD thesis, University of Perpignan, 2021, available at: <https://theses.hal.science/tel-03611325/>. Accessed: 15/12/2023.
- [128] A. Boubault et al., Aging of solar absorber materials under highly concentrated solar fluxes, *Solar Energy Materials and Solar Cells*, 123 (2014), 211-219. <https://doi.org/10.1016/j.solmat.2014.01.010>
- [129] A. Boubault et al., Durability of solar absorber coatings and their cost-effectiveness, *Solar Energy Materials and Solar Cells*, 166 (2017), 176-184. <https://doi.org/10.1016/j.solmat.2017.03.010>
- [130] R. Reoyo-Prats et al., Accelerated aging of absorber coatings for CSP receivers under real high solar flux – Evolution of their optical properties, *Solar Energy Materials and Solar Cells*, 193 (2019), 92-100. <https://doi.org/10.1016/j.solmat.2018.12.030>



- [131] J.F. Torres, I. Ellis, J. Coventry, Degradation mechanisms and non-linear thermal cycling effects in a high-temperature light-absorber coating, *Solar Energy Materials and Solar Cells*, 218 (2020),110719. <https://doi.org/10.1016/j.solmat.2020.110719>
- [132] S. Hosseini et al., Long-term thermal stability and failure mechanisms of Pyromark 2500 for high-temperature solar thermal receivers, *Solar Energy Materials and Solar Cells*, 246 (2022),111898. <https://doi.org/10.1016/j.solmat.2022.111898>
- [133] N. Martinez et al., Influence of different thermal degradation processes on the optical property of Pyromark-2500, *Solar Energy*, 253 (2023), 58-72. <https://doi.org/10.1016/j.solener.2023.02.004>
- [134] ASTM International, Standard Tables for Reference Solar Spectral Irradiances: Direct Normal and Hemispherical on 37° Tilted Surface, ASTM G173-03 (2020). <https://doi.org/10.1520/G0173-03R20>
- [135] NREL, SMARTS: Simple Model of the Atmospheric Radiative Transfer of Sunshine, available at: <https://www.nrel.gov/grid/solarresource/smarts.html>. Accessed: 15/12/2023.
- [136] C.A. Gueymard, The sun's total and spectral irradiance for solar energy applications and solar radiation models. *Solar Energy*, 76(4) (2004),423–453. <https://doi.org/10.1016/j.solener.2003.08.039>
- [137] C.A. Gueymard, Revised composite extraterrestrial spectrum based on recent solar irradiance observations, *Solar Energy*, 169 (2018), 434–440. <https://doi.org/10.1016/j.solener.2018.04.067>
- [138] F. Kasten, A.T. Young, Revised optical air mass tables and approximation formula, *Applied Optics*, (28) 22 (1989), 4735-4738. <https://doi.org/10.1364/AO.28.004735>
- [139] Labsphere, Reflectance Coatings and Materials, Technical Guide, (2023), available at: <https://www.labsphere.com/wp-content/uploads/2023/06/ReflectanceCoatingsMaterialsTechGuide.pdf>. Accessed: 15/12/2023.
- [140] A. Fernandez-Garcia et al., Equipment and methods for measuring reflectance of concentrating solar reflector materials, *Solar Energy Materials and Solar Cells*, 167 (2017), 28-52. <https://doi.org/10.1016/j.solmat.2017.03.036>
- [141] F. Sutter et al., Method to evaluate the reflectance, absorptance and emittance of particles for concentrating solar power technology, *SolarPACES Guideline* (2022), available at: [https://www.solarpaces.org/wp-content/uploads/Document-4\\_SolarPACES\\_Particle-Optical-Properties-Guideline\\_V1.0.pdf](https://www.solarpaces.org/wp-content/uploads/Document-4_SolarPACES_Particle-Optical-Properties-Guideline_V1.0.pdf). Accessed: 15/12/2023.
- [142] Surface Optics, 410-Vis-IR Portable Emisometer & Solar Reflectometer, available at: <https://surfaceoptics.com/products/reflectometers-emissometers/410-vis-ir/>, Accessed: 15/12/2023.
- [143] Surface Optics, ET10 In-Band Handheld Emisometer, available: <https://surfaceoptics.com/products/reflectometers-emissometers/et10-in-band-emissometer-hand-held/>. Accessed: 15/12/2023.
- [144] L. del Campo et al., New experimental device for infrared spectral directional emissivity measurements in a controlled environment, *Review of scientific instruments*, 77 (2006), 113111. <https://doi.org/10.1063/1.2393157>
- [145] P. Honnerova et al., New experimental device for high-temperature normal spectral emissivity measurements of coatings, *Measurement Science and Technology*, 25 (2014), 095501. DOI 10.1088/0957-0233/25/9/095501.
- [146] P. Giraud et al., Development of optical tools for the characterization of selective solar absorber at elevated temperature, *AIP Conference Proceedings*, 1734 (2016) 130008. <https://doi.org/10.1063/1.4949218>

- [147] M. Honner, P. Honnerova, Survey of emissivity measurement by radiometric methods, *Applied Optics*, 54(4) (2015), 559-683. <https://doi.org/10.1364/AO.54.000669>
- [148] P. Giraud, J. Braillon, O. Raccurt, Selective solar absorber emittance measurement at elevated temperature, *AIP Conference Proceedings*, 1850 (2017), 130004. <https://doi.org/10.1063/1.4984498>
- [149] I. Setién-Fernández et al., First spectral emissivity study of a solar selective coating in the 150–600 °C temperature range, *Solar Energy Materials and Solar Cells*, 117 (2013), 390-395. <https://doi.org/10.1016/j.solmat.2013.07.002>
- [150] T. Echaniz et al., Importance of the spectral emissivity measurements at working temperature to determine the efficiency of a solar selective coating, *Solar Energy Materials and Solar Cells*, 140 (2015), 249-252. <https://doi.org/10.1016/j.solmat.2015.04.009>
- [151] I. González de Arrieta et al., Infrared emissivity of copper-alloyed spinel black coatings for concentrated solar power systems, *Solar Energy Materials and Solar Cells*, 200 (2019), 109961. <https://doi.org/10.1016/j.solmat.2019.109961>
- [152] N. Azzali et al., Spectral emittance of ceramics for high temperature solar receivers, *Solar Energy*, 222 (2021), 74-83. <https://doi.org/10.1016/j.solener.2021.05.019>
- [153] J. Chen et al., High-temperature optical and radiative properties of alumina–silica-based ceramic materials for solar thermal applications, *Solar Energy Materials and Solar Cells*, 242 (2022), 111710. <https://doi.org/10.1016/j.solmat.2022.111710>
- [154] L. Yang, Y. Zhang, G. Huang, Measuring the spectral emissivity of single particle at high temperature, *Solar Energy*, 234 (2022), 222-230. <https://doi.org/10.1016/j.solener.2022.01.050>
- [155] E. Le Baron et al., Solar Energy Materials and Solar Cells, Round Robin Test for the comparison of spectral emittance measurement apparatuses, *Solar Energy Materials and Solar Cells*, 191 (2019), 476-485. <https://doi.org/10.1016/j.solmat.2018.11.026>
- [156] M. Balat-Pichelin et al., Emissivity at high temperature of Ni-based superalloys for the design of solar receivers for future tower power plants, *Solar Energy Materials and Solar Cells*, 227 (2021), 111066. <https://doi.org/10.1016/j.solmat.2021.111066>
- [157] M. Balat-Pichelin, A. Bousquet, Total hemispherical emissivity of sintered SiC up to 1850 K in high vacuum and in air at different pressures, *Journal of the European Ceramic Society*, 38 (10), (2018), 3447-3456. <https://doi.org/10.1016/j.jeurceramsoc.2018.03.050>
- [158] University of West Bohemia, New Technologies Research Centre, Spectral normal emissivity at high temperatures (SNEHT), available at: <https://irt.zcu.cz/en/research/photo-thermal-properties/sneht/>, Accessed: 15/12/2023.
- [159] D. Hernandez et al., Experimental validation of a pyroreflectometric method to determine the true temperature on opaque surface without hampering reflections, *Measurement*, 42(6), (2009), 836-843. <https://doi.org/10.1016/j.measurement.2009.01.012>
- [160] CI Systems, SR-5000N Spectroradiometer, available at: <https://www.ci-systems.com/SR-5000NSpectroradiometer>. Accessed: 15/12/2023.
- [161] A. Rogalski, K. Chrzanowski, Infrared devices and techniques (revision), *Metrology and Measurement Systems*, XXI (4) (2014), 565-618. DOI: 10.2478/mms-2014-0057
- [162] M. Völlmer, K.P. Möllmann, *Infrared Thermal imaging: Fundamentals, Research and Applications*, Second Edition, Wiley Edition (2018). DOI:10.1002/9783527630868
- [163] W. Minkina, S. Dudzik, *Infrared Thermography: Errors and Uncertainties*, Wiley Edition (2009). ISBN: 978-0-470-68224-1.

- [164] B.D. Maione, C. Baldrige, M. W. Kudenov, Microbolometer with a multi-aperture polymer thin-film array for neural-network-based target identification, *Applied Optics*, 58 (27) (2019), 7285-7297. <https://doi.org/10.1364/AO.58.007285>
- [165] D. Hernandez et al., Analysis and Experimental Results of Solar-Blind Temperature Measurements in Solar Furnaces, *Journal of Solar Energy Engineering*, 126(1) (2004), 645-653. <https://doi.org/10.1115/1.1636191>
- [166] J. Ballestrin et al., Testing a solar-blind pyrometer, *Metrologia*, 47 (2010), 646. doi:10.1088/0026-1394/47/6/003
- [167] A. Marzo et al., Solar blind pyrometry not relying on atmospheric absorption bands, *Solar Energy*, 107 (2014), 415-422. <https://doi.org/10.1016/j.solener.2014.04.031>
- [168] M. Pfänder, E. Lüpfer, P. Heller, Pyrometric Temperature Measurements on Solar Thermal High Temperature Receivers, *Journal of Solar Energy Engineering*, 128(3) (2006), 285-292. <https://doi.org/10.1115/1.2210499>
- [169] M. Pfänder, E. Lüpfer, P. Pistor, Infrared temperature measurements on solar trough absorber tubes, *Solar Energy*, 81(5) (2007), 629-635. <https://doi.org/10.1016/j.solener.2006.08.016>
- [170] Spectral Sciences Inc., MODTRAN®, available at: <http://modtran.spectral.com/>. Accessed: 15/12/2023.
- [171] A. Berk et al., MODTRAN6: a major upgrade of the MODTRAN radiative transfer code, *SPIE Proceedings: Algorithms and Technologies for Multispectral, Hyperspectral, and Ultraspectral Imagery XX*, 9088 (2014), 90880H. <https://doi.org/10.1117/12.2050433>.
- [172] Vaisala, Humidity conversions: Formulas and methods for calculating humidity parameters, available at: <https://www.vaisala.com/en/lp/make-your-job-easier-humidity-conversion-formulas>. Accessed: 15/12/2023
- [173] F. Sakuma, M. Kobayashi, "Interpolation equations of scales of radiation thermometers", *Proceedings of TEMPMEKO 1996*, pp. 305-310 (1996).
- [174] ASTM International, Standard Test Method for Calibration and Accuracy Verification of Wideband Infrared Thermometers, ASTM E2847-21 (2021). DOI: 10.1520/E2847-21
- [175] ASTM International, Standard Test Methods for Radiation Thermometers (Single Waveband Type), ASTM E1256-17, (2017). DOI: 10.1520/E1256-17.
- [176] Advanced Energy, Mikron M305 blackbody, available at: [Mikron M305 | Advanced Energy](https://www.advancedenergy.com/mikron-m305-blackbody). Accessed: 15/12/2023.
- [177] HGH Infrared, High temperature extended area blackbodies, available at: <https://hgh-infrared.com/ecn-100-series/>. Accessed: 15/12/2023.
- [178] University of West Bohemia, New Technologies Research Centre, Effective directional emissivity at high temperatures (EDEHT), available at: <https://irt.zcu.cz/en/research/photo-thermal-properties/edeht/>. Accessed: 15/12/2023.
- [179] W. Minkina, D. Klecha, Atmospheric transmission coefficient modelling in the infrared for thermovision measurements, *Journal of Sensors and Sensors Systems*, 5 (2016) 17-23. <https://doi.org/10.5194/jsss-5-17-2016>
- [180] A. Eitan et al., Accurate Flux Calculations Using Thermographic IR cameras in Concentrated Solar Power Fields, *Quantitative Infrared Thermography (QIRT) 2014 Conference Proceedings*, <http://qirt.org/archives/qirt2014doi/papers/QIRT-2014-220.pdf>
- [181] InfraTec GmbH, Industrial Automation; Thermographic Monitoring of Solar Power Tower - SPTC, available at: <https://www.infratec.eu/thermography/industrial-automation/solar-power-tower-check-sptc/>. Accessed: 15/12/2023.



## **Chapter 2. Investigation plan**



## 2 Investigation plan

### 2.1 Hypotheses

The purpose of this thesis is to investigate the following hypotheses:

- i) The opto-thermal performance of a solar thermal absorber coating designed to operate under concentrated solar radiation is sensitive to operating conditions, i.e. the concentration factor  $C_x$  and its surface temperature  $T$ .
- ii) Solar absorptance  $\alpha_{sol}$  and thermal emittance  $\varepsilon_{th}$  are two key figures of merit for solar thermal absorber coatings. Value derived from laboratory spectral measurements are sensitive to temperature.
- iii) The remote sensing of a solar thermal absorber coating surface temperature and band emittance is feasible in a Central Receiver System (CRS), using shortwave infrared thermography, both for on-sun and off-sun operating conditions.

### 2.2 Objectives

The main objective of this thesis is to develop a framework for the opto-thermal analysis of solar thermal absorber coatings used in Concentrated Solar Power. This analysis is mostly based on infrared measurement techniques, such as spectrophotometry and multispectral radiometry. The analysis is developed for relevant materials, first under laboratory conditions, both at ambient and operating temperature, up to 800 °C. A new measurement technique is developed for the in-situ opto-thermal characterisation of solar thermal absorber coatings in Central Receiver Systems.

The main objective is translated in the following objectives, developed in the next chapters:

- Analyse and compare relevant opto-thermal figures of merit for solar thermal absorber coatings. In particular, compare the impact of solar absorptance and thermal emittance on the opto-thermal performance of a material, as a function of operating conditions. **(Publication n°1)**.
- Compare solar absorptance and thermal emittance values obtained for a solar selective coating and a black coating, derived from room temperature measurements, using laboratory spectrophotometers and portable devices **(Publication n°2)**.
- Compare solar absorptance and thermal emittance values obtained for a metal oxide, a set of black coatings and silicon carbide. Thermal emittance values are compared between measurements performed from 25 °C to 800 °C, with laboratory spectrophotometers and custom experimental setups **(Publication n°3)**.
- Analyse the feasibility of two shortwave infrared ratio thermometers for the remote sensing of a solar thermal absorber coating surface temperature and band emittance, applicable for the in-situ coating opto-thermal characterization in a Central Receiver System. **(Publication n°4)**

## 2.3 Methodology

This thesis is based on a compendium of scientific publications, consisting of four contributions, three of them are published in international journals indexed in Journal Citation Reports (JCR) while one is being reviewed for publication. The characteristics of each contribution are outlined below.

### Publication n°1:

This publication is presented in Chapter 3. It analyses and compares a set of opto-thermal figures of merit derived from spectral measurements for comparing the respective performance of two solar thermal absorber coatings.

**Title:** A comparative analysis of opto-thermal figures of merit for high temperature solar thermal absorber coatings

**Authors:** S. Caron, J. Garrido, J. Ballestrín, F. Sutter, M. Röger, F. Manzano-Agugliaro

**Journal:** *Renewable and Sustainable Energy Reviews*

**Volume:** 154, 111818 (21 pages). **Year of publication:** 2022

**DOI:** <https://doi.org/10.1016/j.rser.2021.111818>

### **Highlights:**

- Opto-thermal figures of merit for solar thermal absorber coatings are analysed.
- Black and spectral selective reference coatings are chosen for the comparison.
- Selectivity ratio and solar reflectance index are normalized for high temperature.
- A trade-off factor between solar absorptance and thermal emittance is defined.

Quality indices for the year of publication, 2022:

**Journal Impact Factor (JIF):** 15.9

CATEGORY	JIF RANK	JIF QUARTILE
ENERGY & FUELS	8/119	Q1
GREEN & SUSTAINABLE SCIENCE & TECHNOLOGY	2/46	Q1

### Publication n°2:

This publication is presented in Chapter 4. It compares solar absorptance and thermal emittance values obtained for a solar selective coating and a black coating, derived from room temperature measurements, using laboratory spectrophotometers and portable devices.

**Title:** Laboratory intercomparison of solar absorptance and thermal emittance measurements at room temperature

**Authors:** S. Caron, L. Herding, Y. Binyamin, M. Baidossi, Y. Vinetsky, A. Morales, C. Hildebrandt, R. Reoyo-Prats, O. Faugeroux, A. Agüero, S. Rodriguez, F. Sutter, M. Röger, F. Manzano Agugliaro

**Journal:** *Solar Energy Materials and Solar Cells*,

**Volume:** 238, 111579 (15 pages). **Year of publication:** 2022.

**DOI:** <https://doi.org/10.1016/j.solmat.2022.111579>



**Highlights:**

- Spectral measurements of absorber coatings are compared at room temperature.
- Spectral mismatch from 1.5  $\mu\text{m}$  to 2.5  $\mu\text{m}$  is analyzed for spectrophotometers.
- Solar absorptance and thermal emittance calculations are homogenized.
- The uncertainty propagation on the coating opto-thermal efficiency is evaluated.

Quality indices for the year of publication, 2022:

**Journal Impact Factor (JIF):** 6.9

CATEGORY	JIF RANK	JIF QUARTILE
MATERIALS SCIENCE, MULTIDISCIPLINARY	80/344	Q1
PHYSICS, APPLIED	2/46	Q1

Publication n°3:

This publication is presented in Chapter 5. It compares solar absorptance and thermal emittance values obtained for a metal oxide, a set of black coatings and silicon carbide. Thermal emittance values are compared between measurements performed from 25 to 800 °C.

**Title:** Intercomparison of opto-thermal spectral measurements for concentrating solar thermal receiver materials from room temperature up to 800 °C

**Authors:** S. Caron, M. Farchado, G. San Vicente, A. Morales, J. Ballestrín, M. Joao Carvalho, S. Pascoa, E. Le Baron, A. Disdier, E. Guillot, C. Escape, J.-L. Sans, Y. Binyamin, M. Baidossi, F. Sutter, M. Röger, F. Manzano-Agugliaro

**Journal:** *Solar Energy Materials and Solar Cells*

**Volume:** 266, 112677 (17 pages). **Year of publication:** 2024.

**DOI:** <https://doi.org/10.1016/j.solmat.2023.112677>

**Highlights:**

- Spectral measurements of receiver materials for Concentrating Solar Power are performed from room temperature up to 800 °C.
- Material substrates include H230 and silicon carbide. Three different surface finishes are investigated for H230 (oxide, black coatings).
- Solar absorptance is analyzed at room temperature, while thermal emittance is analyzed from room temperature up to 800 °C.

Quality indices (2022):

**Journal Impact Factor (JIF):** 6.9

CATEGORY	JIF RANK	JIF QUARTILE
MATERIALS SCIENCE, MULTIDISCIPLINARY	80/344	Q1
PHYSICS, APPLIED	2/46	Q1

Publication n°4:

This draft manuscript is presented in Chapter 6. It analyses the feasibility of two shortwave infrared ratio thermometers for the remote sensing of a solar thermal absorber coating surface temperature and band emittance.

**Title:** Simulation of shortwave infrared ratio thermometers for the remote opto-thermal characterization of central external cylindrical receivers

**Authors:** S. Caron, R. Larue, A. Kämpgen, F. Sutter, M. Röger, F. Manzano-Agugliaro,

**Journal:** *Solar Energy* (Under review)

**Reference:** SEJ-D-23-03730

**Highlights:**

- A new measurement principle relying on passive shortwave infrared (SWIR) thermography is introduced for the remote opto-thermal characterization of central receivers.
- A MATLAB software tool has been developed and coupled to MODTRAN6 radiative transfer code for the spectral simulation of relevant radiometric chains in Concentrated Solar Power.
- Two shortwave infrared ratio thermometers have been analyzed with respect to atmospheric and operating conditions in the context of central receiver systems.
- The grey hypothesis can be assumed valid for black coatings or oxidized metals, but it is a priori not valid for the atmosphere.
- A model-based non-grey compensation factor (NGCF) is estimated for the atmosphere using available ground meteorological data and MODTRAN6 radiative transfer code.

Quality indices (2022):

**Journal Impact Factor (JIF):** 6.7

CATEGORY	JIF RANK	JIF QUARTILE
ENERGY AND FUELS	37/119	Q2

## **Chapter 3. A comparative analysis of opto-thermal figures of merit for high temperature solar thermal absorber coatings**



## 3 A comparative analysis of opto-thermal figures of merit for high temperature solar thermal absorber coatings

### 3.0 Abstract

Solar thermal absorber coatings play a key role in the thermal efficiency of receivers for applications in the field of Concentrated Solar Power. The development of stable spectral selective coatings with a high solar absorptance  $\alpha_{sol}$  and a low thermal emittance  $\varepsilon_{th}$  is often desired to reduce thermal losses. However, quantitative indicators describing selectivity and the trade-off between solar absorptance and thermal emittance is seldom discussed in the literature.

In this chapter, relevant opto-thermal figures of merit are analysed for the comparison of reference solar thermal absorber coatings, including real and ideal coatings, both black and spectral selective. The comparison is made for a temperature  $T$  ranging from 25 °C to 1000 °C and for a concentration factor  $C_x$  ranging from 20 to 1000, based on spectral data measured at room temperature from 0.25  $\mu\text{m}$  to 20  $\mu\text{m}$ .

New figures of merit are introduced, i.e. a normalised selectivity ratio  $Si^*$ ; a trade-off factor  $Z_{trade-off}$ ; a normalised solar reflectance index  $SRI^*$  and a peak efficiency temperature  $T_{peak,opt}$ . These metrics are derived from existing figures of merit and adapted for CSP.

The set of figures of merit analysed in this chapter offer a complementary perspective for the detailed characterization of any coating opto-thermal performance. For solar thermal absorber coatings, thermal efficiency  $\eta_{thermal}$  and peak efficiency temperature  $T_{peak,opt}$  are respectively deemed more insightful than opto-thermal efficiency  $\eta_{opt-th}$  and maximum steady-state temperature  $T_{SST,max}$ , when comparing the relative opto-thermal performance of two coating formulations.

### 3.1 Introduction

Concentrated solar radiation can be harnessed and converted into electrical power by different technologies. Direct conversion can be achieved by Concentrated Photovoltaics (CPV) [1,2] or Solar Thermoelectric Generators (STEG) [3-5]. Alternatively, conventional thermodynamic power cycles can be driven by the heat generated with Concentrated Solar Thermal (CST) systems, such as Parabolic Trough Collectors (PTC) [6-8] Linear Fresnel Collectors [9,10], Central Receiver Systems CRS [11-14] or dish concentrators [15,16]. Hybrid solar concentrators also exist, for example taking advantage of spectral beam-splitting devices, to focus solar radiation on multiple receiver types and thus increase further the conversion efficiency [17-19].

These concentrating systems consist of optical concentrators tracking the sun and focusing Direct Normal Irradiance (DNI) onto a receiver. Increasing the concentration factor  $C_x$  allows miniaturizing PV cells, at the cost of parasitic losses for device cooling [20,21]. For solar thermal processes, increasing the concentration factor allows reaching higher operating temperature levels, while miniaturizing the thermal receiver and consequently reducing heat losses, thus improving the thermodynamic efficiency. Today, CST power plants, in particular parabolic troughs (PTC) and solar towers (CRS), have achieved technical maturity for commercial systems [22]. The integration of molten salt thermal storage tanks allows a cost-efficient and dispatchable power generation [23].

Solar thermal receivers are one of the most critical components of CST power plants. Commercial PTC and CRS power plants, illustrated in Figure 3.1, use tubular receiver designs. A Parabolic Trough Receiver (PTR) consists of an absorber tube inserted into an evacuated glass envelope [24,25]. External tubular receivers mounted in CRS consist of several panels of parallel absorber tubes [26,27]. In both receiver configurations, the absorber tube is made of a metal substrate, for instance a stainless steel or a nickel-based alloy, on which a Solar Thermal Absorber Coating (STAC) is applied.

Different STAC formulations are applied in state-of-the-art commercial PTC and CRS power plants: Spectral Selective Coatings (SSC) are typical for PTRs [28,29] while non-selective, High Solar Absorptance (HSA) coatings are preferred for CRS [30-32]. A SSC is characterised by a high solar absorptance  $\alpha_{sol}$  and a low thermal emittance  $\varepsilon_{th}$ , while a HSA black coating only exhibits a high  $\alpha_{sol}$  value (>95%). Several considerations drive the selection of a coating, beside its opto-thermal performance: i) the heat transfer fluid (HTF) operating temperature range [33,34], ii) the coating durability in operating conditions [35-37] and iii) the Levelised Cost of Coating (LCOC) [38,39]. These design considerations are outlined in Table 3.1 and briefly discussed further.

For PTC systems, Diphenyl Oxide / Biphenyl based thermal oils are the current state-of-the-art HTF, [40,41], operating from 290 °C at the inlet up to 390 °C at the outlet of a PTC loop, while new silicone oils currently operate up to 430 °C [42,43]. Next generation power plants consider molten nitrate salts as a HTF, shifting the maximum operating temperature toward 600 °C [44,45]. In the case of CRS, molten salts are currently a state of the art HTF. Next generation CRS power plants consider new HTF formulations [46], for instance new ternary molten salt mixtures [47,48], liquid sodium [34,49,50] or solid particles [51-55] as a HTF to achieve a higher outlet temperature, toward 1000 °C. STAC formulations for PTC applications are thus typically designed for a maximum operating temperature of 600 °C in vacuum, while these formulations are designed to withstand an operating temperature above 600 °C in air for CRS applications.

The receiver assembly and its durability are further parameters to consider when selecting a STAC formulation. PTR absorber tubes are typically sealed in vacuum [56]. The vacuum is designed to remain stable in the field over the receiver lifetime [57]. This vacuum improves the receiver thermal efficiency by canceling convection losses, but it also protects the STAC from high temperature oxidation. The glass envelope protects the STAC from environmental stresses, such as sandstorms. In case of a vacuum loss, the STAC performance may remain stable in air up to the maximum operating temperature [58]. For CRS, the receiver is mounted on top of a tower at a height typically above 100 m in desert environments. STAC are exposed in air to higher operating temperatures, oxidation and corrosion, as well as further environmental stresses. In case of degradation, defect absorber coatings in PTRs cannot be replaced, but single receivers can be replaced in the worst case [59]. For CRS, a periodical recoating could be performed on site [36-39,60], while current research tries to identify more efficient and durable STAC formulations [61-63].

For each CSP technology, a different coating process is applied. For PTR systems, industrial grade SSC formulations are typically applied using Physical Vapor Deposition (PVD) or sol-gel dip-coating techniques [29,35,64,65], which are cost-efficient in large series production. One typical SSC architecture is a multilayered thin film coating (< 1  $\mu\text{m}$ ) applied on a polished metal

substrate, consisting of an infrared (IR) layer, a composite absorbing ceramic-metallic (CERMET) layer and a top antireflection (AR) layer, with intermediate diffusion barrier layers to improve further thermal stability [66-68]. For CRS, industrial grade black coatings are typically applied by spraying techniques in the workshop or on site for tubular absorber panels. These coatings are typically silicon-based ceramic paint formulations including black spinel pigments [31,32,37,61-63]. Such coatings may require a thermal treatment (curing) in custom muffle furnaces or directly on site. These coatings have a thickness of  $\sim 30\text{-}50\ \mu\text{m}$  and can be applied as a single layer or combined with a primer coating.

Finally, an accurate online monitoring of the absorber temperature is also a critical part of plant operation, which may also be affected by the STAC choice. In PTR, the HTF inlet and outlet temperatures are measured and controlled in real time with built-in temperature sensors. The absorber surface temperature  $T_{abs}$  does not have to be monitored in real time, as the concentration factor  $C_x$  remains nearly constant. The glass envelope temperature can be monitored periodically with ground based or airborne LWIR (8-14  $\mu\text{m}$ ) cameras to detect partial vacuum loss [52,69-72].

In CRS, the HTF loop temperature is also monitored in real time with a similar instrumentation. Online temperature monitoring is particularly critical for molten salts, to avoid HTF freezing below  $300\ \text{°C}$  and pronounced corrosion around  $600\ \text{°C}$  [44,45]. To comply with these constraints, a dynamic heliostat field aiming strategy allows defining a variable concentration factor and an "Allowable Flux Density" (AFD) on the receiver surface [73-76]. In order to avoid local overheating, the absorber surface temperature  $T_{abs}$  has to be monitored in real time with ground mounted LWIR cameras (8-14  $\mu\text{m}$ ) to optimise the heliostat field aiming strategy [77,78]. These cameras are nearly "solar blind" in this spectral range if the absorber coating is similar to a blackbody [79].

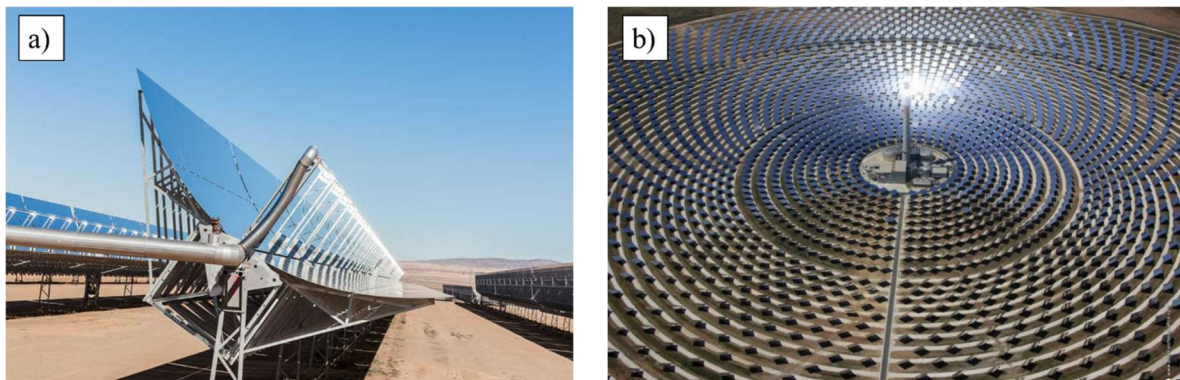


*Figure 3.1: Illustration of PTC and CRS technologies. a) Parabolic Trough Concentrator (Andasol 3, Spain) [80]. b) Central Receiver System (Gemasolar, Spain) [81].*

Table 3.1: Summary of boundary conditions for PTC and CRS applications relevant for STAC selection.

Parameter	Parabolic Trough Collector (PTC)	Central Receiver System (CRS)
Concentration factor $C_x$	Constant, $\sim x20...x100$ [6-8]	Variable, $x100... x1000$ [11-14]
Solar field aperture area ( $m^2$ )	500,000 $m^2$ for 50 $MW_e$ [82]	300,000 $m^2$ for 20 $MW_e$ [81]
HTF operating temperature range ( $^{\circ}C$ )	<i>Thermal oils:</i> 290 $^{\circ}C$ to 425 $^{\circ}C$ [33,40-43] <i>Molten nitrate salts:</i> 270 $^{\circ}C$ to 600 $^{\circ}C$ [33,44-45]	<i>Molten nitrate salts:</i> 270 $^{\circ}C$ to 600 $^{\circ}C$ [33,44-45] <i>Liquid sodium:</i> 100 $^{\circ}C$ to 800 $^{\circ}C$ [33,34,49,50]
Receiver and absorber geometrical dimensions	<i>Parabolic trough receiver:</i> "Standard" dimensions [24-25] Receiver height above ground: < 5m Absorber tube diameter: 70 mm Receiver length: 4 m	<i>External tubular receiver:</i> Custom dimensions [26,27,72-76] Tower height: $\sim 100...250$ m Receiver height: $\sim 10...20$ m Receiver diameter: $\sim 10 \dots 20$ m
Industrial production scale	<i>Standardised design, large series</i> > 20,000 PTR units for a 50 $MW_e$ PTC solar thermal power plant [82]	<i>Custom design, small series</i> $\sim 20$ receiver panels per tower $\sim x 50$ tubes per receiver panel [26,27,72-76]
STAC formulation and application process	Thin film multilayered SSC (CERMET) PVD or sol-gel dip coating [28,29,64-68]	Silicon based black paint Thermal spraying technique [30-32,37,61-63]
Atmospheric conditions and STAC maintenance/durability	Vacuum sealed, maintenance free Stable in vacuum, oxidation in air [35,56-59]	Atmospheric pressure (air) re-coating allowed on site [36-39,60]
STAC service lifetime	$\geq 25$ years [35,56-59]	5-10 years [36-39,60]

Today, there are two main research paths in the field of coating development for CRS applications, i.e. the development of stable high temperature SSC and HSA coatings. Two standard opto-thermal figures of Merit (FoM) are the solar absorptance  $\alpha_{sol}$  and thermal emittance  $\epsilon_{th}$  [83-92]. The selection of a research path is driven by a ranking and trade-off between these reference FoMs: Is it rather worth selecting a high temperature "space" black coating to maximise the  $\alpha_{sol}$  value towards 100%, or selecting a high temperature SSC instead, with a high  $\alpha_{sol}$  and a low  $\epsilon_{th}$  values?

In addition to these reference FoMs, further FoMs have been previously reported in the literature to compare the performance of different STAC formulations:

- Selectivity ratio  $\alpha_{sol} / \epsilon_{th}$  [92,93]
- Spectral parameters, i.e. shape factor  $f_{shape}$ , cut-off wavelength  $\lambda_{cut-off}$  [94,95]
- The useful heat gained by the STAC  $\dot{q}_{use}''$  [96,97]
- The coating opto-thermal efficiency  $\eta_{opt-th}$  [11-13,30,38-39]
- The trade-off factor between  $\alpha_{sol}$  and  $\epsilon_{th}$  [30,98]
- The stagnation temperature  $T_{SST,max}$  [92,99]
- The receiver thermal efficiency  $\eta_{thermal}$  [11,12,96,97]
- The Solar Reflectance Index  $SRI$  [87-89,100,101]

The aim of this chapter is to provide a comparative analysis of FoMs outlined above, relevant for characterizing the performance of high temperature STACs. These FoMs are calculated on



the basis of spectral data measured at room temperature for reference coatings. The respective influence of solar concentration  $C_x$  and absorber surface temperature  $T_{abs}$  are highlighted where relevant. FoM equations are introduced and renormalised, if necessary. Section 3.2 presents a framework describing the system definition, reference coatings. FoM equations are defined and reviewed in Section 3.3. FoM values are calculated for reference coatings and analysed in Section 3.4.

## 3.2 Materials and methods

### 3.2.1 System definition

A heat flux diagram is sketched in Figure 3.2 for CST systems and for a high temperature STAC applied on a metal substrate. The Direct Normal Irradiance (DNI) is specularly reflected by tracking mirrors and transmitted through the atmosphere toward the receiver surface. The DNI is concentrated by an optical concentration factor  $C_x$ . The STAC absorbs a fraction  $\alpha_{sol}$  of the concentrated solar flux  $\dot{q}''_{sol}$ , which heats up the STAC to a surface temperature  $T_{abs}$ . The complementary fraction  $(1 - \alpha_{sol})$  is reflected to the ambient. The STAC loses heat by radiation ( $\dot{q}''_{rad,sky}$ ) toward the sky and by convection ( $\dot{q}''_{conv,amb}$ ) to the ambient.

The net heat flux balance is written in (Eq.3.1), defining the useful heat flux  $\dot{q}''_{use}$ . This heat flux is transferred by conduction ( $\dot{q}''_{cond}$ ) through the coating and metal substrate, inducing a first temperature drop at the interface between coating and metal ( $\Delta T_{coating}$ ) and another one at the interface between metal and fluid ( $\Delta T_{metal}$ ) (Eq.3.2). According to Fourier's law, both temperature drops are proportional to the respective thermal conductivities ( $k_{coating}$ ,  $k_{metal}$ ) and thicknesses. The useful heat flux is then transferred by convection to the HTF (Eq.3.3).

$$\dot{q}''_{use} = \alpha_{sol} \dot{q}''_{sol} - \dot{q}''_{rad,sky} - \dot{q}''_{conv,amb} \quad (3.1)$$

$$\Delta T = \Delta T_{coating} + \Delta T_{metal} \quad (3.2)$$

$$\dot{q}''_{use} = \dot{q}''_{cond} = \dot{q}''_{conv,HTF} \quad (3.3)$$

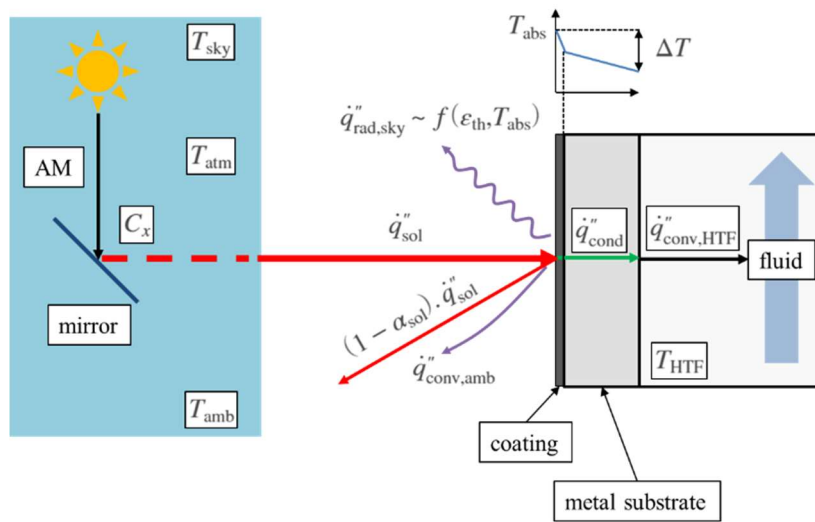


Figure 3.2: Heat flux diagram for a high temperature STAC.

### 3.2.2 Modelling assumptions

In order to compare the performance of different STACs for a wide range of applications, further calculations are performed using the following set of assumptions for simplification:

- a) The atmosphere is not attenuating the radiation transfer between mirrors and the receiver ( $\tau_{atm} \sim 100\%$ ).
- b) The mirror is perfectly specular and it exhibits an ideal spectral reflectivity, i.e. it reflects 100% of solar DNI from 0.28  $\mu\text{m}$  to 2.5  $\mu\text{m}$ . Beyond this wavelength, the reflectivity is negligible.
- c) The incidence angle  $\theta$  of DNI onto the mirror surface is nearly normal ( $\theta \sim 10^\circ$ )
- d) The incidence angle  $\theta$  of concentrated irradiance onto the receiver surface is nearly normal.
- e) The concentrated solar flux  $\dot{q}''_{sol}$  is homogeneous on the receiver surface.
- f) The ambient and sky temperature are equal ( $T_{amb} = T_{sky}$ ) and set to 25 °C.
- g) The convection heat loss from the STAC to the ambient is neglected ( $\dot{q}''_{conv,amb}$ ).
- h) The receiver is not covered by any glass envelope.
- i) The receiver geometry is flat.
- j) The view factor  $F_{view}$  to the surroundings is equal to 1.
- k) The STAC is Lambertian, i.e. it is a diffusely reflecting surface.
- l) The STAC is opaque, i.e. its transmittance is null.
- m) The STAC is isothermal and adiabatically insulated.

This set of assumptions is obviously ideal, in order to focus on a STAC opto-thermal performance instead of other secondary variables. The validity of these assumptions is briefly discussed in Table 3.2 for PTC and CRS applications, including relevant references. The heat transfer from the STAC to the HTF is not modelled in this chapter.

Table 3.2: Validity and limitations of modelling assumptions for PTC and CRS applications.

	<b>Modelling assumption</b>	<b>Parabolic Trough Collector (PTC)</b>	<b>Central Receiver System (CRS)</b>
a)	Atmospheric attenuation between mirrors and receiver	Short range (< 10 m) Assumption valid	Medium range (100 m ... 1 km); Assumption not valid [102-104]
b)	Ideal mirror specular solar reflectance [0.28- 2.5] $\mu\text{m}$	Ideal assumption for clean second surface glass silvered mirrors (solar weighted hemispherical reflectance > 95 %) [105-107]	
c)	Near normal incidence angle of DNI onto mirrors	Variable incidence on one axis tracking parabolic mirrors [7,95, 108]	Variable incidence angle on two axis tracking heliostats [13,14,108]
d)	Near normal incidence of irradiance onto receiver	Variable incidence on tubular receiver [7,95]	Variable incidence on receiver surface due to aiming strategy [109]
e)	Homogeneous concentrated solar flux $\dot{q}''_{sol}$	Assumption approximately valid, circumferential variations [7,95]	Assumption not valid, variable flux due to heliostat field layout dynamic aiming strategy [72-76]
f)	Isothermal ambient and sky temperatures ( $T_{amb} = T_{sky}$ )	Assumption only valid under laboratory room; PTR facing mirror and sky [24,25,56,71]	Assumption only valid under laboratory conditions; Receiver vertically mounted [26,27]
g)	Negligible convection from STAC to ambient	Assumption valid for an evacuated receiver tube [7,24,25,56,57, 69-71]	Assumption not valid, convection losses cannot be neglected at tower height [26,110]
h)	Receiver without glass cover	Assumption not valid, concentric glass envelope [24,25]	Valid assumption [26,27]
i)	Flat receiver geometry	Assumption not valid (Diameter: $\geq 70$ mm) [24,25]	Assumption not valid Variable tube diameter [72-76]
j)	View factor $F_{view} = 1$	Assumption not valid, concentric glass envelope [24,25]	Assumption not valid, neighboring absorber tubes [109]
k)	The STAC is Lambertian	Assumption not valid, SSC is specular [111]	Assumption nearly valid for a diffuse black paint [111,112]
l)	The STAC is opaque	Assumption not valid for a thin film STAC with multiple layers [28,29,66-68]	Assumption valid for a micrometric black coating [30-32,37,61-63,98]
m)	The STAC is isothermal	Assumption valid for a receiver section, thin film SSC with high thermal conductivity [113]	Assumption valid for a receiver section. Thermal gradient across the black coating (few $\mu\text{m}$ thick, with low thermal conductivity) [31]

### 3.2.3 Reference coatings

For the comparative analysis, four reference STAC are defined: i) a reference SSC, ii) an ideal SSC with a sharp cut-off wavelength at 2.5  $\mu\text{m}$ , iii) a reference black coating, iv) an ideal black-body coating. Their spectral directional hemispherical reflectivity (SDHR)  $\rho_{SDHR}$  are plotted in Figure 3.3. The SDHR has been measured [86] at OMT Solutions BV optical laboratory in the Netherlands [114], at room temperature, with two complementary spectrophotometers, for a near normal incidence angle  $\theta$  of 10°. The SDHR is measured from 0.25  $\mu\text{m}$  to 2.5  $\mu\text{m}$  with an ultraviolet-visible-near infrared (UV-VIS-NIR) spectrophotometer, using a NIST traceable white

diffuse sintered PTFE standard (e.g. Spectralon, [115]). The SDHR is then measured from 1.6  $\mu\text{m}$  to 20  $\mu\text{m}$  with a Fourier Transform Infrared (FTIR) spectrophotometer, using a NIST traceable specular gold standard (e.g., Infragold, [115]). A consistent spectral overlap is observed in the range from 1.6  $\mu\text{m}$  to 2.5  $\mu\text{m}$ , with an average residual mismatch smaller than 2 percentage points (p.p.).

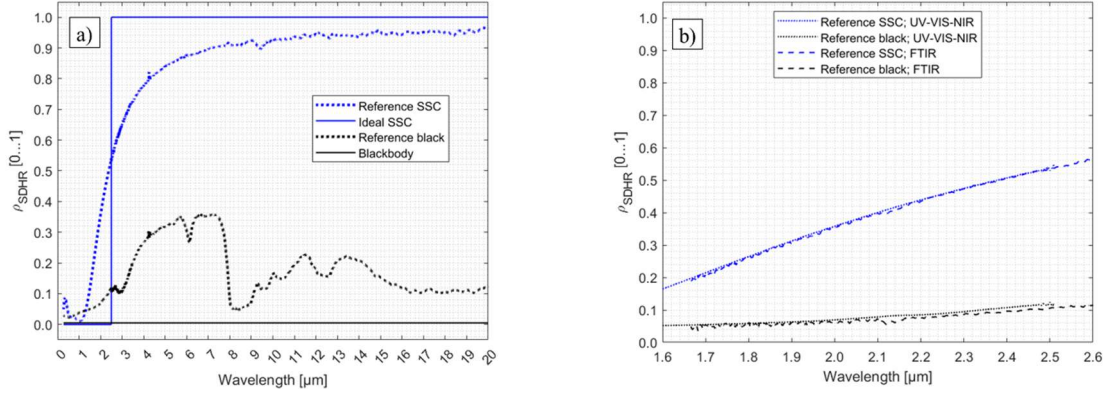


Figure 3.3: Spectral directional hemispherical reflectivity (SDHR) data for reference STAC. a) SDHR for reference STAC plotted from 0.28  $\mu\text{m}$  to 20  $\mu\text{m}$ . b) Spectral overlap from 1.6  $\mu\text{m}$  to 2.5  $\mu\text{m}$  between UV-VIS-NIR and FTIR spectrophotometers.

Reference SSC and HSA flat samples are shown in Figure 3.4 along with bare and coated tubular samples. Similar samples have been tested within the European research project Raiselife [116,117] for temperature levels above 600  $^{\circ}\text{C}$ .

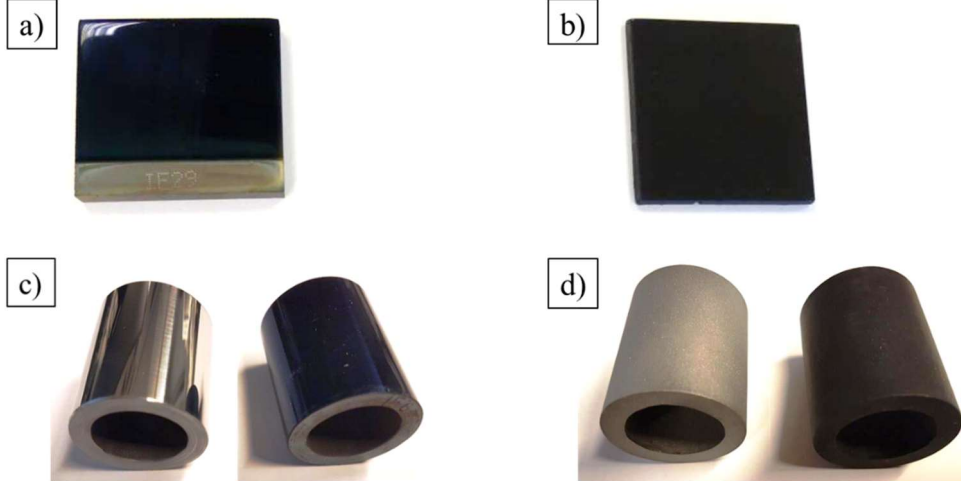


Figure 3.4: Pictures of absorber coatings applied on T91 flat and tubular metal substrates. a) Flat reference sample coated with the ref. SSC b) Flat reference sample coated with the ref. HSA black coating. c) Tubular samples, bare polished substrate and coated with the ref. SSC. d) Tubular samples, bare sand blasted substrate and coated with the ref. HSA black coating.

References spectra for ideal selective and black coatings were both modeled by a Heavyside unit step function (Eq.3.4), with respective cut-off wavelengths  $\lambda_{\text{cut-off}}$  of 2.5  $\mu\text{m}$  and 0  $\mu\text{m}$ . Both reference coatings are designed to maximise  $\alpha_{\text{sol}}$ , regardless of the operating point  $\{C_x, T_{\text{abs}}\}$ . The reference SSC is not necessarily optimal in terms of efficiency [94,95].

$$\rho_{SDHR,ideal}(\lambda) = \begin{cases} 0; & \lambda \leq \lambda_{\text{cut-off}} \\ 1; & \lambda > \lambda_{\text{cut-off}} \end{cases} \quad (3.4)$$

A few assumptions are made regarding coating spectral properties in subsequent calculations. First, it is assumed that these reference coatings are thermally stable for any temperature, i.e.  $\rho_{SDHR}$  remains constant before and after isothermal exposure and does not age. Furthermore, it is assumed that  $\rho_{SDHR}$  is not temperature dependent (Eq.3.5), i.e. SDHR does not shift when the sample is heated up. Previous research has shown that this assumption is not necessarily valid, requiring more sophisticated instrumentation to measure SDHR at operating temperature [90,91,119-123].

$$\frac{d\rho_{SDHR}(\lambda, \theta, T_{abs})}{dT_{abs}} \sim 0 \tag{3.5}$$

### 3.2.4 Inventory of FoMs

A list of relevant opto-thermal FoMs for the characterization of STAC performance has been outlined in Section 3.1. A synoptical diagram is shown in Figure 3.5 to illustrate interactions between FoMs. Their equations are developed in the next subsections.

The synoptical diagram shown in Figure 3.5 is split into four levels, sorting FoMs by increasing level of complexity. Spectra are listed on the top level as inputs for the calculation process. Spectral data include coating SDHR (Fig.3), Solar Spectral Irradiance (Fig. 5), Blackbody Spectral Irradiance (Fig.6). Information about the operating conditions  $\{C_x; T_{abs}\}$  are also relevant.

The first level includes elementary FoMs, i.e. the SSC model, the solar absorptance as a function of air mass  $AM$ ,  $\alpha_{sol}(AM)$  and the thermal emittance as a function of absorber temperature,  $\epsilon_{th}(T_{abs})$ . The second level includes compound FoMs, i.e. Selectivity ratios ( $S_i, S_i^*$ ), the useful heat flux  $\dot{q}_{use}''$ , the opto-thermal efficiency  $\eta_{opt-th}$  and the trade-off factor  $Z_{trade-off}$ . Third level FoMs are built from Level 2 FoMs, introducing reference "cold" and "hot" temperatures. These FoMs are the maximum steady-state temperature  $T_{SST,max}$ , solar reflectance indices ( $SRI, SRI^*$ ), the receiver thermal efficiency  $\eta_{thermal}$  and the peak efficiency temperature  $T_{peak,opt}$ .

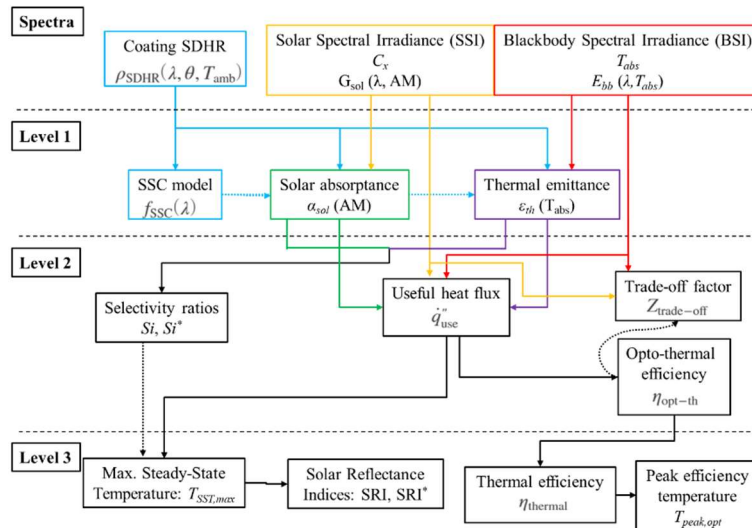


Figure 3.5: Synoptical diagram of STAC opto-thermal FoMs

Relevant FoMs for the comparative analysis of STAC performance are listed in Table 3.3 with their respective symbols, units, input variables, targets for STAC and ranges.

Table 3.3: Inventory of selected STAC opto-thermal FoMs.

Level	Label	FoM	Units	Variables	Target	Range
1	Solar absorptance	$\alpha_{sol}$	[%]	$\rho_{SDHR}, AM$	Max	0-100%
	Thermal emittance	$\epsilon_{th,calc}$	[%]	$\rho_{SDHR}, T_{abs}$	Min	0 -100 %
	SSC model	$f_{SSC}(\lambda)$	[-]	$f_{shape}, \lambda_{cut-off}, asymptotes$	Curve fit	0...1
2	Selectivity ratio	$S_i$	[-]	$\alpha_{sol}, \epsilon_{th,calc}, AM, T_{abs}$	Max	> 0
	Normalised selectivity ratio	$S_i^*$	[-]	$\alpha_{sol}, \epsilon_{th,calc}, AM, T_{abs}$	Max	Infinite
	Useful heat flux	$\dot{q}_{use}''$	[W/m <sup>2</sup> ]	$\alpha_{sol}, \epsilon_{th,calc}, C_x, AM, h_{conv}, T_{abs}, T_{sky}, T_{amb}$	Max	> 0
	Opto-thermal efficiency	$\eta_{opt-th}$	[%]	$\alpha_{sol}, \epsilon_{th,calc}, C_x, AM, h_{conv}, T_{abs}, T_{sky}, T_{amb}$	Max	0 -100%
	Trade-off factor	$Z_{trade-off}$	[-]	$\alpha_{sol}, \epsilon_{th,calc}, C_x, AM, h_{conv}, T_{abs}, T_{sky}, T_{amb}$	[-]	Infinite
3	Maximum Steady-State Temperature	$T_{SST,max}$	[K]	$\dot{q}_{use}'' = 0$	Max	> 0
	Solar Reflective Index	$SRI$	[-]	$T_{SST,max}, T_{SST,white}, T_{SST,black}$	Min	-
	Normalised SRI	$SRI^*$	[%]	$T_{SST,max}, T_{ref,min}, T_{ref,max}$	Min	0 -100%
	Thermal efficiency	$\eta_{thermal}$	[%]	$\eta_{coating,opt-th}, \eta_{carnot}$	Max	0 -100%
	Peak efficiency temperature	$T_{peak,opt}$	[K]	$\eta_{thermal}$	Max	> 0

### 3.3 Figures of Merits (FoMs)

#### 3.3.1 FoMs : Level 1

##### 3.3.1.1 Solar absorptance

The solar absorptance  $\alpha_{sol}$  is a standard FoM for STAC [83,86,87]. The formula is expressed below in (Eq.3.6):

$$\alpha_{sol}(AM) = \frac{\int_{\lambda_1}^{\lambda_2} [1 - \rho_{SDHR}(\lambda, \theta, T_{amb})] G_{sol}(\lambda, AM) d\lambda}{\int_{\lambda_1}^{\lambda_2} G_{sol}(\lambda, AM) d\lambda} \quad (3.6)$$

Where  $G_{sol}(\lambda, AM)$  is the solar spectral irradiance for a given  $AM$ ,  $\rho_{SDHR}(\lambda, \theta, T_{amb})$  is the SDHR measured at near normal incidence ( $\theta \sim 10^\circ$ ) and at ambient temperature ( $T_{amb} \sim 25^\circ\text{C}$ ) [83, 86].

The SDHR is weighted by a reference solar spectral irradiance (1 Sun, i.e.  $C_x = 1$ ) on the wavelength range  $[\lambda_1; \lambda_2]$ . In practice, calculations for CSP relevant materials are carried out with the ASTM G173-03 spectrum and reported for  $AM1.5d$ , considering direct+circumsolar irradiance [124]. The wavelength interval considered for integration usually spans from  $\lambda_1 = 0.28 \mu\text{m}$  to  $\lambda_2 = 2.5 \mu\text{m}$ . The influence of the mirror spectral specular reflectivity [105] is not considered here. In this chapter, the spectral resolution is set to  $10^{-3} \mu\text{m}$  (1 nm).

The ASTM G173-03 is computed with SMARTS v2.9.2 [125] for the U.S. 1976 Standard Atmosphere from 0.28  $\mu\text{m}$  to 4  $\mu\text{m}$  [126-128], using the *AM0* extraterrestrial spectrum derived in [129], recently updated in [130]. The reference solar spectral irradiance data for calculation is plotted in Figure 3.6.a. In this chapter, the *AM* variable is allowed to vary between *AM0* to *AM5* to assess its influence on the solar absorptance calculation. For *AM1.5d* conditions, the solar spectral irradiance  $G_{sol}(\lambda)$  integrated from 0.28  $\mu\text{m}$  to 4  $\mu\text{m}$  equals  $900 \text{ W}\cdot\text{m}^{-2}$ .

The cumulative fraction of solar spectral irradiance  $SSI_{cum,rel}$  is expressed in (Eq.3.7) and plotted in Figure 3.6.b after normalization with respect to *AM1* ( $1 \text{ kW}/\text{m}^2$ ). This indicator allows a better visualization of the spectral weight distribution. It also corresponds to the solar absorptance of an ideal blackbody ( $\rho_{SDHR} = 0$ ). The *AM0* curve is smooth, as the atmosphere does not hamper extraterrestrial solar irradiance. This spectrum can be reasonably approximated by a blackbody at a temperature of 5777 K [96]. As the *AM* value increases, the weight distribution shifts slightly toward higher wavelengths, as the solar spectrum peak shifts toward the near IR range. A few atmospheric absorption bands (0.9, 1.2, 1.4, 1.9  $\mu\text{m}$ ) do not contribute to the spectral weight distribution, as solar spectral irradiance is spectrally filtered by the atmosphere. An asymptotical value of 99% is reached at 2.5  $\mu\text{m}$ , if  $\lambda_2=4 \mu\text{m}$ .

$$SSI_{cum,rel} = \frac{\int_{\lambda_1}^{\lambda_2} G_{sol}(\lambda, AM) d\lambda}{\int_{\lambda_1}^{\lambda_2} G_{sol}(\lambda, AM) d\lambda} \quad (3.7)$$

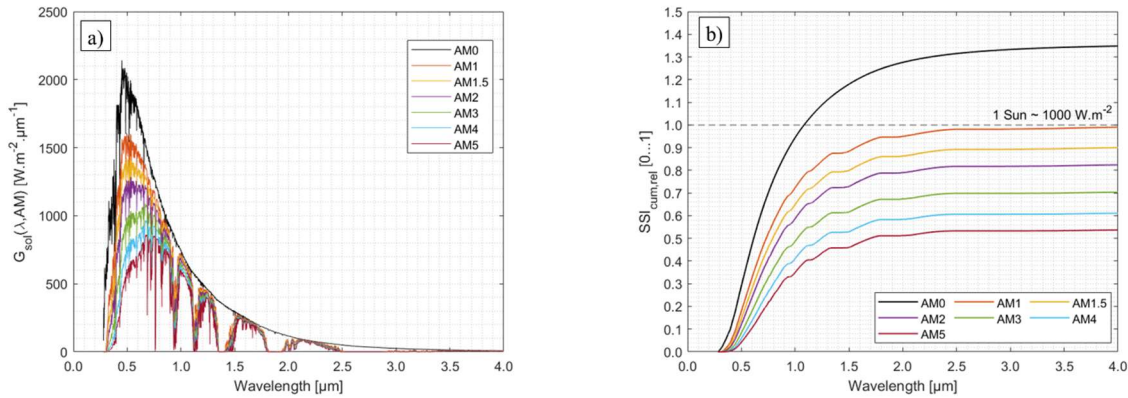


Figure 3.6: Reference data for Solar Spectral Irradiance. a) SSI plotted for different AM values. b) Cumulative SSI fraction normalised by  $1000 \text{ W}/\text{m}^2$  for different AM values.

### 3.3.1.2 Thermal emittance

Thermal emittance  $\varepsilon_{th,calc}$  is another standard FoM for STAC [83,88-92]. The formula is expressed in (Eq.3.8), where  $E_{bb}(\lambda, T_{abs})$  is the blackbody spectral irradiance (Eq.3.9). The SDHR measured at room temperature is weighted by a reference blackbody spectral irradiance at an absorber temperature  $T_{abs}$  on the wavelength range  $[\lambda_1, \lambda_3]$ .

$$\varepsilon_{th,calc}(T_{abs}) = \frac{\int_{\lambda_1}^{\lambda_3} [1 - \rho_{SDHR}(\lambda, \theta, T_{amb})] E_{bb}(\lambda, T_{abs}) d\lambda}{\int_{\lambda_1}^{\lambda_3} E_{bb}(\lambda, T_{abs}) d\lambda} \quad (3.8)$$

$$E_{bb}(\lambda, T_{abs}) = \frac{2\pi hc^2}{\lambda^5 \left[ \exp\left(\frac{hc}{\lambda k T_{abs}}\right) - 1 \right]} \quad (3.9)$$

The wavelength interval  $[\lambda_1; \lambda_3]$  considered for integration is not consistent in the literature. Ideally, the interval range should be as wide as possible to cover the highest fraction of Stefan Boltzmann’s law. In this chapter, we set  $\lambda_1 = 0.28 \mu\text{m}$  and  $\lambda_3 = 20 \mu\text{m}$ . In practice, the interval range is often limited to the FT-IR spectrophotometer working range, typically from  $2 \mu\text{m}$  to  $16 \mu\text{m}$ . The start wavelength  $\lambda_1$  should however match to the UV-VIS-NIR spectrophotometer, as a fraction of thermal radiation may be emitted at short wavelength (Figure 3.7.a). The SDHR measurement data should thus be concatenated, checking for the spectral mismatch in the overlap range (Figure 3.3.b). Another common reporting shortcoming consists in communicating a  $\epsilon_{th}$  value only for one absorber temperature  $T_{abs}$ . The calculation should be preferably reported over a temperature range.

The blackbody spectral irradiance  $E_{bb}(\lambda, T_{abs})$  is plotted in Figure 3.7.a on a semi-logarithmic plot and the cumulative fraction of blackbody spectral irradiance  $BSI_{cum,rel}$  (Eq.3.10) is shown in Figure 3.7.b as a fraction of Stefan Boltzmann law ( $\sigma T^4$ ). As  $T_{abs}$  increases, blackbody spectral irradiance peak shifts towards shorter wavelengths, accordingly to Wien’s displacement law. The cumulative fraction  $BSI_{cum,rel}$  below  $2.5 \mu\text{m}$  thus increases for higher temperature, starting from  $200 \text{ }^\circ\text{C}$  (Figure 3.6.b). The cumulative fraction  $BSI_{cum,rel}$  up to  $20 \mu\text{m}$  approaches Stefan’s Boltzmann law as temperature increases. At  $25 \text{ }^\circ\text{C}$ , this fraction only reaches 73.5%, while it reaches 97.9% at  $600 \text{ }^\circ\text{C}$ .

$$BSI_{cum,rel} = \frac{\int_{\lambda_1}^{\lambda \leq \lambda_3} E_{bb}(\lambda, T_{abs}) d\lambda}{\int_{\lambda_1}^{\lambda_3} E_{bb}(\lambda, T_{abs}) d\lambda} \quad (3.10)$$

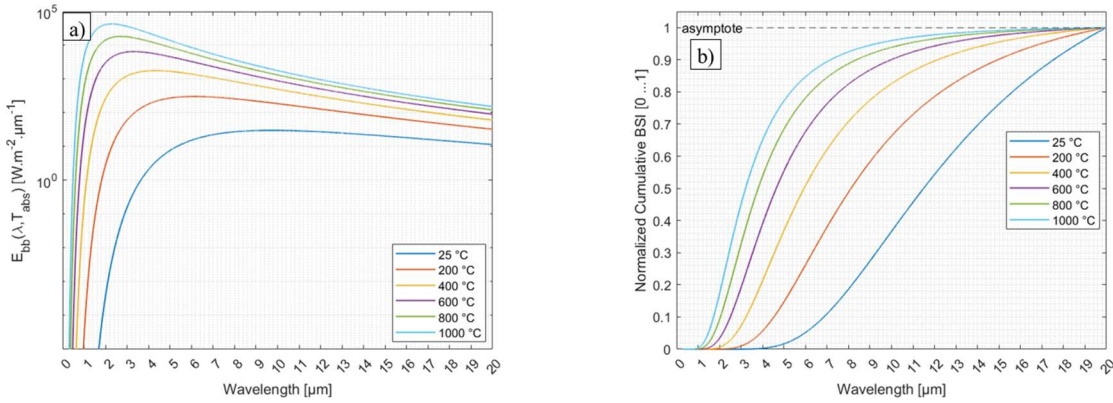


Figure 3.7: Blackbody spectral irradiance. a) Planck’s law of blackbody radiation for a temperature ranging from  $25 \text{ }^\circ\text{C}$  to  $1000 \text{ }^\circ\text{C}$  b) Cumulative fraction of Stefan-Boltzmann law.

It is worth observing that solar and blackbody spectral irradiances partially overlap (Figure 3.8). In Figure 3.8.a, the respective spectral irradiances are normalised by their maximum values, while cumulative spectral irradiances are shown in Figure 3.8.b. For a high temperature STAC, the influence of this overlap on the opto-thermal performance is a function of  $C_x$  and  $T_{abs}$ . This overlap affects the trade-off between  $\alpha_{sol}$  and  $\epsilon_{th}$  for any SSC.



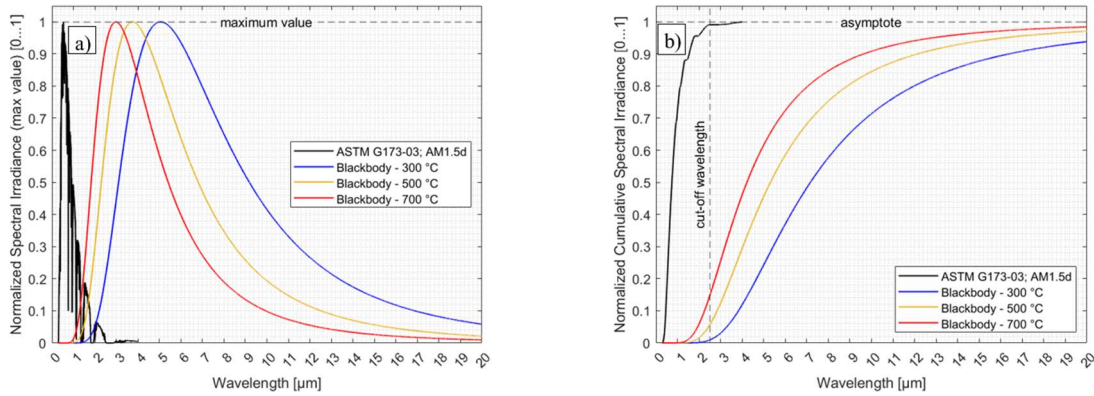


Figure 3.8: Comparison of solar and blackbody spectral irradiances. a) Spectral irradiances normalised by their maximum value. b) Normalised cumulative spectral irradiances. The solar spectral irradiance is normalised by the integral value computed at AM1.5d from 0.28 μm to 4 μm, while the blackbody spectral irradiance is normalised with respect to Stefan Boltzmann law ( $\sigma T^4$ ).

### 3.3.1.3 SSC model parameters

A STAC is often simply defined as SSC when it has a “high” solar absorptance  $\alpha_{sol}$  and a “low” thermal emittance  $\epsilon_{th}$ . A few scientific instruments, i.e. portable solar reflectometers and emissometers [131-134] allow a quick measurement of these FoMs in the field according to defined standards [87-89]. Due to their moderate spectral resolution, information is however lost about relevant spectral features of the STAC. The coating designer should thus rather rely on calibrated spectrophotometric data. As observed in in Figure 3.3.a, SSCs exhibit a rather smooth sigmoid shaped spectrum. This allows defining a spectral model  $f_{SSC}(\lambda)$  for the SDHR, described by a few parameters that can be easily interpreted as specific FoMs for SSC, assuming the residual error is negligible.

Simple models have been proposed in the literature, such as step functions and logistic functions [94,95]. The Heavyside unit step function has been expressed in (Eq.3.4), a modified step function [94] is described in (Eq.3.11), while a versatile logistic model [95] is formulated in (Eq.3.12). SSC spectral models are summarised in Table 3.4 with their characteristics. These models capture at least one of the following features:

- Cut-off wavelength  $\lambda_{cut-off}$
- Shape factor  $f_{shape}$ , describing the steepness of the curve
- Asymptotical values, i.e. when  $\lambda \rightarrow 0$  and  $\lambda \rightarrow +\infty$

$$\rho_{SDHR}(\lambda) = \begin{cases} \rho_{low}; & \lambda \leq \lambda_{cut-off} \\ \rho_{high}; & \lambda > \lambda_{cut-off} \end{cases} \quad (3.11)$$

$$\rho_{SDHR}(\lambda) = \frac{L}{1 + \exp \left[ f_{shape} \left( \frac{1}{\lambda} - \frac{1}{\lambda_{cut-off}} \right) \right]} + Offset \quad (3.12)$$

Table 3.4: Summary of SSC model parameterization.

Model	Unit step function	Ref. [94] 3 parameters	Ref. [95] 2 parameters	Ref. [95] 4 parameters	Logistic function (3 parameters)
Equation	(11)	(11)	(12)	(12)	(12)
Parameters and values	$\rho_{low} = 0$ $\rho_{high} = 1$ $\lambda_{cut-off} > 0$ $f_{shape} = +\infty$	$0 < \rho_{low} < 1$ $0 < \rho_{high} < 1$ $\lambda_{cut-off} > 0$ $f_{shape} = +\infty$	$L = 1$ $Offset = 0$ $\lambda_{cut-off} > 0$ $f_{shape} > 0$	$0 < L$ $Offset > 0$ $\lambda_{cut-off} > 0$ $f_{shape} > 0$	$0 < L$ $Offset = 0$ $\lambda_{cut-off} > 0$ $f_{shape} > 0$
# parameters	1	3	2	4	3
$\lambda_{cut-off}$	Explicit	Explicit	Explicit	Explicit	Explicit
$f_{shape}$	Not defined	Not defined	Explicit	Explicit	Explicit
Value at $\lambda_{cut-off}$	0	$\rho_{low}$	$L/2=0.5$	$Offset+L/2$	$L/2$
Asymptote 1 $\lambda \rightarrow 0$	0	$\rho_{low}$	$Offset = 0$	$Offset > 0$	$Offset = 0$
Asymptote 2 $\lambda \rightarrow +\infty$	1	$\rho_{high}$	$\frac{L}{1 + \exp \left[ f_{shape} \left( -\frac{1}{\lambda_{cut-off}} \right) \right]} + Offset$		

### 3.3.2 FoMs: Level 2

#### 3.3.2.1 Selectivity indices

The next FoM is the selectivity ratio (Eq.3.13), [92,93] introducing here the symbol  $S_i$ . This FoM allows a simple discrimination between SSCs and black coatings. The  $S_i$  index is maximised for a SSC and close to 1 for a non-selective, grey body.

$$S_i = \frac{\alpha_{sol}(AM)}{\varepsilon_{th}(T_{abs})} \quad (3.13)$$

One potential issue with this FoM occurs for SSC at low temperatures, because thermal emittance  $\varepsilon_{th}$  could achieve infinitesimally small values. This would yield a nearly infinite  $S_i$  value. As such, the  $S_i$  index is re-normalised to correct this issue, coining the Simon's number  $S_i^*$  as expressed in (Eq.3.14). With this variant formulation, a grey body achieves a null value and a SSC reaches a positive value.

$$S_i^* = \ln(S_i) \quad (3.14)$$

#### 3.3.2.2 Useful heat flux

The useful heat flux  $\dot{q}_{use}''$  ( $W.m^{-2}$ ) is a common FoM [96,97], already introduced in (Eq.3.1). This equation is further developed in (Eq.3.15) for the case of a small flat or convex surface, e.g. a receiver tube, surrounded by an enclosure (view factor  $F_{view}=1$ ) at a temperature  $T_{sky}$  [135,136].

$$\dot{q}_{use}'' = \alpha_{sol} \dot{q}_{sol}'' - \varepsilon_{th}(T_{abs}) \sigma (T_{abs}^4 - T_{sky}^4) - h_{conv}(T_{abs} - T_{amb}) \quad (3.15)$$

where  $h_{conv}$  is the convection heat transfer coefficient expressed in  $W/m^2.K$ .

An analogous heat transfer coefficient  $h_{rad}$  can be defined for radiation (Eq.3.16):

$$h_{rad} = \frac{\varepsilon_{th}(T_{abs}) \sigma (T_{abs}^4 - T_{sky}^4)}{T_{abs} - T_{sky}} \quad (3.16)$$

A dimensionless number  $Cr$  can be introduced to compare respective heat transfer coefficients for convection and radiation (Eq.3.17):

$$Cr = \ln\left(\frac{h_{conv}}{h_{rad}}\right) \quad (3.17)$$

The  $Cr$  number approaches zero if convection and radiation are of the same order of magnitude. It is expressed in logarithmic form as both  $h_{conv}$  and  $h_{rad}$  coefficients can be infinitesimally small, respectively for a vacuum enclosure and a low emittance coating. According to our assumptions (subsection 3.2.2), our analysis is carried out for a regime where convection is negligible in comparison to radiation heat transfer (i.e.  $Cr \rightarrow -\infty$ ).

Neglecting convection, (Eq.3.16) simplifies to (Eq.3.18) in lumped form:

$$\dot{q}_{use}'' = \alpha_{sol} \dot{q}_{sol}'' - \varepsilon_{th}(T_{abs})\sigma(T_{abs}^4 - T_{sky}^4) \quad (3.18)$$

Where  $\dot{q}_{sol}''$  is defined according to the following integral (Eq.3.19):

$$\dot{q}_{sol}'' = C_x \int_{\lambda_1}^{\lambda_2} G_{sol}(\lambda, AM) d\lambda \quad (3.19)$$

(Eq.3.18) can also be formulated in integral form (Eq.3.20), if spectral data is available over a given spectral range  $[\lambda_1; \lambda_3]$ , assuming further that  $T_{sky}$  is negligible in comparison to  $T_{abs}$ :

$$\dot{q}_{use}'' \approx C_x \int_{\lambda_1}^{\lambda_2} [1 - \rho_{SDHR}(\lambda, \theta, T_{amb})] G_{sol}(\lambda, AM) d\lambda - \int_{\lambda_1}^{\lambda_3} [1 - \rho_{SDHR}(\lambda, \theta, T_{amb})] E_{bb}(\lambda, T_{abs}) d\lambda \quad (3.20)$$

For a STAC performance comparison, the absolute value  $\dot{q}_{use}''$  may be difficult to interpret out of context, the marginal useful heat difference  $\Delta\dot{q}_{use}''$  is thus considered to compare for instance the performance of a black coating and a SSC at a given operation point  $\{C_x; T_{abs}\}$  (Eq.3.21):

$$\Delta\dot{q}_{use}''(C_x, T_{abs}) = \dot{q}_{use,black}'' - \dot{q}_{use,SSC}'' \quad (3.21)$$

For a given operation point  $\{C_x; T_{abs}\}$ , the marginal useful heat difference is here defined positive if the black coating performs better than a SSC, and negative otherwise.

### 3.3.2.3 Opto-thermal efficiency

The coating opto-thermal efficiency  $\eta_{opt-th}$  is a FoM [11-13,30,38-39] defined as the ratio of the useful heat flux  $\dot{q}_{use}''$  and the concentrated solar flux  $\dot{q}_{sol}''$ . Assuming convection is negligible (i.e.  $Cr \rightarrow -\infty$ ),  $\eta_{opt-th}$  can be expressed in lumped form (Eq.22):

$$\eta_{opt-th} = \frac{\dot{q}_{use}''}{\dot{q}_{sol}''} \approx \alpha_{sol} - \frac{\varepsilon_{th}(T_{abs})\sigma(T_{abs}^4 - T_{sky}^4)}{\dot{q}_{sol}''} \quad (3.22)$$

This FoM can also be written in integral form (Eq.23), by dividing (Eq.20) and (Eq.19):

$$\eta_{opt-th} \approx \frac{C_x \int_{\lambda_1}^{\lambda_2} [1 - \rho_{SDHR}(\lambda, \theta, T_{amb})] G_{sol}(\lambda, AM) d\lambda - \int_{\lambda_1}^{\lambda_3} [1 - \rho_{SDHR}(\lambda, \theta, T_{amb})] E_{bb}(\lambda, T_{abs}) d\lambda}{C_x \int_{\lambda_1}^{\lambda_2} G_{sol}(\lambda, AM) d\lambda} \quad (3.23)$$

The marginal opto-thermal efficiency difference  $\Delta\eta_{opt-th}$  is expressed in (Eq.24) as above in (Eq.21) to compare a black coating and a SSC at a given operation point  $\{C_x; T_{abs}\}$ :

$$\Delta\eta_{opt-th}(C_x, T_{abs}) = \eta_{opt-th,black} - \eta_{opt-th,SSC} \quad (3.24)$$

### 3.3.2.4 Trade-off factor

The coating opto-thermal efficiency  $\eta_{opt-th}$  allows deriving a first trade-off factor  $Z_{trade-off}$  [30,98], a compound FoM describing the trade-off between  $\alpha_{sol}$  and  $\varepsilon_{th}$ , as a function of the operation point  $\{C_x, T_{abs}\}$ . Partial derivatives are expressed in (Eq.3.25):

$$\frac{\partial \eta_{opt-th}}{\partial \alpha_{sol}} = 1; \quad \frac{\partial \eta_{opt-th}}{\partial \varepsilon_{th}} = - \frac{\sigma(T_{abs}^4 - T_{sky}^4)}{C_x \int_{\lambda_1}^{\lambda_2} G_{sol}(\lambda, AM) d\lambda} \quad (3.25)$$

$Z_{trade-off}$  is defined in (Eq.3.26) by dividing both partial derivatives in (Eq.3.25):

$$Z_{trade-off} = \frac{\Delta \varepsilon_{th}}{\Delta \alpha_{sol}} = - \frac{C_x \int_{\lambda_1}^{\lambda_2} G_{sol}(\lambda, AM) d\lambda}{\sigma(T_{abs}^4 - T_{sky}^4)} \quad (3.26)$$

According to (Eq.3.26), varying  $\alpha_{sol}$  by 1 p.p. has the same effect on the opto-thermal efficiency  $\eta_{opt-th}$  as varying  $\varepsilon_{th}$  by  $-Z_{trade-off}$  p.p. The solar absorptance  $\alpha_{sol}$  is thus a dominant opto-thermal FoM. However, its initial value for a STAC should be above 95%, the remaining useful range for improvement is thus limited. The influence of the thermal emittance  $\varepsilon_{th}$  depends on the operating point  $\{C_x, T_{abs}\}$ .

A similar sensitivity analysis as in (Eq.3.25) could be derived with respect to the parameter  $C_x$  yielding further trade-off factors between the respective STAC and the concentrator designs. The  $\eta_{opt-th}$  FoM can be improved either by increasing solar absorptance  $\alpha_{sol}$ , reducing thermal emittance  $\varepsilon_{th}$  or increasing concentration factor  $C_x$  as illustrated in Table 3.5.

Table 3.5: Sensitivity of opto-thermal efficiency  $\eta_{opt-th}$ ;  $G_{sol}(AM1.5d) = 900 \text{ W/m}^2$ ;  $T_{abs} = 600 \text{ }^\circ\text{C}$ ;  $T_{sky} = 25 \text{ }^\circ\text{C}$ .

Scenario	$\alpha_{sol}$ [0...1]	$\varepsilon_{th}$ [0...1]	$C_x$ [-]	$\eta_{opt-th}$ [%]
Ref A (SSC, PTC)	0.95	0.15	100	89.6%
Increase $\alpha_{sol}$ ( $\uparrow$ )	<b>0.96</b> (+1 p.p.)	0.15	100	90.6% (+1 p.p.)
Decrease $\varepsilon_{th}$ ( $\downarrow$ )	0.95	<b>0.122</b> (-2.8 p.p.)	100	90.6% (+1 p.p.)
Increase $C_x$ ( $\uparrow$ )	0.95	0.15	<b>123</b> (+23%)	90.6% (+1 p.p.)
Ref B (Black, CRS)	0.95	0.90	1000	91.7%
Increase $\alpha_{sol}$ ( $\uparrow$ )	<b>0.96</b> (+1 p.p.)	0.90	1000	92.7% (+1 p.p.)
Decrease $\varepsilon_{th}$ ( $\downarrow$ )	0.95	<b>0.65</b> (-30p.p.)	1000	92.7% (+1 p.p.)
Increase $C_x$ ( $\uparrow$ )	0.95	0.90	<b>1400</b> (+40%)	92.7% (+1 p.p.)

Paradoxically, a sensitivity analysis of  $\eta_{opt-th}$  with respect to the parameter  $T_{abs}$  yields a negative value, i.e. the STAC opto-thermal efficiency decreases at higher temperature. This does not reflect the influence of absorber temperature  $T_{abs}$  on the thermal efficiency  $\eta_{thermal}$  of the thermodynamic cycle.

### 3.3.3 FoMs: Level 3

#### 3.3.3.1 Maximum Steady-State Temperature

The next FoM is the maximum Steady-State Temperature  $T_{SST,max}$ , also referred to as the "stagnation" temperature [92,99]. This parameter is measurable for a high temperature STAC in a non-destructive setup [93], for a low concentration factor ( $C_x < 10$ ), otherwise the STAC may exceed its maximal operating temperature and would suffer an irreversible degradation.

By definition,  $T_{SST,max}$  corresponds to the temperature of the STAC when no useful heat can be extracted from the absorber, i.e. (Eq.3.15) equals zero. All the absorbed solar flux is then radiated away by the STAC. Neglecting convection losses, (Eq.3.18) can be rewritten as in (Eq.3.27).

$$T_{SST,max} \approx \left[ \frac{\alpha_{sol}(AM)\dot{q}_{sol}'' + \varepsilon_{th}(T_{SST,max})\sigma T_{sky}^4}{\varepsilon_{th}(T_{SST,max})\sigma} \right]^{0.25} \quad (3.27)$$

The parameter  $T_{SST,max}$  appears on both sides of the equations, as  $\varepsilon_{th}$  is temperature dependent for reference materials. (Eq.3.27) is hence solved numerically for  $T_{SST,max}$ .

### 3.3.3.2 Solar Reflectance Indices

The solar reflective index  $SRI$  [87-89,100,101] is another standard FoM, rather used in the building industry to characterise construction materials suitable for mitigating the Urban Heat Island (UHI) phenomenon [137-141]. This FoM is calculated on the basis of  $\alpha_{sol}$  and  $\varepsilon_{th}$  values measured with portable devices [87-89,131-134]. Its original formulation is related to the computation of maximum steady-state temperature  $T_{SST,max}$  outlined in subsection 3.3.3.1.

For building applications, (Eq.3.15) is solved for  $T_{SST,max}$  with the following parameters [100]:

- $\dot{q}_{sol}'' = 1000 \text{ W.m}^{-2}$ ; ( $C_x = 1$ ;  $AM1.5$ ; global radiation [124])
- $h_{conv} = 12 \text{ W.m}^{-2}\text{.K}^{-1}$
- $T_{sky} = 300 \text{ K}$ ;  $T_{amb} = 310 \text{ K}$

The  $T_{SST,max}$  value computed for a given material is then compared to two reference bodies, for which stagnation temperatures are also computed as outlined above:

- Reference black surface: ( $\alpha_{sol} = 0.95$ ;  $\varepsilon_{th} = 0.90$ )
  - Temperature  $T_{black, SST}$  (82.6 °C)
- Reference white surface; ( $\alpha_{sol} = 0.20$ ;  $\varepsilon_{th} = 0.90$ )
  - Temperature  $T_{white, SST}$  (44.7 °C)

SRI is computed according to (Eq.3.28):

$$SRI = 100 \frac{T_{black, SST} - T_{SST,max}}{T_{black, SST} - T_{white, SST}} \quad (3.28)$$

A low  $SRI$  value indicates a cool roof material, while a high  $SRI$  values indicates a hot roof material. A few issues have been expressed for this FoM in the building industry [101]. Although the SRI is expressed in percent, its value can either reach negative values or values above 100, as the reference black and white materials are not optimised: the solar reflectance or "*albedo*" index is varying between 0.2 and 0.95, while the thermal emittance or "*melano*" index remains constant at 0.9.

The  $SRI$  calculation is adapted in this chapter, first by setting adapted boundary conditions relevant for CSP, according to the modelling assumptions (subsection 3.2.2):

- Solar irradiance:  $AM1.5d$  [124]
- Variable concentration factor  $C_x$  variable
- Negligible convection losses ( $h_{conv} = 0$ )
- Sky temperature  $T_{sky} = 25 \text{ °C}$

Furthermore, a renormalised  $SRI^*$  FoM is defined (Eq.3.29), introducing spectral selective reference coatings, which spectral profiles are defined according to (Eq.3.11) [94]:

- Reference "cold" coating:
  - $\{\lambda_{cut-off}= 2.5 \mu\text{m}; \rho_{low}= 99\%; \rho_{high}= 1\%\}$
- Reference "hot" coating:
  - $\{\lambda_{cut-off}= 2.5 \mu\text{m}; \rho_{low}= 1\%; \rho_{high}= 99\%\}$

$$SRI^* = 100 \frac{T_{hot,ref} - T_{SST,max}}{T_{hot,ref} - T_{cold,ref}} \quad (3.29)$$

The choice is made to define two reference coatings with symmetrical spectral selectivity ( $S_i, S_i^*$ ), i.e. one "cold" reference coating (low  $\alpha_{sol}$ , high  $\varepsilon_{th}$ ) and one "hot" reference coating (high  $\alpha_{sol}$ , low  $\varepsilon_{th}$ ). The "hot" reference coating is nearly equivalent to the ideal SSC introduced in the subsection 3.2.3, while the "cold" reference coating acts as an "anti-solar" surface [142]. Instead of defining a constant value for  $\alpha_{sol}$  and  $\varepsilon_{th}$ , spectral profiles are defined to achieve a constant  $\alpha_{sol}$  value while achieving a realistic  $\varepsilon_{th}$  value at higher temperature.

### 3.3.3.3 Thermal efficiency and peak efficiency temperature

The last FoMs included in this review are the thermal efficiency  $\eta_{thermal}$  [11,12,96,97] and the peak efficiency temperature  $T_{peak,opt}$ . The thermal efficiency of a thermodynamic cycle is bounded by an upper limit, defined by the Carnot cycle (Eq.3.30):

$$\eta_{Carnot} = 1 - \frac{T_{cold}}{T_{hot}} \quad (3.30)$$

where  $T_{cold}$  and  $T_{hot}$  respectively correspond to the temperature of the cold and hot heat sinks. In practice, only a fraction  $f_{Carnot} \sim 0.7$  [12] is accessible due to engineering limitations.

The thermal efficiency  $\eta_{thermal}$  is thus formulated as a product in (Eq.3.31):

$$\eta_{thermal} = \eta_{opt-th} \cdot f_{Carnot} \cdot \eta_{Carnot} \quad (3.31)$$

Assuming negligible convection ( $Cr \rightarrow \infty$ ), a cold heat sink  $T_{cold}$  with a sky temperature  $T_{sky}$ , a hot heat sink  $T_{hot}$  with absorber temperature  $T_{abs}$  and assuming a fraction  $f_{Carnot} = 0.7$ , (Eq.3.32) is derived:

$$\eta_{Carnot} \approx f_{Carnot} \left( \alpha_{sol} - \frac{\varepsilon_{th}(T_{abs})\sigma(T_{abs}^4 - T_{sky}^4)}{\dot{q}''_{sol}} \right) \left( 1 - \frac{T_{sky}}{T_{abs}} \right) \quad (3.32)$$

The thermal efficiency  $\eta_{thermal}$  equals zero for two temperatures, i.e. sky temperature and maximal stagnation temperature. It peaks at an optimal temperature  $T_{peak,opt}$  (Eq.3.33).

$$\left. \frac{\partial \eta_{Carnot}}{\partial T_{abs}} \right|_{T_{peak,opt}} = 0 \quad (3.33)$$

### 3.4 Results and discussion

#### 3.4.1 FoMs: Level 1

##### 3.4.1.1 Solar absorptance

Solar absorptance  $\alpha_{sol}$  is calculated according to (Eq.3.6) for different  $AM$  values, ranging from  $AM0$  to  $AM5$ . Results are illustrated in Figure 3.9.a for reference coatings (Figure 3.3), while the cumulative solar absorptance (Eq.3.7) is shown in Figure 3.9.b for  $AM1.5d$ .

In Figure 3.9.a, ideal SSC and blackbody coatings both achieve a maximum  $\alpha_{sol}$  value (100%), as these coatings absorb all the solar radiation. The reference SSC reaches a  $\alpha_{sol}$  value of 94.6% ( $AM1.5$ ), while the  $\alpha_{sol}$  value reaches 96.6% (+2 p.p.) for the reference black coating. This coating reaches an  $\alpha_{sol}$  value above 96% and is thus qualified as HSA.

As can be observed in Figure 3.9.a, the  $AM$  variable has a weak influence on the  $\alpha_{sol}$  value. For the reference black coating, the same  $\alpha_{sol}$  value (96.6%) is computed from  $AM0$  to  $AM3$ , meanwhile the  $\alpha_{sol}$  value varies from 93.9% ( $AM0$ ) to 94.6% ( $AM1.5...AM3$ ) for the reference SSC.

Looking at the cumulative solar absorptance for  $AM1.5$  (Figure 3.9.b), one observes that the 2 p.p. difference between the reference black coating and SSC first appears and amplifies around  $1.7 \mu\text{m}$ , in the shortwave IR range. At this same wavelength, the reference black coating is already 2.7 p.p. from the ideal profile (red curve) to achieve a maximal  $\alpha_{sol}$  value. This diagram offers a finer appreciation of the spectral deviations to compare STAC formulations.

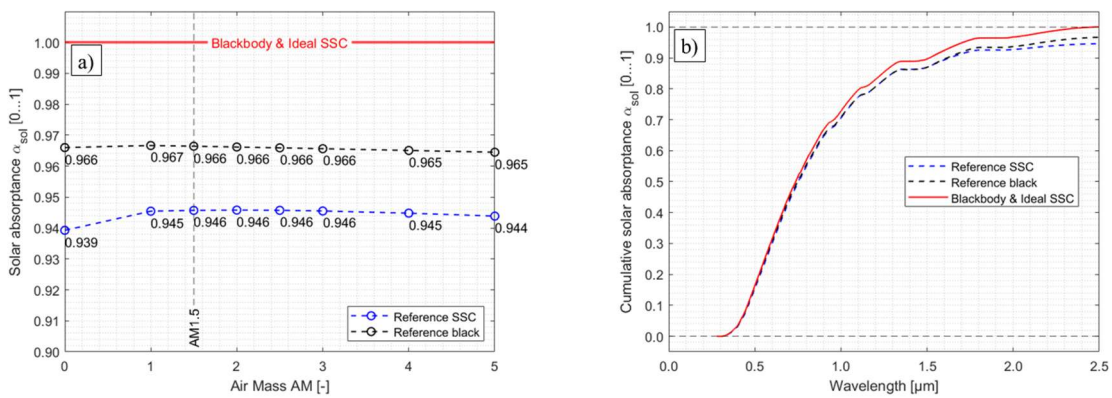


Figure 3.9: Calculation of  $\alpha_{sol}$  (Eq.3.6) from  $0.28 \mu\text{m}$  to  $2.5 \mu\text{m}$  a) as a function of  $AM$  for reference coatings. b) Cumulative solar absorptance according to (Eq.3.7) considering the coating SDHR.

Maximal solar absorptance (99.9+ %) has been achieved with Carbon Nanotubes (CNT) [143]. Such “space black” coatings are typically applied by vacuum deposition or spraying processes. These high-performance coatings are rather designed for stray light suppression on sensitive optical devices for space applications [144,145], considering their cost of application, temperature stability and environmental durability [146]. For high temperature STAC, the current upper limit for stable formulations reaches 98% [98]. A Haynes 230 metal substrate oxidised at temperatures above  $700 \text{ }^\circ\text{C}$  reaches a  $\alpha_{sol}$  value between 92% and 94% [31,98], due to the formation of a duplex oxide scale [147]. For CRS applications, a re-coating threshold value of 95% is reported [37]. The useful  $\alpha_{sol}$  range for a high temperature STAC is thus restricted from 90% to 100%. An increase of a few tenth p.p. for  $\alpha_{sol}$  thus represents a significant improvement.

### 3.4.1.2 Thermal emittance

Thermal emittance  $\epsilon_{th}$  is computed according to (Eq.3.8-3.9) for an absorber temperature  $T_{abs}$  ranging from 25 °C to 1000 °C for the reference coatings and shown in Figure 3.10.a. The cumulative thermal emittance is plotted in Figure 3.10.b for  $T_{abs}= 600$  °C. It is worth remembering that the coverage fraction of Stefan Boltzmann law increases with temperature (Figure 3.7.b) and the spectral calculation is here performed over the spectral range [0.28; 20  $\mu\text{m}$ ] for the available spectral data (Figure 3.3.a).

ISO 22975-3 [83] recommends for instance a spectral range from 2  $\mu\text{m}$  to 50  $\mu\text{m}$  for lower temperatures, extrapolating spectral data beyond 20  $\mu\text{m}$ . Omitting data above 20  $\mu\text{m}$  would influence the  $\epsilon_{th}$  calculation. For the reference black coating, its spectral reflectivity should remain low (Figure 3.3.a) and the  $\epsilon_{th}$  value should thus increase moderately by a few p.p. For a SSC, the spectral reflectivity reaches an asymptotical value in the IR range (Figure 3.3.a) and the extrapolation can be justified, the  $\epsilon_{th}$  value should decrease marginally by a few p.p.

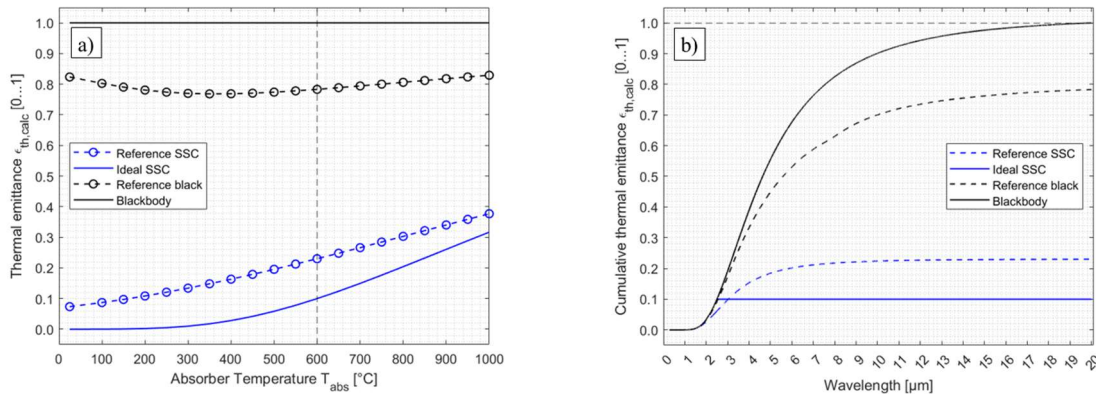


Figure 3.10: Calculation of thermal emittance  $\epsilon_{th}$  (Eq.3.8-3.9) a) as a function of  $T_{abs}$  for reference coatings. b) Cumulative thermal emittance at 600 °C according to (Eq.3.10) considering the coating SDHR.

From 25 °C to 1000 °C, the ideal SSC reaches the lowest  $\epsilon_{th}$  value for any temperature (Figure 3.10.a). Its  $\epsilon_{th}$  value is lower than 10% below and 600 °C. For the reference SSC, the  $\epsilon_{th}$  value approaches 23% at 600 °C. For the reference black coating, the  $\epsilon_{th}$  value reaches 78% at 600 °C. The ideal blackbody is obviously the worst coating, with a maximal  $\epsilon_{th}$  value (100%).

The useful optimization range for  $\epsilon_{th}$  is constrained, although the ideal SSC is here only optimised to maximise  $\alpha_{sol}$ . This value is 55 p.p. above the reference SSC and 68 p.p. above the ideal SSC at the same temperature. The  $\epsilon_{th}$  value can thus be potentially improved by some decades in the best case. The temperature dependence of the  $\epsilon_{th}$  value is more pronounced for SSCs than for black coatings. For SSCs, the  $\epsilon_{th}$  value increases at higher temperature. For a black coating, this temperature dependence is moderate.

Looking at the cumulative thermal emittance (Figure 3.10.b) calculated at 600 °C, one can notice that asymptote  $\epsilon_{th}$  value is reached earlier on for SSCs. In the case of an ideal SSC; there is a sharp transition at 2.5  $\mu\text{m}$  ( $\lambda_{cut-off}$ ). Before this wavelength, the ideal SSC is first aligned with the ideal blackbody. Beyond 2.5  $\mu\text{m}$ , the ideal SSC does not emit radiation. The reference SSC converges to 99% of its asymptote  $\epsilon_{th}$  value around 12  $\mu\text{m}$ . For black coatings, the asymptotical convergence is not completed at 20  $\mu\text{m}$ , this effect is more pronounced at lower temperatures.



Instead of reporting  $\epsilon_{th}$  values at arbitrary temperature levels, temperature correlations or tables should be documented, for example with fourth order polynomial fits. Such polynomial fits are implemented for further calculations in this chapter.

### 3.4.1.3 SSC model parameters

SSC models (Table 3.4) are fitted to the reference SSC (Figure 3.3.a), applying ordinary least squares for logistic models (Eq.3.12) to minimise the root mean square error (*RMSE*). Fitted parameter values are listed in Table 3.6. Spectral curves are shown in Figure 3.11.a, while residuals are shown for logistic functions in Figure 3.11.b.

A better fit is achieved for the reference SSC (Figure 3.11.a) with logistic models (Eq.3.12) than with step functions (Eq.3.11). The residual analysis (Figure 3.11.b) indicates that the maximal deviation is observed in the shortwave range ( $< 2.5 \mu\text{m}$ ), which would directly affect the  $\alpha_{sol}$  calculation (Eq.3.6). A higher noise is observed beyond  $2.5 \mu\text{m}$  for FTIR data. A spike is observed at  $4.3 \mu\text{m}$ , corresponding to a strong  $\text{CO}_2$  absorption band, as the instrument has not been purged during the measurement.

The identified parameters of the SSC spectral curve slightly differ from one logistic model to the other, depending on the applied constraints for (Eq.3.12). The cut-off wavelength  $\lambda_{cut-off}$  spans from  $2.4 \mu\text{m}$  to  $2.46 \mu\text{m}$ , while the spectral shape factor  $f_{shape}$  spans from 7.37 to 7.92. The logistic model with 4 parameters seems to be the most flexible and accurate model, with the minimal RMSE value.

These logistic models can simulate the ideal blackbody and SSC for asymptotical parameter values, as listed below:

- blackbody:  $\{Offset= 0; L \rightarrow 0; \lambda_{cut-off} \rightarrow +\infty; f_{shape} \rightarrow +\infty\}$
- ideal SSC:  $\{Offset= 0; L \rightarrow 1; \lambda_{cut-off} \rightarrow 2.5 \mu\text{m}; f_{shape} \rightarrow +\infty\}$

However, these functions are not appropriate for modeling the black coating spectrum.

*Table 3.6: Results of SSC spectral model curve fitting applying ordinary least squares.*

<b>Model</b>	<b>Ref. [94]</b> <i>(3 parameters)</i>	<b>Ref. [95]</b> <i>(2 parameters)</i>	<b>Ref. [95]</b> <i>(4 parameters)</i>	<b>Logistic function</b> <i>(3 parameters)</i>
Identified parameters	$\rho_{low}= 0.01$ $\rho_{high}= 0.95$ $\lambda_{cut-off}= 2.4 \mu\text{m}$	$L= 1$ $Offset= 0$ $\lambda_{cut-off}= 2.4003$ $f_{shape}= 7.9179$	$L= 0.9970$ $Offset= 0.0182$ $\lambda_{cut-off}= 2.4645$ $f_{shape}= 7.6227$	$L= 1.0207$ $Offset= 0$ $\lambda_{cut-off}= 2.4367$ $f_{shape}= 7.3696$
RMSE	0.1182	0.0112	0.0093	0.0101

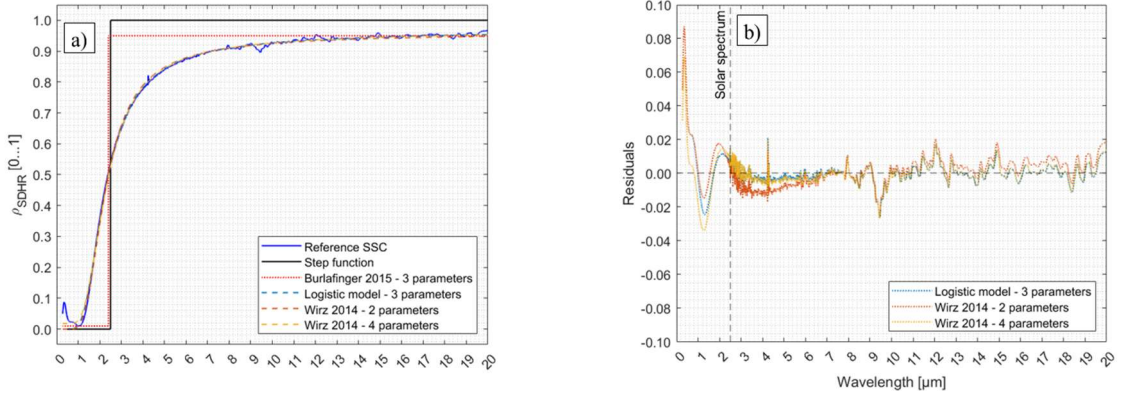


Figure 3.11: Spectral curve fitting of reference SSC with parameterised spectral models. a) Comparison of spectral models. b) Residuals for logistic models derived from (Eq.3.12).

### 3.4.2 FoMs: Level 2

#### 3.4.2.1 Selectivity indices

Selectivity indices  $S_i$  and  $S_i^*$  (Eq.3.13-3.14) are plotted for reference coatings at  $AM1.5$  as a function of  $T_{abs}$  in Figure 3.12. The  $S_i$  index spans a wide range, from 1 for an ideal blackbody to  $\sim 10^4$  for an ideal SSC at 100 °C. After logarithmic scaling, the  $S_i^*$  index spans from 0 for an ideal blackbody to  $\sim 10$  for an ideal SSC at 100 °C. As an order of magnitude, the best  $S_i^*$  value that can be achieved at 600 °C is about 2.3 for an ideal SSC, i.e. the  $\epsilon_{th}$  value can only be reduced down up to a tenth of  $\alpha_{sol}$  for a STAC, as the contribution of blackbody spectral irradiance below 2.5  $\mu\text{m}$  increases at higher temperatures.

Selectivity indices  $S_i$  and  $S_i^*$  are temperature dependent, because of the temperature dependence of  $\epsilon_{th}$ , especially for SSCs. The selectivity of a SSC thus decreases at a higher absorber temperature, as the  $\epsilon_{th}$  value increases.

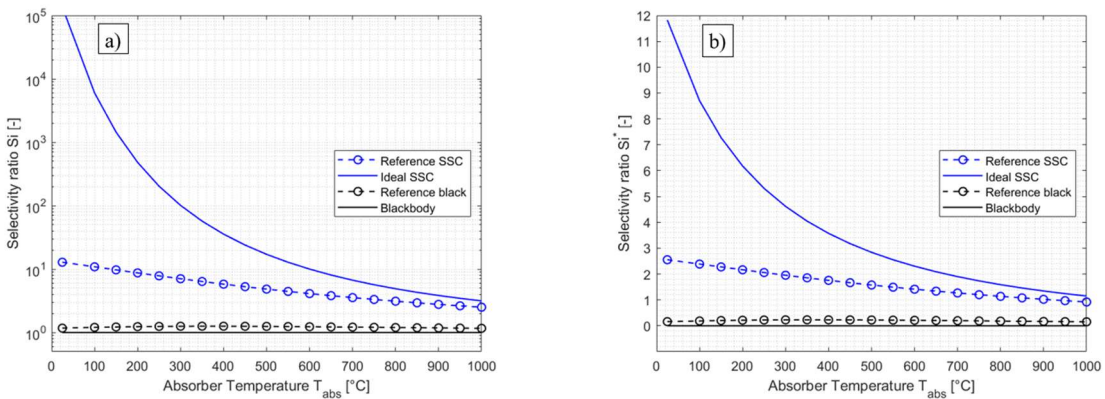
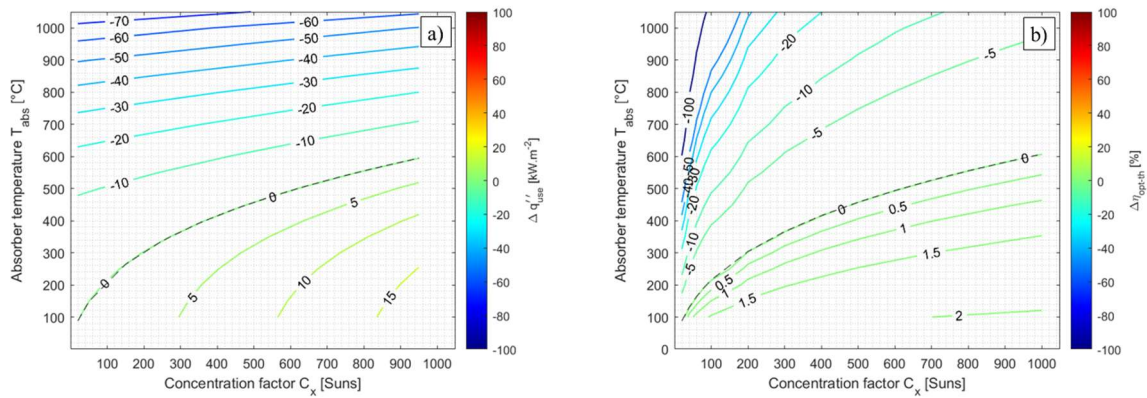


Figure 3.12: Selectivity indices as a function of absorber temperature  $T_{abs}$  a) Selectivity ratio  $S_i$  b) normalised selectivity ratio  $S_i^*$ .

#### 3.4.2.2 Useful heat flux and opto-thermal efficiency

Marginal differences in useful heat flux  $\Delta \dot{q}_{use}''$  (Eq.3.21) and opto-thermal efficiency  $\Delta \eta_{opt-th}$  (Eq.3.24) between the black coating and the reference SSC are plotted in Figure 3.13 as a contour map of  $C_x$  and  $T_{abs}$ .

The  $\alpha_{sol}$  value for reference black coating is 2 p.p. higher than in comparison to the  $\alpha_{sol}$  value for the reference SSC (subsection 3.4.1.1). This advantage outweighs the benefit of a low  $\epsilon_{th}$  value for high  $C_x$  and low  $T_{abs}$  values (Figure 3.13, bottom right corners). In these regions, i.e.  $\Delta\dot{q}''_{use}$  and  $\Delta\eta_{opt-th}$  are both positive and the black coating is more efficient than the reference SSC. The reference SSC is more efficient in comparison to the black coating for low  $C_x$  and high  $T_{abs}$  values (Figure 3.13, top left corners). A Pareto front can be identified on both contour maps (Figure 3.13, black dotted line), where both coatings are equally efficient.



*Figure 3.13: Comparison of the reference black coating and SSC as a function of  $C_x$  and  $T_{abs}$ . a) Marginal useful heat flux difference  $\Delta\dot{q}''_{use}$  b) Marginal opto-thermal efficiency  $\Delta\eta_{opt-th}$*

For PTC configurations, the  $C_x$  value is typically lower than 100 and the temperature ranges from 300 °C up to 600 °C. For this configuration, Figure 3.13 confirms that a SSC is more efficient than a black coating. For a CRS configuration, the allowable flux density (AFD) [72-76] are implemented for a molten salt HTF to avoid metal corrosion. For the Solar Two power plant [26,27,72] A solar flux of  $850 \text{ kW}\cdot\text{m}^{-2}$  is allowed at the 290 °C receiver inlet, while a lower solar flux of  $240 \text{ kW}\cdot\text{m}^{-2}$  is allowed at the 565 °C receiver outlet. Such constraints are rather favorable for the black coating according to Figure 3.13, although the Pareto front is crossed. The real SSC is thus not always optimal for this later application. In order to select the most efficient coating, the FoMs  $\Delta\dot{q}''_{use}$  or  $\Delta\eta_{opt-th}$  have to be integrated over the relevant  $C_x$  and  $T_{abs}$  domains, considering their correlation.

### 3.4.2.3 Comparison of spectral STAC opto-thermal efficiencies

Respective STAC cumulative opto-thermal efficiencies are analysed spectrally according to (Eq.3.20;  $\lambda_2= 2.5 \mu\text{m}$ ;  $\lambda_3= 20 \mu\text{m}$ ) in Figure 3.14. Two extreme configurations are selected according to the above discussion, i.e. one configuration in favor of the reference SSC (Figure 3.14.a;  $C_x= 250$ ,  $T_{abs}= 600 \text{ °C}$ ) and another in favor of the reference black coating (Figure 3.14.b;  $C_x= 850$ ,  $T_{abs}= 300 \text{ °C}$ ). These graphs illustrate a "spectral race", i.e. the detailed integration from  $0.28 \mu\text{m}$  up to a wavelength  $\lambda$ .

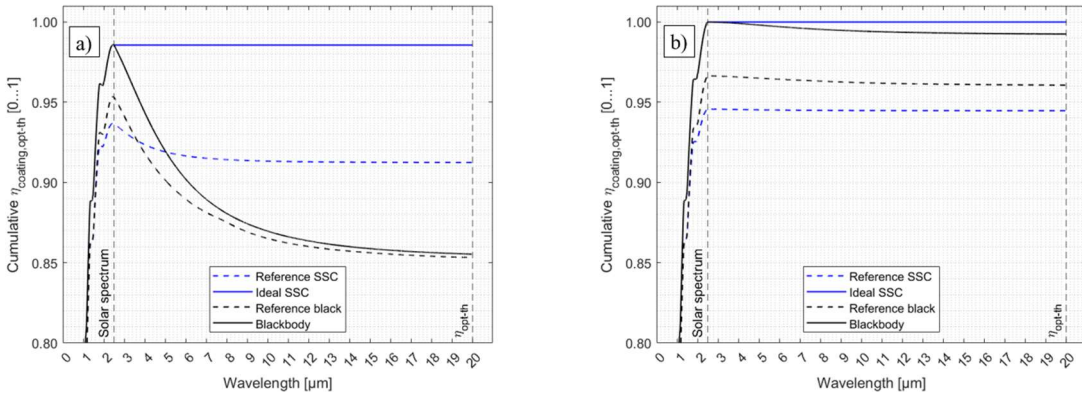


Figure 3.14: Spectral analysis of STAC opto-thermal efficiency. a)  $C_x=250$ ,  $T_{abs}=600$  °C. b)  $C_x=850$ ,  $T_{abs}=300$  °C.

It is worth remarking from Figure 3.14 that The STAC ranking differ slightly from one configuration to the other. In both cases, the ideal SSC is best ranked STAC (blue line). All other curves peak around 2.5  $\mu\text{m}$ , at which point solar radiation is fully absorbed.

In the first case (Figure 3.14.a;  $C_x=250$ ,  $T_{abs}=600$  °C), the reference SSC ranks second (blue dotted line), the ideal blackbody third (black line) and the reference black coating fourth (black dotted line), nearly on par with the ideal blackbody. The gap in  $\eta_{\text{opt-th}}$  between the reference SSC and the ideal blackbody after integration up to 20  $\mu\text{m}$  is about 6 p.p. The curve for the reference SSC respectively crosses the reference black coating curve at 3.5  $\mu\text{m}$  and the ideal blackbody at 5  $\mu\text{m}$ .

In the second case (Figure 3.14.b;  $C_x=850$ ,  $T_{abs}=300$ °C), the ranking is different: the ideal blackbody ranks second (black line), the reference black coating third (black dotted line) and the reference SSC fourth (blue dotted line). This time, the spectral curves do not cross. The reference SSC is the least efficient coating this time.

Both graphs offer a valuable perspective on the respective benefits of SSC and black coatings in terms of opto-thermal efficiency. In the first case, improving the coating spectral selectivity is relevant. In the second case, maximizing  $\alpha_{sol}$  is more relevant. Improving the coating spectral selectivity becomes a secondary goal.

### 3.4.2.4 Trade-off factor

The trade-off factor  $Z_{\text{trade-off}}$  (Eq.3.26) is plotted as a function of  $C_x$  and  $T_{abs}$  in Figure 3.15. This figure confirms previous observations made in subsections 3.4.2.2 and 3.4.2.3. At ( $C_x=250$ ,  $T_{abs}=600$  °C),  $Z_{\text{trade-off}}=-6.85$ , i.e. an increase of 1 p.p. in  $\alpha_{sol}$  has the same effect on  $\eta_{\text{opt-th}}$  as reducing  $\varepsilon_{th}$  by 6.85 p.p. At ( $C_x=850$ ,  $T_{abs}=300$  °C),  $Z_{\text{trade-off}}=134$ , i.e. an increase of 1 p.p. in  $\alpha_{sol}$  would be compensated by a reduction of -134 p.p. in  $\varepsilon_{th}$ . Considering the respective useful optimization ranges discussed previously in subsections 3.3.1.1 and 3.3.1.2, it is confirmed that selecting a SSC is not necessarily the best design option, the operating range  $\{C_x; T_{abs}\}$  has to be carefully examined.

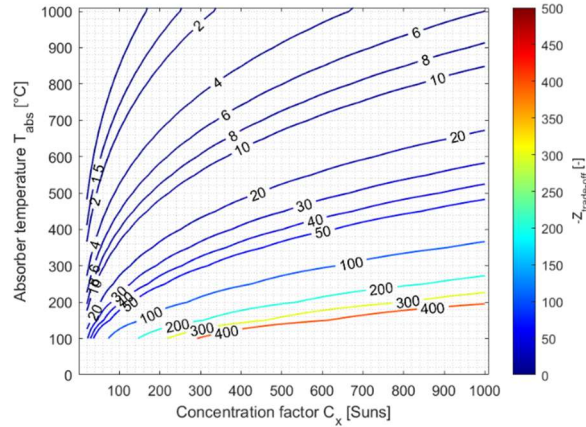


Figure 3.15: Contour map of trade-off factor as a function of  $C_x$  and  $T_{abs}$ .

### 3.4.3 FoMs: Level 3

#### 3.4.3.1 Maximum Steady-State Temperature

The maximum Steady-State Temperature  $T_{SST,max}$  is calculated for reference STACs (subsection 3.2.3) and further references introduced in subsection 3.3.3.2 according to (Eq.3.27). The results are shown in Figure 3.16.a on a semi-log plot while the search process is illustrated in Figure 3.16.b at  $C_x=1000$  for reference STACs. The  $T_{abs}$  variable is swept beyond the allowed maximum operating temperature (600 °C).

$T_{SST,max}$  increases with respect to  $C_x$  according to a logarithmic profile, in compliance with (Eq.3.27). According to thermodynamic constraints,  $T_{SST,max}$  cannot exceed the apparent sun temperature ( $T_{sun} \sim 5777$  K) and the upper theoretical bound concentration factor  $C_x$  is limited to 215 for linear focusing concentrators and 46250 for point focusing concentrators [96,97].

For the FoM  $T_{SST,max}$ , the following STAC ranking is observed in Figure 3.16.a: i) Ideal and reference SSC achieve the highest  $T_{SST,max}$  value (blue line and blue dotted line), ii) The reference black coating ranks third (black dotted line) and the ideal blackbody ranks fourth (black line).

More precisely, the ideal SSC ranks first up to  $C_x=750$ . The reference SSC then surpasses the ideal SSC beyond  $C_x=750$ , only by a few Kelvins. It is worth remarking that  $\epsilon_{th}$  curves shown in Figure 3.10.a actually cross for SSCs around  $T_{abs}=1400$  °C, i.e. the ideal SSC has then a higher  $\epsilon_{th}$  value than the reference SSC. The ideal SSC is thus not optimised for high temperatures.

This reasoning is of course hypothetical, as the reference SSC is not designed to withstand such high temperature levels. In practice, it is technically impossible to measure  $T_{SST,max}$  at high solar fluxes in a non-destructive setup, as irreversible degradation of the STAC and the metal substrate is expected.

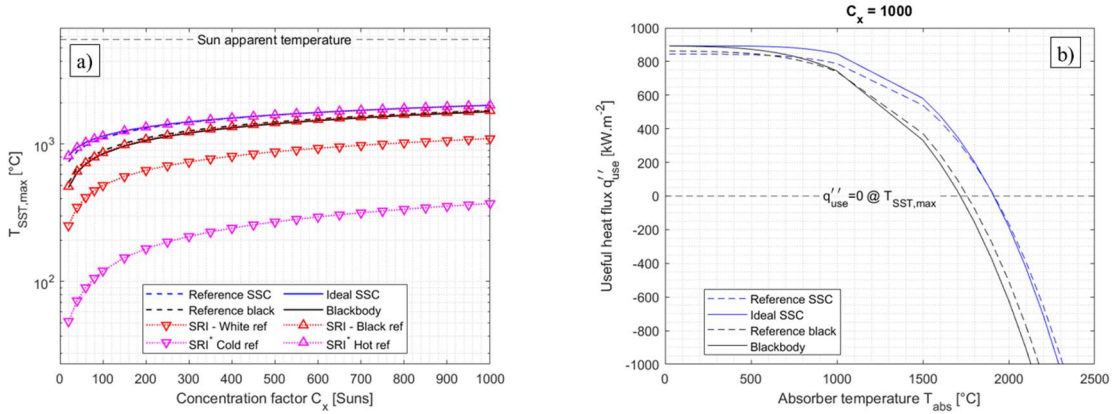


Figure 3.16: Calculation of  $T_{SST,max}$  a) as a function of  $C_x$  for all reference coatings. b) Calculation at  $C_x = 1000$  for reference STACs, sweeping the  $T_{abs}$  parameter beyond the reference coating operating temperature range.

### 3.4.3.2 Solar Reflectance Indices

Solar reflectance indices  $SRI$  and  $SRI^*$  are respectively calculated according to (Eq.3.28) and (Eq.3.29) for all reference coatings defined in this chapter. The results are plotted for  $SRI$  in Figure 3.17.a and for  $SRI^*$  in Figure 3.17.b, as a function of  $C_x$ .

In Figure 3.17, The  $SRI$  scaling bias is confirmed, as several reference coatings achieve a value beyond the interval [0-100]. For instance, All STACs except the ideal blackbody reach negative  $SRI$  values. This is explained according to Figure 3.16.a.: these STACs reach a higher stagnation temperature  $T_{SST,max}$  in comparison to the  $SRI$ /black reference. The  $SRI$  scale is also not adapted for the cold reference introduced to define the normalized  $SRI^*$ , as this coating achieves a  $SRI$  approaching 200.

The normalised  $SRI^*$  is bound between 0% and 100% for all defined reference coatings (Figure 3.17.b), except for the ideal SSC, which  $SRI^*$  value is negative, but not exceeding -1.  $SRI^*$  decreases with increasing  $C_x$  and the hierarchy observed for  $T_{SST,max}$  is respected (Figure 3.16.a). All STACs achieve a  $SRI^*$  lower than 50%. Meanwhile, the  $SRI$  white reference reaches the highest  $SRI^*$  value (>50%).

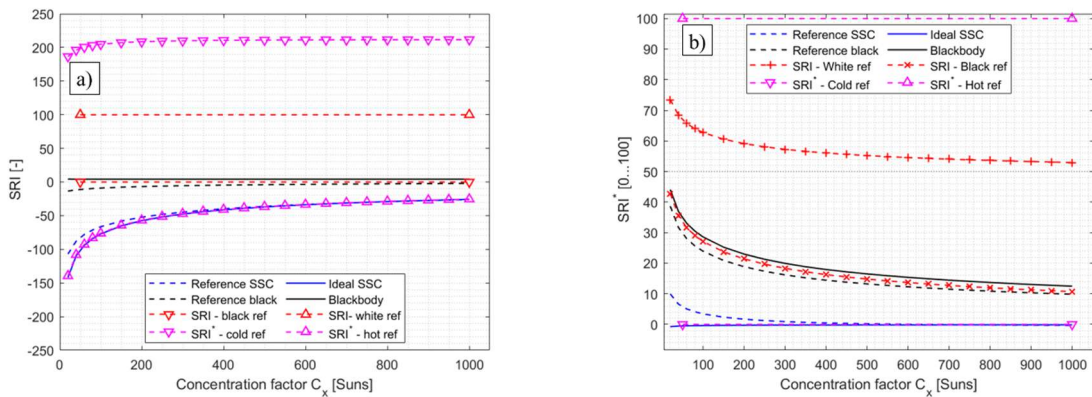


Figure 3.17: Calculation of solar reflectance indices as a function of  $C_x$ . a)  $SRI$  b)  $SRI^*$ .

A correlation can be noticed between selectivity indices ( $S_i$ ;  $S_i^*$ ) and  $T_{SST,max}$ , justifying a re-scaling of the  $SRI$ . This is illustrated in Figure 3.18, taking respectively as x-axis and y-axis the thermal emittance  $\epsilon_{th}$  and the solar absorptance  $\alpha_{sol}$ .

In Figure 3.18.a, the diagram can be divided into two sectors along the axis  $Si^*=0$  (grey body, black dotted line). Reference STACs are located in the upper half (blue and black lines).  $SRI$  reference coatings span on a vertical red dotted line, as their  $\epsilon_{th}$  is constant (90%).  $SRI^*$  references span on an orthogonal line to the axis  $Si^*=0$  (purple dotted line). As  $Si^*$  increases, the stagnation temperature  $T_{SST,max}$  increases (Figure 3.18.b).  $SRI^*$  reference coatings thus cover a wider temperature range in comparison to  $SRI$  reference coatings and are more appropriate for CSP applications.

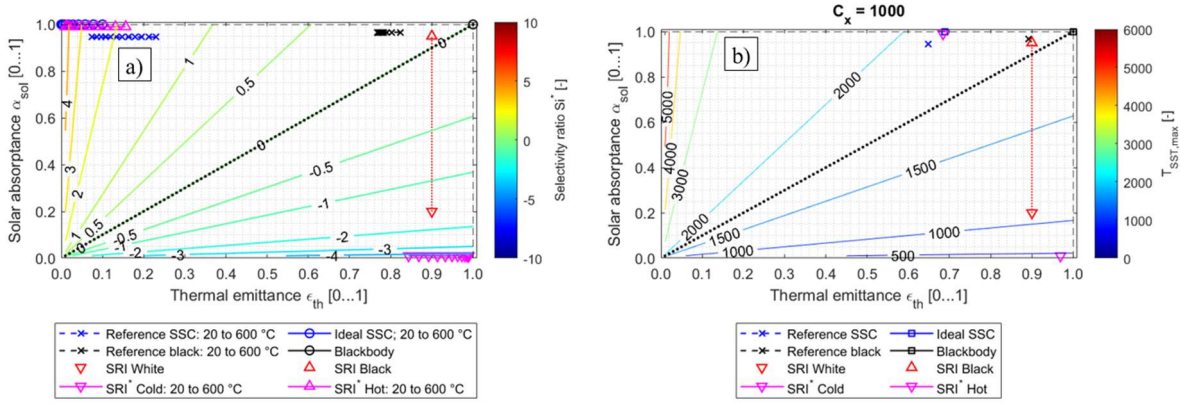


Figure 3.18: a)  $Si^*$  as a function of  $\alpha_{sol}$  and  $\epsilon_{th}$ . b)  $T_{SST,max}$  as a function of  $\alpha_{sol}$  and  $\epsilon_{th}$  ( $C_x = 1000$ )

#### 4.3.3. Thermal efficiency and peak efficiency temperature

The thermal efficiency  $\eta_{thermal}$  (Eq.3.31-3.32) is calculated for reference STAC as a function of  $T_{abs}$  at  $C_x = 100$  (Figure 3.19.a) and  $C_x = 1000$  in (Figure 3.19.b), including Carnot efficiency  $\eta_{Carnot}$  (Eq.3.30) as an upper limit. This representation offers a global perspective for the comparison of STAC performance: the thermal efficiency curve increases steeply from 0% at 25 °C above ~50% at 100 °C, it reaches a maximum plateau and it then drops down to 0% at  $T_{SST,max}$ . The length of the plateau indicates the optimal operating temperature range for a given concentration factor  $C_x$ .

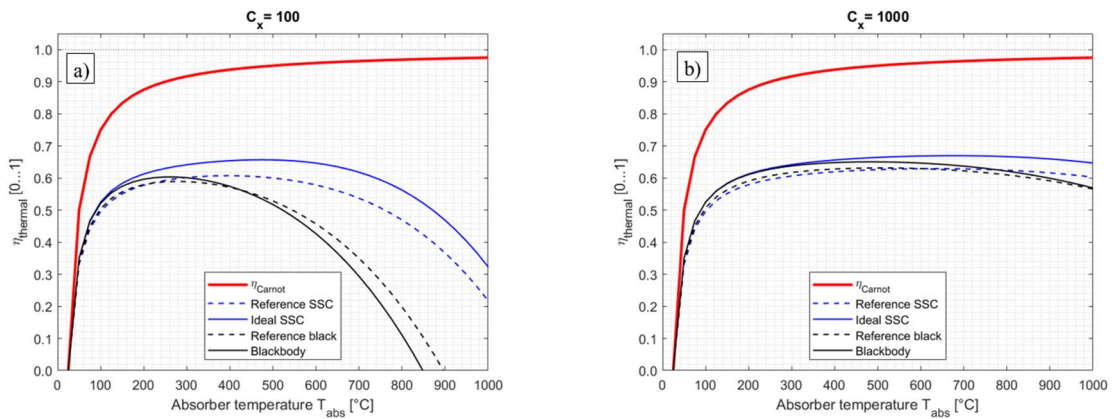


Figure 3.19: Thermal efficiency  $\eta_{thermal}$  for STAC with  $f_{carnot} = 70\%$  a)  $C_x = 100$  b)  $C_x = 1000$ .

In Figure 3.19, the ideal SSC reaches the maximal  $\eta_{thermal}$  value among STAC for any temperature. At  $C_x = 100$  (Figure 3.19.a), the ideal blackbody ranks second up to 300 °C, while the reference SSC and black coating are on par up to 300 °C. Above 300 °C, the reference SSC then ranks second, while black coatings drop in thermal efficiency  $\eta_{thermal}$  until they achieve  $T_{SST,max}$ . Both SSCs exhibit a wider plateau at maximal efficiency, from 300 °C to 600 °C for the ideal SSC

and from 250 °C to 450 °C for the real SSC. These temperature ranges are compatible with the PTC application. For this configuration, a selecting a SSC is thus more efficient than a black coating, as discussed previously in subsection 3.4.2.3.

At  $C_x= 1000$ , the ranking is different: the ideal blackbody (black line) ranks second up to 800 °C. The reference black coating (black dotted line) ranks third up to 600 °C. The reference SSC (blue dotted line) respectively surpasses the reference black coating at 600 °C and the ideal blackbody at 800 °C. A wide plateau is observed for the reference SSC and black coating, from 300 °C to 650 °C. As discussed in subsection 3.4.2.3, black coatings perform quite well in these conditions for a wide temperature range, compatible with the CRS application.

The peak efficiency temperature  $T_{peak,opt}$  (Eq.3.30) is plotted for all STAC in Figure 3.20 as a function of  $C_x$ . This plot confirms the observation that a SSC (blue lines) reach its optimal  $\eta_{thermal}$  value at a higher temperature than a black coating (black lines). The ranking is consistent with (Figure 3.16) for the FoM  $T_{SST,max}$ : the ideal SSC ranks first (blue line), the reference SSC second (blue dotted line), the reference black coating third (black dotted line) and the ideal blackbody fourth (black line) .A SSC thus allows operating efficiently at higher temperature level than a black coating, for any  $C_x$  value.

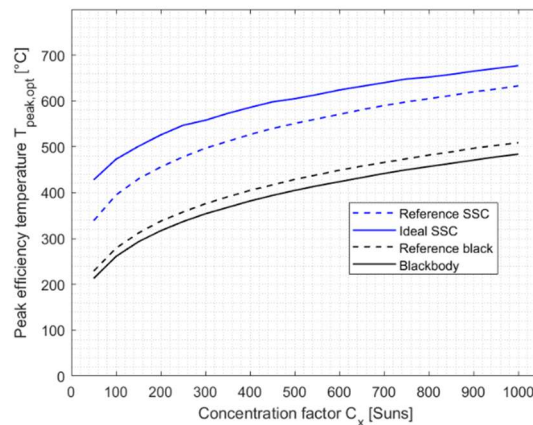


Figure 3.20: Peak efficiency temperature  $T_{peak,opt}$  as a function of  $C_x$  for reference STAC.

The current definition of  $\eta_{thermal}$  neglects the temperature drop across the STAC and metal substrate (Figure 3.2), as the heat transfer from the STAC to the HTF is not modelled in this chapter. Assuming a thin film SSC ( $<<1 \mu\text{m}$ ) with high thermal conductivity ( $\sim 10 \text{ W}\cdot\text{m}^{-1}\cdot\text{K}^{-1}$ ), the temperature drop across the STAC can be neglected ( $\Delta T << 1 \text{ K}$ ). However, for a sprayable ceramic black coating ( $\sim 40 \mu\text{m}$ ), and a low thermal conductivity of ( $\sim 1 \text{ W}\cdot\text{m}^{-1}\cdot\text{K}^{-1}$ ), the temperature drop across the STAC should not be negligible ( $\Delta T \sim 10 \text{ K}$ ) and the coating would then act as a Thermal Barrier Coating (TBC) [148]. The lack of experimental data for STAC thermal conductivity at operating temperature does not yet allow to correct this effect.

### 3.4.4 Summary and discussion

To summarise our comparative analysis of FoMs, references STAC (subsection 3.2.3) are evaluated and ranked in Table 3.7 for opto-thermal FoMs listed in Table 3.3 and analysed in this chapter.



The four reference coatings are divided into two subgroups, i.e. two black coatings on the one hand and two SSCs on the other hand. Black coatings respectively exhibit high  $\alpha_{sol}$  and  $\epsilon_{th}$  values ( $\alpha_{sol} > 95\%$ ,  $\epsilon_{th} > 80\%$ ), while SSC exhibit a high  $\alpha_{sol}$  and a low  $\epsilon_{th}$  values ( $\alpha_{sol} > 95\%$ ,  $\epsilon_{th} < 80\%$ ). Both reference FoMs are coupled, as there exists an overlap between solar and blackbody spectral irradiance (Figure 3.8). Compound FoMs allow a finer ranking of STAC based on their opto-thermal performance.

*Table 3.7: Comparison of reference STACs for different opto-thermal FoMs.*

Level	Figure of Merit (FoM)	Optimisation Target	Reference SSC	Ideal SSC	Reference black	Blackbody
1	$\alpha_{sol}$ (AM1.5d)	Max	94.6% (4 <sup>th</sup> )	100% (1 <sup>st</sup> )	96.6% (3 <sup>rd</sup> )	100% (1 <sup>st</sup> )
	$\epsilon_{th,calc}(T_{abs})$ (100 °C < $T_{abs}$ < 1000 °C)	Min	10 → 40% (2 <sup>nd</sup> )	0 → 30% (1 <sup>st</sup> )	77 → 83% (3 <sup>rd</sup> )	100% (4 <sup>th</sup> )
1	$f_{SSC}(\lambda)$	Min (RMSE)	Logistic model	Unit step function	N.A.	Constant
	$\lambda_{cut-off}$	≤ 2.5 μm	~2.4	2.5		→ + ∞
	$f_{shape}$	Max	~ 7	→ + ∞		→ 0
	Asymptote 1: $\rho_{low}$	Min	~ 0.018	0		→ 0
	Asymptote 2: $\rho_{high}$	Max	~ 0.972	1		→ 0
$S_i$ (100 °C < $T_{abs}$ < 1000 °C)	Max	10.9 → 2.5 (2 <sup>nd</sup> )	6.10 <sup>3</sup> → ~ 3 (1 <sup>st</sup> )	1.16 → 1.25 (3 <sup>rd</sup> )		1 (4 <sup>th</sup> )
2	$S_i^*$ (100 °C < $T_{abs}$ < 1000 °C)	Max	2.4 → 0.9 (2 <sup>nd</sup> )	8.7 → 1.15 (1 <sup>st</sup> )	0.15 → 0.23 (3 <sup>rd</sup> )	0 (4 <sup>th</sup> )
	$\dot{q}_{use}''$	Max	Dynamic ranking (Pareto fronts)			
	$\eta_{opt-th}$	Max	Ideal SSC always ranked first			
	$Z_{trade-off}$	[-]	Reference SSC more efficient for low values (<30) Reference black coating favored for high values (>30)			
	$T_{SST,max}$ (20 < $C_x$ < 1000)	Max	740 °C → 1915 °C	820 °C → 1920 °C	520 °C → 1760 °C	480 °C → 1720 °C
3	$SRI$ (20 < $C_x$ < 1000)	Min	-110 → -26 (2 <sup>nd</sup> )	-140 → -26 (1 <sup>st</sup> )	-13 → -2 (3 <sup>rd</sup> )	~ 4 (4 <sup>th</sup> )
	$SRI^*$ (20 < $C_x$ < 1000)	Min	10 → -0.3 (2 <sup>nd</sup> )	-0.75 → -0.1 (1 <sup>st</sup> )	39 → 10 (3 <sup>rd</sup> )	44 → 13 (4 <sup>th</sup> )
	$\eta_{thermal}$ (20 < $C_x$ < 1000)	Max	Dynamic ranking (Pareto fronts)			
	$T_{peak,opt}$ (20 < $C_x$ < 1000)	Max	2 <sup>nd</sup>	1 <sup>st</sup>	3 <sup>rd</sup>	4 <sup>th</sup>

Any SSC can be characterised in first approximation by a simple spectral model  $f_{SSC}(\lambda)$ , parameterised with a few spectral FoMs, i.e. a cut-off wavelength  $\lambda_{cut-off}$ , a shape factor  $f_{shape}$  and asymptotical reflectivity values  $\rho_{low}$  and  $\rho_{high}$ . This spectral model is however not suitable for black coatings. The goodness of fit of such spectral models thus allow discriminating between SSCs and black coatings.

Some FoMs allow a categorical discrimination of our reference STAC into two subgroups, i.e. black coating and SSC, while being applicable for any coating. These FoMs are namely the selective index  $S_i$ , the maximum steady-state temperature  $T_{SST,max}$  and the solar reflectance index  $SRI$  (Figure 3.18). These FoMs do not require a detailed knowledge of spectral features.

Two of these FoMs (Si and SRI) have been tentatively renormalised ( $Si^*$  and  $SRI^*$ ).  $Si^*$  is a logarithmic transformation of  $Si$ , to re-scale its range. Boundary conditions and reference coatings are updated for  $SRI^*$  to correct shortcomings of the  $SRI$ . Both  $SRI$  and  $SRI^*$  calculations rely on a theoretical FoM, i.e.  $T_{SST,max}$ . This later FoM typically exceeds the maximal operating temperature allowed for the STAC.

Other FoMs, i.e.  $\dot{q}_{use}''$ ,  $\eta_{opt-th}$ ,  $\eta_{thermal}$ , allow a dynamic ranking depending on the operating point  $\{C_x; T_{abs}\}$ . These FoMs are directly related to the STAC opto-thermal efficiency. The dynamic ranking among STAC is a function of the trade-off FoM, i.e.  $Z_{trade-off}$ . For these three FoMs, the ideal SSC always ranked first in the considered operating range [ $C_x$ : 20-1000;  $T_{abs}$ : 25 °C-1000 °C]. Different cases could be identified: i) for a "low"  $C_x$  and a "high"  $T_{abs}$ , the solar absorptance  $\alpha_{sol}$  is dominant over the thermal emittance  $\epsilon_{th}$ . It is thus preferable to maximise  $\alpha_{sol}$  (black coating) before minimising  $\epsilon_{th}$  (SSC); ii) for a "high"  $C_x$  and a "low"  $T_{abs}$ ,  $\alpha_{sol}$  has a lower weight and it thus clearly relevant to minimise  $\epsilon_{th}$ . and thus, select a SSC, for instance in PTC applications; iii) for intermediate operating ranges, a Pareto front could be identified, where both the reference black coating and SSC perform equally well. (Figure 3.13). The Pareto front for  $\dot{q}_{use}''$  and  $\eta_{opt-th}$  could be analysed from a spectral perspective (Figure 3.14), to better understand at which wavelength the ranking among STAC may evolve, before reaching an asymptotical value.

However, by definition,  $\dot{q}_{use}''$  and  $\eta_{opt-th}$  monotonously decrease at higher absorber temperature  $T_{abs}$ . This is not the case for  $\eta_{thermal}$ , which reach an optimum at the peak efficiency temperature  $T_{peak,opt}$  before dropping to zero at  $T_{SST,max}$  ( $T_{peak,opt} < T_{SST,max}$ ). The FoM  $\eta_{opt-th}$  offers a more realistic perspective of the system efficiency and the FoM  $T_{peak,opt}$  indicates the optimal temperature range for the STAC operation.

The FoM set analyzed in this chapter offer a complementarity perspective for ranking different STAC formulations, while the methodological framework is also applicable for solar selective reflective materials [141,142,149,150].

### 3.5 Conclusion and outlook

In this chapter, opto-thermal figures of merit relevant for the characterization of solar thermal absorber coatings were analysed and compared. These figures of merit were calculated on the basis of spectral measurements (0.25  $\mu\text{m}$  to 20  $\mu\text{m}$ ) made at room temperature for a near-normal angle of incidence. Reference solar thermal absorber coatings included two types of coatings, i.e. solar selective and black coatings. For each coating type, a reference coating and an ideal coating were analysed.

For the comparative analysis, a set of modelling assumptions were made for simplification, in particular a flat geometry, negligible angular effects, negligible convection and stable optical properties at operating temperature. The list of figures of merit includes two standard indicators, i.e. solar absorptance  $\alpha_{sol}$  and thermal emittance  $\epsilon_{th}$ , spectral parameters for a solar selective coating model ( $f_{SSC}(\lambda)$ ), i.e. cut-off wavelength ( $\lambda_{cut-off}$ ), shape factor ( $f_{shape}$ ) and reflectivity asymptotes ( $\rho_{low}$  and  $\rho_{high}$ ). Further existing compound figures of merit were analysed, i.e. Selectivity ratio Si, useful heat flux  $\dot{q}_{use}''$ , opto-thermal efficiency  $\eta_{opt-th}$ , Maximum steady-state temperature  $T_{SST,max}$ , Solar reflectance index SRI and thermal efficiency  $\eta_{thermal}$ . Additional figures of merit were introduced, i.e. a normalised selectivity ratio  $Si^*$  and solar

reflectance index  $SR/\lambda^*$ , a trade-off factor  $Z_{trade-off}$  and a peak efficiency temperature  $T_{peak,opt}$ . The interactions between all figures of merit were summarised in a synoptical diagram.

A first subset of figures of merit allows a finer characterization of selectivity, i.e. spectral model parameters  $\{\lambda_{cut-off}, f_{shape}, \rho_{low}$  and  $\rho_{high}\}$ , the selectivity ratio  $S_i$ , the maximum steady-state temperature  $T_{SST,max}$  and the solar reflectance index  $SR/\lambda$ . Both  $S_i$  and  $SR/\lambda$  figures of merit have been tentatively normalised ( $S_i^*$  and  $SR/\lambda^*$ ) for a better adaptation in the field of CSP. Their correlation to the absorber temperature  $T_{abs}$  and the maximum steady-state temperature  $T_{SST,max}$  has also been highlighted.

A second subset of figures of merit, i.e. useful heat flux  $q''_{use}$ , opto-thermal efficiency  $\eta_{opt-th}$  and thermal efficiency  $\eta_{thermal}$  allow a dynamic ranking of solar thermal absorber coatings, depending on the specific operating point  $\{C_x, T_{abs}\}$  and the corresponding trade-off factor  $Z_{trade-off}$  between solar absorptance  $\alpha_{sol}$  and thermal emittance  $\epsilon_{th}$ . The existence of a Pareto front between a reference black coating and a reference solar selective coating has been shown and a spectral evolution of cumulative opto-thermal efficiency has also been illustrated. At high concentration and low temperature, the influence of solar absorptance is dominant over thermal emittance, favoring black coatings for central receiver systems. Spectral selectivity is more important to achieve at lower concentration and higher temperature, for instance in parabolic trough applications.

The thermal efficiency  $\eta_{thermal}$  corrects a shortcoming of the opto-thermal efficiency  $\eta_{opt-th}$ , which decreases at higher temperature by definition, while a higher temperature is desired to maximise the thermal efficiency. Thermal efficiency  $\eta_{thermal}$  offers the most comprehensive perspective: it increases up to a plateau around the peak efficiency temperature  $T_{peak,opt}$  then it decreases until the maximum steady-state temperature  $T_{SST,max}$ . The figure of merit  $T_{peak,opt}$  is deemed more relevant as the figure of merit  $T_{SST,max}$  as  $T_{peak,opt}$  indicates the optimal operating temperature range of a solar thermal absorber coating, while  $T_{SST,max}$  typically exceeds the maximal operating temperature of such coatings.

Further research is conducted within the EU project SFERA-III to verify whether spectral properties measured at room temperature for oxidised substrates and black coatings are stable at higher temperature up to 800 °C, without compromising the coating durability. These measurements have on the one hand a potential impact on the calculation of  $\alpha_{sol}$  and  $\epsilon_{th}$  if any spectral shift is detected. On the other hand, potential spectral shifts at higher temperature may also affect infrared temperature measurements, requiring a new method for retrieving the effective band emissivity and calibrating in-situ the infrared thermography setup.

### 3.6 References: Chapter 3

- [1] M. Wiesenfarth et al., Current Status of Concentrator Photovoltaic (CPV) Technology, 2017, Version 1.3, available at: <https://www.ise.fraunhofer.de/content/dam/ise/de/documents/publications/studies/cpv-report-ise-nrel.pdf>. Accessed: 15/05/2021.
- [2] W.T. Xie et al., Concentrated solar energy applications using Fresnel lenses: a review, *Renewable and Sustainable Energy Reviews*, 15(6) (2011), 2588-2606, <https://doi.org/10.1016/j.rser.2011.03.031>

- [3] P. Sundarraj et al., Recent advances in thermoelectric materials and solar thermoelectric generators – a critical review, *RSC Advances*, 4 (2014), 46860-46874, <https://doi.org/10.1039/C4RA05322B>
- [4] D. Champier, Thermoelectric generators: A review of applications, *Energy Conversion and Management*, 140 (2017), 167-181. <https://doi.org/10.1016/j.enconman.2017.02.070>
- [5] D. Kraemer et al., Concentrating solar thermoelectric generators with peak efficiency of 7.4%, *Nature Energy*, 1 (2016), 16153. <https://doi.org/10.1038/nenergy.2016.153>
- [6] A. Fernandez-Garcia et al., Parabolic-trough solar collectors and their applications, *Renewable and Sustainable Energy Reviews*, 14(7) (2010), 1695-1721, <https://doi.org/10.1016/j.rser.2010.03.012>
- [7] G.K. Manikandan, S. Iniyan, R. Goic, Enhancing the optical and thermal efficiency of a parabolic trough collector – A review, *Applied Energy*, 235(1) (2019), 1524-1540. <https://doi.org/10.1016/j.apenergy.2018.11.048>
- [8] J. Frederiksson et al., A comparison and evaluation of innovative parabolic trough collector concepts for large-scale application, *Solar Energy*, 215(2021), 266-310. <https://doi.org/10.1016/j.solener.2020.12.017>
- [9] G. Zhu et al., History, Current State, and future of linear Fresnel concentrating solar collectors, *Solar Energy*, 103(2014), 69-652, <https://doi.org/10.1016/j.solener.2013.05.021>
- [10] G. Morin et al., Comparison of Linear Fresnel and Parabolic Trough Collector power plants, *Solar Energy*, 86(1) (2012), 1-12. <https://doi.org/10.1016/j.solener.2011.06.020>
- [11] C.K. Ho, B. D. Iverson, Review of high-temperature central receiver designs for concentrated solar power, *Renewable and Sustainable Energy Reviews*, 29 (2014), 835-846, <https://doi.org/10.1016/j.rser.2013.08.099>
- [12] C.K. Ho, Advances in central receivers for concentrating solar applications, *Solar Energy*, 152 (2017), 38-56. <https://doi.org/10.1016/j.solener.2017.03.048>
- [13] L. Li et al., Optics of solar central receiver systems: a review, *Optics Express*, 24(14) (2016), A985-A1007. <https://doi.org/10.1364/OE.24.00A985>
- [14] A.A. Rizvi et al., A review and classification of layouts and optimization techniques used in design of heliostat fields in solar central receiver systems, *Solar Energy*, 218 (2021), 296-311. <https://doi.org/10.1016/j.solener.2021.02.011>
- [15] J. Coventry, C. Andraka, Dish Systems for CSP, *Solar Energy*, 152 (2017), 140-170. <https://doi.org/10.1016/j.solener.2017.02.056>
- [16] M.E. Zayed et al., A comprehensive review on Dish/Stirling concentrated solar power systems: Design, optical and geometrical analyses, thermal performance assessment and applications, *Journal of Cleaner Production*, 283 (2021), 124664. <https://doi.org/10.1016/j.jclepro.2020.124664>
- [17] A.G. Imenes, D.R. Mills, Spectral beam splitting technology for increased conversion efficiency in solar concentrating systems: a review, *Solar Energy Materials and Solar Cells*, 84 (1-4) (2004), 19-69. <https://doi.org/10.1016/j.solmat.2004.01.038>
- [18] A. Mojiri et al., Spectral beam splitting for efficient conversion of solar energy – A review, *Renewable and Sustainable Energy Reviews*, 28 (2013), 654-663, <https://doi.org/10.1016/j.rser.2013.08.026>
- [19] H. Liang et al., Progress in full spectrum solar energy utilization by spectral beam splitting hybrid PV/T system, *Renewable and Sustainable Energy Reviews*, 141(2021), 119785. <https://doi.org/10.1016/j.rser.2021.110785>

- [20] A. Royne, C.J. Dey, R. Mills, Cooling of photovoltaic cells under concentrated illumination: a critical review, *Solar Energy Materials and Solar Cells*, 86(4) (2005), 451-483. <https://doi.org/10.1016/j.solmat.2004.09.003>
- [21] A. Hasan, J. Sawar, A.H. Shah, Concentrated photovoltaic: A review of thermal aspects, challenges and opportunities, *Renewable and Sustainable Energy Reviews*, 94 (2018), 835-852. <https://doi.org/10.1016/j.rser.2018.06.014>
- [22] J. Lilliestam, R. Pitz-Paal, Concentrating solar power for less than USD 0.07 per kWh : finally the breakthrough, *Renewable Energy Focus*, 26 (2018), 17-21, <https://doi.org/10.1016/j.ref.2018.06.002>
- [23] F. Schöninger et al., Making the sun shine at night: comparing the cost of dispatchable concentrating solar power and photovoltaics with storage, *Energy Sources, Part B: Economics, Planning, and Policy*, 16(1) (2021), 55-74, <https://doi.org/10.1080/15567249.2020.1843565>
- [24] R. Forristall, Heat transfer analysis and modelling of a parabolic trough solar receiver implemented in Engineering Equation Solver, 2003, *NREL Technical Report*, NREL/TP-550-34169, <https://doi.org/10.2172/15004820>.
- [25] S.A. Kalogirou, A detailed thermal model of a parabolic trough collector receiver, *Energy*, 48 (1) (2012), 298-306. <https://doi.org/10.1016/j.energy.2012.06.023>
- [26] R.W. Bradshaw et al., Final Test and Evaluation Results from the Solar Two Project, 2002, Sandia National Laboratories, *Technical Report SAND2002-0120*, <https://doi.org/10.2172/793226>.
- [27] R.Z. Litwin, J.E. Pacheco, Receiver System: Lessons Learned from Solar Two, 2002, Sandia National Laboratories, *Technical Report SAND2002-0084*, <https://doi.org/10.2172/800776>
- [28] C.E. Kennedy, Review of Mid- to High-Temperature Solar Selective Absorber Materials, 2002, *NREL Technical Report*, NREL/TP-520-31267, <https://doi.org/10.2172/15000706>
- [29] K. Xu et al., A review of high-temperature selective absorber coatings for solar thermal applications, *Journal of Materiomics*, 6(1) (2020), 167-182, <https://doi.org/10.1016/j.jmat.2019.12.012>
- [30] C.K. Ho et al., Characterization of Pyromark 2500 Paint for High-Temperature Solar Receivers, *Journal of Solar Energy Engineering*, 136(1) (2014), 014502. <https://doi.org/10.1115/1.4024031>
- [31] J. Coventry, P. Burge, Optical properties of Pyromark 2500 coatings of variable thicknesses on a range of materials for concentrating solar thermal applications, *AIP Conference Proceedings*, 1850 (2017), 030012. <https://doi.org/10.1063/1.4984355>
- [32] A. Ambrosini et al., Influence of application parameters on stability of Pyromark® 2500 receiver coatings, *AIP Conference Proceedings*, 2126 (2019) 030002. . <https://doi.org/10.1063/1.5117514>
- [33] H. Benoit et al., Review of heat transfer fluids in tube-receivers in concentrating solar thermal systems: Properties and heat transfer coefficients, *Renewable and Sustainable Energy Reviews*, 55 (2016), 298-315, <https://doi.org/10.1016/j.rser.2015.10.059>
- [34] N. Lorenzin, A. Abanades, A review on the application of liquid metals as heat transfer fluid in Concentrated Solar Power technologies, *International Journal of Hydrogen Energy*, 41(17) (2016), 6990-6995, <https://doi.org/10.1016/j.ijhydene.2016.01.030>
- [35] K. Zhang et al., A review on thermal stability and high temperature induced ageing mechanisms of solar absorber coatings, *Renewable and Sustainable Energy Reviews*, 67 (2017), 1282-1299, <https://doi.org/10.1016/j.rser.2016.09.083>

- [36] A. Boubault et al., Durability of solar absorber coatings and their cost-effectiveness, *Solar Energy Materials and Solar Cells*, 166 (2017), 176-184. <https://doi.org/10.1016/j.solmat.2017.03.010>
- [37] L. Noč et al., High-solar-absorptance CSP coating characterization and reliability testing with isothermal cyclic loads for service-life prediction, *Energy & Environmental Science*, 12 (2019), 1679-1694, <https://doi.org/10.1039/C8EE03536A>
- [38] C.K. Ho, J.E. Pacheco, Levelized Cost of Coating (LCOC) for selective absorber materials, *Solar Energy*, 108 (2014), 315-321. <https://doi.org/10.1016/j.solener.2014.05.017>
- [39] A. Boubault et al., Levelized cost of energy (LCOE) metric to characterize solar absorber coatings for the CSP industry, *Renewable Energy*, 85(2016), 472-483, <https://doi.org/10.1016/j.renene.2015.06.059>
- [40] L. Moens, D.M. Blake, Advanced heat transfer and thermal storage fluids, *Proceedings of the ASME 2005 International Solar Energy Conference*, ISEC2005-76192, (2005), 791-793. <https://doi.org/10.1115/ISEC2005-76192>
- [41] L. Moens, D.M. Blake, Mechanisms of hydrogen formation in solar parabolic trough receivers, *Journal of Solar Energy Engineering*, 132 (3) 2010, :0410006. <https://doi.org/10.1115/1.4001402>
- [42] C. Jung et al., Technological perspectives of silicon heat transfer fluids for Concentrated Solar Power, *Energy Procedia*, 69 (2015) 663-671. <https://doi.org/10.1016/j.egypro.2015.03.076>
- [43] C. Jung, M. Senholdt, Comparative study on hydrogen issues of Biphenyl/Diphenyl oxide and polydimethylsiloxane heat transfer fluids, *AIP Conference Proceedings*, 2303 (2020),150009. <https://doi.org/10.1063/5.0028894>
- [44] A. Bonk et al., Advanced heat transfer fluids for direct molten salt line-focusing CSP plants, *Progress in Energy and Combustion Science*, 67 (2018), 69-87. <https://doi.org/10.1016/j.pecs.2018.02.002>
- [45] A. Bonk et al., Solar Salt – Pushing an old material for energy storage to a new limit, *Applied Energy*, 262(15) (2020), 114535. <https://doi.org/10.1016/j.apenergy.2020.114535>
- [46] G. Zhu, C. Libby, Review and future perspective of central receiver design and performance, *AIP Conference Proceedings*, 1850 (2017), 030052. <https://doi.org/10.1063/1.4984395>
- [47] C. Prieto et al., Carbonate molten salt solar thermal pilot facility: Plant design, commissioning and operation up to 700 °C, *Renewable Energy*, 151 (2020), 528-541. <https://doi.org/10.1016/j.renene.2019.11.045>
- [48] W. Ding W., T. Bauer, Progress in Research and Development of Molten Chloride Salt Technology for Next Generation Concentrated Solar Power Plants, *Engineering*, 7(3) (2021),334-347. <https://doi.org/10.1016/j.eng.2020.06.027>
- [49] J. Coventry et al., A review of sodium receiver technologies for central receiver solar power plants, *Solar Energy*, 122 (2015), 749-762. <https://doi.org/10.1016/j.solener.2015.09.023>
- [50] A. Fritsch, C. Frantz, R. Uhlig, Techno-economic analysis of solar thermal power plants using liquid sodium as heat transfer fluid, *Solar Energy*, 177 (2019),155-162. <https://doi.org/10.1016/j.solener.2018.10.005>
- [51] A. Calderon et al., Review of solid particle materials for heat transfer fluid and thermal energy storage in solar thermal power plants, *Energy Storage*, 1(4) (2019), 1-20. <https://doi.org/10.1002/est2.63>

- [52] T. Galiullin et al., High temperature oxidation and erosion of candidates materials for particle receivers of concentrated solar power tower systems, *Solar Energy*, 188 (2019), 883-889. <https://doi.org/10.1016/j.solener.2019.06.057>
- [53] B. Gobereit et al., Assessment and improvement of optical properties of particles for solid particle receiver, *Solar Energy*, 199 (2020), 844-851. <https://doi.org/10.1016/j.solener.2020.02.076>
- [54] A. Gimeno-Furio et al., New coloured coatings to enhance silica sand absorbance for direct particle solar receiver applications, *Renewable Energy*, 152 (2020),1-8. <https://doi.org/10.1016/j.renene.2020.01.053>
- [55] W. Zhao, Z. Sun, Z.T. Alwahabi, Emissivity and absorption function measurements of Al<sub>2</sub>O<sub>3</sub> and SiC particles at elevated temperature for the utilization in concentrated solar receivers, *Solar Energy*, 207 (2020), 83-191. <https://doi.org/10.1016/j.solener.2020.06.079>
- [56] J.L. Navarro Hermoso et al., Parabolic trough solar receiver characterization using specific test bench for transmittance, absorptance and heat loss simultaneous measurement, *Solar Energy*, 136 (2016), 268-277, <https://doi.org/10.1016/j.solener.2016.07.012>
- [57] G. Espinosa-Rueda et al., Vacuum evaluation of parabolic trough receiver tubes in a 50 MW concentrated solar power plant, *Solar Energy*, 139 (2016), 36-46, <https://doi.org/10.1016/j.solener.2016.09.017>
- [58] O. Raccurt et al., In air durability study of solar selective coating for parabolic trough technology, *AIP Conference Proceedings*, 1850 (2017), 130010, <https://doi.org/10.1063/1.4984504>
- [59] M. Röger et al., Techno-economic analysis of receiver replacement scenarios in a parabolic trough field, *AIP Conference Proceedings*, 1734 (2016), 040030. <https://doi.org/10.1063/1.4949082>
- [60] T. Zoschke et al., Techno-economic assessment of new material developments in central receiver solar power plants, *AIP Conference Proceedings*, 2126 (2019), 030068. <https://doi.org/10.1063/1.5117580>
- [61] K. Tsuda et al., Development of high absorption, high durability coatings for solar receivers in CSP plants, *AIP Conference Proceedings*, 2033 (2018), 040039. <https://doi.org/10.1063/1.5067075>
- [62] R. Harzallah et al., Development of high performances solar absorber coatings, *AIP Conference Proceedings*, 2126 (2019), 030026. <https://doi.org/10.1063/1.5117538>
- [63] I. Jerman et al., High-temperature "ion baseball" for enhancing concentrated solar power efficiency, *Solar Energy Materials and Solar Cells*, 200 (2019), 109974. <https://doi.org/10.1016/j.solmat.2019.109974>
- [64] N. Selvakumar, H.C. Barshilia, Review of physical vapor deposited (PVD) spectrally selective coatings for mid- and high- temperature solar thermal applications, *Solar Energy Materials and Solar Cells*, 98 (2012), 1-23. <https://doi.org/10.1016/j.solmat.2011.10.028>
- [65] M. Joly et al., Novel black selective coating for tubular solar absorbers based on a sol-gel method, *Solar Energy*, 94 (2013), 233-239. <https://doi.org/10.1016/j.solener.2013.05.009>
- [66] F. Cao et al., A review of cermet-based spectrally selective solar absorbers, *Energy & Environmental Science*, 7 (2014), 1615-1627. <https://doi.org/10.1039/C3EE43825B>

- [67] C. Hildebrandt, High-temperature stable absorber coatings for linear concentrating solar thermal power plants, *PhD thesis*, Stuttgart University, 2009. <http://dx.doi.org/10.18419/opus-1802>
- [68] I. Heras Pérez, Multilayer solar selective coatings for high temperature solar applications: from concept to design, *PhD thesis*, Sevilla University, 2016, available at: <http://hdl.handle.net/11441/47789>. Accessed: 15/05/2021.
- [69] H. Price et al., Field Survey of Parabolic Trough Receiver Thermal Performance, *ASME 2006 International Solar Energy Conference Proceedings*, ISEC 2006-99167 (2006), 109-116. <https://doi.org/10.1115/ISEC2006-99167>
- [70] X. Olano et al., Outcomes and features of the inspection of receiver tubes (ITR) system for improved O&M in parabolic trough plants, *AIP Conference Proceedings*, 2033 (2018), 030011. <https://doi.org/10.1063/1.5067027>
- [71] E. Setien, R. Lopez-Martin, L. Valenzuela, Methodology for partial vacuum pressure and heat losses analysis of parabolic troughs receivers by infrared radiometry, *Infrared Physics & Technology*, 98 (2019), 341-353. <https://doi.org/10.1016/j.infrared.2019.02.011>
- [72] L.L. Vant-Hull, The Role of "Allowable Flux Density" in the Design and Operation of Molten-Salt Solar Central Receivers, *Journal of Solar Energy Engineering*, 124(2) (2002), 165-169. <https://doi.org/10.1115/1.1464124>
- [73] Z. Liao et al., Allowable flux density on a solar central receiver, *Renewable Energy*, 62 (2014), 747-753. <https://doi.org/10.1016/j.renene.2013.08.044>
- [74] R. Flesch et al., Towards an optimal aiming for molten salt power towers, *Solar Energy*, 155 (2017), 1273-1281. <https://doi.org/10.1016/j.solener.2017.07.067>
- [75] A. Sanchez-Gonzalez, M.R. Rodriguez-Sanchez, D. Santana, Aiming strategy model based on allowable flux densities for molten salt central receivers, *Solar Energy*, 157 (2017), 1130-1144. <https://doi.org/10.1016/j.solener.2015.12.055>
- [76] A. Sanchez-Gonzalez, M.R. Rodriguez-Sanchez, D. Santana, Allowable solar flux densities for molten-salt receivers: Input to the aiming strategy, *Results in Engineering*, 5 (2020) 100074. <https://doi.org/10.1016/j.rineng.2019.100074>
- [77] A. Eitan et al., Accurate flux calculations using thermographic IR cameras in concentrated solar power fields, *Quantitative InfraRed Thermography (QIRT) International Conference Proceedings*, (2014). <http://dx.doi.org/10.21611/qirt.2014.220>
- [78] InfraTec GmbH, Industrial Automation; Thermographic Monitoring of Solar Power Tower - SPTC, available at: <https://www.infratec.eu/thermography/industrial-automation/solar-power-tower-check-sptc/>. Accessed:15/05/2021.
- [79] D. Hernandez et al., Analysis and Experimental Results of Solar-Blind Temperature Measurements in Solar Furnaces, *Journal of Solar Energy Engineering*, 126(1) (2004), 645-653. <https://doi.org/10.1115/1.1636191>
- [80] Marquesado Solar, Andasol 3 solar thermal power plant, available at: <https://marquesadosolar.com/foto/solar-field/>. Accessed: 15/05/2021.
- [81] SENER, Gemasolar solar thermal power plant, available at: <https://www.energy.sener/projects/gemasolar>. Accessed: 15/05/2021.
- [82] Marquesado Solar, Andasol 3 solar thermal power plant, available at: <https://marquesadosolar.com/plant-andasol-3/>. Accessed: 15/05/2021.
- [83] International Organization for Standardization, Solar energy – Collector components and materials – Part3: Absorber surface durability ISO 22975-3:2014, (2014), available at: <https://www.iso.org/standard/61758.html>. Accessed: 15/05/2021.



- [84] International Organization for Standardization, Space systems – Thermal control coatings for spacecraft – General requirements, ISO 16691:2014, (2014), available at: <https://www.iso.org/standard/57440.html>. Accessed: 15/05/2021.
- [85] International Organization for Standardization, Space systems – Measurement of thermo-optical properties of thermal control materials, ISO 16378:2013, (2013), available at: <https://www.iso.org/standard/56558.html>. Accessed: 15/05/2021.
- [86] ASTM International, Standard test method for solar absorptance, reflectance, and transmittance of materials using integrating spheres, ASTM E903:2020, (2020). <https://dx.doi.org/10.1520/E0903-20>
- [87] ASTM International, Standard test method for determination of solar reflectance near ambient temperature using a portable solar reflectometer, ASTM C1549:2016, (2016). <https://doi.org/10.1520/C1549-16>.
- [88] ASTM International, Standard test method for determination of emittance of materials near room temperature using portable emissometers, ASTM C1371:2015, (2015). <https://doi.org/10.1520/C1371-15>.
- [89] ASTM International, Standard test methods for total normal emittance of surfaces using inspection-meter techniques, ASTM E408:2013, (2019). <https://doi.org/10.1520/E0408-13R19>
- [90] ASTM International, Standard test method for normal spectral emittance at elevated temperatures, ASTM E307:1972 (2019). <https://dx.doi.org/10.1520/E0307-72R19>
- [91] ASTM International, Standard test method for total hemispherical emittance of surfaces up to 1400 °C, ASTM C835:2006 (2020). <https://dx.doi.org/10.1520/C0835-06R20>
- [92] ASTM International, Standard test method for calorimetric determination of hemispherical emittance and the ratio of solar absorptance to hemispherical emittance using solar simulation, ASTM E434:2010, (2020). <https://dx.doi.org/10.1520/E0434-10R20>
- [93] L. Cindrella, The real utility ranges of the solar selective coatings, *Solar Energy Materials and Solar Cells*, 91 (20) (2007), 1898-1901. <https://doi.org/10.1016/j.solmat.2007.07.006>
- [94] K. Burlafinger, A. Vetter, C.J. Brabec, Maximizing concentrated solar power (CSP) plant overall efficiencies by using spectral selective absorbers at optimal operation temperatures, *Solar Energy*, 120 (2015), 428-438. <https://doi.org/10.1016/j.solener.2015.07.023>
- [95] M. Wirz et al., Potential improvements in the optical and thermal efficiencies of parabolic trough concentrators, *Solar Energy*, 107 (2014), 398-414. <https://doi.org/10.1016/j.solener.2014.05.002>
- [96] J.A. Duffie, W.A. Beckman, *Solar engineering of thermal processes*, Fourth Edition, Wiley and Sons, 2013. <https://doi.org/10.1002/9781118671603>
- [97] K. Lovegrove, W. Stein, *Concentrating Solar Power Technology: Principles, Developments and Applications*, Second Edition, Woodhead Publishing, 2020. <https://doi.org/10.1016/C2018-0-04978-6>.
- [98] S. Caron et al., Forty shades of black: A benchmark of high temperature sprayable black coatings applied on Haynes 230, *AIP Conference Proceedings*, 2303 (2020), 1560007. <https://doi.org/10.1063/5.0028773>
- [99] ASTM International, Standard practice for exposure of solar collector cover materials to natural weathering under conditions simulating stagnation mode, ASTM E881: 1992, (2015). <https://doi.org/10.1520/E881-02R15>

- [100] ASTM International, Standard practice for calculating solar reflectance index of horizontal and low-sloped opaque surfaces, ASTM E1980:2011, (2019). <https://www.astm.org/e1980-11r19.html>
- [101] A. Muscio, The solar reflectance index as a tool to forecast the heat released to the urban environment: potentiality and assessment issues, *Climate*, 6(1) (2018), 12. <https://doi.org/10.3390/cli6010012>
- [102] J. Ballestrin, A. Marzo, Solar radiation attenuation in solar tower plants, *Solar Energy*, 86(1) (2012), 388-392. <https://doi.org/10.1016/j.solener.2011.10.010>
- [103] N. Hanrieder et al., Atmospheric extinction in solar tower plants – A review, *Solar Energy*, 152 (2017), 193-207. <https://doi.org/10.1016/j.solener.2017.01.013>
- [104] A. Marzo et al., Solar extinction map in Chile for applications in solar power tower plants, comparison with other places from sunbelt and impact on LCOE, *Renewable Energy*, 170 (2021), 197-211. <https://doi.org/10.1016/j.renene.2021.01.126>
- [105] F. Sutter et al., Spectral characterization of specular reflectance of solar mirrors, *Solar Energy Materials and Solar Cells*, 145(3) (2016), 248-254. <https://doi.org/10.1016/j.solmat.2015.10.030>
- [106] A. Garcia-Segura et al., Durability studies of solar reflectors: A review, *Renewable and Sustainable Energy Reviews*, 62 (2016), 453-467. <https://doi.org/10.1016/j.rser.2015.01.015>
- [107] A. Garcia-Segura et al., Degradation types of reflector materials used in concentrating solar thermal systems, *Renewable and Sustainable Energy Reviews*, 143(2021), 110879. <https://doi.org/10.1016/j.rser.2021.110879>
- [108] F. Sutter et al., The effect of incidence angle on the reflectance of solar mirrors, *Solar Energy Materials and Solar Cells*, 176 (2018), 119-133. <https://doi.org/10.1016/j.solmat.2017.11.029>
- [109] T.W. Paret et al., Incidence angle on cylindrical receivers of solar power towers, *Solar Energy*, 201 (2020), 1-7. <https://doi.org/10.1016/j.solener.2020.02.077>
- [110] J. Kim, J.S. Kim, W. Stein, Simplified heat loss model for central tower solar receiver, *Solar Energy*, 116 (2015), 314-322. <https://doi.org/10.1016/j.solener.2015.02.022>
- [111] D. Hernandez, J.L. Sans, M. Pfänder, Pyroreflectometry to determine the true temperature and optical properties of surfaces, *Journal of Solar Energy Engineering*, 130(3) (2008), 0310003. <https://doi.org/10.1115/1.2840575>
- [112] M. Bitterling et al., Physical models of the bidirectional reflectance of solar receiver coatings, *Solar Energy*, 209 (2020), 653-661. <https://doi.org/10.1016/j.solener.2020.08.054>
- [113] J.D. Macia et al., Optical and thermal properties of selective absorber coatings under CSP conditions, *AIP Conference Proceedings*, 1850 (2017) 120001. <https://doi.org/10.1063/1.4984492>
- [114] OMT Solution BV, World Class Innovative Solutions for Optical Materials Characterization (2021), available at: <https://omtsolutions.com/>. Accessed 15/05/2021.
- [115] Labsphere Inc., Technical Guide: Reflectance materials and coatings, (2021), available at: <https://www.labsphere.com/site/assets/files/2553/a-guide-to-reflectance-materials-and-coatings.pdf> Accessed 15/05/2021.
- [116] S. Caron et al., Accelerated ageing of solar receiver coatings: Experimental results for T91 and VM12 steel substrates, *AIP Conference Proceedings*, 2033 (2018), 230002. <https://doi.org/10.1063/1.5067230>

- [117] S. Caron et al., Durability testing of solar receiver coatings: Experimental results for T91 and VM12 steel substrates, *AIP Conference Proceedings*, 2303 (2020), 150006. <https://doi.org/10.1063/5.0028772>
- [118] L. del Campo et al., New experimental device for infrared spectral directional emissivity measurements in a controlled environment, *Review of Scientific Instruments*, 77 (2006), 113111. <https://doi.org/10.1063/1.2393157>
- [119] P. Honnerova et al. New experimental device for high-temperature normal spectral emissivity measurement of coatings, *Measurement Science and Technology*, 25(9) (2014), 095501. <https://doi.org/10.1088/0957-0233/25/9/095501>
- [120] I. Setien-Fernandez et al., First spectral emissivity study of a solar selective coating in the 150-600 °C temperature range, *Solar Energy Materials and Solar Cells*, 117 (2013), 390-395. <https://doi.org/10.1016/j.solmat.2013.07.002>
- [121] T. Echaniz et al., Importance of the spectral emissivity measurements at working temperature to determine the efficiency of a solar selective coating, *Solar Energy Materials and Solar Cells*, 140 (2015), 249-252. <https://doi.org/10.1016/j.solmat.2015.04.009>
- [122] I. Gonzalez de Arrieta et al., Infrared emissivity of copper-alloyed spinel black coatings for concentrated solar power systems, *Solar Energy Materials and Solar Cells*, 200 (2019), 109961. <https://doi.org/10.1016/j.solmat.2019.109961>
- [123] E. Le Baron et al., Round Robin Test for the comparison of spectral emittance measurement apparatuses, *Solar Energy Materials and Solar Cells*, 191(2019), 476-485. <https://doi.org/10.1016/j.solmat.2018.11.026>
- [124] ASTM International, Standard Tables for Reference Solar Spectral Irradiances: Direct Normal and Hemispherical on 37° Tilted Surface, ASTM G173:2003, (2020). <https://www.astm.org/g0173-03r20.html>
- [125] NREL, SMARTS: Simple Model of the Atmospheric Radiative Transfer of Sunshine, available at: <https://www.nrel.gov/grid/solar-resource/smarts.html>  
Accessed: 15/05/2021.
- [126] C.A: Gueymard, Parameterized transmittance model for direct beam and circumsolar spectral irradiance, *Solar Energy*, 71(5)(2001), 325-346. [https://doi.org/10.1016/S0038-092X\(01\)00054-8](https://doi.org/10.1016/S0038-092X(01)00054-8)
- [127] C.A. Gueymard, D. Myers, K. Emery, Proposed reference irradiance spectra for solar energy system testing, *Solar Energy*, 73(6) (2002), 443-467. [https://doi.org/10.1016/S0038-092X\(03\)00005-7](https://doi.org/10.1016/S0038-092X(03)00005-7)
- [128] W. Jessen et al., Proposal and evaluation of subordinate standard solar irradiance spectra for application in solar energy systems, *Solar Energy*, 168 (2018), 30-43. <https://doi.org/10.1016/j.solener.2018.03.043>
- [129] C.A. Gueymard, The sun's total and spectral irradiance for solar energy applications and solar radiation models, *Solar Energy*, 76(4) (2004), 423-453. <https://doi.org/10.1016/j.solener.2003.08.039>
- [130] C.A. Gueymard, Revised composite extraterrestrial spectrum based on recent solar irradiance observations, *Solar Energy*, 169 (2018), 434-440. <https://doi.org/10.1016/j.solener.2018.04.067>
- [131] Optosol GmbH, Absorber control, available at: <http://optosol.com/absorber-control/>.  
Accessed: 15/05/2021.
- [132] Surface Optics, 410-Vis-IR Portable Emissometer & Solar Reflectometer, available at: <https://surfaceoptics.com/products/reflectometers-emissometers/410-vis-ir/>.  
Accessed: 15/05/2021.

- [133] AZ Technology, Reflectometers and Emissometers, available at: <http://www.aztechnology.com/products/reflectometers-and-emissometers.html>. Accessed:15/05/2021.
- [134] Devices and Services Company, Emissometer Model AE1 and RD1 Voltmeter, available at: <https://www.devicesandservices.com/AE1%20RD1%20Spec%20Sheet.pdf>. Accessed: 15/05/2021.
- [135] M.F. Modest, *Radiative Heat Transfer*, Third Edition, Elsevier, 2013. <https://doi.org/10.1016/C2010-0-65874-3>
- [136] J.R. Howell et al., *Thermal Radiation Heat Transfer*, Seventh Edition, CRC Press, Taylor and Francis Group, 2021. ISBN 9780367347079.
- [137] M. Santamouris et al., On the impact of urban heat island and global warming on the power demand and electricity consumption in buildings – A review, *Energy and Buildings*, 98 (2015), 119-124. <https://doi.org/10.1016/j.enbuild.2014.09.052>
- [138] M. Santamouris, F. Fiorito, On the impact of the modified urban albedo on ambient temperature and heat related mortality, *Solar Energy*, 216 (2021), 495-507. <https://doi.org/10.1016/j.solener.2021.01.031>
- [139] A.B. Besir, E. Cuce, Green roofs and facades: A comprehensive review, *Renewable and Sustainable Energy Reviews*, 82(1) (2018), 915-939. <https://doi.org/10.1016/j.rser.2017.09.106>
- [140] C. Wang et al., Cool pavements for urban heat island mitigation: A synthetic review, *Renewable and Sustainable Energy Reviews*, 146 (2021), 11171. <https://doi.org/10.1016/j.rser.2021.111171>
- [141] A.S. Farooq et al., Emerging radiative materials and prospective applications of radiative sky cooling – A review, *Renewable and Sustainable Energy Reviews*, 2021; 144:110910. <https://doi.org/10.1016/j.rser.2021.110910>
- [142] A. Libbra et al., Assessment and improvement of the performance of antisolar coatings and surfaces, *Progress in Organic Coatings*, 72(1-2) (2011), 73-80. <https://doi.org/10.1016/j.porgcoat.2011.02.019>
- [143] J. Lehman et al., Carbon nanotube-based black coatings, *Applied Physics Reviews*, 5 (2018), 011103. <https://doi.org/10.1063/1.5009190>
- [144] Acktar Advanced Coatings, World leader in black coatings, available at: <https://acktar.com/>. Accessed: 15/05/2021.
- [145] Surrey Nanosystems, Vantablack Coating Technology, available at: <https://www.surreynanosystems.com/>. Accessed: 15/05/2021.
- [146] M.R. Dury et al., Common black coatings – reflectance and ageing characteristics in the 0.32 – 14.3  $\mu\text{m}$  wavelength range, *Optics Communications*, 270(2) (2007), 262-272. <https://doi.org/10.1016/j.optcom.2006.08.038>
- [147] L. Jian et al., Oxidation kinetics of Haynes 230 alloy in air at temperatures between 650 and 850  $^{\circ}\text{C}$ , *Journal of Power Sources*, 159(1) (2006), 641-645. <https://doi.org/10.1016/j.jpowsour.2005.09.065>
- [148] J.G. Thakare et al., Thermal Barrier Coatings – A state of the art review, *Metals and Materials International*, 27 (2021), 1947-1968. <https://doi.org/10.1007/s12540-020-00705-w>
- [149] J. Garrido et al., Experimental and numerical performance analyses of Dish-Stirling cavity receivers: Radiative property study and design, *Energy*, 169 (2019), 478-488. <https://doi.org/10.1016/j.energy.2018.12.033>
- [150] W. Wang et al., Solar selective reflector materials: Another option for enhancing the efficiency of the high-temperature solar receivers/reactors, *Solar Energy Materials and Solar Cells*, 224 (2021),110995. <https://doi.org/10.1016/j.solmat.2021.110995>

## **Chapter 4. Laboratory intercomparison of solar absorptance and thermal emittance measurements at room temperature**



## 4 Laboratory intercomparison of solar absorptance and thermal emittance measurements at room temperature

### 4.0 Abstract

Solar thermal absorber coatings play an important role in the opto-thermal efficiency of receivers in Concentrated Solar Power (CSP). Two standard figures of merit are the solar absorptance  $\alpha_{sol}$  and thermal emittance  $\varepsilon_{th}$ , derived from spectral directional hemispherical reflectivity measurements at room temperature. These two figures of merit allow comparing coating formulations in terms of performance and durability.

In this chapter, a black coating and a solar selective coating are optically characterised by different laboratories to compare spectral datasets, solar absorptance  $\alpha_{sol}$  and thermal emittance  $\varepsilon_{th}$  calculations. The comparison includes various benchtop spectrophotometers operating in the UV-VIS-NIR and Infrared spectral ranges as well as three commercial portable reflectometers/emissometers.

A good agreement is found between the nine parties participating in this intercomparison campaign. The black coating  $\alpha_{sol}$  value is  $96.6 \pm 0.2\%$ , while the solar selective coating  $\alpha_{sol}$  value is  $94.5 \pm 0.4\%$ . For the thermal emittance, spectral data is concatenated and integrated from  $0.3 \mu\text{m}$  to  $16 \mu\text{m}$ . The black coating  $\varepsilon_{th}$  value calculated at  $650 \text{ }^\circ\text{C}$  is  $80.8 \pm 3.8\%$ , while the solar selective coating  $\varepsilon_{th}$  value calculated at  $650 \text{ }^\circ\text{C}$  is  $25.0 \pm 0.5\%$ .

### 4.1 Introduction

Concentrated Solar Power (CSP) technologies coupled to thermal storage can provide fossil-free electricity, process heat or synthetic fuels around the clock at a competitive price, especially in sunniest regions of the world [1-4]. CSP technologies use a mirror field to concentrate Direct Normal Irradiance (DNI) on a thermal receiver. A Heat Transfer Fluid (HTF) absorbs the heat and transports it to a thermodynamic process. Four types of mirror field configurations are typically identified for CSP technologies, i.e. parabolic troughs [5,6], solar towers, also known as Central Receiver Systems (CRS) [7,8], Linear Fresnel [9] and Dish systems [10].

One key component for any CSP technology is the thermal receiver. Tubular receiver designs are most common among commercial plants. Parabolic trough and Linear Fresnel receivers consist of an absorber tube inserted in an evacuated glass envelope, while solar towers use external tubular bundle heat exchanger designs, with several parallel absorber tubes assembled in panels. The absorber tube is made of a metal substrate, for instance stainless steel or a nickel-based alloy, on which a Solar Thermal Absorber Coating (STAC) is applied. The typical absorber operating temperature ranges from  $300 \text{ }^\circ\text{C}$  to  $600 \text{ }^\circ\text{C}$  for parabolic troughs and solar towers using molten salt as a HTF [11,12]. For solar towers, allowable flux density constraints (AFD) have to be considered to avoid molten salt freezing below  $300 \text{ }^\circ\text{C}$  or severe corrosion above  $600 \text{ }^\circ\text{C}$  [13,14].

The STAC opto-thermal performance is characterised by two key figures of merit [15], i.e. solar absorptance  $\alpha_{sol}$  and thermal emittance  $\varepsilon_{th}$ , both measurable according to international standards [16-23]. High Solar Absorptance (HSA) coatings [24-27] maximise primarily the  $\alpha_{sol}$  parameter, while Solar Selective Coatings (SSC) [28-31] also minimise the  $\varepsilon_{th}$  parameter. The

selection of an absorber coating formulation depends on the optimization of the coating opto-thermal efficiency [32,33], considering coating durability [24-25,34-38] in order to minimise the levelised cost of coating (LCOC) [38,39].

New STAC formulations have been developed within the EU project Raisalife [41] and their durability has been tested [42-44]. In this chapter, we compare  $\alpha_{sol}$  and  $\epsilon_{th}$  measurements made at room temperature in different laboratories. On the one hand, both measurements are important to compare new coating formulations in pristine state. On the other hand, these measurements are also relevant to measure deviations with respect to the pristine state and thus track any optical coating degradation that may occur during durability test campaigns. Measurements at operating temperature have been discussed previously in the literature [45-50] for similar coatings and are here first considered out of scope for this laboratory inter-comparison, but investigated in the next chapter.

The laboratory intercomparison includes both benchtop spectrophotometers and a few commercial portable devices. While spectrophotometers provide a fine spectral resolution, Fourier Transform Infrared (FTIR) spectrophotometers typically require a cryogenic cooling of the detector. Meanwhile, portable devices have a limited spectral resolution, but allow performing a coating inspection on site. The intercomparison is here outlined for two reference STAC, i.e. one HSA coating and one SSC, which have been exchanged between laboratories.

The measurement protocol is first explained, describing the instrumentation set for optical measurements, the set of reference samples and the equations for processing spectral measurements. Spectral data is then compared, discussing spectral mismatch between optical instruments. Solar absorptance and thermal emittance calculations are then analysed, introducing some variants for the weighting, for instance air mass or infrared spectral range. Finally, the propagation of uncertainty on the opto-thermal efficiency is discussed.

## **4.2 Materials and methods**

### **4.2.1 Organization and participants**

This laboratory intercomparison test campaign involved 9 participants from 5 countries (France, Germany, Israel, Netherlands and Spain). Participating laboratories are listed in Table 3.2 and their location is shown on Figure 3.2. Four reference flat samples, further described in the subsection 4.2.3, were prepared for this campaign. Brightsource Industries and Fraunhofer Institute for Solar Energy Systems (ISE) respectively applied their STAC on two flat samples.

For each STAC, one sample was submitted to OMT Solutions B.V. [51] for an independent calibration against NIST traceable standards. These calibrated samples were then returned to OPAC laboratory, a joint CIEMAT-DLR cooperation, at the Plataforma Solar de Almería (PSA) in Tabernas, Spain. Meanwhile, the other samples circulated between participating laboratories, except OMT Solutions. After this laboratory intercomparison test campaign, these samples were stored at OPAC laboratory. Each participant submitted its processed dataset obtained after instrument calibration to CIEMAT-DLR for evaluation.



Table 4.1: List of participants.

Participant	Location	Role
Brightsource Industries	Jerusalem, Israel	Sample preparation (x2) Measurement
CIEMAT (Madrid)	Madrid, Spain	Measurement
CIEMAT-DLR (OPAC, PSA)	Plataforma Solar de Almeria Tabernas, Spain	Measurement Evaluation
DLR	Cologne, Germany	Measurement
Fraunhofer ISE	Freiburg, Germany	Sample preparation (x2) Measurement
HUJI	Jerusalem, Israel	Measurement
INTA	Madrid, Spain	Measurement
PROMES-CNRS	Perpignan, France	Measurement
OMT Solutions B.V.	Eindhoven, Netherlands	Calibration

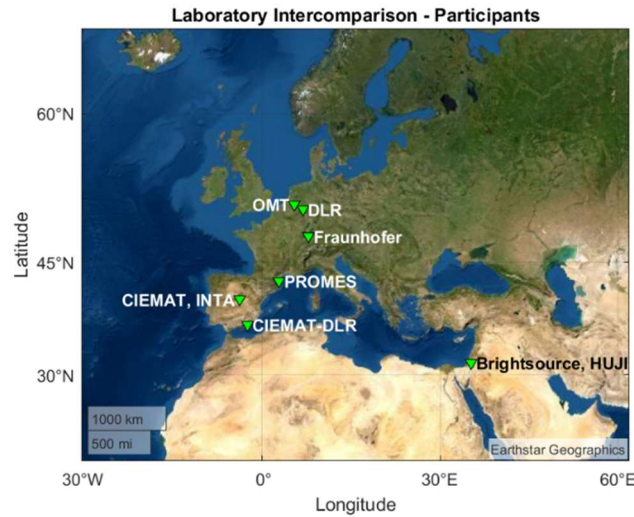


Figure 4.1: Laboratory intercomparison – location of participants.

#### 4.2.2 Instrumentation

For each participating laboratory, measurement instruments are listed in Table 4.2. Each laboratory uses two optical measurement instruments to characterise  $\alpha_{sol}$  and  $\epsilon_{th}$  at room temperature. These instruments operate in complementary spectral ranges, i.e. UV-VIS-NIR from 0.3  $\mu\text{m}$  to 2.5  $\mu\text{m}$ , relevant for  $\alpha_{sol}$  and the infrared range above 2.5  $\mu\text{m}$ , most relevant for  $\epsilon_{th}$ .

Brightsource Industries is the only participant to use a portable device for both measurements, namely the SOC 410-VIS-IR modular solar reflectometer/emissometer, developed by Surface Optics [52], which combines two measurement heads (410-Solar [53] and ET-100 [54]). This portable device can be transported in the field to measure  $\alpha_{sol}$  and  $\epsilon_{th}$  on flat or tubular samples.

Four participants use two benchtop spectrophotometers, i.e. CIEMAT, CIEMAT-DLR, Fraunhofer ISE and PROMES-CNRS. Fraunhofer ISE is the only participant using a single benchtop instrument (Bruker Vertex 80) to cover the full spectral range. In the UV-VIS-NIR spectral range, a Perkin Elmer Lambda 950 or 1050 spectrophotometer is used by four participants, i.e. CIEMAT, DLR, PROMES-CNRS and OMT Solutions. In the infrared range, CIEMAT and CIEMAT-DLR (OPAC) both use a Perkin Elmer Frontier Fourier FTIR spectrophotometer, while PROMES-CNRS uses a SOC 100 HDR model.

INTA and HUJI adopt an alternative approach: both use a benchtop spectrophotometer (Agilent, Cary 500/5000), in the UV-VIS-NIR range for  $\alpha_{sol}$  measurements, while they use a portable emissometer, respectively AZ Technology, Temp 2000A [55,56] and D&S AE1/RD1 [57,58] for  $\varepsilon_{th}$  measurements.

*Table 4.2: Inventory of measurement instruments.*

Participant	UV-VIS-NIR ( $\leq 2.5 \mu\text{m}$ )			Infrared ( $> 1.5 \mu\text{m}$ )		
	Spectro photometer?	Portable device ?	Device Model	Spectro photometer?	Portable device ?	Device Model
Brightsource Industries	-	✓	SOC 410-Solar	-	✓	SOC ET-100
CIEMAT (Madrid)	✓	-	Perkin Elmer Lambda 950	✓	-	Perkin Elmer Frontier FTIR
CIEMAT-DLR (OPAC, PSA)	✓	-	Perkin Elmer Lambda 1050	✓	-	Perkin Elmer Frontier FTIR
DLR	✓	-	Perkin Elmer Lambda 1050	-	-	N.A.
Fraunhofer ISE	✓	-	Bruker Vertex 80	✓	-	Bruker Vertex 80
HUJI	✓	-	Agilent Cary 5000	-	✓	D&S AE1/RD1
INTA	✓	-	Agilent Cary 5000	-	✓	AZ Technology Temp 2000A
PROMES-CNRS	✓	-	Perkin Elmer Lambda 950	✓	-	SOC 100 HDR + Nicolet 6700 FTIR
OMT Solutions	✓	-	Perkin Elmer Lambda 1050	✓	-	Perkin Elmer 983 FTIR

Measurement spectral ranges and resolutions are detailed for each participant in Table 4.3 and displayed in Figure 4.2.a on a logarithmic scale, while spectral bands of the SOC portable device are detailed in Figure 4.2.b. The spectral resolution reported by each participant for benchtop spectrophotometers is shown in Figure 4.3 as a function of wavelength. It corresponds to the wavelength steps reported by each participant for raw spectral measurements.

The common spectral range of interest for UV-VIS-NIR measurements is defined from 0.3  $\mu\text{m}$  to 2.5  $\mu\text{m}$ , while infrared measurements are provided at least until 16  $\mu\text{m}$ . For the SOC portable device and some benchtop spectrophotometers, a spectral overlap exists between 1.5  $\mu\text{m}$  and 2.5  $\mu\text{m}$  (Brightsource Industries, CIEMAT-DLR, Fraunhofer ISE, PROMES-CNRS, OMT Solutions).

For benchtop spectrophotometers, a constant spectral resolution is observed for UV-VIS-NIR measurements, ranging from 1 nm to 10 nm, while the spectral resolution is variable for Infrared measurements. This is partly explained by the instrument optical setup, as UV-VIS-NIR spectrophotometers typically use a monochromator to sample light at different wavelengths, while FTIR spectrophotometers typically use an interferometer and their spectral resolution is often defined in wavenumber ( $\text{cm}^{-1}$ ), which translate in a variable wavelength step. For further analysis, spectral datasets are interpolated with a 1 nm wavelength step.

Table 4.3: Comparison of spectral ranges reported in raw spectral datasets.

Participant	Spectral range [ $\mu\text{m}$ ]		Spectral resolution [nm]	
	UV-VIS-NIR	Infrared	UV-VIS-NIR	Infrared
Brightsource Industries	[0.335-2.5]	[1.5-21]	7 bands	6 bands
CIEMAT (Madrid)	[0.25-2.5]	[2.5-16]	10 nm	$\sim 2$ nm
CIEMAT-DLR (OPAC, PSA)	[0.28-2.5]	[2.0-16]	5 nm	4 nm
DLR	[0.28-2.5]	N.A.	5 nm	N.A.
Fraunhofer ISE	[0.32-2.4]	[1.5-16]	2.5 nm	$\sim 4$ nm
HUJI	[0.28-2.5]	[2-50]	1 nm	Broadband
INTA	[0.25-2.5]	[3-35]	1 nm ( $<0.8 \mu\text{m}$ ) 2 nm ( $>0.8 \mu\text{m}$ )	Broadband
PROMES-CNRS	[0.25-2.5]	[1.5-25]	10 nm	Variable
OMT Solutions	[0.22-2.5]	[1.66-21.6]	5 nm	Variable

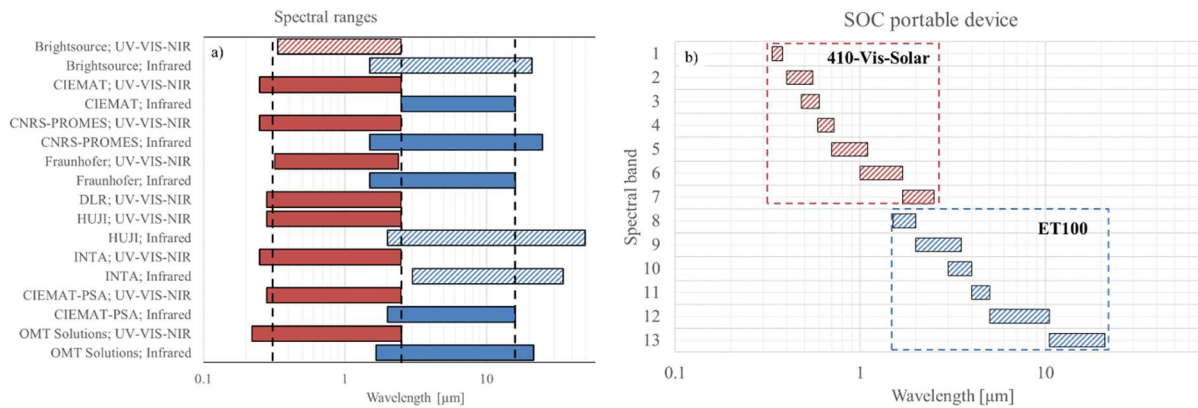


Figure 4.2: Comparison of spectral ranges. a) Global overview b) SOC portable devices.

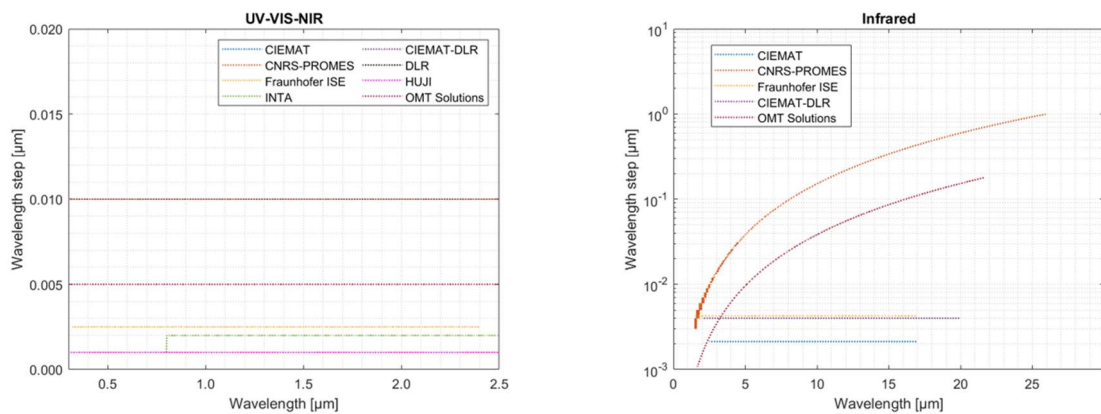


Figure 4.3: Comparison of spectral ranges for benchtop spectrophotometers.

Further instrumentation details related to the light source, detector type and integrating sphere are respectively listed in Table 4.4 for the UV-VIS-NIR spectral range and in Table 4.5 for the infrared range. Pictures of benchtop spectrophotometers and portable instruments are respectively shown in Figure 4.4 and Figure 4.5.

Table 4.4: UV-VIS-NIR instrument specifications..

Participant	Light source	Detector(s)	Integrating sphere
Brightsource Industries	Tungsten filament	7 spectral bands	$\theta$ : 20°; $\varnothing$ : N.A.
CIEMAT (Madrid)	UV: Deuterium VIS-NIR: Tungsten Halogen	InGaAs & PbS; Peltier cooling	$\theta$ : 8°; $\varnothing$ : 150 mm white, diffuse
CIEMAT-DLR (OPAC, PSA)	UV: Deuterium VIS-NIR: Tungsten Halogen	InGaAs & PbS; Peltier cooling	$\theta$ : 8°; $\varnothing$ : 150 mm white, diffuse
DLR	UV: Deuterium VIS-NIR: Tungsten Halogen	InGaAs & PbS; Peltier cooling	$\theta$ : 8°; $\varnothing$ : 150 mm white, diffuse
Fraunhofer ISE	UV: Deuterium VIS-NIR: Tungsten	Photomultipliers Si & InGaAs diodes	$\theta$ : 8°; $\varnothing$ : 200 mm white, diffuse
HUJI	UV: Deuterium VIS-NIR: Tungsten Halogen	InGaAs & PbS; Peltier cooling	$\theta$ : 8°; $\varnothing$ : 150 mm white, diffuse
INTA	UV: Deuterium VIS-NIR: Tungsten Halogen	InGaAs & PbS; Peltier cooling	$\theta$ : 8°; $\varnothing$ : 150 mm white, diffuse
PROMES-CNRS	UV: Deuterium VIS-NIR: Tungsten Halogen	InGaAs & PbS; Peltier cooling	$\theta$ : 8°; $\varnothing$ : 150 mm white, diffuse

Table 4.5: Infrared instrument specifications.

Participant	Light source	Detector	Integrating sphere
Brightsource Industries	IR filament	6 spectral bands 1.5-5 $\mu$ m: PbSe, Peltier Cooling 5-21 $\mu$ m: DTGS	$\theta$ : 20°; $\varnothing$ : N.A.
CIEMAT (Madrid)	IR filament	Detector: MCT Liquid nitrogen cooling	$\theta$ : 12°; $\varnothing$ : 76.2 mm Gold, diffuse
CIEMAT-DLR (OPAC, PSA)	IR filament	Detector: MCT Liquid nitrogen cooling	$\theta$ : 12°; $\varnothing$ : 76.2 mm Gold, diffuse
Fraunhofer ISE	IR filament (glow bar)	Detector: MCT Liquid nitrogen cooling	$\theta$ : 8°; $\varnothing$ : 200 mm Gold, diffuse
HUJI	Electrical heated detector	Broadband detector	N.A., $\varnothing$ : 57 mm
INTA	Heated cavity	Pyroelectric detector	N.A.
PROMES-CNRS	IR filament	Detector: DTGS	$\theta$ : 8°; Adjustable [8-80°] $\varnothing$ : N.A.



Figure 4.4: Benchtop spectrophotometers a) Perkin Elmer Lambda 1050 b) Perkin Elmer Frontier FTIR with Pike Ltd integrating sphere (upward sample positioning). c) Bruker Vertex 80 with both integrating spheres.

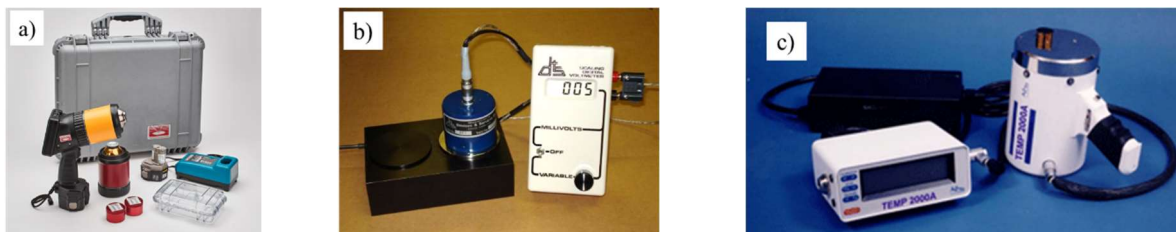


Figure 4.5: Portable reflectometers and emissometers. a) SOC 410-Vis-IR portable solar reflectometer and emissometer. b) D&S AE1/RD1 c) AZ Technology Temp 2000A.

### 4.2.3 Reference and calibration samples

Four flat absorber samples were prepared for this test campaign. The metal substrate is made of ferrensitic/martensitic steel T91/P91 and the sample size is 50x50 mm. Two samples were coated with a black coating, while two samples were coated with a SSC. One sample of each coating is shown in Figure 4.6. The black coating is applied on a sand blasted substrate, while the SSC is applied on a polished substrate.

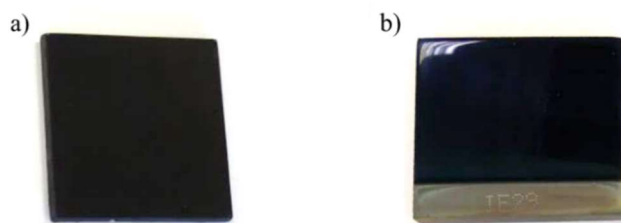


Figure 4.6: Flat coated samples a) Black coating b) SSC.

One sample of each coating was submitted to OMT Solutions for calibration, using NIST traceable calibration coupons as a baseline, respectively a white diffuse sample for the UV-VIS-NIR spectral range and a gold diffuse or specular sample for the infrared spectral range. Spectral data is shown on Figure 4.7 for samples calibrated by OMT Solutions as well as commercially available calibrated sample coupons, i.e. white diffuse Spectralon<sup>®</sup> (99% reflectance) and gold diffuse Infragold<sup>®</sup> [59].

These reference calibrated sample coupons exhibit a nearly constant spectral response in the range of interest and thus can be approximated as grey bodies. The black coating shows on the one hand a nearly flat and low reflectivity in the UV-VIS-NIR spectral range and on the other hand a variable response in the infrared range, while the SSC spectrum approaches a sigmoid profile, with a low reflectivity in the UV-VIS-NIR range and a high reflectivity asymptote in the infrared range.

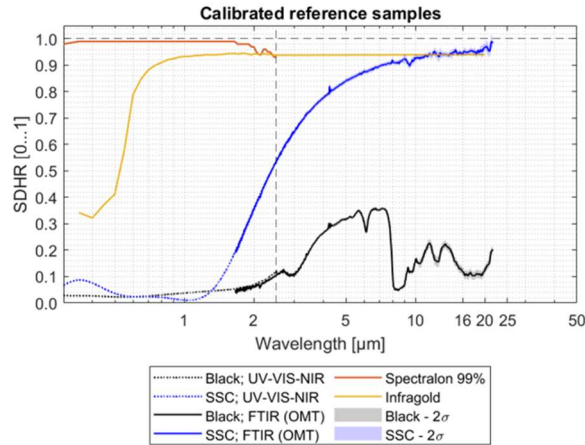


Figure 4.7: Spectral directional hemispherical reflectivity (SDHR) of calibrated reference samples, including  $2\sigma$  spectral uncertainty bands in the infrared range for black and SSC calibrated reference samples.

Available measurement datasets are listed in Table 4.6. The black samples could be measured by all participating laboratories, while the SSC sample could not be measured in the UV-VIS-NIR range by HUJI and DLR (Cologne) due to technical issues. Infrared measurements could not be performed at DLR Cologne as no instrument was available for this measurement.

Calibrated reference samples used for baseline measurements are listed in Table 4.7 for each participant. It is worth mentioning that Fraunhofer ISE does not perform baseline measurements. Different baseline samples may be used to measure the black coating and the SSC, considering whether the surface is diffuse (black coating) or specular (SSC). These baseline samples are traceable to primary standards calibrated by reference laboratories (NIST, OMT Solutions, TNO, NPL).

Table 4.6: Inventory of measurement datasets.

Participant	Black coating		Solar selective coating	
	UV-VIS-NIR	Infrared	UV-VIS-NIR	Infrared
Brightsource Industries	✓	✓	✓	✓
CIEMAT (Madrid)	✓	✓	✓	✓
CIEMAT-DLR (OPAC, PSA)	✓	✓	✓	✓
DLR (Cologne)	✓	N.A.	✗	N.A.
Fraunhofer ISE	✓	✓	✓	✓
HUJI	✓	✓	✗	✓
INTA	✓	✓	✓	✓
PROMES-CNRS	✓	✓	✓	✓
<b>Number of participants</b>	8	7	6	7

Table 4.7: Calibrated reference samples for baseline measurements.

Reference sample	Black coating		SSC	
	UV-VIS-NIR	Infrared	UV-VIS-NIR	Infrared
Brightsource Industries	NIST traceable, diffuse sample	NIST traceable, specular gold coupon	NIST traceable, diffuse coupon	NIST traceable, specular gold coupon
CIEMAT (Madrid)	Labsphere calibrated, White diffuse	Gold diffuse	Labsphere calibrated, White diffuse	Gold diffuse
CIEMAT-DLR (OPAC, PSA)	OMT calibrated, Black sample	OMT calibrated, Black sample	OMT calibrated, Black sample	OMT calibrated, SSC sample
DLR (Cologne)	Black sample, OMT calibrated	N.A.	N.A.	N.A.
Fraunhofer ISE	NIST traceable, white diffuse	NPL calibrated, sprayed aluminum	TNO calibrated, aluminum mirror	NPL calibrated, aluminum mirror
HUJI	White diffuse	Carbon or stainless steel	White diffuse	Carbon or stainless steel
INTA	Labsphere calibrated, White diffuse	AZ Technology, Gold diffuse	Labsphere calibrated, White diffuse	AZ Technology, Gold specular
PROMES-CNRS	Labsphere calibrated, White diffuse	AVIAN Technologies, Gold diffuse	Labsphere calibrated, White diffuse	NIST traceable, Gold specular

#### 4.2.4 Optical characterization

Applicable standards for benchtop spectrophotometers using integrating spheres are ISO 22973:2014 [16], ISO 16378:2013 [17] or ASTM E903:2020 [18]. For portable devices, ASTM C1549:2016 [19] is applicable for solar absorptance, while ASTM C1371:2015 [20] or ASTM E408:2013 [21] apply for portable emissometers. In this subsection, the processing of spectral data is outlined further for benchtop spectrophotometers.

##### 4.2.4.1 Spectral processing

Benchtop spectrophotometers measure the spectral directional hemispherical reflectivity (SDHR) for any sample, using an integrating sphere. For all spectrophotometers, except for the FTIR measurement at Fraunhofer ISE, a background spectrum are first recorded. A reference sample (Table 4.7) is then mounted on the integrating sphere sample port and its SDHR is measured as a baseline. This sample is then removed and replaced by the material to be measured. Knowing the zeroline  $I_{zero, meas}$ , the baseline calibrated reflectivity  $\rho_{ref, calib}$ , the baseline and reference sample measured intensities  $I_{base, meas}$  and  $I_{sample, meas}$ , one derives the sample reflectivity  $\rho_{sample, SDHR}$  applying (Eq.4.1). This reflectivity is measured for a wavelength  $\lambda$  (Table 4.3), at a near normal incidence angle  $\theta$  (8-12°) (Table 4.4 - Table 4.5), at room temperature.

$$\rho_{sample, SDHR}(\lambda, \theta, T) = \frac{I_{sample, meas} - I_{zero}}{I_{base, meas} - I_{zero}} \rho_{ref, calib} \quad (4.1)$$

For the FTIR spectrometer at Fraunhofer ISE a different procedure is applied. A calibration is done every 3 months approximately using the reference coupon cited in Table 4.7. In a sample measurement, the reference and samples are measured in alternating minute intervals. The

reference is either the diffuse wall of the UV/VIS integrating sphere or a gold IR mirror within the IR integrating sphere. The mean value of the measurements is formed and the measurement is corrected with the respective calibration curve from the calibration.

Sample reflectivity is assumed to remain stable for any wavelength at higher temperature (Eq.4.2). Measurements at higher temperature require more sophisticated instrumentation [22,23,45,46], experimental data for other similar absorber coatings has been previously published [47-50].

$$\frac{d\rho_{sample}(\lambda, \theta, T)}{dT} \sim 0 \quad (4.2)$$

The spectral deviation between both spectrophotometers is calculated according to (Eq.4.3), using interpolated spectral data with a 1 nm wavelength step. The common interval for comparison between CIEMAT-DLR, Fraunhofer ISE, CNRS-PROMES and OMT-Solutions ranges from 2  $\mu\text{m}$  to 2.5  $\mu\text{m}$ . Spectral mismatch statistics (average, standard deviation) are derived in this common interval.

$$\Delta\rho(\lambda) = \rho_{sample,FTIR}(\lambda) - \rho_{sample,UV-VIS-NIR}(\lambda) \quad (4.3)$$

For further calculations, available experimental spectral data is concatenated, considering UV-VIS-NIR measurements until 2.5  $\mu\text{m}$  and then infrared measurements above 2.5  $\mu\text{m}$ .

#### 4.2.4.2 Spectral weighting

The solar absorptance  $\alpha_{sol}$  is calculated for each reference sample, weighting the sample reflectivity  $\rho_{sample,corr}$  with a reference solar spectrum according to (Eq.3.4). The common integration interval is defined from  $\lambda_1= 0.3 \mu\text{m}$  to  $\lambda_2= 2.5 \mu\text{m}$ . The reference solar spectrum  $G_{sol}(\lambda, AM)$  is defined according to ASTM G173-03 [60] derived from SMARTS v2.9.2. [61]. Three spectra are considered for the comparison, i.e. extraterrestrial (Air Mass  $AM0$ ),  $AM1.5g$  (global) and,  $AM1.5d$  (direct+circumsolar).

$$\alpha_{sol}(AM) = \frac{\int_{\lambda_1}^{\lambda_2} [1 - \rho_{sample,corr}(\lambda, \theta, T_{amb})] G_{sol}(\lambda, AM) d\lambda}{\int_{\lambda_1}^{\lambda_2} G_{sol}(\lambda, AM) d\lambda} \quad (3.4)$$

The thermal emittance  $\varepsilon_{th}$  is calculated for each reference sample, weighting the sample reflectivity  $\rho_{sample,corr}$  with a reference blackbody spectrum at a given absorber temperature  $T_{abs}$  according to (Eq.4.5-4.6). The common integration interval is defined from  $\lambda_1= 0.3 \mu\text{m}$  to  $\lambda_3= 16 \mu\text{m}$ . For a given integration interval  $[\lambda_1; \lambda_3]$ , the fraction  $f_{\sigma T^4}$  of Stefan Boltzmann law is expressed in (Eq.4.7).

Alternative upper limits are considered, i.e. 20  $\mu\text{m}$ , 25  $\mu\text{m}$  and 50  $\mu\text{m}$ , using spectral data up to 25  $\mu\text{m}$ , if available, or extrapolating spectra otherwise, assuming reflectivity is constant beyond 16  $\mu\text{m}$ . While ISO 22975-3:2014 [16] suggests that a constant value may be assumed beyond 25  $\mu\text{m}$ , this is not always valid and this assumption depends on the coating [62-63].

$$\varepsilon_{th,calc}(T_{abs}) = \frac{\int_{\lambda_1}^{\lambda_3} [1 - \rho_{sample,corr}(\lambda, \theta, T_{amb})] E_{bb}(\lambda, T_{abs}) d\lambda}{\int_{\lambda_1}^{\lambda_3} E_{bb}(\lambda, T_{abs}) d\lambda} \quad (4.5)$$



$$E_{bb}(\lambda, T_{abs}) = \frac{2\pi hc^2}{\lambda^5 \left[ \exp\left(\frac{hc}{\lambda k T_{abs}}\right) - 1 \right]} \quad (4.6)$$

$$f_{\sigma T^4} = \frac{\int_{\lambda_1}^{\lambda_3} E_{bb}(\lambda, T_{abs}) d\lambda}{\int_0^{\infty} E_{bb}(\lambda, T_{abs}) d\lambda} = \frac{\int_{\lambda_1}^{\lambda_3} E_{bb}(\lambda, T_{abs}) d\lambda}{\sigma T^4} \quad (4.7)$$

Reference solar spectra are plotted in Figure 4.8.a from 0.3 μm to 4 μm, while the *AM1.5d* spectrum is compared against blackbody spectra at 25 °C and 750 °C from 0 μm to 50 μm in Figure 4.8.b. The coverage fraction  $f_{\sigma T^4}$  is shown as a function of blackbody temperature, respectively for benchtop spectrophotometers in Figure 4.8.c and portable emissometers in Figure 4.8.d.

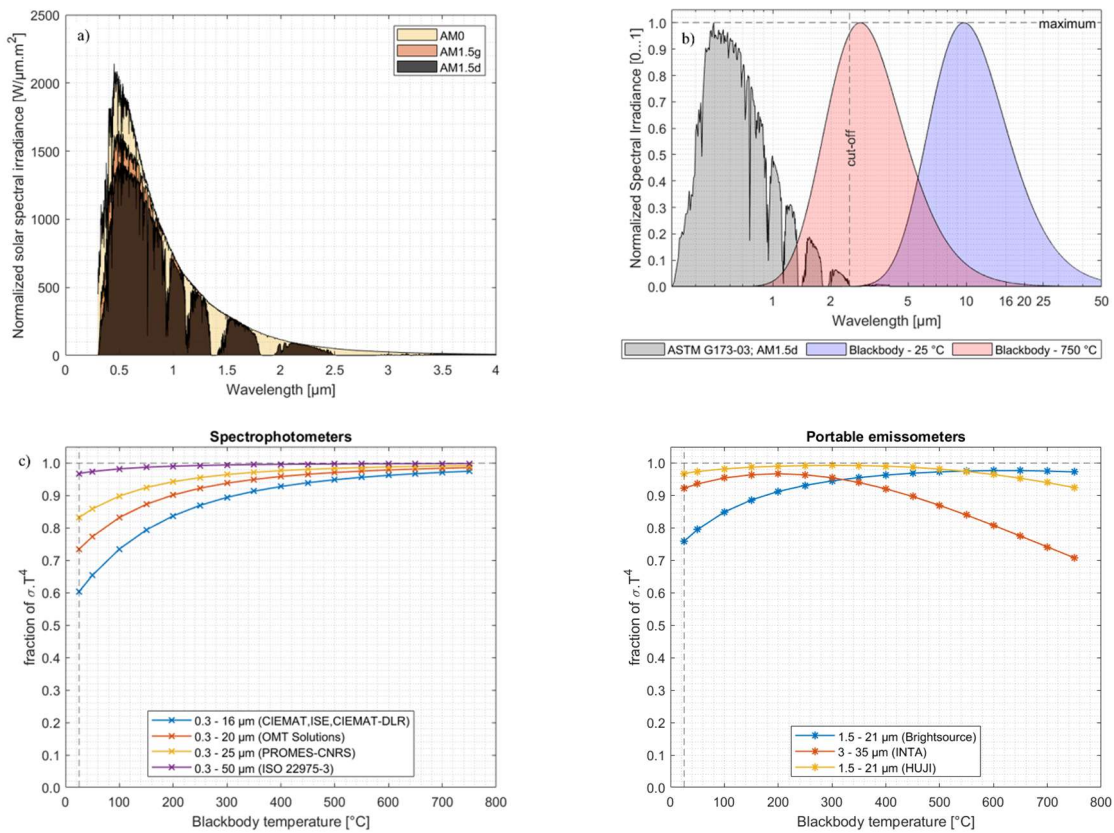


Figure 4.8: Spectral weighting functions. a) ASTM G173-03 reference solar spectra. b) ASTM G173-03 AM1.5d and blackbody spectra at 25 °C and 750 °C. c) Fraction of Stefan Boltzmann law ( $\sigma T^4$ ) as a function of blackbody temperature for benchtop spectrophotometers d) Fraction of  $\sigma T^4$  for portable emissometers.

As the blackbody temperature increases, the blackbody spectrum progressively overlaps with the solar spectrum in the UV-VIS-NIR range according to Wien's displacement law (Figure 4.8.b), justifying the concatenation of UV-VIS-NIR and Infrared spectral datasets. Adjusting the upper integration limit toward 50 μm allows achieving a higher coverage fraction at lower temperature (Figure 4.8.c). Portable emissometers show variable behavior in terms of coverage fraction (Figure 4.8.d). While the SOC device allows computing a  $\epsilon_{th}$  value at a given absorber temperature, AZ Temp2000A only reports a value at ambient temperature 25 °C, D&S AE1/RD1 reports a  $\epsilon_{th}$  value at an intermediate temperature of 65 °C, as its calorimetric measurement principle requires heating the sample on a heat sink plate.

#### 4.2.4.3 Opto-thermal efficiency

Both standard figures of merit  $\alpha_{sol}$  and  $\varepsilon_{th}$  can be combined into a compound figure of merit, namely the opto-thermal efficiency  $\eta_{opt-th}$  [31,37-38], which is expressed in (Eq.4.8). This equation assumes a flat plate geometry, negligible convection losses and a negligible heat sink temperature. Furthermore, the thermal emittance is supposedly calculated for a coverage fraction  $f_{\sigma T^4} = 100\%$ .

$$\eta_{opt-th} \approx \frac{\alpha_{sol} \cdot \dot{q}_{sol}'' - \varepsilon_{th}(T) \cdot \sigma T^4}{\dot{q}_{sol}''} = \alpha_{sol} - \frac{\sigma T^4}{\dot{q}_{sol}''} \cdot \varepsilon_{th}(T) \quad (4.8)$$

Taking the partial derivative of  $\eta_{opt-th}$  with respect to  $\alpha_{sol}$  and  $\varepsilon_{th}$  (Eq.4.9), a trade-off factor  $Z$  can be defined between both figures of merit (Eq.4.10), which is a function of the operating conditions, i.e. absorber temperature  $T$  and the concentrated solar flux  $\dot{q}_{sol}''$ .

$$\frac{\partial \eta_{opt-th}}{\partial \alpha_{sol}} = 1; \quad \frac{\partial \eta_{opt-th}}{\partial \varepsilon_{th}} = -\frac{\sigma T^4}{\dot{q}_{sol}''} \quad (4.9)$$

$$Z = \frac{\Delta \varepsilon_{th}}{\Delta \alpha_{sol}} = -\frac{\dot{q}_{sol}''}{\sigma T^4} \quad (4.10)$$

The trade-off factor can be interpreted as follows: if  $\alpha_{sol}$  is increased by +1 p.p., by how many percentage points does the  $\varepsilon_{th}$  value have to be reduced to achieve a constant  $\eta_{opt-th}$ ?

Partial derivatives can also be used further to calculate the uncertainty propagation of  $\alpha_{sol}$  and  $\varepsilon_{th}$  on the compound figure of merit  $\eta_{opt-th}$ , as expressed in (Eq.4.11-4.12).

$$u_c(\eta_{opt-th})|_{\{\dot{q}_{sol}'', T\}} = \sqrt{\left(\frac{\partial \eta_{opt-th}}{\partial \alpha_{sol}} \cdot \Delta \alpha_{sol}\right)^2 + \left(\frac{\partial \eta_{opt-th}}{\partial \varepsilon_{th}} \cdot \Delta \varepsilon_{th}\right)^2} \quad (4.11)$$

$$u_c(\eta_{opt-th})|_{\{\dot{q}_{sol}'', T\}} = \sqrt{\Delta \alpha_{sol}^2 + \left(-\frac{\sigma T^4}{\dot{q}_{sol}''} \cdot \Delta \varepsilon_{th}\right)^2} \quad (4.12)$$

The trade-off factor  $Z$  is shown in Figure 4.9.a. as a function of the operating point, i.e. the absorber temperature and the concentration ratio  $\{C_x, T_{abs}\}$ , while the weighting coefficient of the  $\varepsilon_{th}$  error, i.e.  $1/Z$ , is shown in Figure 4.9.b. Thermal emittance is important at a low concentration ratio and a high absorber temperature (top left corner), while solar absorptance is dominant at a high concentration ratio and a low absorber temperature (bottom right corner). For example, at  $C_x = 20$  and  $T_{abs} = 300$  °C (parabolic trough), increasing  $\alpha_{sol}$  by +1 p.p. has the same effect on  $\eta_{opt-th}$  as reducing  $\varepsilon_{th}$  by  $Z \sim -3.3$  p.p, thus favoring solar selective coatings. At  $C_x = 1000$  and  $T_{abs} = 300$  °C (central receiver system), the value of the trade-off factor  $Z$  is -163 p.p, in this case HSA black coatings become more relevant.

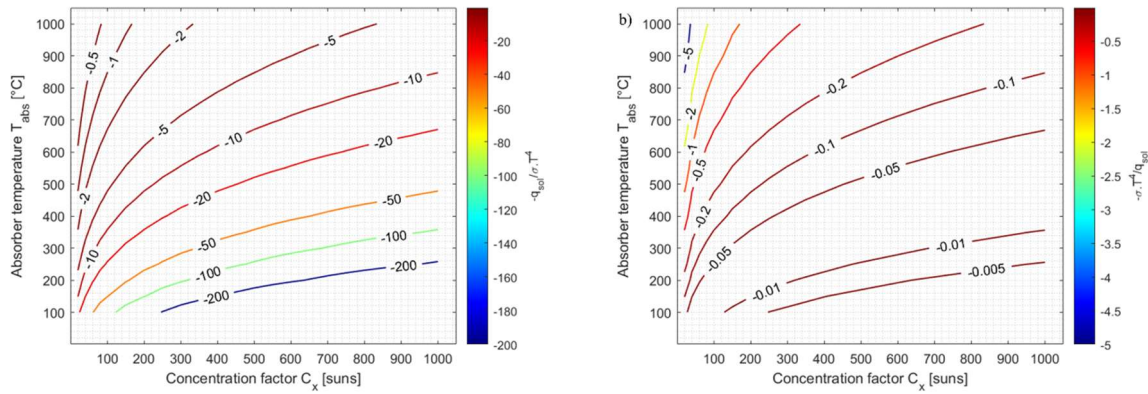


Figure 4.9: Opto-thermal efficiency a) trade-off factor  $Z$  b) weighting coefficient for  $\epsilon_{th}$  uncertainty.

### 4.3 Results and discussion

#### 4.3.1 Spectral processing

Spectral datasets obtained from benchtop spectrophotometers for black and SSC samples are respectively plotted over the UV-VIS-NIR spectral range in Figure 4.10 and over the infrared range in Figure 4.11. In the UV-VIS-NIR range, spectral datasets are consistent among participant up to 2  $\mu\text{m}$ . In the infrared range, a dispersion of a few percentage points can be observed for the black coating, while a consistent spectral behavior is observed for the SSC up to 16  $\mu\text{m}$ . For CIEMAT-DLR dataset, the low detector sensitivity above 16  $\mu\text{m}$  induces an important waviness. A spike can be observed around 4.3  $\mu\text{m}$  in some datasets, as  $\text{CO}_2$  atmospheric absorption is not corrected by nitrogen purging during spectral measurements.

Concatenated spectral datasets from 0.3  $\mu\text{m}$  to 16  $\mu\text{m}$  are shown in Figure 4.12. Spectral datasets from 0.3  $\mu\text{m}$  to 2.5  $\mu\text{m}$  are taken from UV-VIS-NIR measurements (Figure 4.10), while datasets above 2.5  $\mu\text{m}$  are taken from FTIR measurements (Figure 4.11). The spectral mismatch in the overlap range between UV-VIS-NIR and infrared spectrophotometers is analysed in Figure 4.13, including mismatch statistics computed over the common overlapping spectral range from 2  $\mu\text{m}$  to 2.5  $\mu\text{m}$ , according to (Eq.4.3). Detailed mismatch statistics is listed in Table 4.8 for this spectral range.

It is worth observing on Figure 4.12 that spectral datasets agree reasonably well, considering the experimental uncertainty of acquired reflectivity spectra. The experimental uncertainty of the Perkin Elmer Lambda 1050 has been analysed in details for specular mirrors in [64] and a maximum combined standard uncertainty  $u_c = 0.008$  ( $k=1$ ) has been reported. For FTIR measurements, OMT Solutions communicates a combined standard uncertainty  $u_c = 0.01$  ( $k=2$ ) for accurate measurements on flat diffuse gold samples.

For UV-VIS-NIS measurements, spectral datasets agree within  $\pm 1$  p.p. for the black and SSC samples, up to 2  $\mu\text{m}$ . For FTIR measurements, spectral datasets agree within  $\pm 2$  p.p. for the solar selective coating, while a standard deviation of  $\pm 3$  p.p. is observed for the black coating beyond 2  $\mu\text{m}$ , affecting spectral weighting.

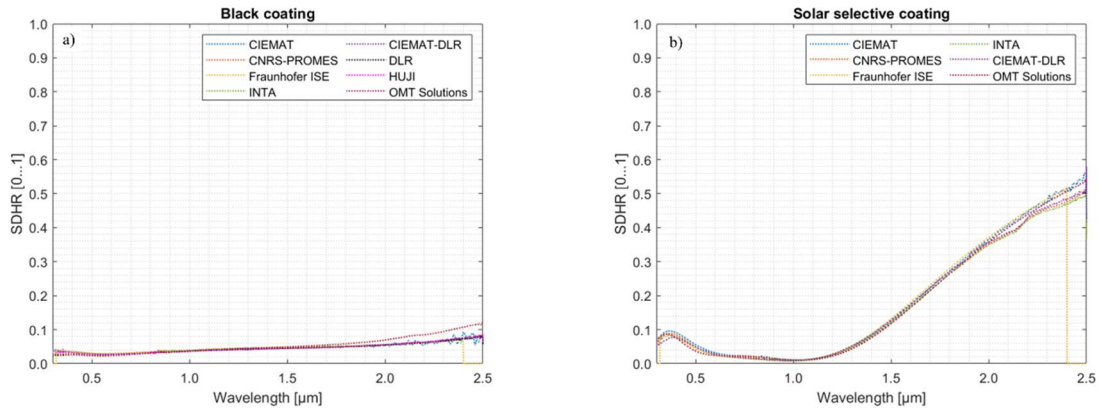


Figure 4.10: UV-VIS-NIR spectral datasets. a) Black coating, b) Solar selective coating.

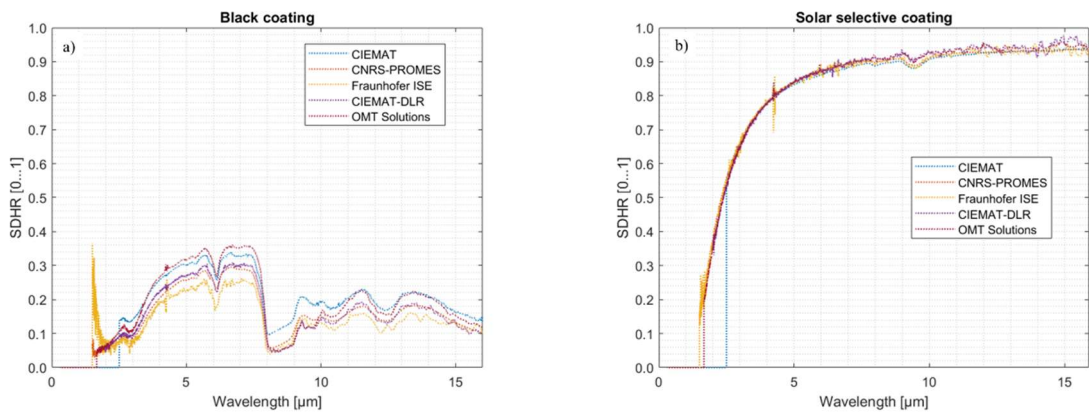


Figure 4.11: Infrared spectral datasets. a) Black coating, b) Solar selective coating.

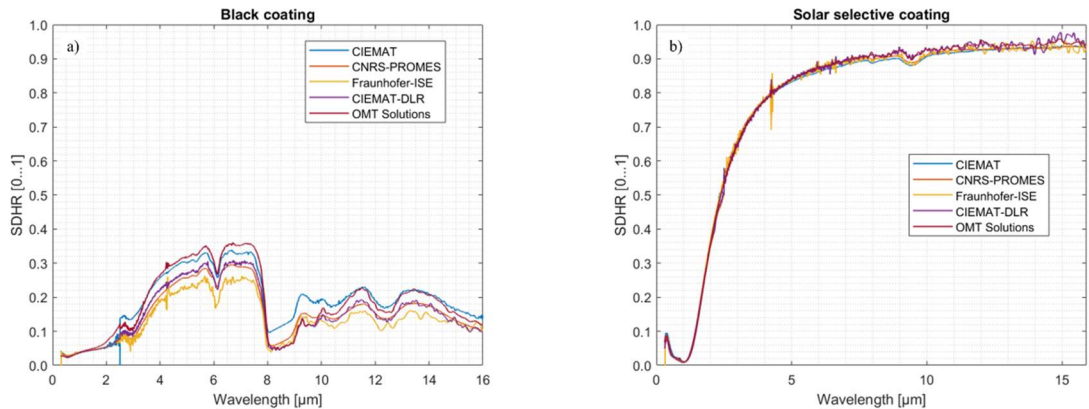


Figure 4.12: Concatenated spectral datasets from 0.3  $\mu\text{m}$  to 16  $\mu\text{m}$ . a) Black coating, b) Solar selective coating.

The spectral mismatch characterises the deviation between UV-VIS-NIR and FTIR spectrophotometers in a common spectral range. A significant spectral deviation is observed from 1.5  $\mu\text{m}$  to 2  $\mu\text{m}$  for the black coating in Fraunhofer ISE dataset. This spectral range is discarded from the statistical analysis. The average spectral mismatch over the spectral range [2.0;2.5]  $\mu\text{m}$  lies respectively between -1.1% and 0.8% for the black coating and between -0.3% and 4.3% for the SSC.

Spectral mismatch is seldom described in the literature. However, it is a valuable quality indicator for the optical measurement process and baseline selection. A minimal value should be ideally achieved. Nonetheless, noisy detector signals, reference sample choices and integrating sphere configurations are mainly responsible for this mismatch.

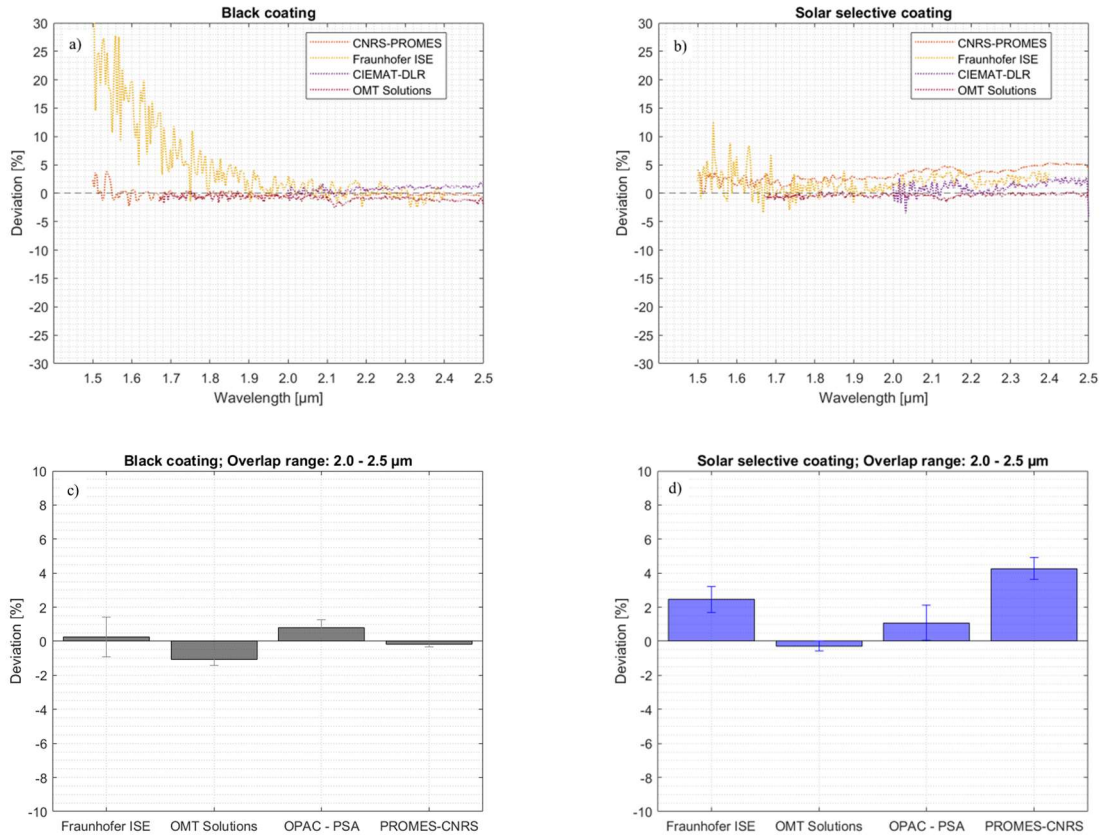


Figure 4.13: Spectral deviation between UV-VIS-NIR and FTIR spectrophotometers. a) Spectral deviation, black coating b) Spectral deviation, solar selective coating. c) Average mismatch (2 – 2.5 μm), black coating. d) Average mismatch (2 – 2.5 μm), solar selective coating.

Table 4.8: Spectral mismatch statistics.

Participant	Black coating		Solar selective coating	
	mean [%]	stdev [%]	mean [%]	stdev [%]
CIEMAT-DLR (OPAC, PSA)	0.8%	0.5%	1.1%	1.1%
Fraunhofer ISE	0.3%	1.2%	2.5%	0.7%
PROMES-CNRS	-0.2%	0.2%	4.3%	0.6%
OMT Solutions	-1.1%	0.4%	-0.3%	0.3%

### 4.3.2 Spectral weighting

Calculated  $\alpha_{sol}$  values according to ASTM G173-03 are shown in Figure 4.14 and reported in Table 4.9. At  $AM1.5d$ , the black coating has a mean  $\alpha_{sol}$  value of 96.6% and a standard deviation of 0.16%, while the SSC a mean  $\alpha_{sol}$  value of 94.5% and a standard deviation of 0.35%. A higher deviation is thus observed for the SSC. A higher sensitivity to the solar spectrum is also observed for the SSC (Spread  $AM0$  vs.  $AM1.5d$ : 0.5 %) than for the black coating (Spread  $AM0$  vs.  $AM1.5d$ : 0.03 %).

Calculated  $\epsilon_{th}$  values are shown in Figure 4.15 and reported in Table 4.10. Values are reported over the temperature range from 25 °C to 750 °C. Consistent curves are calculated for the SSC, while a deviation of a few p.p. is observed for the black coating, in line with spectral deviations observed in Figure 4.11.a. At 650 °C, the standard deviation on  $\epsilon_{th}$  is respectively 3.8% for the black coating and 0.5% for the SSC.

Values reported by portable devices are also displayed on Figure 4.15.a and Figure 4.15.b. Although a direct comparison is not feasible, due to different spectral ranges and reference temperatures, values obtained with the TEMP2000A at 25 °C are in line with thermal emittance curves for both samples. The SOC ET-100 portable emissometer computes an accurate value at 650 °C for the SSC, while the value reported for the black coating is lower than the mean value by a few p.p. Finally, the D&S AE1/RD1 emissometer reports a correct value for the black coating, but the value reported for the SSC lies significantly above the mean  $\epsilon_{th}$  value.

The D&S AE1/RD1 device has a lower resolution, as values are reported without any decimal unit, with a reported uncertainty of  $\pm 1.4$  p.p. Meanwhile, the TEMP2000 A portable device reports values with one decimal unit, with an uncertainty of  $\pm 1$  p.p. for grey samples and  $\pm 3$  p.p. for non-grey samples according to the device manual [55]. For the SOC portable device, the reflectivity accuracy for the 20° incidence angle reported by the manufacturer [52-54] is  $\pm 3$  p.p. for any spectral band, i.e. for the 410-Solar and the ET-100 measurement heads.

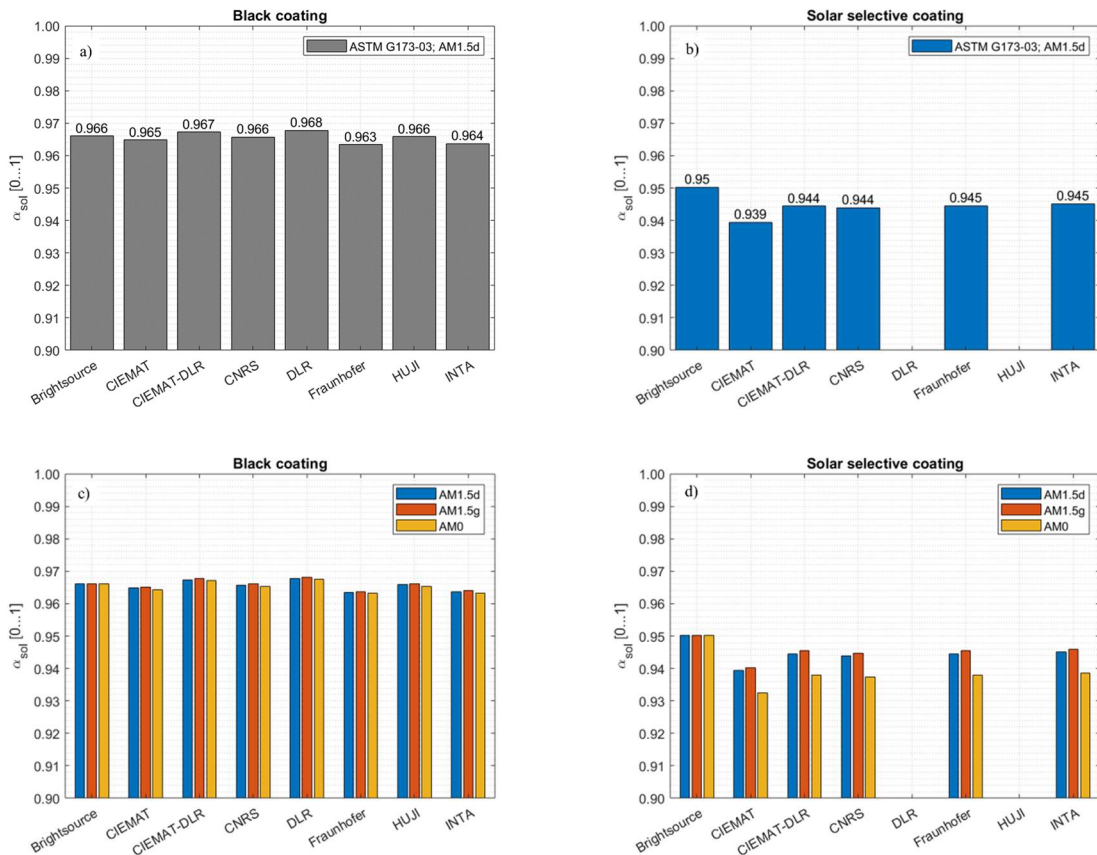


Figure 4.14: Solar absorptance calculations according to ASTM G173-03 a) Black coating, direct+circumsolar, b) Solar selective coating, direct+circumsolar, c) HSA Black coating, AM0/AM1.5g/AM1.5d d) Solar selective coating, AM0/AM1.5g/AM1.5d.

Table 4.9: Solar absorptance calculations according to ASTM G173-03.

Measurand	$\alpha_{sol}$ (ASTM G173-03) [%]					
	Sample	Black coating (HSA)			Solar selective coating	
Participant	AM0	AM1.5g	AM1.5d	AM0	AM1.5g	AM1.5d
Brightsource Industries	-	96.6%	-	-	95.0%	-
CIEMAT (Madrid)	96.42%	96.50%	96.48%	93.24%	94.00%	93.93%
CIEMAT-DLR (OPAC, PSA)	96.71%	96.77%	96.73%	93.81%	94.53%	94.43%
DLR (Cologne)	96.76%	96.82%	96.78%	-	-	-
Fraunhofer ISE	96.32%	96.36%	96.34%	93.79%	94.54%	94.44%
HUJI	96.53%	96.61%	96.58%	-	-	-
INTA	96.33%	96.40%	96.37%	93.86%	94.58%	94.50%
PROMES-CNRS	96.53%	96.60%	96.57%	93.73%	94.45%	94.38%
Mean value	96.53%	96.58%	96.56%	93.91%	94.52%	94.45%
Standard deviation	0.16%	0.16%	0.16%	0.59%	0.33%	0.35%

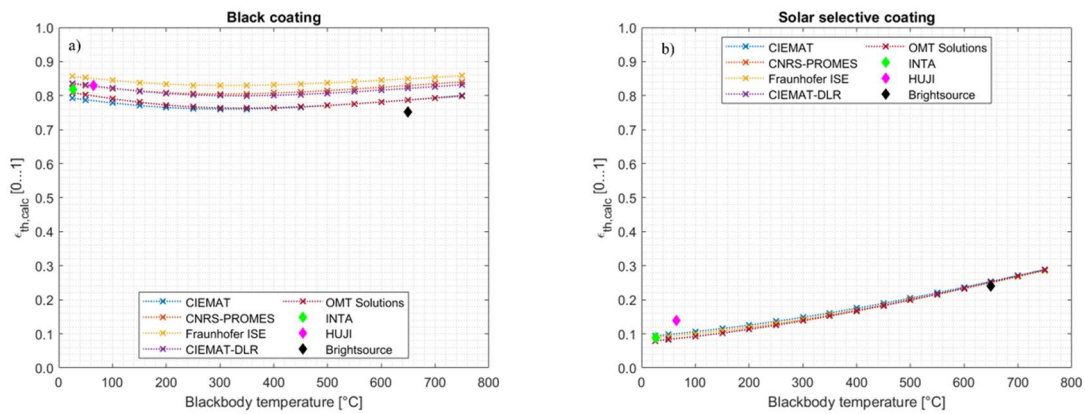


Figure 4.15: Thermal emittance calculations. For benchtop spectrophotometers, the integration interval spans here from 0.3  $\mu\text{m}$  to 16  $\mu\text{m}$ . a) Black coating b) Solar selective coating.

Table 4.10: Thermal emittance calculations. Integration interval for spectrophotometers: from 0.3  $\mu\text{m}$  to 16  $\mu\text{m}$ . (\*) The outlying value reported for the SSC by the D&S AE1/RD1 is omitted in the standard deviation calculation.

Measurand	Spectral range	$\epsilon_{th,calc}(T)$			
		Black coating		SSC	
Participant	[ $\mu\text{m}$ ]	25 °C	650 °C	25 °C	650 °C
Brightsource Industries (*)	[1.5-21]	N.A.	75.2%	N.A.	24.0%
CIEMAT (Madrid)	[0.3-16]	79.3%	78.7%	9.39%	25.4%
CIEMAT-DLR (OPAC, PSA)	[0.3-16]	83.6%	82.1%	7.96%	25.2%
Fraunhofer ISE	[0.32-16]	85.6%	84.9%	8.88%	25.0%
HUJI (* 65 °C)	[2-50]	83%	N.A.	14%	N.A.
INTA	[3-35]	81.9%	N.A.	8.76%	N.A.
PROMES-CNRS	[0.3-16]	83.4%	83.0%	8.90%	25.1%
Mean value		<b>82.8%</b>	<b>80.8%</b>	<b>9.7%</b>	<b>25.0%</b>
Standard deviation		<b>2.1%</b>	<b>3.8%</b>	<b>0.5%(*)</b>	<b>0.5%</b>

The wavelength interval upper limit is extended from 16  $\mu\text{m}$  toward 50  $\mu\text{m}$  for  $\epsilon_{th}$  calculations with benchtop spectrophotometers. Deviations with respect to 16  $\mu\text{m}$  are shown in Figure 4.16. For the black coating, calculated  $\epsilon_{th}$  values increase by a few percentage points at lower temperature as the upper limit shifts toward 50  $\mu\text{m}$ , as the fraction  $f_{\sigma T^4}$  increases (Figure 4.8.c). The opposite trend is observed for the SSC, i.e. calculated  $\epsilon_{th}$  values decrease for similar conditions.

At higher temperatures, calculated values converge while the dispersion decreases, regardless of the upper integration limit for the black coating. As the blackbody spectral irradiance shifts to shorter wavelengths according to Wien's displacement law, the far infrared spectrum has a lower influence in the calculation. For the solar selective coating, a systematic offset, lower than one percentage point, remains at higher temperature. Shifting the upper wavelength limit gives more weight to the high reflectivity asymptote in the calculation (Figure 4.7). Nonetheless, assuming a constant reflectivity level beyond 16  $\mu\text{m}$ , following the ISO 22975-3 as a guideline [16], may not be an appropriate rule for a SSC, as shown in the literature [62,63]. A sigmoid spectral model [15] may be a better alternative to estimate the asymptotical behavior and smooth far infrared spectral measurement noise.

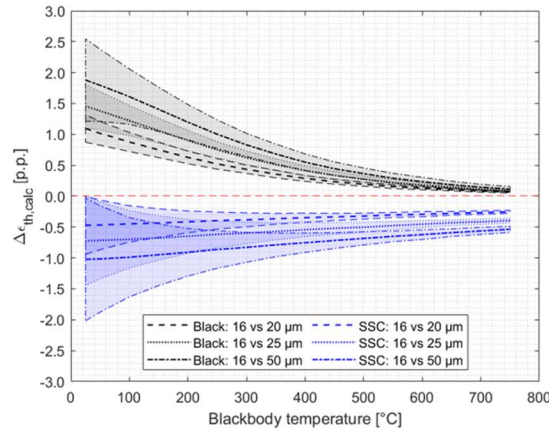


Figure 4.16: Deviation in  $\epsilon_{th}$  calculations after adjusting the integration interval from 16  $\mu\text{m}$  toward 50  $\mu\text{m}$ .

### 4.3.3 Opto-thermal efficiency

The opto-thermal efficiency  $\eta_{opt-th}$  is calculated for a set of operating points  $\{C_x, T_{abs}\}$  according to (Eq.4.8), using  $\alpha_{sol}$  and temperature dependent  $\epsilon_{th}$  values derived in subsection 4.3.2. Contour maps are shown for both coatings in Figure 4.17. The  $\eta_{opt-th}$  value converges towards  $\alpha_{sol}$  at low temperature, as the thermal emission becomes negligible. The black coating outperforms the solar selective coating at low temperature and high concentration (bottom right corner), while the solar selective coating performs better than the black coating at higher temperature and low concentration (top left corner). A Pareto front exists where both coatings have a similar opto-thermal efficiency [15].



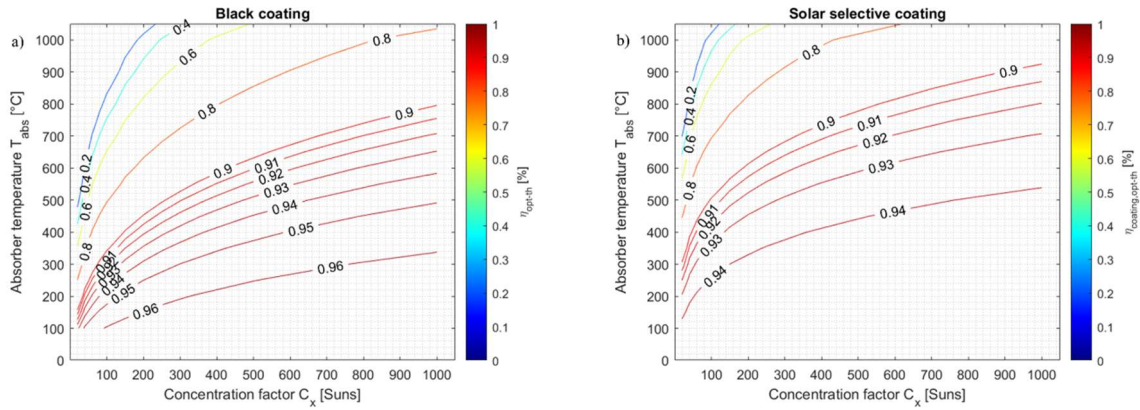


Figure 4.17: Opto-thermal efficiency  $\eta_{opt-th}$  a) Black coating b) Solar selective coating.

The propagation of measurement uncertainties on  $\eta_{opt-th}$  is calculated according to (Eq.4.12), estimating the respective uncertainties on  $\Delta\alpha_{sol}$  and  $\Delta\epsilon_{th}$  from subsection 4.3.2, neglecting any temperature dependence. Results are shown for both coatings in Figure 4.18. The uncertainty term  $\Delta\alpha_{sol}$  is dominant, according to Figure 4.9. It corresponds to the lower uncertainty bound  $u_c(\eta_{opt-th})$ . On the other hand, the uncertainty term  $\Delta\epsilon_{th}$  gains weight at higher temperature and becomes dominant for low concentration factor ( $C_x < 10$ ).

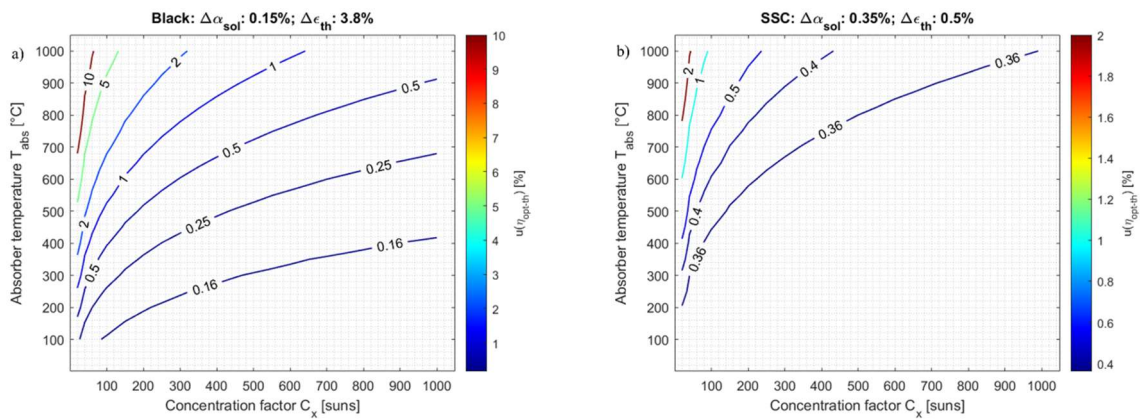


Figure 4.18: Propagation of uncertainty on the opto-thermal efficiency.

## 4.4 Conclusion and outlook

In this chapter, spectral directional hemispherical reflectivity measurements have been compared at several laboratories on two flat solar thermal absorber coatings, i.e. a high absorbing black coating and a solar selective coating. Measurements have been carried out at room temperature both with benchtop spectrophotometers and portable devices.

A good agreement was found between spectrophotometer datasets. In the UV-VIS-NIR range, all datasets agree well until 2.0  $\mu\text{m}$ . Above 2.5  $\mu\text{m}$ , a minor deviation can be observed for both coatings. In the Infrared range, a good agreement is observed for the solar selective coating until 16  $\mu\text{m}$ . For the black coating, a higher dispersion is noticeable. Spectral mismatch in the range from 2  $\mu\text{m}$  to 2.5  $\mu\text{m}$  is less than 1 p.p. for the black coating, while a slightly higher deviation is noticed for the SSC.

Applying ASTM G173-03 (AM1.5 direct+circumsolar), the average and standard deviation for the solar absorptance  $\alpha_{sol}$  are respectively  $96.6 \pm 0.16\%$  for the black coating and  $94.5 \pm 0.35\%$

for the SSC. The selection of the reference solar spectrum does not significantly affect the  $\alpha_{sol}$  calculation for the black coating, while the sensitivity is more pronounced for the solar selective coating. The SOC 410-Solar portable device delivers values in agreement with benchtop spectrophotometers.

For thermal emittance  $\varepsilon_{th}$  calculations, a good agreement is found for the SSC (650 °C:  $\varepsilon_{th,calc}=25.0\pm0.5\%$ ), while a larger deviation can be noticed for the black coating (650 °C:  $\varepsilon_{th,calc}=80.8\pm3.8\%$ ), mainly explained by the dispersion of infrared spectra. The calculated temperature dependence of  $\varepsilon_{th}$  is moderate for the black coating and more pronounced for the solar selective coating, as the overlap of the blackbody and solar spectra increases.

Extrapolating spectral data from 16  $\mu\text{m}$  to 50  $\mu\text{m}$  has a moderate impact on  $\varepsilon_{th}$  calculation results. For the black coating,  $\varepsilon_{th}$  values converge at higher temperature, while their dispersion decreases. For the solar selective coating, a systematic offset of 1 p.p. remains for  $\varepsilon_{th}$  at higher temperature, as more weight is given to the solar selective coating high reflectivity at long wavelengths. Extrapolating spectral data beyond 16  $\mu\text{m}$  according to ISO 22975-3 may not be a suitable guideline for any coating. In the case of solar selective coating, sigmoid models or far infrared measurements provide a more realistic asymptotical reflectivity value.

The comparison of portable emissometers show that the AZ Technology Temp 2000A device agrees best with benchtop spectrophotometers. It reports however a single value at 300 K, while the SOC ET-100 can perform calculations over a broader temperature range, thanks to its multispectral configuration.

The propagation of  $\alpha_{sol}$  and  $\varepsilon_{th}$  uncertainties on the opto-thermal efficiency  $\eta_{opt-th}$  were further analysed. At low temperature and high concentration factor, the  $\alpha_{sol}$  parameter is dominant and its uncertainty defines the lower bound for the combined uncertainty  $u_c(\eta_{opt-th})$ , while the  $\varepsilon_{th}$  parameter is more dominant at high temperature and low concentration factor and its accuracy gradually affects the combined uncertainty  $u_c(\eta_{opt-th})$ .

#### 4.5 References: Chapter 4

- [1] K. Lovegrove, W. Stein, *Concentrating Solar Power Technology: Principles, Developments and Applications*, Second Edition, Woodhead Publishing, 2020. <https://doi.org/10.1016/C2018-0-04978-6>.
- [2] World Bank, Concentrating Solar Power: Clean Power on Demand 24/7, (2021), available at: <https://pubdocs.worldbank.org/en/849341611761898393/WorldBank-CSP-Report-Concentrating-Solar-Power-Clean-Power-on-Demand-24-7-FINAL.pdf>. Accessed 28/07/2021.
- [3] German Aerospace Center (DLR) Institute of Solar Research, Solar thermal power plants: Heat, electricity and fuels from concentrated solar power, (2021), available at: [https://www.dlr.de/sf/en/PortalData/73/Resources/dokumente/publikationen\\_medien/dlr\\_und\\_sf/Study\\_Solar\\_thermal\\_power\\_plants\\_DLR\\_2021-05.pdf](https://www.dlr.de/sf/en/PortalData/73/Resources/dokumente/publikationen_medien/dlr_und_sf/Study_Solar_thermal_power_plants_DLR_2021-05.pdf). Accessed 28/07/2021.
- [4] J. Lilliestam, R. Pitz-Paal, Concentrating solar power for less than USD 0.07 per kWh : finally the breakthrough, *Renewable Energy Focus*, 26 (2018)17-21, <https://doi.org/10.1016/j.ref.2018.06.002>

- [5] A. Fernandez-Garcia et al., Parabolic-trough solar collectors and their applications, *Renewable and Sustainable Energy Reviews*, 14(7) (2010), 1695-1721, <https://doi.org/10.1016/j.rser.2010.03.012>
- [6] J. Frederiksson et al., A comparison and evaluation of innovative parabolic trough collector concepts for large-scale application, *Solar Energy*, 215 (2021), 266-310, <https://doi.org/10.1016/j.solener.2020.12.017>
- [7] C.K. Ho, B.D. Iverson, Review of high-temperature central receiver designs for concentrated solar power, *Renewable and Sustainable Energy Reviews*, 29 (2014), 835-846, <https://doi.org/10.1016/j.rser.2013.08.099>
- [8] C.K. Ho, Advances in central receivers for concentrating solar applications, *Solar Energy*, 152 (2017), 38-56, <https://doi.org/10.1016/j.solener.2017.03.048>
- [9] G. Zhu et al., History, Current State, and future of linear Fresnel concentrating solar collectors, *Solar Energy*, 103 (2014), 69-652, <https://doi.org/10.1016/j.solener.2013.05.021>
- [10] J. Coventry, C. Andraka, Dish Systems for CSP, *Solar Energy*, 152 (2017), 140-170, <https://doi.org/10.1016/j.solener.2017.02.056>
- [11] A. Bonk et al., Advanced heat transfer fluids for direct molten salt line-focusing CSP plants, *Progress in Energy and Combustion Science*, 67 (2018), 69-87. <https://doi.org/10.1016/j.pecs.2018.02.002>
- [12] A. Bonk et al., Solar Salt – Pushing an old material for energy storage to a new limit, *Applied Energy*, 262(15) (2020), 114535. <https://doi.org/10.1016/j.apenergy.2020.114535>
- [13] L.L. Vant-Hull, The Role of "Allowable Flux Density" in the Design and Operation of Molten-Salt Solar Central Receivers, *Journal of Solar Energy Engineering*, 124(2) (2002), 165-169. <https://doi.org/10.1115/1.1464124>
- [14] Z. Liao et al., Allowable flux density on a solar central receiver, *Renewable Energy*, 2014; 62:747-753. <https://doi.org/10.1016/j.renene.2013.08.044>
- [15] S. Caron et al., A comparative analysis of opto-thermal figures of merit for high temperature solar thermal absorber coatings, *Renewable and Sustainable Energy Reviews*, 154 (2022), 111818. <https://doi.org/10.1016/j.rser.2021.111818>
- [16] International Organization for Standardization, Solar energy – Collector components and materials – Part3: Absorber surface durability, ISO 22975-3:2014 (2014), available at: <https://www.iso.org/standard/61758.html>. Accessed: 28/07/2021.
- [17] International Organization for Standardization, Space systems – Measurement of thermo-optical properties of thermal control materials, ISO 16378:2013, (2013), available at: <https://www.iso.org/standard/56558.html>. Accessed 28/07/2021.
- [18] ASTM International, Standard test method for solar absorptance, reflectance, and transmittance of materials using integrating spheres, ASTM E903:2020, (2020). <https://dx.doi.org/10.1520/E0903-20>
- [19] ASTM International, Standard test method for determination of solar reflectance near ambient temperature using a portable solar reflectometer, ASTM C1549:2016, (2016). <https://doi.org/10.1520/C1549-16>.
- [20] ASTM International, Standard test method for determination of emittance of materials near room temperature using portable emissometers, ASTM C1371:2015, (2015). <https://doi.org/10.1520/C1371-15>
- [21] ASTM International, Standard test methods for total normal emittance of surfaces using inspection-meter techniques, ASTM E408:2013, (2019). <https://doi.org/10.1520/E0408-13R19>

- [22] ASTM International, Standard test method for normal spectral emittance at elevated temperatures, ASTM E307:1972, (2019). <https://dx.doi.org/10.1520/E0307-72R19>
- [23] ASTM International, Standard test method for total hemispherical emittance of surfaces up to 1400°C, ASTM C835:2006, (2020). <https://dx.doi.org/10.1520/C0835-06R20>
- [24] L. Noč et al., High-solar-absorptance CSP coating characterization and reliability testing with isothermal cyclic loads for service-life prediction, *Energy & Environmental Science*, 12 (2019) 1679-1694, <https://doi.org/10.1039/C8EE03536A>
- [25] K. Tsuda et al., Development of high absorption, high durability coatings for solar receivers in CSP plants, *AIP Conference Proceedings*, 2033 (2018), 040039. <https://doi.org/10.1063/1.5067075>
- [26] R. Harzallah et al, Development of high performances solar absorber coatings, *AIP Conference Proceedings*, 2126 (2019), 030026. <https://doi.org/10.1063/1.5117538>
- [27] L. Noč et al., High-temperature “ion baseball” for enhancing concentrated solar power efficiency, *Solar Energy Materials and Solar Cells*, 200 (2019), 109974. <https://doi.org/10.1016/j.solmat.2019.109974>
- [28] F. Cao et al., A review of cermet-based spectrally selective solar absorbers, *Energy & Environmental Science*, 7 (2014), 1615-1627. <https://doi.org/10.1039/C3EE43825B>
- [29] K. Xu et al., A review of high-temperature selective absorber coatings for solar thermal applications, *Journal of Materiomics*, 6(1) (2020), 167-182, <https://doi.org/10.1016/j.jmat.2019.12.012>
- [30] C. Hildebrandt, High-temperature stable absorber coatings for linear concentrating solar thermal power plants, *PhD thesis*, Stuttgart University, (2009), <http://dx.doi.org/10.18419/opus-1802>
- [31] I. Heras Pérez, Multilayer solar selective coatings for high temperature solar applications: from concept to design, *PhD thesis*, Sevilla University, (2016), available at: <http://hdl.handle.net/11441/47789>. Accessed: 28/07/2021.
- [32] C.K. Ho et al., Characterization of Pyromark 2500 Paint for High-Temperature Solar Receivers, *Journal of Solar Energy Engineering*, 136(1) (2014), 014502. <https://doi.org/10.1115/1.4024031>
- [33] K. Burlafinger, A. Vetter, J.C. Brabec, Maximizing concentrated solar power (CSP) plant overall efficiencies by using spectral selective absorbers at optimal operation temperatures, *Solar Energy*, 120 (2015), 428-438. <https://doi.org/10.1016/j.solener.2015.07.023>
- [34] J. Coventry, P. Burge, Optical properties of Pyromark 2500 coatings of variable thicknesses on a range of materials for concentrating solar thermal applications, *AIP Conference Proceedings*, 1850 (2017), 030012. <https://doi.org/10.1063/1.4984355>
- [35] A. Ambrosini et al., Influence of application parameters on stability of Pyromark® 2500 receiver coatings, *AIP Conference Proceedings*, 2126 (2019), 030002. <https://doi.org/10.1063/1.5117514>
- [36] S. Caron et al., Forty shades of black: A benchmark of high temperature sprayable black coatings applied on Haynes 230, *AIP Conference Proceedings*, 2303 (2020), 1560007. <https://doi.org/10.1063/5.0028773>
- [37] K. Zhang et al., A review on thermal stability and high temperature induced ageing mechanisms of solar absorber coatings, *Renewable and Sustainable Energy Reviews*, 67 (2017), 1282-1299, <https://doi.org/10.1016/j.rser.2016.09.083>

- [38] A. Boubault et al., Durability of solar absorber coatings and their cost-effectiveness, *Solar Energy Materials and Solar Cells*, 166 (2017), 176-184. <https://doi.org/10.1016/j.solmat.2017.03.010>
- [39] C.K. Ho, J.E. Pacheco, Levelized Cost of Coating (LCOC) for selective absorber materials, *Solar Energy*, 108 (2014), 315-321. <https://doi.org/10.1016/j.solener.2014.05.017>
- [40] A. Boubault et al., Levelized cost of energy (LCOE) metric to characterize solar absorber coatings for the CSP industry, *Renewable Energy*, 85 (2016), 472-483, <https://doi.org/10.1016/j.renene.2015.06.059>
- [41] Raisalife, EU Project, Horizon 2020, available at: <http://www.raisalife.eu/>. Accessed 28/07/2021.
- [42] S. Caron et al., Accelerated ageing of solar receiver coatings: Experimental results for T91 and VM12 steel substrates, *AIP Conference Proceedings*, 2033 (2018), 230002. <https://doi.org/10.1063/1.5067230>
- [43] S. Caron et al., Durability testing of solar receiver coatings: Experimental results for T91 and VM12 steel substrates, *AIP Conference Proceedings*, 2303 (2020), 150006. <https://doi.org/10.1063/5.0028772>
- [44] R. Reoyo-Prats et al., Accelerated aging of absorber coatings for CSP receivers under real high solar flux – Evolution of their optical properties, *Solar Energy Materials and Solar Cells*, 193 (2019), 92-100. <https://doi.org/10.1016/j.solmat.2018.12.030>
- [45] L. del Campo et al., New experimental device for infrared spectral directional emissivity measurements in a controlled environment, *Review of Scientific Instruments*, 77 (2006), 113111. <https://doi.org/10.1063/1.2393157>
- [46] P. Honnerova et al., New experimental device for high-temperature normal spectral emissivity measurement of coatings, *Measurement Science and Technology*, 25(9) (2014), 095501. <https://doi.org/10.1088/0957-0233/25/9/095501>
- [47] I. Setien-Fernandez et al., First spectral emissivity study of a solar selective coating in the 150-600 °C temperature range, *Solar Energy Materials and Solar Cells*, 117 (2013), 390-395. <https://doi.org/10.1016/j.solmat.2013.07.002>
- [48] T. Echaniz et al., Importance of the spectral emissivity measurements at working temperature to determine the efficiency of a solar selective coating, *Solar Energy Materials and Solar Cells*, 140 (2015), 249-252. <https://doi.org/10.1016/j.solmat.2015.04.009>
- [49] I. Gonzalez de Arrieta et al., Infrared emissivity of copper-alloyed spinel black coatings for concentrated solar power systems, *Solar Energy Materials and Solar Cells*, 200 (2019), 109961. <https://doi.org/10.1016/j.solmat.2019.109961>
- [50] E. Le Baron et al., Round Robin Test for the comparison of spectral emittance measurement apparatuses, *Solar Energy Materials and Solar Cells*, 191 (2019), 476-485. <https://doi.org/10.1016/j.solmat.2018.11.026>
- [51] OMT Solution BV, World Class Innovative Solutions for Optical Materials Characterization (2021), available at: <https://omtsolutions.com/>. Accessed 28/07/2021.
- [52] Surface Optics, 410-Vis-IR Portable Emissometer & Solar Reflectometer, (2021), available at: <https://surfaceoptics.com/products/reflectometers-emissometers/410-vis-ir/>. Accessed: 28/07/2021.
- [53] Surface Optics, 10-Solar Visible / NIR Portable Reflectometer, (2021), available at: <https://surfaceoptics.com/products/reflectometers-emissometers/solar-absorptance-measurements-410/>. Accessed: 28/07/2021.

- [54] Surface Optics, ET-100 Thermal Handheld Emissometer, (2021), available at: <https://surfaceoptics.com/products/reflectometers-emissometers/et100-thermal-hand-held-emissometer/>. Accessed: 28/07/2021.
- [55] AZ Technology, TEMP 2000A, Portable Emissometer/Reflectometer, (2021), available at: <http://www.aztechnology.com/products/reflectometers-and-emissometers/temp-2000a.html>. Accessed: 28/07/2021.
- [56] K. Lauder, Spacecraft Thermal Control Coatings and References, *NASA Technical Report*, NASA/TP-2005-212792, (2005), available at: <http://www.aztechnology.com/wp-content/uploads/PDFs/NASA-TP-2005-212792-Lauder.pdf>. Accessed 28/07/2021.
- [57] Devices and Services Company, Emissometer Model AE1 and RD1 Voltmeter (2021), available at: <https://www.devicesandservices.com/AE1%20RD1%20Spec%20Sheet.pdf>. Accessed 28/07/2021.
- [58] T.G. Kollie, F.J. Weaver, D.L. McElroy, Evaluation of a commercial, portable, ambient-temperature emissometer, *Review of Scientific Instruments*, 61 (1990), 1509-1517. <https://doi.org/10.1063/1.1141162>
- [59] Labsphere Inc., Technical Guide: Reflectance materials and coatings, (2021), available at: <https://www.labsphere.com/site/assets/files/2553/a-guide-to-reflectance-materials-and-coatings.pdf>. Accessed: 28/07/2021.
- [60] ASTM International, Standard Tables for Reference Solar Spectral Irradiances: Direct Normal and Hemispherical on 37° Tilted Surface, ASTM G173:2012, (2020). <https://dx.doi.org/10.1520/G0173-03R20>
- [61] NREL, SMARTS: Simple Model of the Atmospheric Radiative Transfer of Sunshine, (2021), available at: <https://www.nrel.gov/grid/solar-resource/smarts.html>. Accessed: 28/07/2021.
- [62] S. Pratesi, E. Sani, M. De Lucia, Optical and Structural Characterization of Nickel Coatings for Solar Collector Receivers, *International Journal of Photoenergy*, (2014), 834128. <http://dx.doi.org/10.1155/2014/834128>
- [63] S. Pratesi et al., Structural and optical properties of copper-coated substrates for solar thermal absorbers, *Superlattices and Microstructures*, 98 (2016), 342-350. <https://doi.org/10.1016/j.spmi.2016.08.031>
- [64] F. Buendia-Martinez et al., Uncertainty Study of Reflectance Measurements for Concentrating Solar Reflectors, *IEEE Transactions on Instrumentation and Measurement*, 69(9) (2020). DOI: 10.1109/TIM.2020.2975387

**Chapter 5. Intercomparison of opto-thermal spectral measurements for concentrating solar thermal receiver materials from room temperature up to 800 °C**





## 5 Intercomparison of opto-thermal spectral measurements for concentrating solar thermal receiver materials from room temperature up to 800 °C

### 5.0 Abstract

An intercomparison of opto-thermal spectral measurements has been performed for some relevant receiver materials in concentrating solar thermal applications, from room temperature up to 800 °C. Five European laboratories performed spectral measurements at room temperature, while two laboratories performed infrared spectral measurements at operating temperature up to 800 °C. Relevant materials include Haynes 230 (oxidised, Pyromark 2500 and industrial black coating) and silicon carbide. Two key figures of merit were analysed: i) solar absorptance  $\alpha_{sol}$  at room temperature, over the spectral range [0.3; 2.5]  $\mu\text{m}$ , ii) thermal emittance  $\epsilon_{th}(T)$ , over the common spectral range [2; 14]  $\mu\text{m}$ , derived from spectral measurements performed from room temperature up to 800 °C.

Oxidised Haynes 230 reached an  $\alpha_{sol}$  value of  $90.9 \pm 1.0\%$ . Pyromark 2500 reached an  $\alpha_{sol}$  value of  $96.3 \pm 0.5\%$ , while the industrial black coating achieved an  $\alpha_{sol}$  value of  $97.0 \pm 0.4\%$ . Silicon carbide reached an  $\alpha_{sol}$  value of  $93.5 \pm 1.1\%$ . Low standard deviations in  $\alpha_{sol}$  indicate reproducible measurements at room temperature.

For oxidised Haynes 230, the  $\epsilon_{th,calc}(T)$  value derived from room temperature varied from 55% at 25 °C up to 81% at 800 °C. For Pyromark 2500 and the industrial black coating,  $\epsilon_{th,calc}(T)$  fluctuated between 90% and 95%, with a weak temperature dependence. For silicon carbide,  $\epsilon_{th,calc}(T)$  varied from 70% at room temperature up to 86% at 800 °C. The typical standard deviation among participating laboratories is about 3%.  $\epsilon_{th,meas}(T)$  values derived from spectral measurements at operating temperature were consistent within a few percentage points in comparison to  $\epsilon_{th,calc}(T)$  values derived from spectral measurements at room temperature.

### 5.1 Introduction

Solar energy is a key player in the ongoing global energy transition towards decarbonization [1]. Concentrated Solar Thermal (CST) technology [2,3] could provide solar heat for a variety of industrial processes, especially high temperature processes above 400 °C, which may be difficult to electrify. CST combine a mirror field coupled to a thermal receiver to convert direct sunlight into useful heat. The thermal receiver is a key component, which absorbs solar power concentrated by the mirror field and transfers it to a heat transfer fluid (HTF). Two configurations exist, i.e. line focusing systems such as parabolic troughs and point focusing systems, such as Central Receiver Systems (CRS) [4-6].

The opto-thermal performance and durability of receiver materials and coatings is of particular importance [7-9]. Two key figures of merit, i.e. solar absorptance  $\alpha_{sol}$  and thermal emittance  $\epsilon_{th}$  are considered for the characterization of such materials [10]. These figures are most often calculated on the basis of room temperature (RT) optical measurements performed with laboratory spectrophotometers [11,12]. Such spectral measurements have also been performed on some relevant materials and coatings at operating temperature up to 800 °C (OT) [13-16].

Spectral emissivity datasets at RT and OT are not only important for the evaluation and comparison of materials, but also for the design, calibration and operation of radiometric instrumentation, such as infrared thermography [17,18]. The following questions are relevant for scientists and engineers:

- i) Are significant deviations observed for figures of merit derived from RT and OT spectral measurements?
- ii) Does the material exhibit a grey or a selective behavior in certain spectral ranges ?
- iii) Are local spectral shifts observed at higher temperature, outside of known atmospheric absorption bands?
- iv) Does the emittance vary with the angular incidence of measurement at OT ?

This chapter focuses on the intercomparison of spectral emissivity datasets for relevant materials in CRS applications. Substrates include nickel-chromium based superalloys (Haynes 230, short H230) [19] and Silicon Carbide (SiC) [20-21]. H230 samples are either oxidised or coated with black paints, such as Pyromark 2500 [22-26] or an industrial black coating provided by Brightsource Industries. Spectral emissivity is measured and compared between five different laboratories, first at RT. Two laboratories (CEA, CNRS) further measure spectral emissivity at OT, up to 800 °C, with three complimentary experimental setups.

The first section of this paper describes materials and methods, i.e. test campaign organization, reference materials, laboratory instrumentation and data processing. The second section covers the analysis and comparison of available experimental results at RT and OT.

## 5.2 Materials and methods

### 5.2.1 Organization and participants

This test campaign involved five research centres (CEA, CIEMAT, CNRS, DLR, LNEG), which laboratories are located in three European countries (France, Portugal, Spain). Participants and their role are described in Table 5.1. H230 samples were sequentially measured by each laboratory at RT, then submitted to CEA and CNRS for independent measurements at OT. SiC samples were measured independently by each laboratory. CIEMAT Madrid was included in this test campaign upon the completion of OT spectral measurements.

*Table 5.1: Test campaign participants and roles.*

<b>Participant</b>	<b>Location</b>	<b>Role</b>	<b>Campaigns</b>
CEA	Bourget-du-Lac, France	Measurements	RR-RT RR-OT (x1)
CIEMAT Madrid	Madrid, Spain	Measurements (a posteriori)	RR-RT
CIEMAT-PSA	Tabernas, Spain	Sample preparation (SiC)	[-]
CIEMAT-DLR (OPAC)	Tabernas, Spain	Measurements (initial)	RR-RT
PROMES-CNRS	Odeillo, France Perpignan, France	Measurements Sample preparation (cut)	RR-RT RR-OT (x2)
DLR	Almería, Spain	Sample preparation (H230) Campaign coordination Data curation, evaluation	[-]
LNEG	Lisbon, Portugal	Measurements	RR-RT

### 5.2.2 Reference samples

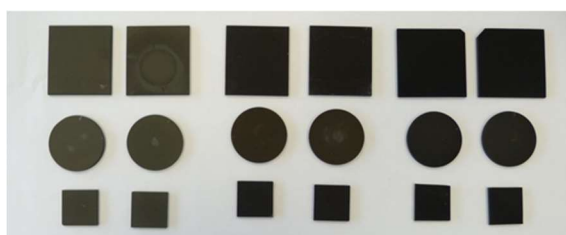
Eighteen H230 flat sample coupons were prepared for the RT and OT test campaigns. These coupons are described in Table 5.2 and are shown in Figure 5.1.a. This sample lot is divided in three batches: i) oxidised H230, ii) Pyromark 2500 and iii) an industrial black coating. For each batch, three geometries were prepared (rectangular, disk, square inch), to comply with specifications for OT measurements. For each geometry, two duplicates were prepared and samples were previously exposed in a muffle furnace up to 800 °C before starting the test campaign.

A subset of SiC sample coupons is shown in Figure 5.1.b. Square samples (50x50 mm, 5 mm thickness) were originally submitted for RT and OT measurements. Without appropriate machining, OT measurements could only be satisfactorily performed by PROMES-CNRS laboratory up to 500 °C.

*Table 5.2: H230 flat sample coupons for RT and OT campaigns. Sample thickness: 2 mm.*

Sample ID	Geometry	Coating	Surface preparation	Coating application	Thermal treatment
R01A/R01B	Rectangle, 45x50 mm	Uncoated	Sand blasted	N.A.	Oxidation 100 h at 800 °C
D01A/D01B	Disk, Ø 40 mm		Sand blasted		
A1/A2	Square, side length 25.4 mm		Sand blasted		
R02A/R02B	Rectangle, 45x50 mm	Pyromark 2500	Sand blasted	Workshop, Spray gun	Curing: 2h at 250 °C 2h at 540 °C Pre-aging: 100h at 800 °C
D02A/D02B	Disk, Ø 40 mm		Sand blasted		
B1/B2	Square, side length 25.4 mm		Sand blasted		
S1/S2	Rectangle, 45x50 mm	Industrial, black	Sand blasted	External, proprietary	External, proprietary
S3/S4	Disk, Ø 40 mm		Sand blasted		
S5/S6	Square, side length 25.4 mm		Sand blasted		

a) H230 samples



b) SiC samples

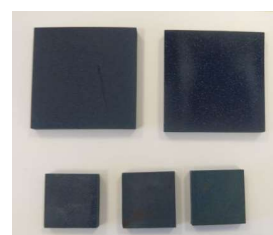


*Figure 5.1: a) H230 sample coupons submitted for RT and OT measurements. Samples are shown upon return after both RT and OT test campaigns. b) SiC samples submitted for RT and OT measurements. Top: original samples. Bottom: Square inch samples cut by PROMES-CNRS for OT measurements up to 500 °C.*

## 5.2.3 Instrumentation

### 5.2.3.1 RT measurements

#### 5.2.3.1.1 Laboratory spectrophotometers

For RT measurements, spectral measurements are carried out from ultraviolet (UV) up to infrared (IR) wavelengths. This requires each participating laboratory to combine spectral measurements from two complementary spectrophotometers. Some laboratory spectrophotometers and integrating sphere geometries are illustrated in Figure 5.2. An inventory of instrumentation is described in Table 5.3, while some spectrophotometer characteristics are listed in Table 5.4. Spectral ranges and raw dataset resolutions are summarised in Table 5.5.

In the UV, visible and near IR (UV-VIS-NIR), all laboratories used similar instrumentation, i.e. a Perkin Elmer Lambda 950 or 1050 spectrophotometer, with a white Ba<sub>2</sub>SO<sub>4</sub> coated integrating sphere of diameter 150 mm. The light source incidence angle on the sample is near normal ( $\theta = 8^\circ$ ). In the IR spectral range, all laboratories use a Fourier Transform (FTIR) spectrophotometer. There are however diverse models, i.e. Perkin Elmer Frontier, Bruker Vertex 70 and Nicolet 6700. All participants except PROMES-CNRS use a Pike Ltd Mid-IR gold diffuse coated integrating sphere of diameter 76.2 mm. The light source incidence angle on the sample is also near normal ( $\theta = 12^\circ$ ). PROMES-CNRS used the SOC 100 HDR hemi-ellipsoid coated with specular gold, for which the light source incidence angle  $\theta$  is adjustable from  $8^\circ$  to  $80^\circ$  and set to  $8^\circ$  for these measurements.

For each participant, there is a partial spectral overlap between UV-VIS-NIR and FTIR datasets, at least from  $2 \mu\text{m}$  to  $2.5 \mu\text{m}$ . A spectral mismatch may be induced during measurements, hypothetically explained by different instrument configurations (integrating sphere, detector type, calibration procedure). This mismatch should be ideally minimal for any sample.

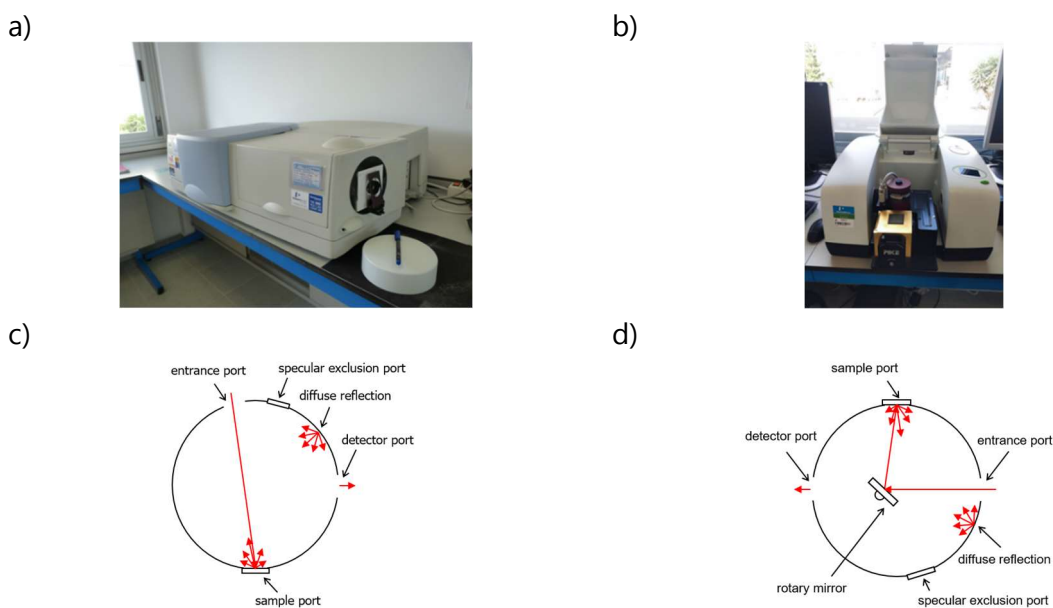


*Figure 5.2: a) Perkin Elmer Lambda 1050 spectrophotometer. b) Perkin Elmer Frontier FTIR with Pike Ltd Mid-IR downward looking integrating sphere. c) Geometrical configuration for the Lambda 950/1050 integrating sphere. d) Geometrical configuration for the Pike Ltd mid-IR integrating sphere.*

Table 5.3: Inventory of spectrophotometer for RT measurements.

Participant	UV-VIS-NIR ( $\leq 2.5 \mu\text{m}$ )		Infrared ( $> 1.5 \mu\text{m}$ )	
	Instrument	Integrating sphere	Instrument	Integrating sphere
CEA	Perkin Elmer Lambda 950	Perkin Elmer White diffuse $\theta: 8^\circ; \text{Ø}: 150 \text{ mm}$	Bruker Vertex 70 FTIR	Pike Ltd Mid-IR Gold diffuse $\theta: 12^\circ; \text{Ø}: 76.2 \text{ mm}$
CIEMAT Madrid	Perkin Elmer Lambda 950	Perkin Elmer White diffuse $\theta: 8^\circ; \text{Ø}: 150 \text{ mm}$	Perkin Elmer Frontier FTIR	Pike Ltd Mid-IR Gold diffuse $\theta: 12^\circ; \text{Ø}: 76.2 \text{ mm}$
CIEMAT-DLR (OPAC)	Perkin Elmer Lambda 1050	Perkin Elmer White diffuse $\theta: 8^\circ; \text{Ø}: 150 \text{ mm}$	Perkin Elmer Frontier FTIR	Pike Ltd Mid-IR Gold diffuse $\theta: 12^\circ; \text{Ø}: 76.2 \text{ mm}$
PROMES-CNRS	Perkin Elmer Lambda 950	Perkin Elmer White diffuse $\theta: 8^\circ; \text{Ø}: 150 \text{ mm}$	Nicolet 6700 FTIR	SOC 100 HDR Specular gold Hemiellipsoid $\theta: 8^\circ; \text{Range: } 8\text{-}80^\circ$
LNEG	Perkin Elmer Lambda 950	Perkin Elmer White diffuse $\theta: 8^\circ; \text{Ø}: 150 \text{ mm}$	Perkin Elmer Frontier FTIR	Pike Ltd Mid-IR Gold diffuse $\theta: 12^\circ; \text{Ø}: 76.2 \text{ mm}$

Table 5.4: Overview of spectrophotometer characteristics.

Participant	UV-VIS-NIR ( $\leq 2.5 \mu\text{m}$ )		Infrared ( $> 1.5 \mu\text{m}$ )	
	Light sources	Detectors (PMT)	Light sources	Detectors
CEA	UV: Deuterium ( $^2\text{H}$ ); VIS-IR: Tungsten (W)	InGaAs & PbS Peltier cooling	IR filament	MCT LN <sub>2</sub> cooling
CIEMAT Madrid	UV: Deuterium ( $^2\text{H}$ ); VIS-IR: Tungsten (W)	InGaAs & PbS Peltier cooling	IR filament	MCT LN <sub>2</sub> cooling
CIEMAT-DLR (OPAC)	UV: Deuterium ( $^2\text{H}$ ); VIS-IR: Tungsten (W)	InGaAs & PbS Peltier cooling	IR filament	MCT LN <sub>2</sub> cooling
PROMES-CNRS	UV: Deuterium ( $^2\text{H}$ ); VIS-IR: Tungsten (W)	InGaAs & PbS Peltier cooling	Blackbody (700 °C)	InGaAs & DTGS Peltier cooling
LNEG	UV: Deuterium ( $^2\text{H}$ ); VIS-IR: Tungsten (W)	InGaAs & PbS Peltier cooling	IR filament	DTGS without cooling

Table 5.5: Spectral ranges and sampling resolutions of raw datasets.

Participant	UV-VIS-NIR ( $\leq 2.5 \mu\text{m}$ )		Infrared ( $> 1.5 \mu\text{m}$ )	
	Spectral range [ $\mu\text{m}$ ]	Spectral resolution [nm]	Spectral range [ $\mu\text{m}$ ]	Spectral resolution [nm]
CEA	0.28 – 2.5 $\mu\text{m}$	5 nm	1.8 – 16 $\mu\text{m}$	10 nm
CIEMAT Madrid	0.28 – 2.5 $\mu\text{m}$	10 nm	2 – 17 $\mu\text{m}$	~ 2 nm
CIEMAT-DLR (OPAC)	0.28 – 2.5 $\mu\text{m}$	5 nm	2 – 16 $\mu\text{m}$	4 nm
PROMES-CNRS	0.25 – 2.5 $\mu\text{m}$	5 nm	1.5 – 26 $\mu\text{m}$	variable
LNEG	0.3 – 2.5 $\mu\text{m}$	5 nm	2 – 16 $\mu\text{m}$	16 or 20 nm

### 5.2.3.1.2 Baseline coupons

An inventory of flat baseline coupons is provided in Table 5.6, while typical reflectivity spectra are shown in Figure 3. These baseline coupons are used as reference for the calibration of spectral datasets. All participants expect CIEMAT-DLR (OPAC) used a white diffuse flat coupon (Spectralon, 99% reflectance) for UV-VIS-NIR measurements while a gold diffuse (Infragold, 94% reflectance) or gold specular flat coupon is used for FTIR measurements. These coupons are traceable to primary standards. CIEMAT-DLR used custom secondary standards, i.e. a black coated sample for UV-VIS-NIR and a black or solar selective coupon for FTIR measurements. These secondary standards were calibrated by OMT Solutions, Netherlands [11].

The selection of a baseline is a subjective decision made by the operator, depending on the sample to be measured. An empirical rule of thumb consists in selecting a baseline “similar” to the sample to be measured. If the baseline has a flat spectral response, it may be suitable for a broader range of materials, while custom secondary standards are more prone to induce spectral mismatches.

Table 5.6: Baseline flat reference coupons used for calibration.

	UV-VIS-NIR ( $\leq 2.5 \mu\text{m}$ )	Infrared ( $> 1.5 \mu\text{m}$ )
Participant	Baseline	Baseline
CEA	White diffuse, Spectralon 99%, certified yearly at LNE, France	Gold diffuse, Infragold certified yearly at LNE, France
CIEMAT Madrid	White diffuse, Spectralon 99% Labsphere calibration	Gold diffuse, Infragold
CIEMAT-DLR (OPAC)	Black (secondary standard, OMT)	Black (secondary standard, OMT) Selective (secondary standard, OMT)
PROMES-CNRS	White diffuse, Spectralon 99% Labsphere calibration	Gold diffuse (Infragold) Specular gold, NIST traceable
LNEG	White diffuse, Spectralon 99% Labsphere calibration	Gold diffuse (Infragold), Avian Tech

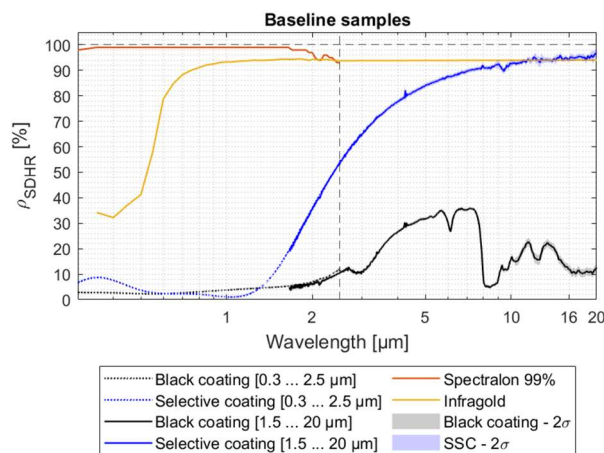


Figure 5.3: Spectral directional hemispherical reflectivity (SDHR) of flat baseline coupons.

### 5.2.3.2 OT measurements

CEA and PROMES-CNRS performed OT measurements with independent experimental setups. Temperature and spectral ranges are summarised in Table 5.7.

Table 5.7: Temperature and spectral ranges for OT measurements.

Participant	Instrument	Temperature range	Spectral range
CEA	Bruker Vertex 70 FTIR + IR 563/301 blackbody	200 to 800 °C	DTGS: 2 to 26 μm
PROMES-CNRS	Nicolet 6700 FTIR + SOC 100 HDR	RT to 500 °C	InGaAs: 1 to 2 μm DTGS: 2 to 26 μm
PROMES-CNRS	MEDIASE SR 5000N spectroradiometer	~ 700 to 800 °C Tentative < 700 °C	InSb+MCT (77 K): 1.34 to 14 μm

### 5.2.3.2.1 CEA laboratory setup

CEA laboratory setup development is described in [27] and the equipment is shown in Figure 4. This setup consists of a Bruker Vertex 70 FTIR spectrophotometer, with a modified optical path, including a custom optical bench. This optical bench is mounted between the heated sample and a blackbody source IR 563/301. Inside the optical bench, a rotary parabolic mirror is alternatively switched towards the heated sample and the blackbody source. The sample holder integrates a thermal shield and a thermal control unit. The sample surface temperature  $T_{sample}$  is measured on its front side with six thermocouples.

The spectral emissivity  $\epsilon(\lambda, T)$  of the sample is the ratio between the radiance of the sample  $L_{sample}(\lambda, T)$  and the radiance of the blackbody  $L_{BB}(\lambda, T)$  at the same temperature  $T$ . The response of the spectrophotometer is compared to the theoretical blackbody spectrum to determine a correction function for this instrument.

During OT measurements, the sample temperature could be controlled from 200 °C to 750 °C. The angle of incidence  $\theta$  is set to 12°. The spectral range spans from 2 μm to 26 μm with a variable resolution.

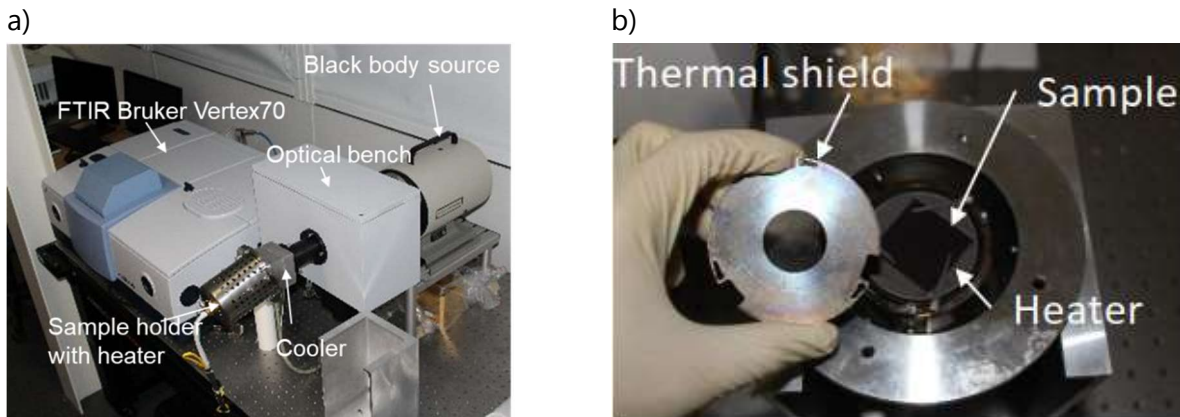


Figure 5.4: CEA laboratory setup for spectral emissivity measurements at operating temperature. a) Benchtop optical assembly. b) Sample holder overview.

### 5.2.3.2.2 PROMES-CNRS laboratory setup

PROMES-CNRS laboratory setup consists of a Nicolet 6700 FTIR combined with the hemi-ellipsoid SOC 100 HDR. The sample is mounted on a sample holder, which includes a heater which can heat the sample from RT (25 °C) up to 500 °C. Two detectors are used for OT measurements: InGaAs (1 μm to 2 μm) and DTGS (2 μm to 26 μm). This measurement setup does not require a blackbody and there is no modification of the spectrophotometer optical path in comparison to RT measurements.

### 5.2.3.2.3 MEDIASE setup

The MEDIASE setup operated by PROMES-CNRS is shown in Figure 5.5 and described in [19,20]. The sample is mounted at the focus of the 1 MW solar furnace and heated on its backside with concentrated solar radiation (up to  $10 \text{ MW/m}^2$ ), through a hemispherical silica window. The disk sample is maintained in the water-cooled sample holder by three thin alumina needles placed every  $120^\circ$  around the sample circumference.

The sample temperature is measured on the front side with a two-colour pyro-reflectometer developed at PROMES-CNRS [29]. Given the very low reflectivity of tested materials, the temperature measurement by pyro-reflectometry was actually not possible. The sample temperature was thus measured by applying the two-colour pyrometry technique with the installed two-colour pyro-reflectometer. The setup is equipped with a turbo-molecular vacuum pump, which allows operating under vacuum conditions to minimise sample oxidation. During OT measurements, all experiments were performed under secondary vacuum at  $\sim 2 \cdot 10^{-3} \text{ Pa}$ .

The radiance measurements are carried out with a SR-5000N spectroradiometer [30]. The spectroradiometer is equipped with an InSb – MCT sandwich detector cooled to 77 K with liquid nitrogen ( $\text{LN}_2$ ), superseding a MCT detector cooled by Peltier effect to 213 K. Spectral measurements are carried out from  $1.34 \mu\text{m}$  up to  $14 \mu\text{m}$ . The spectral resolution increases stepwise from 13 nm ( $1.34 - 2.55 \mu\text{m}$ ) to 74 nm ( $8.4 - 14 \mu\text{m}$ ). The distance between the sample and the spectroradiometer is 1 m. The spectroradiometer looks on the heated sample through a thallium-iodo-bromide (KRS5) window. Using an original three mirror goniometer system developed by PROMES-CNRS, spectral directional emissivity measurements are obtained for several incidence angles, i.e. from  $0^\circ$  to  $80^\circ$ , in steps of  $10^\circ$ , as well as for  $45^\circ$  and  $75^\circ$ . The spectroradiometer-goniometer optical assembly and the pyroreflectometer were calibrated before the test campaign, in front of a blackbody which reference temperature is measured with a standard pyrometer.

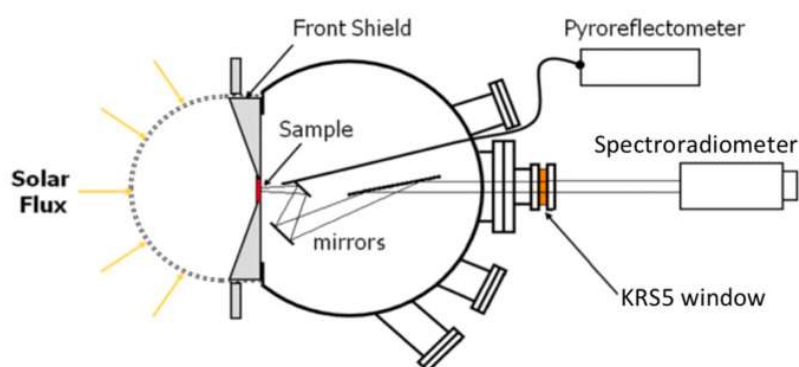


*Figure 5.5: MEDIASE setup mounted at the 1 MW solar furnace in Odeillo, France.*

## 5.2.4 Data processing

### 5.2.4.1 Data curation

A common spectral range is defined for the calculation of figures of merit:  $\alpha_{sol}$  and  $\epsilon_{th}$ . The common UV-VIS-NIR spectral range spans from  $0.3 \mu\text{m}$  to  $2.5 \mu\text{m}$ , while the common spectral range for IR measurements spans from  $2 \mu\text{m}$  to  $14 \mu\text{m}$ , according to Table 5.5 and Table 5.7.



Both spectral ranges overlap from 2  $\mu\text{m}$  to 2.5  $\mu\text{m}$ . The spectral resolution is set to 5 nm by linear interpolation of spectral datasets.

### 5.2.4.2 Reflectivity measurements

For all RT and OT reflectivity measurements, the sample SDHR ( $\rho_{sample,SDHR}$ ) is calculated with a set of spectrophotometer measurements according to (Eq.5.1). First the sample port is left empty for a zeroline or background measurement ( $I_{zero,meas}$ ). A baseline coupon is then measured ( $I_{base,meas}$ ). Its reference calibration data is referred as  $\rho_{base,calib}$ . The sample coupon is then measured after its temperature is stabilised to the desired setpoint ( $I_{sample,meas}$ ).

$$\rho_{sample,SDHR}(\lambda, \theta, T) = \frac{I_{sample,meas}(\lambda, \theta, T) - I_{zero,meas}(\lambda, \theta, RT)}{I_{base,meas}(\lambda, \theta, RT) - I_{zero,meas}(\lambda, \theta, RT)} \rho_{base,calib} \quad (5.1)$$

Assuming opaque samples, the spectral absorptivity or emissivity is derived according to Kirchhoff's law of thermal radiation (Eq.5.2):

$$\alpha(\lambda) = 1 - \rho(\lambda); \quad \alpha(\lambda) = \varepsilon(\lambda) \quad (5.2)$$

### 5.2.4.3 Radiance measurements

For OT measurements involving a blackbody reference, the sample radiance  $L_{sample}$  is measured instead of its spectral reflectivity. CEA setup involves a direct comparison with a blackbody reference during the measurement, while MEDIASE setup involves a comparison with an a priori radiometric calibration of the spectroradiometer under laboratory conditions.

#### 5.2.4.3.1 CEA setup

The spectrophotometer measures the radiance of the hot sample but also the luminance reflected by the surrounding environment. The measured signal  $L^*(\lambda, T)$  is the sum of two radiance terms (Eq.5.3).

$$L^*(\lambda, T) = \varepsilon(\lambda, T_{sample})L_{BB}(\lambda, T_{sample}) + [1 - \varepsilon(\lambda, T_{sample})]L_{BB}(\lambda, T_{env}) \quad (5.3)$$

The spectral emissivity  $\varepsilon(\lambda, T_{sample})$  of a sample is thus calculated according to (Eq.5.4):

$$\varepsilon(\lambda, T) = \frac{L^*(\lambda, T_{sample}) - L_{BB}(\lambda, T_{env})}{L_{BB}(\lambda, T_{sample}) - L_{BB}(\lambda, T_{env})} \quad (5.4)$$

#### 5.2.4.3.2 MEDIASE setup

The spectroradiometer signal measures the spectral directional radiance of the heated sample  $L_s(\lambda, \theta, T)$ . The spectral directional emissivity  $\varepsilon(\lambda, \theta, T)$  is calculated according to (Eq.5.5), for measurements at temperature significantly higher than RT:

$$\varepsilon(\lambda, \theta, T) = \frac{L_{sample}(\lambda, \theta, T) \tau_{atm,sample}(\lambda, d = 1 \text{ m})}{L_{BB}(\lambda, T) \tau_{atm,BB}(\lambda, d = 1 \text{ m})} \quad (5.5)$$

If sample and blackbody measurements are performed in a short period of time, the effect of atmospheric spectral transmissivity on the measurement would cancel out ( $\tau_{atm,sample}/\tau_{atm,BB} \sim 1$ ). During OT measurements, this time interval varied from a few days to a few months. Local atmospheric absorption effects could be observed in some spectra, mainly due to H<sub>2</sub>O and CO<sub>2</sub>. The most visible absorption bands are located around 1.37, 1.87, 2.7, 4.2 and 5.5-7.3  $\mu\text{m}$ .

The spectral hemispherical emissivity  $\varepsilon(\lambda, T)$  is calculated according to (Eq.5.6), assuming that  $\varepsilon(\theta=90^\circ)=0$ :

$$\varepsilon(\lambda, T) = \int_0^{\pi/2} \varepsilon(\lambda, \theta, T) \sin(2\theta) d\theta \quad (5.6)$$

#### 5.2.4.4 Figures of merit

##### 5.2.4.4.1 Solar absorptance

Solar absorptance  $\alpha_{sol}(AM)$  is calculated for UV-VIS-NIR measurements at RT according to (Eq.5.7).  $G_{sol}(\lambda, AM)$  corresponds to the reference solar spectrum for a given Air Mass ( $AM$ ). This spectrum is defined according to ASTM G173-03 [16], using SMARTS v2.9.2, for direct and circumsolar radiation, setting  $AM$  to 1.5d. The common UV-VIS-NIR spectral range is selected, i.e.  $\lambda_1=0.3 \mu\text{m}$ ;  $\lambda_2=2.5 \mu\text{m}$ .

$$\alpha_{sol}(AM) = \frac{\int_{\lambda_1}^{\lambda_2} [1 - \rho_{sample,SDHR}(\lambda, \theta, RT)] G_{sol}(\lambda, AM) d\lambda}{\int_{\lambda_1}^{\lambda_2} G_{sol}(\lambda, AM) d\lambda} \quad (5.7)$$

##### 5.2.4.4.2 Thermal emittance

Thermal emittance  $\varepsilon_{th}(T)$  is calculated from IR measurements at RT and OT according to (Eq.5.8). The common IR spectral range is defined for integration, i.e.  $\lambda_3=2 \mu\text{m}$  and  $\lambda_4=14 \mu\text{m}$ . FTIR and radiance measurements are considered for this calculation.

$$\varepsilon_{th}(T) = \frac{\int_{\lambda_3}^{\lambda_4} \varepsilon(\lambda, T) L_{BB}(\lambda, T) d\lambda}{\int_{\lambda_3}^{\lambda_4} L_{BB}(\lambda, T) d\lambda} \quad (5.8)$$

$L_{BB}$  corresponds to the blackbody radiance, calculated according to Planck's law (Eq.5.9):

$$L_{BB}(\lambda, T) = \frac{2\pi hc^2}{\lambda^5 \left[ \exp\left(\frac{hc}{\lambda k T_{abs}}\right) - 1 \right]} \quad (5.9)$$

For RT measurements,  $\varepsilon(\lambda, T)$  is assumed to remain constant at any temperature (Eq.5.10). The thermal emittance  $\varepsilon_{th}(T)$  calculated according to (Eq.5.8) is labeled  $\varepsilon_{th,calc}(T)$ .

$$\frac{\partial \varepsilon(\lambda, T)}{\partial T} \sim 0 \quad (5.10)$$

For OT measurements,  $\varepsilon(\lambda, T)$  is directly measured, assuming there is no sample degradation at higher temperature. The thermal emittance  $\varepsilon_{th}(T)$  is then labeled  $\varepsilon_{th,meas}(T)$ . The main objective of this chapter is to observe whether there are significant deviations between  $\varepsilon_{th,calc}(T)$  and  $\varepsilon_{th,meas}(T)$  for selected materials (Eq.5.11).

$$\Delta\varepsilon(T) = \varepsilon_{th,meas}(T) - \varepsilon_{th,calc}(T) \quad (5.11)$$

It is worth observing that the common IR spectral range [2; 14]  $\mu\text{m}$  covers a fraction  $f_{\sigma T^4}$  of the total blackbody radiance (Eq.5.12). The thermal emittance  $\varepsilon_{th}(T)$  defined above (Eq.5.8) thus approximates the total thermal emittance of the reference surface.

$$f_{\sigma T^4} = \frac{\int_{\lambda_3}^{\lambda_4} E_{bb}(\lambda, T) d\lambda}{\int_0^{\infty} E_{bb}(\lambda, T) d\lambda} = \frac{\int_{\lambda_3}^{\lambda_4} E_{bb}(\lambda, T) d\lambda}{\sigma T^4} \quad (5.12)$$

The reference solar spectrum [31] is shown in Figure 5.6.a) and compared to the blackbody spectral radiance at 25 °C and 800 °C. The fraction  $f_{\sigma T^4}$  is shown for different spectral bands as a function of blackbody temperature in Figure 5.6 b). At low temperature, the spectral overlap of the blackbody and the reference solar spectra is negligible (Figure 5.6.a), while the spectral overlap below 2 μm is no longer negligible as the blackbody temperature increases.

The analysis of  $f_{\sigma T^4}$  (Figure 5.6.b) shows that the upper integration limit (14 - 50 μm) has a significant impact on the thermal emittance calculation (Eq.8) as the temperature decreases. The lower integration limit (0.3 - 2 μm) has a significant impact on the thermal emittance calculation as the temperature increases. The red curve (interval 0.3 - 14 μm) and dark blue curve (interval 2 - 14 μm) overlap within 1% from 25 °C to 450 °C, while the deviation increases at higher temperature levels. Consequently,  $\epsilon_{th}$  values integrated from 2 μm to 14 μm are slightly underestimated in comparison to  $\epsilon_{th}$  values integrated from 0.3 μm to 16 μm for the selected materials, above 500 °C. This deviation increases with temperature and its average value is estimated at 0.4% for 800 °C.

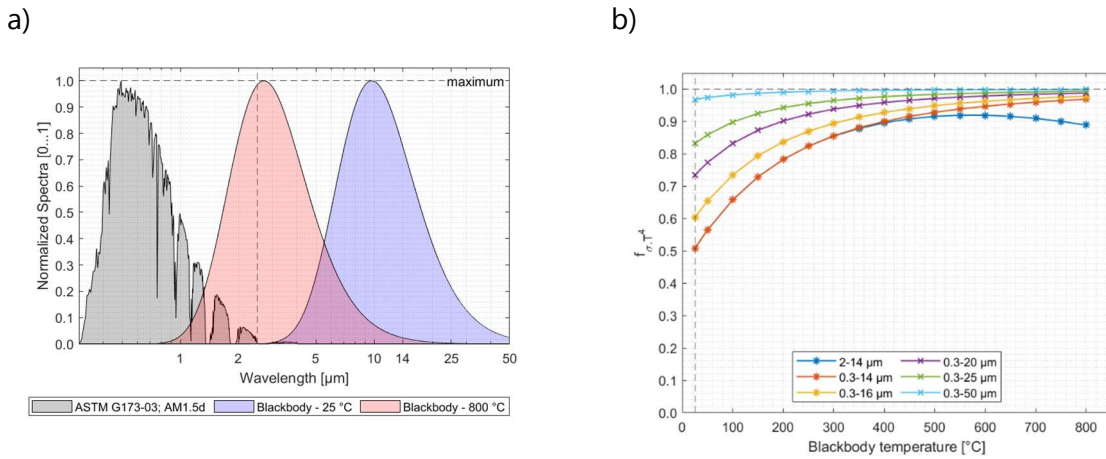


Figure 5.6: a) Reference solar spectrum [31] and blackbody spectra at 25 °C and 800 °C. b) Fraction of Stefan-Boltzmann law ( $f_{\sigma T^4}$ ) as a function of blackbody temperature for different spectral ranges.

### 5.2.4.5 Statistical treatment

For each measured sample (j), a set of statistical indicators is computed for figures of merit  $\alpha_{sol}$  and  $\epsilon_{th}(T)$  when applicable, from each participating laboratory (i). Following statistical indicators are calculated: i) Mean value  $\mu_j$  ii) Standard deviation  $\sigma_j$  iii) Coefficient of variation  $CV_j = \sigma_j/\mu_j$  iv) the Z-score, defined according to ISO 13528:2015 [32] (Eq.5.13).

$$Z_{i,j} = \frac{x_{i,j} - \mu_j}{\sigma_j} \quad (5.13)$$

The Z-score  $Z_{i,j}$  is calculated for each participating laboratory (i), considering the corresponding figure of merit  $x_{i,j}$  for a given sample j. The Z-score is interpreted as follows:

- if  $|Z\text{-score}| < 2$ , the comparison is satisfactory
- if  $2 < |Z\text{-score}| < 3$ , the comparison is questionable
- if  $|Z\text{-score}| > 3$ , the comparison is unsatisfactory

## 5.3 Results and discussion

### 5.3.1 Room temperature

#### 5.3.1.1 Solar absorptance

Solar absorptance results for H230 and SiC sample coupons are summarised in Table 5.8 and shown in Figure 5.7. Oxidised H230 sample coupons reach an  $\alpha_{sol}$  value of  $90.9 \pm 1.0\%$ . Meanwhile, Pyromark 2500 sample coupons reach an  $\alpha_{sol}$  value of  $96.3 \pm 0.5\%$ , while the industrial grade black coating achieves an  $\alpha_{sol}$  value of  $97.0 \pm 0.4\%$ . The low standard deviation indicates reproducible measurements over a quite homogeneous sample batch. Each participating laboratory performed spectral measurements on three spots. The typical standard deviation for  $\alpha_{sol}$  due to coating inhomogeneity was less than 0.1%. For SiC samples,  $\alpha_{sol}$  value reaches  $93.5 \pm 1.1\%$ . A slightly higher standard deviation is observed for SiC in comparison to black coated samples, probably explained by the initial sample batch slight inhomogeneity. All measurements lie within one standard deviation.

A few patterns can be identified analysing Z-scores in Figure 5.7. For instance, CIEMAT-DLR (OPAC) laboratory tends to underestimate  $\alpha_{sol}$  for oxidised H230 sample coupons ( $Z \sim -1.5$ ). Measurements performed by CIEMAT Madrid after the OT test campaign tend to be consistent with previous measurements, except for a few flat disk samples which degraded during transport (D02A/D02B, S3/S4;  $Z \sim -1.8$ ). All Z-scores are lower than 2, the comparison is thus statistically satisfactory.

*Table 5.8: Summary of solar absorptance  $\alpha_{sol}$  results for H230 and SiC samples at RT.*

<b>Sample</b>	<b>CEA</b>	<b>CIEMAT-DLR (OPAC)</b>	<b>PROMES-CNRS</b>	<b>LNEG</b>	<b>CIEMAT Madrid</b>	<b>Mean <math>\mu</math></b>	<b>Stdev <math>\sigma</math></b>	<b>CV <math>\sigma/\mu</math></b>
R01A	90.4%	88.9%	90.3%	91.5%	91.0%	90.4%	1.0%	1.1%
R01B	90.6%	89.1%	90.6%	91.6%	91.2%	90.6%	1.0%	1.1%
D01A	90.2%	88.1%	89.8%	91.0%	91.3%	90.1%	1.3%	1.4%
D01B	91.2%	89.9%	90.9%	92.1%	91.8%	91.2%	0.9%	1.0%
A1	91.4%	90.0%	91.1%	92.4%	91.6%	91.3%	0.9%	0.9%
A2	91.7%	90.4%	91.4%	92.6%	91.9%	91.6%	0.8%	0.9%
R02A	96.2%	96.7%	96.1%	96.7%	96.5%	96.4%	0.3%	0.3%
R02B	96.4%	96.9%	96.4%	96.8%	96.7%	96.6%	0.2%	0.2%
D02A	96.3%	96.8%	96.2%	96.8%	91.2%	95.5%	2.4%	2.5%
D02B	96.2%	96.7%	96.0%	96.6%	89.9%	95.1%	2.9%	3.1%
B1	96.0%	96.5%	95.9%	96.4%	95.6%	96.1%	0.4%	0.4%
B2	96.3%	96.7%	96.1%	96.7%	95.7%	96.3%	0.4%	0.4%
S1	97.1%	97.4%	97.0%	97.3%	97.7%	97.3%	0.3%	0.3%
S2	97.0%	97.4%	96.9%	97.3%	97.7%	97.3%	0.3%	0.3%
S3	97.0%	97.3%	97.0%	97.2%	93.9%	96.5%	1.5%	1.5%
S4	96.9%	97.3%	97.0%	97.2%	93.2%	96.3%	1.8%	1.8%
S5	96.7%	97.1%	96.6%	97.0%	96.6%	96.8%	0.3%	0.3%
S6	96.7%	97.2%	96.5%	97.0%	96.4%	96.7%	0.3%	0.3%
SiC	93.3%	94.2%	92.3%	93.6%	93.9%	93.5%	1.1%	1.2%

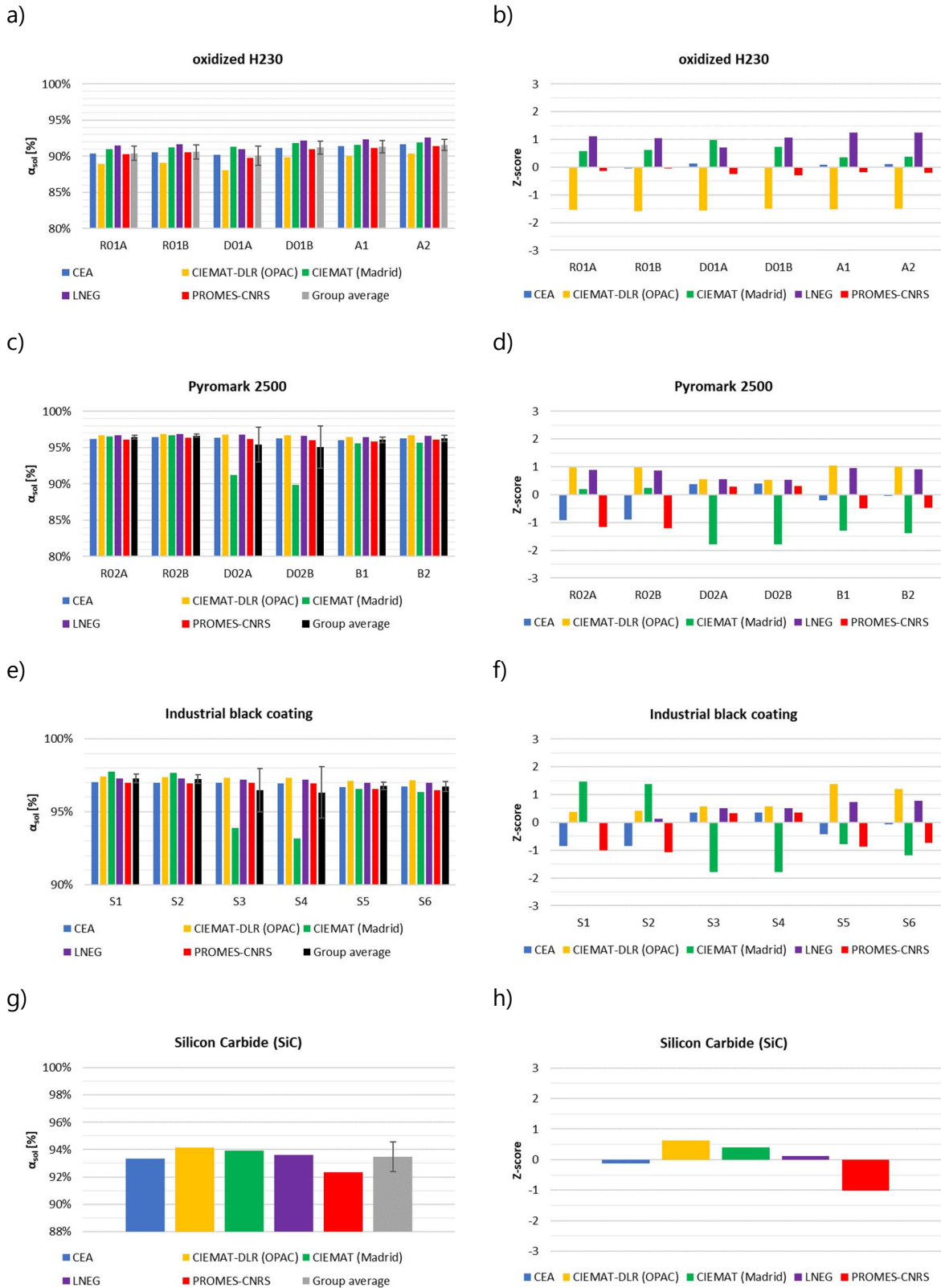


Figure 5.7: Solar absorptance  $\alpha_{sol}$  results for H230 sample coupons (RT measurements). a) oxidised H230, absolute values. b) oxidised H230, Z-score. c) Pyromark 2500, absolute values. d) Pyromark 2500, Z-score. e) Industrial black coating, absolute values. f) Industrial black coating, Z-score. g) SiC samples, absolute values. h) SiC samples, Z-score.

### 5.3.1.2 Thermal emittance

Thermal emittance results  $\epsilon_{th,calc}$  for H230 and SiC sample coupons are summarised in Table 5.9 and shown in Figure 5.8 and Figure 5.9. Values are reported at 800 °C for comparison.

Figure 5.8 indicates how the mean  $\epsilon_{calc}(T)$  value varies with blackbody temperature for each H230 sample coupon. For oxidised H230 sample coupons, the  $\epsilon_{th,calc}$  value calculated from 2  $\mu\text{m}$  to 14  $\mu\text{m}$  varies from 55% at RT up to 85% at 1000 °C. For Pyromark 2500 and the industrial black coating, the  $\epsilon_{th,calc}$  value lies between 90% and 95%. For SiC samples, the  $\epsilon_{th,calc}$  value varies from 70% at RT up to 87% at 1000 °C. The typical standard deviation among participating laboratories is about 3%. A good homogeneity is observed for each group of sample coupons. Each participating laboratory performed spectral measurements on three spots. The typical standard deviation for  $\epsilon_{th}$  due to coating inhomogeneity was less than 0.2%.

The Z-score is shown in Figure 5.9 b), d) and f). It is worth observing that  $\epsilon_{th,calc}$  values obtained from CIEMAT Madrid are systematically lower in comparison to other participating laboratories, for any sample type ( $Z \sim -1.6$ ). It is difficult to determine the exact origin of this deviation, i.e. if it is related to the instrumentation itself or to any sample degradation which may have occurred during measurements at operating temperature. Low spectral mismatches were observed for measurements in the overlap range [2; 2.5]  $\mu\text{m}$  for most participating laboratories, in particular for CEA and PROMES-CNRS ( $\Delta < 1$  p.p.). Higher spectral mismatches were noticed for CIEMAT Madrid. All absolute Z-score values are lower than 2, indicating a satisfactory comparison.

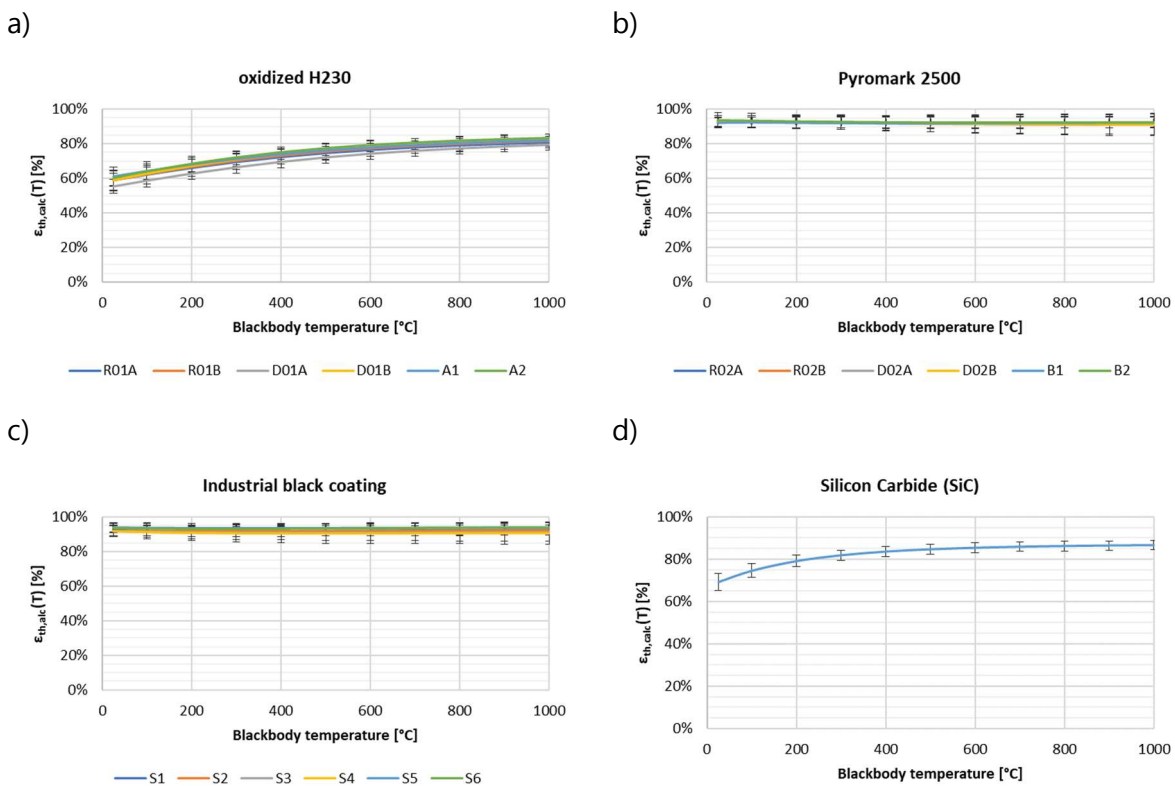


Figure 5.8: Thermal emittance  $\epsilon_{th,calc}(T)$  for H230 and SiC sample coupons (RT measurements). a) oxidised H230, b) Pyromark 2500, c) Industrial black coating, d) SiC sample coupons.

*Table 5.9: Thermal emittance  $\epsilon_{th,calc}$  (800 °C) results for H230 sample coupons (RT measurements).*

<b>Sample</b>	<b>CEA</b>	<b>CIEMAT-DLR (OPAC)</b>	<b>PROMES CNRS</b>	<b>LNEG</b>	<b>CIEMAT Madrid</b>	<b>Mean <math>\mu</math></b>	<b>Stdev <math>\sigma</math></b>	<b>CV <math>\sigma/\mu</math></b>
R01A	81.2%	80.1%	78.5%	82.8%	74.4%	79.2%	3.6%	4.5%
R01B	80.6%	80.5%	80.8%	84.3%	74.2%	79.9%	4.1%	5.1%
D01A	79.6%	78.8%	77.8%	78.8%	72.8%	77.3%	3.2%	4.2%
D01B	82.5%	82.7%	81.3%	82.8%	76.3%	81.0%	3.2%	3.9%
A1	81.8%	80.8%	80.1%	84.0%	76.4%	80.5%	2.9%	3.7%
A2	83.2%	83.2%	81.9%	85.5%	76.8%	81.9%	3.6%	4.4%
R02A	92.0%	94.1%	93.6%	94.8%	87.1%	92.3%	3.1%	3.4%
R02B	92.3%	94.6%	93.6%	95.2%	87.3%	92.6%	3.2%	3.5%
D02A	92.7%	94.7%	93.7%	93.8%	81.0%	91.3%	5.5%	6.0%
D02B	92.6%	94.5%	93.7%	94.9%	80.2%	91.3%	5.9%	6.5%
B1	92.3%	94.3%	93.2%	94.8%	86.8%	92.2%	3.2%	3.5%
B2	92.6%	94.6%	93.8%	94.9%	86.9%	92.6%	3.3%	3.6%
S1	91.8%	93.5%	93.5%	94.9%	87.4%	92.2%	2.9%	3.2%
S2	91.7%	93.6%	93.5%	94.8%	87.6%	92.2%	2.9%	3.1%
S3	91.9%	93.4%	93.5%	94.8%	82.1%	91.2%	5.1%	5.6%
S4	91.7%	93.0%	93.3%	95.1%	79.6%	90.6%	6.2%	6.8%
S5	93.4%	95.2%	95.4%	96.2%	89.3%	93.9%	2.8%	3.0%
S6	93.2%	94.9%	95.1%	96.1%	89.1%	93.7%	2.8%	3.0%
SiC	87.9%	84.6%	87.0%	88.3%	83.5%	86.2%	2.1%	2.5%



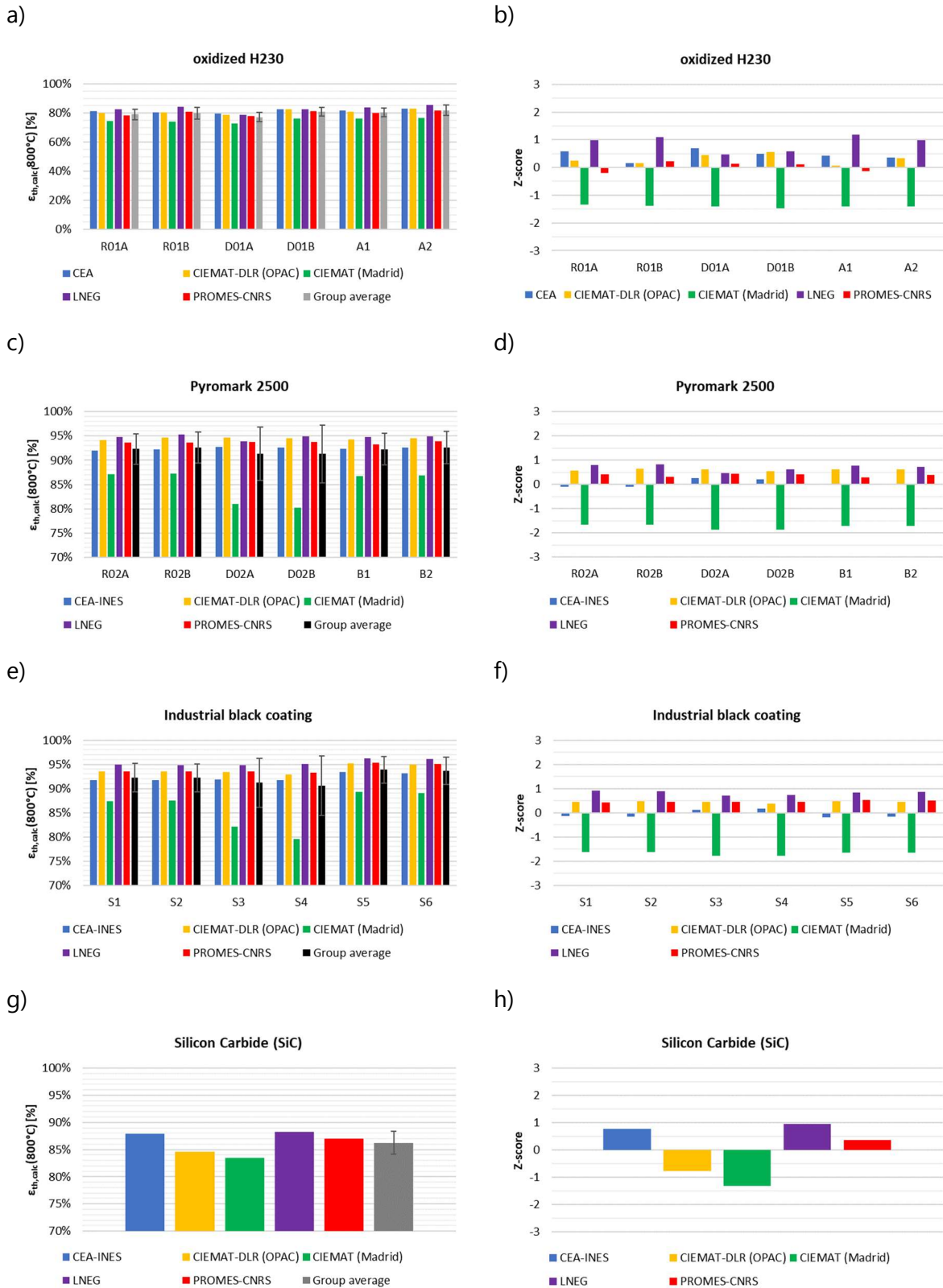


Figure 5.9: Thermal emittance  $\epsilon_{th,calc}(800^\circ\text{C})$  for H230 and SiC samples measured at RT. a) oxidised H230, absolute values. b) oxidised H230, Z-score. c) Pyromark 2500, absolute values. d) Pyromark 2500, Z-score. e) Industrial black coating, absolute values. f) Industrial black coating, Z-score. f) SiC, absolute values. g) SiC, Z-score.

### 5.3.2 Operating temperature

H230 sample coupons could be measured at OT with all experimental setups, while SiC sample coupons could be only measured satisfactorily with PROMES-CNRS laboratory setup.

#### 5.3.2.1 CEA laboratory setup

Spectral measurements for H230 sample coupons recorded from 220 °C to 760 °C by CEA are shown in Figure 5.10. The spectral behaviour is consistent for each pair of sample coupons. These samples tend to exhibit stable optical spectra at OT, although weak temperature dependent spectral shifts are locally observed at short wavelengths ( $< 3 \mu\text{m}$ ) and lower temperatures. Significant noise can be observed in this case, yielding local spectral emissivity values above 100%. Local artefacts caused by atmospheric absorption bands are also observed locally, distorting spectra around 2.7, 3.4, 4.2 and 5.7  $\mu\text{m}$ .

Oxidised H230 sample coupons (R01A/R02B) exhibit a selective spectrum, i.e. their spectral emissivity decreases from 90% to 50% over the recorded spectral range. Pyromark 2500 sample coupons (R02A/R02B) rather exhibit a gray spectral profile, their spectral emissivity fluctuated above 90%. A similar behaviour is observed for the industrial black coating (S1/S2).

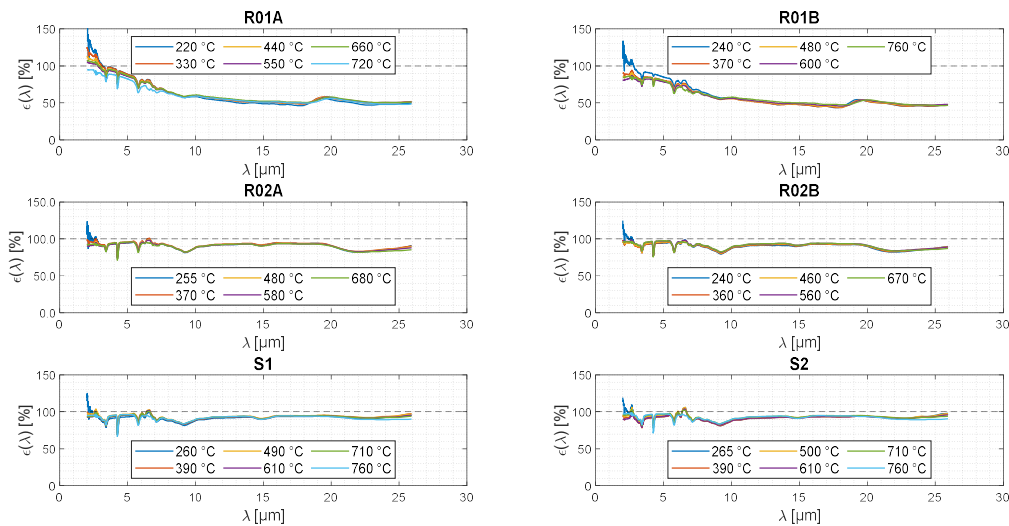


Figure 5.10: Spectral measurements recorded for H230 samples coupons from 220 °C to 760 °C by CEA laboratory.

#### 5.3.2.2 PROMES-CNRS laboratory setup

Spectral measurements for H230 sample coupons recorded by PROMES-CNRS from 25 °C to 500 °C are respectively shown for the InGaAs and DTGS detectors in Figure 5.11 and Figure 5.12. Spectral measurement for SiC sample coupons are shown Figure 5.13 (InGaAs) and Figure 5.14 (DTGS). Consistent values are measured with both detectors, without any significant detector noise or atmospheric artefact. For each material, a consistent spectral behaviour is observed among available sample coupons.

For H230 sample coupons, no significant spectral shift is observed from 25 °C to 500 °C (Figure 5.11) and a greybody behavior is observed for oxidised and black coated samples from 1  $\mu\text{m}$  to 2  $\mu\text{m}$ . Oxidised H230 (A1/A2) achieves a mean emittance of 90% over this spectral range, while Pyromark 2500 (B1/B2) and the industrial black coating (S5/S6) achieve a mean emittance of 95%. It would thus be possible to discriminate optically oxidised H230 from black coated

H230 at short IR wavelengths with an InGaAs infrared detector in IR thermography applications. For DTGS measurements (Figure 5.12), weak temperature dependent spectral shifts are observed, H230 sample coupons are however optically stable from 25 °C to 500 °C. Spectral profiles are consistent with previous observations made from Figure 5.10.

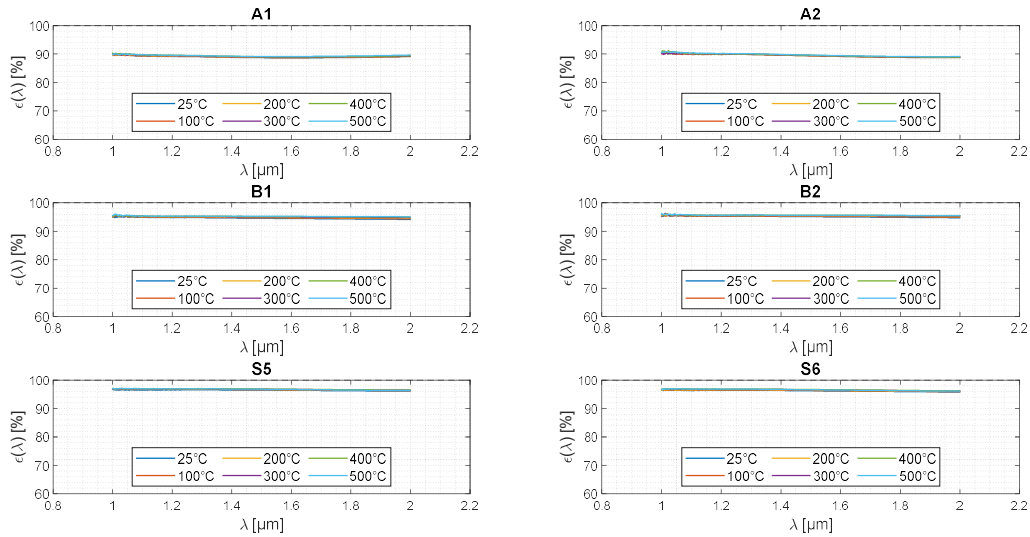


*Figure 5.11: Spectral measurements recorded for H230 sample coupons from 25 °C to 500 °C by PROMES-CNRS laboratory with the InGaAs detector (1-2 μm).*

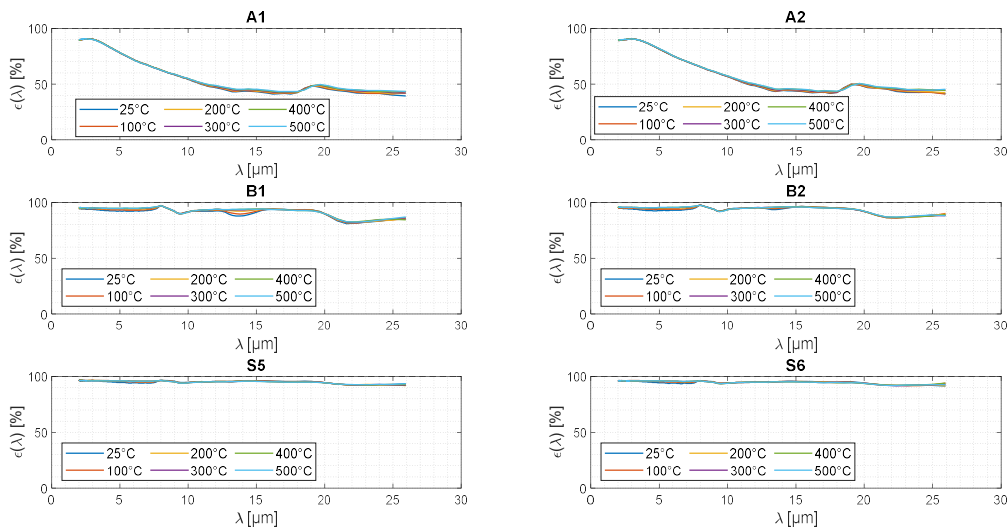


*Figure 5.12: Spectral measurements recorded for H230 sample coupons from 25 °C to 500 °C by PROMES-CNRS laboratory with the DTGS detector (>2 μm).*

For SiC sample coupons, no significant spectral shifts are observed from 1 μm to 1.5 μm (Figure 5.13), while minor temperature dependent spectral shifts are observed above 2 μm (Figure 5.14), especially in the shoulder from 10 μm to 12 μm. SiC behaves nearly as a greybody from 1.5 to 9 μm, a shoulder is then observed from 9 μm to 14 μm. This infrared signature is relevant for longwave IR thermography.

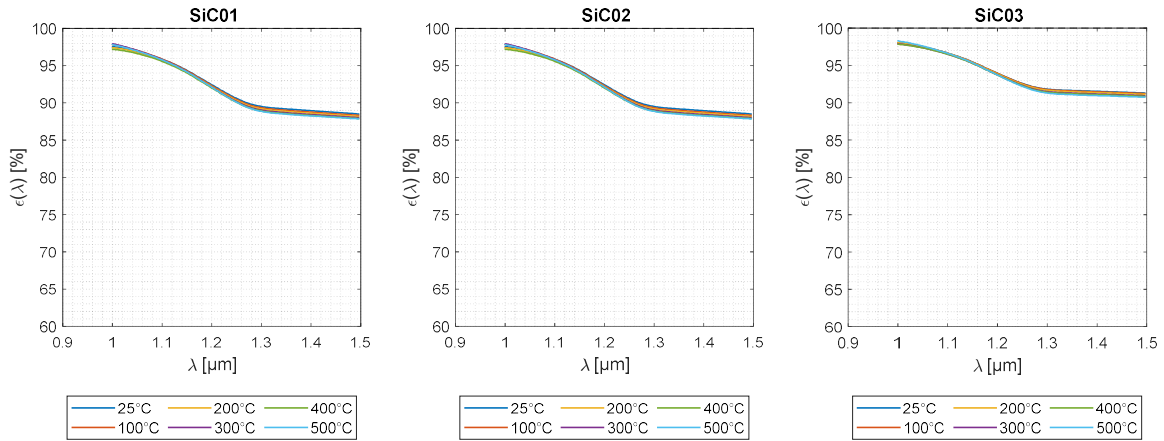


Figure 5.13: Spectral measurements recorded for SiC sample coupons from 25 °C to 500 °C by PROMES-CNRS laboratory with the InGaAs detector (1-1.5 μm).

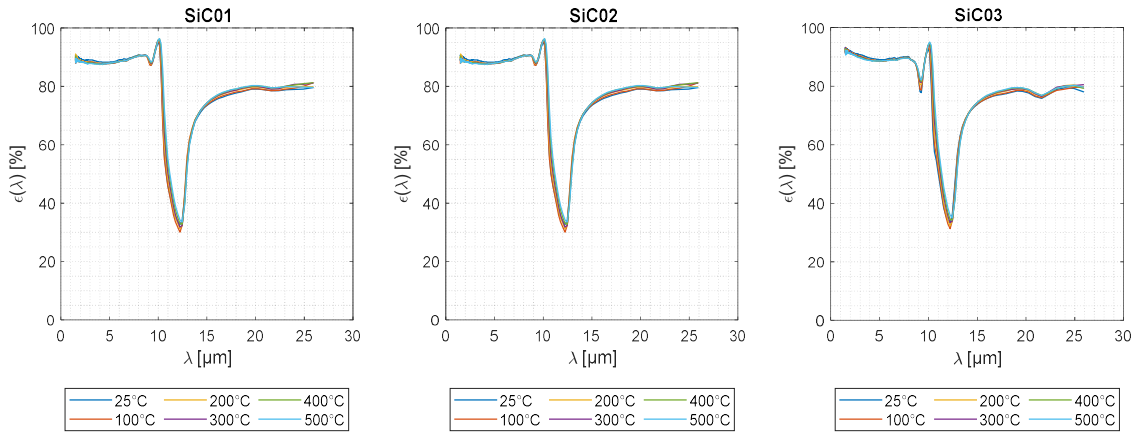


Figure 5.14: Spectral measurements recorded for SiC sample coupons from 25 °C to 500 °C by PROMES-CNRS laboratory with the DTGS detector (> 1.5 μm).

### 5.3.2.3 MEDIASE setup

Spectral measurements for H230 sample coupons recorded by PROMES-CNRS at MEDIASE setup from 620 °C to 805 °C are shown in Figure 5.15. Weak temperature dependent spectral shifts are observed, with a lower confidence for datasets obtained below 650 °C due to the applied temperature measurement principle [29]. Local artefacts caused by atmospheric absorption bands are observed around 2.7, 4.2 and 5.5 μm, despite the short range between the detector and the measured sample. These artefacts, caused by residual water vapor and carbon dioxide distort locally the emissivity spectrum, which locally reaches values above 100%.

The spectral behaviour is consistent for each pair of sample coupons. Spectral profiles are similar to previous measurements shown in Figure 5.10, Figure 5.11 and Figure 5.12 for other experimental setups.

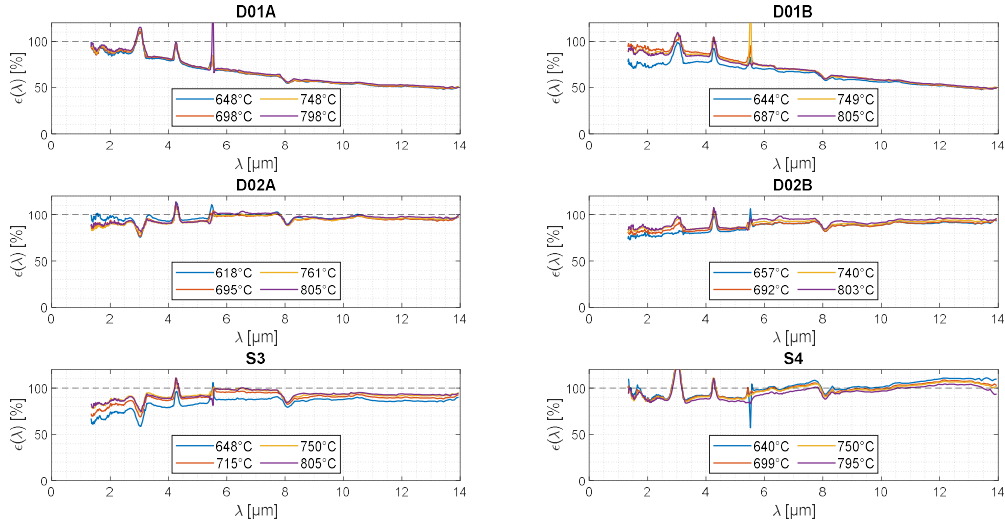


Figure 5.15: Spectral measurement datasets recorded at OT from 618 °C to 805 °C by PROMES-CNRS with MEDIASE setup. Samples investigated: D01A, D01B, D02A, D02B, S3, S4.

MEDIASE setup allows investigating the influence of the incidence angle thanks to the goniometer optical assembly (Figure 5.5). Experimental results are shown in Figure 5.16, weighting spectral emissivity curves according to (Eq.5.12) from 2 to 14  $\mu\text{m}$ . For H230 sample coupons, a weak angular dependence of thermal emittance is observed from 0° up to 45° ( $\Delta\epsilon_{meas} \sim 1\%$ ). Above 45°, the deviation is more pronounced. Oxidised H230 or black coated samples can be considered as diffuse surfaces.

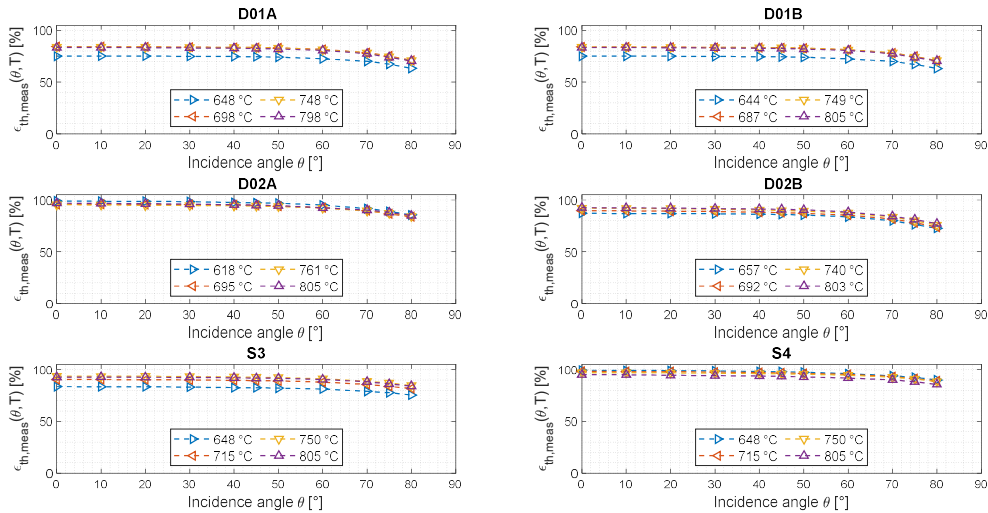


Figure 5.16: Influence of incidence angle on thermal emittance  $\epsilon_{th,meas}(T)$  for measurements recorded at OT from 618 °C up to 805 °C by PROMES-CNRS with MEDIASE setup.

### 5.3.3 Comparison

Spectral measurements at RT and OT are weighted according to (Eq.5.12) from 2  $\mu\text{m}$  to 14  $\mu\text{m}$  in order to compare thermal emittance  $\epsilon_{th}(T)$  for H230 and SiC sample coupons at RT and OT. Results are shown in Figure 5.17. For RT measurements,  $\epsilon_{th,calc}(T)$  values are averaged for each sample batch and the corresponding standard deviation is shown. For OT measurements,  $\epsilon_{th,meas}(T)$  values are shown for each test samples.

In the case of H230 sample coupons, a direct comparison between OT experimental setups is not feasible, as different samples from homogeneous batches were measured by each participating laboratory. Each setup also operated over a different temperature range, with only a partial overlap.

Overall, a fairly consistent agreement is observed between RT and OT measurements for  $\epsilon_{th}(T)$ , apart for a few outliers in the case of H230 sample coupons, for instance MEDIASE measurements below 650 °C. For oxidised H230,  $\epsilon_{th}(T)$  increases from 55% at RT to nearly 80% at 800 °C (Figure 5.17.a). For Pyromark 2500 and the industrial black coating,  $\epsilon_{th}(T)$  fluctuates around 90% and a weak temperature dependence is observed (Figure 5.17 b-c.). For SiC sample coupons, only PROMES-CNRS OT measurements are exploitable. For this lot,  $\epsilon_{th}(T)$  raises from 70% at RT up to 85% at 500 °C.

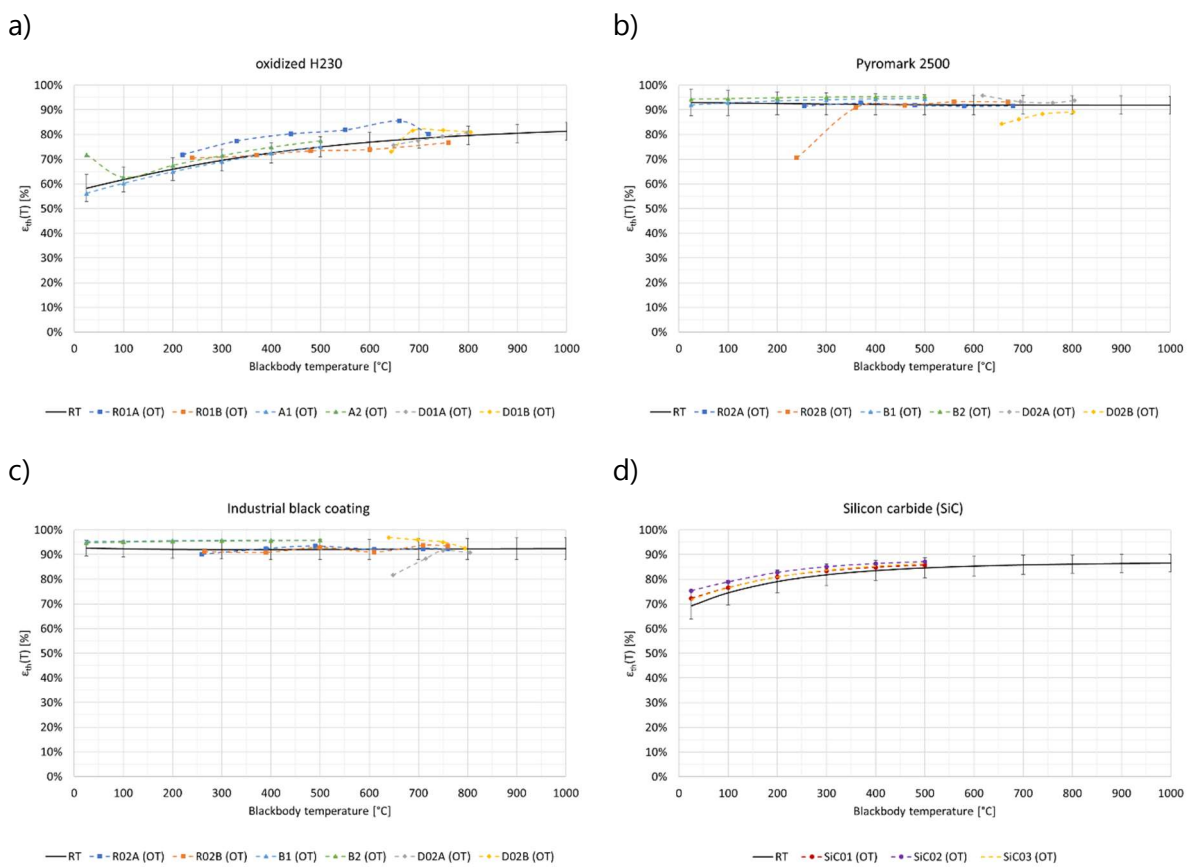


Figure 5.17: Comparison of thermal emittance  $\epsilon_{th}(T)$  for H230 and SiC sample coupons obtained from RT and OT measurements. a) oxidised H230, b) Pyromark 2500, c) Industrial grade black coating, d) SiC sample coupons.

## 5.4 Conclusion and outlook

In this chapter, spectral measurements performed by five different European laboratories from room temperature up to 800 °C have been evaluated and compared for relevant receiver materials used in Concentrating Solar Thermal applications. Two relevant receiver material substrates were considered Haynes 230 and Silicon carbide. Haynes 230 was investigated with three different surface finishes i) oxidised, ii) Pyromark 2500, iii) an industrial black coating.

Two key figures of merits were analysed for all samples: solar absorptance  $\alpha_{sol}$  and thermal emittance  $\epsilon_{th}(T)$ . Solar absorptance  $\alpha_{sol}$  was calculated for room temperature measurements

over the spectral interval [0.3; 2.5]  $\mu\text{m}$ , while thermal emittance  $\varepsilon_{th}(T)$  was calculated for measurements performed from 25 °C up to 800 °C, over the common spectral range [2;14]  $\mu\text{m}$ .

Oxidised Haynes 230 sample coupons reached an  $\alpha_{sol}$  value of  $90.9 \pm 1.0\%$ . Pyromark 2500 sample coupons reached an  $\alpha_{sol}$  value of  $96.3 \pm 0.5\%$  and the industrial black coating achieved an  $\alpha_{sol}$  value of  $97.0 \pm 0.4\%$ . Silicon carbide sample coupons reached an  $\alpha_{sol}$  value of  $93.5 \pm 1.1\%$ . Low standard deviations indicated reproducible measurements at room temperature for  $\alpha_{sol}$ .

For oxidised H230 sample coupons, the  $\varepsilon_{th,calc}(T)$  value derived from room temperature spectral measurements varied from 55% at 25 °C up to 85% at 1000 °C. For Pyromark 2500 and the industrial black coating, the  $\varepsilon_{th,calc}(T)$  value lied between 90% and 95%, with a weak temperature dependence. For silicon carbide sample coupons, the  $\varepsilon_{th,calc}(T)$  varied from 70% at room temperature up to 87% at 1000 °C. The typical standard deviation among participating laboratories is about 3%. Consistent  $\varepsilon_{th,calc}(T)$  values were obtained for room temperature spectral measurements, with a higher standard deviation in comparison to the solar absorptance  $\alpha_{sol}$ .

For both figures of merit  $\alpha_{sol}$  and  $\varepsilon_{th,calc}(T)$ , all absolute Z-score values were lower than 2, i.e. the intercomparison of both figures of merit at room temperature could be interpreted as statistically satisfactory according to ISO 13528.

Spectral measurements at operating temperature were performed by two laboratories (CEA and PROMES-CNRS) with three different experimental setups. Thermal emittance  $\varepsilon_{th,meas}(T)$  values obtained from spectral measurements at operating temperature up to 800 °C were overall consistent within a few percentage points in comparison to thermal emittance  $\varepsilon_{th,calc}(T)$  values calculated from spectral measurements at room temperature, despite a few outliers.

## 5.5 References: Chapter 5

- [1] IRENA, Solar Energy, available at: <https://www.irena.org/Energy-Transition/Technology/Solar-energy,2020>. Accessed: 24/11/2023.
- [2] World Bank, Concentrating solar power: clean power on demand 24/7 (2021), available at: <https://pubdocs.worldbank.org/en/849341611761898393/WorldBank-CSP-Report-Concentrating-Solar-Power-Clean-Power-on-Demand-24-7-FINAL.pdf>. Accessed: 24/11/2023.
- [3] German Aerospace Center (DLR) Institute of Solar Research, Solar thermal powerplants: heat, electricity and fuels from concentrated solar power, (2021), available at: [https://www.dlr.de/sf/en/PortalData/73/Resources/dokumente/publikationen\\_medien/dlr\\_und\\_sf/Study\\_Solar\\_thermal\\_power\\_plants\\_DLR\\_2021-05.pdf](https://www.dlr.de/sf/en/PortalData/73/Resources/dokumente/publikationen_medien/dlr_und_sf/Study_Solar_thermal_power_plants_DLR_2021-05.pdf). Accessed: 24/11/2023.
- [4] C.K. Ho, B.D. Iverson, Review of high-temperature central receiver designs for concentrated solar power, *Renewable and Sustainable Energy Reviews*, 29 (2014), 835–846. <https://doi.org/10.1016/j.rser.2013.08.099>.
- [5] C.K. Ho, Advances in central receivers for concentrating solar applications, *Solar Energy* 152 (2017), 38–56. <https://doi.org/10.1016/j.solener.2017.03.048>.
- [6] A.L. Avila-Marin, Volumetric receivers in Solar Thermal Power Plants with Central Receiver System technology: A review, *Solar Energy*, 85 (5) (2011), 891–910. <https://doi.org/10.1016/j.solener.2011.02.002>
- [7] L. Noč et al, High solar-absorptance CSP coating characterization and reliability testing with isothermal cyclic loads for service-life prediction, *Energy & Environmental Science*, 12 (2019), 1679–1694. <https://doi.org/10.1039/C8EE03536A>.

- [8] J.F. Torres et al., Highly efficient and durable solar thermal energy harvesting via scalable hierarchical coatings inspired by stony corals. *Energy & Environmental Science*, 15 (2022), 1893-1906. <https://doi.org/10.1039/D1EE03028K>
- [9] A. Boubault et al., Durability of solar absorber coatings and their cost-effectiveness. *Solar Energy Materials and Solar Cells*, 166 (2017), 176-184. <https://doi.org/10.1016/j.solmat.2017.03.010>
- [10] S. Caron et al., A comparative analysis of opto-thermal figures of merit for high temperature solar thermal absorber coatings, *Renewable and Sustainable Energy Reviews*, 154 (2022), 111818. <https://doi.org/10.1016/j.rser.2021.111818>.
- [11] S. Caron et al., A laboratory intercomparison of solar absorptance and thermal emittance measurements at room temperature, *Solar Energy Materials and Solar Cells*, 238 (2022), 111579. <https://doi.org/10.1016/j.solmat.2022.111579>.
- [12] C.K. Ho et al., Characterization of Pyromark 2500 paint for high-temperature solar receivers, *Journal of Solar Energy Engineering*, 136 (1) (2014) 014502. <https://doi.org/10.1115/1.4024031>.
- [13] E. Le Baron et al., Round Robin Test for the comparison of spectral emittance measurement apparatuses, *Solar Energy Materials and Solar Cells*, 191 (2019), 476-485. <https://doi.org/10.1016/j.solmat.2018.11.026>.
- [14] I. Setien-Fernandez et al., First spectral emissivity study of a solar selective coating in the 150-600°C temperature range, *Solar Energy Materials and Solar Cells*, 117 (2013) 390-395. <https://doi.org/10.1016/j.solmat.2013.07.002>
- [15] T. Echaniz et al., Importance of the spectral emissivity measurements at working temperature to determine the efficiency of a solar selective coating, *Solar Energy Materials and Solar Cells*, 140 (2015), 249-252. <https://doi.org/10.1016/j.solmat.2015.04.009>
- [16] I. Gonzalez de Arrieta et al., Infrared emissivity of copper-alloyed spinel black coatings for concentrated solar power systems, *Solar Energy Materials and Solar Cells*, 200 (2019), 109961. <https://doi.org/10.1016/j.solmat.2019.109961>.
- [17] D. Hernandez et al., Analysis and Experimental Results of Solar-Blind Temperature Measurements in Solar Furnaces, *Journal of Solar Energy Engineering*, 126(1) (2004), 645-653. <https://doi.org/10.1115/1.1636191>.
- [18] A. Marzo et al., Solar blind pyrometry not relying on atmospheric absorption bands. *Solar Energy*, 107 (2014), 415-422. <https://doi.org/10.1016/j.solener.2014.04.031>
- [19] M. Balat-Pichelin et al., Emissivity at high temperature of Ni-based superalloys for the design of the solar receiver for future tower power plants, *Solar Energy Materials and Solar Cells* 227 (2021) 111066. <https://doi.org/10.1016/j.solmat.2021.111066>
- [20] M. Balat-Pichelin, A. Bousquet, Total hemispherical emissivity of sintered SiC up to 1850 K in high vacuum and in air at different pressures, *Journal of the European Ceramic Society*, 38 (10), (2018), 3447-3456. <https://doi.org/10.1016/j.jeurceramsoc.2018.03.050>
- [21] N. Azzali et al., Spectral emittance of ceramics for high temperature solar receivers, *Solar Energy*, 222, (2021), 74-83. <https://doi.org/10.1016/j.solener.2021.05.019>
- [22] J. Coventry, P. Burge, Optical properties of Pyromark 2500 coatings of variable thicknesses on a range of materials for concentrating solar thermal applications, *AIP Conference Proceedings*, 1850 (2017) 030012. <https://doi.org/10.1063/1.4984355>
- [23] A. Ambrosini et al., Influence of application parameters on stability of Pyromark 2500 receiver coatings, *AIP Conference Proceedings*, 2126 (2019), 030002. <https://doi.org/10.1063/1.5117514>



- [24] S. Caron et al., Forty shades of black: a benchmark of high temperature sprayable black coatings applied on Haynes 230, *AIP Conference Proceedings*, 2303 (2020), 15600007. <https://doi.org/10.1063/5.0028773>
- [25] S. Hosseini et al., Long-term thermal stability and failure mechanisms of Pyromark 2500 for high-temperature solar thermal receivers. *Solar Energy Materials and Solar Cells*, 246 (2022), 111898. <https://doi.org/10.1016/j.solmat.2022.111898>
- [26] N. Martínez et al., Influence of different thermal degradation processes on the optical property of Pyromark-2500, *Solar Energy*, 253 (2023), 58-72. <https://doi.org/10.1016/j.solener.2023.02.004>
- [27] P. Giraud et al., Development of optical tools for the characterization of selective solar absorber at elevated temperature, *AIP Conference Proceedings*, 1734 (2016), 130008. <https://doi.org/10.1063/1.4949218>
- [28] Infrared System Development Corporation, IR 563/301 Blackbody system, available at: <https://www.infraredsystems.com/Products/blackbody563.html>. Accessed: 24/11/2023.
- [29] D. Hernandez et al., Experimental validation of a pyroreflectometric method to determine the true temperature on opaque surface without hampering reflections, *Measurement*, 42(6) (2009), 836-843. <https://doi.org/10.1016/j.measurement.2009.01.012>
- [30] CI Systems, SR-5000N Spectroradiometer, available at: <https://www.ci-systems.com/SR-5000N-Spectroradiometer>. Accessed: 24/11/2023.
- [31] ASTM International, Standard Tables for Reference Solar Spectral Irradiances: Direct Normal and Hemispherical on 37° Tilted Surface, ASTM G173:2012, (2020). <https://doi.org/10.1520/G0173-03R20>
- [32] International Standard Organization, statistical methods for use in proficiency testing by interlaboratory comparison. ISO 13528:2015, (2015). <https://www.iso.org/standard/56125.html>



**Chapter 6. Simulation of shortwave infrared ratio thermometers  
for the remote opto-thermal characterisation  
of central external cylindrical receivers**



## 6 Simulation of shortwave infrared ratio thermometers for the remote opto-thermal characterisation of central external cylindrical receivers

### 6.0 Abstract

The accurate knowledge of the receiver surface temperature  $T_{surf}$  is important for a safe, efficient and durable power plant operation. Its distribution is typically measured in real time using ground-based longwave infrared (LWIR) thermal cameras. Their calibration requires a priori knowledge of the receiver surface LWIR band emittance  $\epsilon_{LWIR}$ . This parameter can be measured with great effort, using portable reflectometers for on tower optical inspection during periodical power plant maintenance. This chapter analyses a new measurement principle, based on passive shortwave infrared (SWIR) ratio thermography, for the simultaneous measurement of surface temperature  $T_{surf}$  and band emittance  $\epsilon_{SWIR}$ .

The first SWIR ratio thermometer combines two narrow bandpass filters centered on water vapor atmospheric absorption bands (1.4/1.9  $\mu\text{m}$ ). This thermometer is sensitive to water vapor to block solar radiation, however thermal radiation emitted by the receiver is also attenuated. The applicability of this thermometer is limited for remote opto-thermal characterization. Under favorable operating conditions, assuming a scaling of the Mid-Latitude Summer standard atmospheric profile for the temperature and humidity along the measurement path, it could measure temperature levels above 550 °C with a relative temperature error  $\Delta T/T < 2\%$ .

The second SWIR ratio thermometer combines two narrow bandpass filters centered on atmospheric windows (1.64/2.09  $\mu\text{m}$ ). This thermometer is insensitive to water vapor and suited for remote distances, however it can only operate off-sun when receiver surface temperature is still above 300 °C, for instance during the cool down phase, before molten salts drainage. The relative temperature error  $\Delta T/T$  is less than 0.5% for Pyromark 2500 and oxidised Haynes 230, while the absolute band emittance error  $\Delta\epsilon$  is less than 2.5 percentage points.

### 6.1 Introduction

Solar energy is the largest energy resource available on Earth, capable of meeting several times the global primary energy demand [1]. Photovoltaics (PV) and Concentrated Solar Power (CSP) are two relevant technologies for solar energy conversion [2,3]. While the worldwide installed PV capacity has reached 1 TW<sub>p</sub> in 2022 [4], CSP technology is yet at an earlier stage of deployment, with an installed capacity of ~7 GW<sub>e</sub> [5]. Multiple hybrid power plants, combining, CSP, PV/Wind and thermal storage are being planned and constructed in China [6]. While CSP technology may play a marginal but critical role in the stabilization of electrical grids, it should contribute in the decarbonization of Industrial Process Heat (IPH) and the production of synthetic fuels [7-10], especially for high temperature processes which are more challenging for direct electrification.

CSP systems use a tracking mirror field to focus sunlight on a thermal receiver. A Heat Transfer Fluid (HTF) is circulated through the thermal receiver in a primary loop. The collected heat is transferred to any thermal process and to a thermal storage unit. The mirror field can be arranged in a line focusing (LF) or a point focusing (PF) configuration. LF systems, such as

Parabolic Trough Collectors (PTC) [11], use single axis trackers to focus solar radiation on linear receivers. PF systems, such as Central Receiver Systems (CRS) [12], use two axis trackers, also known as heliostats, to focus solar radiation on a surface, for instance an external cylindrical receiver mounted at the top of a tower. In comparison to LF systems, PF systems can achieve a higher concentration factor  $C_x$ , significantly above 100. Higher  $C_x$  values lead to higher HTF operating temperatures, above 600 °C, and thus a higher thermodynamic efficiency [13].

External cylindrical receivers [14,15] are made of high temperature metal alloys, such as nickel-chromium superalloys. The receiver surface is coated with an absorber coating, such as Pyromark 2500 [16-18] or alternative black paints [19-21]. The thermal receiver is subject to high flux densities in operation, up to 1 MW/m<sup>2</sup> and local molten salt temperatures above 600 °C, potentially inducing severe metal corrosion [22]. These constraints may lead to critical thermomechanical damages and reduced service lifetime [23]. Allowable Flux Densities (AFD) are thus defined for a safe receiver operation [24], requiring optimal aiming strategies for the heliostat field [25,26].

The absorber coating is also subject to cyclic thermal stresses during operation, impacting its opto-thermal efficiency  $\eta_{opt-th}$  and durability [17-21,27-30]. The key figures of merit affecting  $\eta_{opt-th}$  are primarily the solar absorptance  $\alpha_{sol}$  and secondarily the thermal emittance  $\epsilon_{th}$  [31,32]. The porous coating may crack and delaminate, uncovering an oxide layer, with a lower  $\eta_{opt-th}$  value [17,27,30]. A periodical recoating of the receiver surface may be considered, optimizing the Levelised Cost of Coating (LCOC) [33,34].

The safe, efficient and durable operation of the central external cylindrical receiver requires monitoring its surface temperature and the absorber coating health status. An accurate temperature measurement and control of the receiver surface allows an efficient CRS operation, while it may prevent coating degradation and more critical thermomechanical damages of the receiver caused by overheating.

The aim of this chapter is to analyse a new measurement principle based on shortwave (SW) infrared (IR) ratio thermometry, designed for the remote opto-thermal characterization of central external cylindrical receivers, i.e. a simultaneous measurement of surface temperature and band emittance. Existing field measurement instruments and scientific measurement concepts are reviewed in the first section. The new measurement principle is then described in the next section. The modelling approach used for the evaluation of this measurement principle is presented in the third section. Simulation results for two SWIR ratio thermometer configurations are then discussed in the fourth section.

## **6.2 State of the art**

### **6.2.1 Measurement instruments**

Two types of measurement instruments are used in the field for CRS opto-thermal monitoring. On the one hand, Longwave (LW) IR thermography (8...14 µm) is used for mapping and monitoring the receiver surface temperature  $T_{surf}$  from the ground in real time during operation. On the other hand, portable devices, such as a solar reflectometer and an emissometer can be used for an optical inspection of the receiver coating on tower during periodical maintenance. The solar reflectometer measures the solar absorptance  $\alpha_{sol}$ , while the emissometer measures

the thermal emittance  $\epsilon_{th}$  or a surface band emittance  $\epsilon_{surf,band}$  for a specific IR spectral range. A set of Commercially Off-The-Shelf (COTS) available instruments [35,36] is illustratively shown in Figure 6.1. Their key specifications are outlined in Table 6.1.

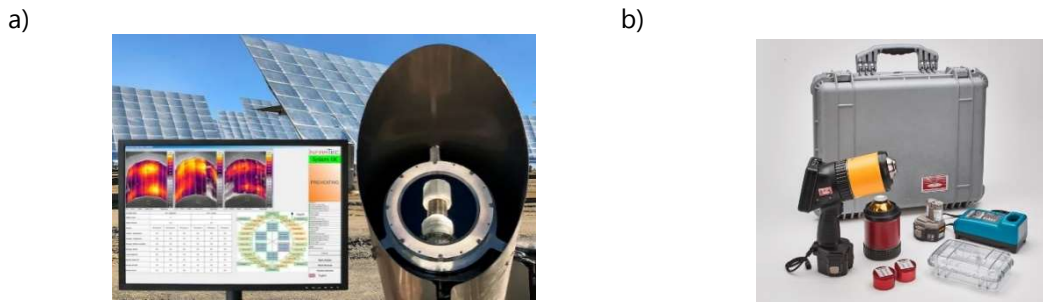


*Figure 6.1: Field Instrumentation for CRS monitoring a) Thermographic Monitoring (LWIR) of Solar Power Tower (Infratec SPTC) [35] b) Surface Optics (SOC) portable 410-Vis-IR solar reflectometer and emissometer [36].*

*Table 6.1: Key instrumentation specifications for CRS monitoring.*

Specification	LWIR thermography	Solar reflectometer	Emissometer
Device model	Infratec SPTC [35]	SOC 410-Solar [36]	SOC ET100 [36]/ ET10
Spectral range	LWIR Broadband Band: 8 – 14 $\mu\text{m}$	UV-VIS-SWIR 6 spectral bands 0.335 – 2.5 $\mu\text{m}$	IR (SW, MW, LW) 7 spectral bands ET100: 1.5 – 21 $\mu\text{m}$ ET10: 3-5 $\mu\text{m}$ / 8-12 $\mu\text{m}$
Resolution	Pixel matrix	Point measurement	Point measurement
Measurand	Surface temperature map from -40 °C up to 2000 °C	$\alpha_{sol}$	ET100: $\epsilon_{th}$ ET10: $\epsilon_{surf,band}$
Operation mode	Continuous Ground based	Periodical maintenance On tower, $T_{amb}$	Periodical maintenance On tower, $T_{amb}$
Calibration inputs	Surface band emittance: $\epsilon_{surf,band}$ Atmospheric transmittance: $\tau_{atm,band}$	NIST traceable calibration coupon (white diffuse)	NIST traceable calibration coupon (gold diffuse)

### 6.2.1.1 LWIR thermography

For external cylindrical receiver designs, multiple LWIR cameras (Figure 6.1.a) are located on the ground around the receiver circumference for a redundant monitoring from different perspectives. The typical view angle of the receiver is about 45°. As the receiver height can be above 200 meters, industrial LWIR cameras with a high resolution (1024x768 pixels) are combined with custom teleobjectives, made of Germanium lenses with anti-reflective coating (ARC), with a focal length above 200 mm in order to resolve single tubes. Each LWIR camera unit uses an uncooled micro-bolometer as a detector and is mounted inside an athermalised protective housing, with a protective window made of Germanium with ARC, to minimise the influence of outdoor conditions, such as solar radiation or ambient temperature, on the temperature measurement accuracy.

LWIR cameras monitor the receiver surface temperature in real time through all operation phases during the day, in particular when molten salts are filled and drained in the central receiver [37]. These phases are particularly important to avoid critical molten salt freezing

below 250 °C. Furthermore, LWIR temperature maps are coupled to the power plant control system and can be used for inverse flux measurements using a receiver thermodynamic model and thus adjusting the aiming point control strategy of the heliostat field [38,39].

The calibration of LWIR camera systems require some a priori knowledge from the operators. On the one hand, the band emittance  $\epsilon_{surf,band}$  of the receiver surface must be estimated, considering potential non-uniformities due to local coating degradation. This calibration may be achieved off-sun at the end of the day, when the receiver cools down and is maintained at an isothermal temperature around 300 °C before molten salts are drained. This calibration method assumes that  $\epsilon_{surf,band}$  is not temperature dependent [40]. On the other hand, the atmospheric band transmittance  $\tau_{atm,band}$  must be estimated for the slant path between the camera and the receiver. This parameter is primarily a function of distance  $d$ , ambient temperature  $T_{amb}$  and relative humidity RH. Empirical correlations based on radiative transfer codes are typically used for this estimation [41].

While LWIR thermography is robust for industrial applications, there are currently some practical obstacles to improve the calibration traceability of such measurement systems in the context of CRS applications. The spectral response of the LWIR optical system is for instance seldom provided for radiometric simulations. The thermography software may also not allow the end user to access the calibration function or the radiometric chain, impeding the direct comparison of radiometric quantities.

### 6.2.1.2 Portable instruments

Portable instruments (Figure 6.1.b) allow performing an in-situ optical inspection of the receiver surface at ambient temperature, comparable with laboratory spectrophotometers [32]. A modular measurement head includes an integrating sphere, with a discretised spectral resolution (Figure 6.2), adjusted for the selected measurand, e.g.  $\alpha_{sol}$ ,  $\epsilon_{th}$  or  $\epsilon_{surf,band}$ . Solar absorptance measurements are for instance used to decide whether re-coating should occur, defining a lower threshold such as 95% for  $\alpha_{sol}$  [20].

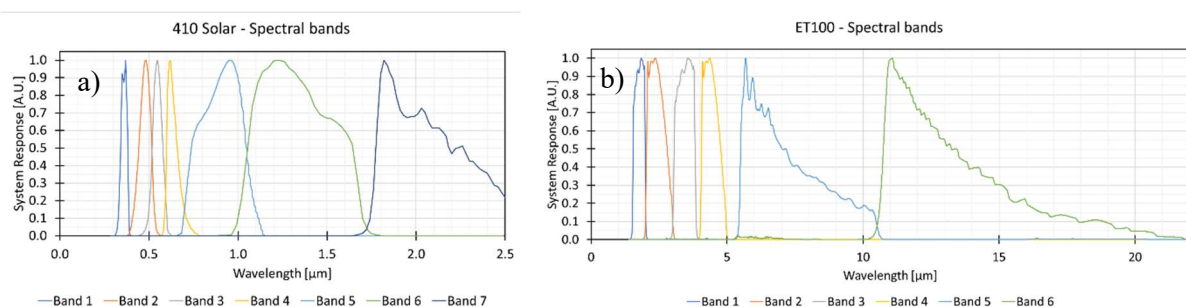


Figure 6.2: Spectral response of portable instrument measurement heads in arbitrary units. a) 410 Solar reflectometer (0.33 - 2.5 μm). b) ET100 emissometer (1.5 - 21 μm).

While the 410-Vis-IR SOC portable device [36] is already known in the CSP community, there is no experience with the ET-10 measurement head, which could allow a ground truthing for LWIR thermography, assuming a comparison of spectral responses is possible for both instruments. One practical disadvantage of such portable instrument is the necessity for operators to climb on tower, above 200 m, during periodical power plant maintenance.



## 6.2.2 Measurement techniques

Different measurement techniques in radiation thermometry have been previously implemented and tested in the field of CSP and other research applications. These measurement techniques can be classified according to:

- i) the selected IR spectral band and its sensitivity to solar radiation (*solar blindness*)
- ii) the number  $N$  of spectral bands used for measurements  
(*Multi-spectral thermometry*)
- iii) the active use of light sources during measurements (*passive vs. active techniques*)

### 6.2.2.1 Solar blindness

The choice of the IR spectral bandwidth is particularly critical, as concentrated solar radiation may hamper the temperature measurement accuracy. So-called "solar-blind" temperature measurements have been performed in solar furnaces [42-44] and on parabolic trough receivers and volumetric absorbers [45,46]. Solar blindness can be achieved with different approaches, after a thorough analysis of the specific radiometric chain [42]:

- i) selecting a Narrow Bandpass (NB) filter centered on an atmospheric absorption band, such as 1.4  $\mu\text{m}$  ( $\text{H}_2\text{O}$ ), 1.9  $\mu\text{m}$  ( $\text{H}_2\text{O}$ ), 2.7  $\mu\text{m}$  ( $\text{H}_2\text{O}+\text{CO}_2$ ), 4.3  $\mu\text{m}$  ( $\text{H}_2\text{O}+\text{CO}_2$ ).
- ii) selecting an infrared spectral range where the mirror specular reflectivity is minimal ( $\rho_{\text{mirror}} \sim 0$ ), for instance playing with the glass layer absorption
- iii) temporarily occulting concentrated solar radiation while maintaining the receiver surface temperature isothermal ( $C_x = 0$ )
- iv) achieving blackbody conditions for the receiver surface ( $\epsilon_{\text{surf,band}} \sim 1$ ).

One can further distinguish near and true solar-blind temperature measurements. The accuracy of near solar-blind temperature measurements depends on atmospheric conditions, such as Air Mass ( $AM$ ) or Solar Zenith Angle ( $SZA$ ) and operating conditions, such as concentration factor  $C_x$  and surface temperature  $T_{\text{surf}}$ . True solar-blind temperature measurements can only be guaranteed if the reflection of the concentrated solar flux is totally cancelled by at least one component of the radiometric chain.

For atmospheric absorptions bands, near solar-blind temperature measurements are achieved at 1.4  $\mu\text{m}$  and 1.9  $\mu\text{m}$ , while true solar-blind temperature measurements are achieved at 2.7  $\mu\text{m}$  and 4.3  $\mu\text{m}$ . Nonetheless, the atmosphere does not only attenuate the concentrated solar radiation, but also the thermal radiation emitted by the receiver surface. For central external cylindrical receivers, near solar-blind temperature measurements can be assumed for LWIR thermometry, as the applied black coating approximates a blackbody. Operating conditions are also less extreme in comparison to a solar furnace. For molten salts, the surface temperature should not exceed 600 °C and the maximum flux is about 1 MW/m<sup>2</sup> [15].

### 6.2.2.2 Multi-spectral thermometry

IR thermography can be performed with a single spectral band ( $N= 1$ ) or with multiple spectral bands. For single band thermography, a priori knowledge is required for the surface band emittance  $\epsilon_{\text{surf,band}}$  and the atmospheric band transmittance  $\tau_{\text{atm,band}}$ . A variant is ratio thermometry ( $N= 2$ ), combining two spectral bands and assuming a grey behavior for the investigated material, i.e. a constant surface band emittance  $\epsilon_{\text{surf,band}}$  and atmospheric band

transmittance  $\tau_{atm,band}$  for the spectral range of interest [47-49]. The grey assumption may be corrected with a Non-Grey Compensation Factor (*NGCF*) [50].

Ratio thermometry allows a simultaneous retrieval of a material surface temperature  $T_{surf}$  and its band emittance  $\epsilon_{surf,band}$ . Published references have focused on short ranges and wavelengths for which the influence of atmospheric band absorption can be considered negligible ( $\tau_{atm,band} \sim 1$ ). Due to blackbody radiation physics, ratio thermometry is more sensitive for SWIR (1 - 2.5  $\mu\text{m}$ ) than for Midwave (MW: 3-5  $\mu\text{m}$ ) or Longwave (LW: 8-14  $\mu\text{m}$ ) IR spectral ranges.

Although multi-spectral thermometry ( $N > 2$ ) exists, it always results in an ill-posed problem with an underdetermined system of equations [51]. There are  $N+1$  unknown for  $N$  band measurements:  $N$  unknown for each spectral band emittance  $\epsilon_{surf,band}$  and one unknown for the surface temperature  $T_{surf}$ . A relationship between emissivity and wavelength has to be assumed, with inherent mathematical difficulties [52].

### **6.2.2.3 Passive versus active techniques**

Passive radiation thermometry concepts exploit only the thermal radiation emitted by the surface for temperature measurements. Active radiation thermometry concepts combine one or several modulated light sources in addition of the radiation thermometer, to extract more information on the surface optical properties. Active radiation thermometry concepts include:

- i) Two-colour pyroreflectometry [53-55]
- ii) Flash-Assisted Multiwavelength Pyrometry (FAMP) [56,57]
- iii) Double Modulation Pyrometry (DMP) [58-61]

These active measurement techniques, originally developed for pyrometry, could be extended in spatial resolution for thermography [62,63].

Two-colour pyroreflectometry is a variant of passive ratio thermometry. It measures simultaneously the sample surface radiance temperature and its reflectivity, retrieving the surface true temperature  $T_{surf}$  introducing a diffusion factor, which is assumed independent of wavelength  $\lambda$ . This technique operates at two different close wavelengths, for instance at 1.3  $\mu\text{m}$  and 1.55  $\mu\text{m}$ , using corresponding NB filters and wavelength compatible modulated light sources.

The FAMP technique measures in-situ the spectral reflectivity of a Lambertian sample, its temperature and the spectral irradiance of the light source by measuring twice the spectral contents of the light from the sample and from a cooled reflectance reference sample situated nearby. Two measurements are made sequentially, one with and one without additional light from an external flash.

The DMP technique has been originally developed for artificial solar furnaces, where solar blind pyrometry is not applicable due to the arc lamp continuous spectrum. It relies on a single colour pyrometric method and thus requires a priori knowledge of the sample band emittance. This technique allows separating the external reflection radiation reflected by a sample from its thermal emission, by modulating the light source.

While active measurement techniques have been successfully experimented at laboratory scale, they are probably difficult to scale for a ground-based temperature measurement of a central

external cylindrical receiver. Furthermore, the addition of modulated light sources increases the complexity of the temperature measurement system.

### 6.3 Measurement principle

The scope of this chapter focuses on the analysis of two passive SWIR ratio thermometers for the ground-based measurement of central external cylindrical receiver surface temperature  $T_{surf}$  and band emittance  $\epsilon_{surf,band}$ . Two configurations are considered for simulation:

- i) a near solar-blind configuration for on-sun measurements, combining two NB filters centered on two neighbor SWIR atmospheric water vapor absorption bands, i.e. 1.4  $\mu\text{m}$  and 1.9  $\mu\text{m}$
- ii) an alternative configuration for off-sun measurements, combining two NB filters centered on two neighbor SWIR atmospheric windows, i.e. 1.64  $\mu\text{m}$  (H band) and 2.09  $\mu\text{m}$  (K band) [64].

This section describes the radiometric chain for central external cylindrical receivers, the rationale for applying ratio thermography and the spectral configuration of the prototype camera system.

#### 6.3.1 Radiometric chain

The radiometric chain for the ground-based thermography of central external cylindrical receivers is illustrated in Figure 6.3. The IR camera is mounted on the ground at a height  $H_0$  (m.a.s.l.) within the heliostat field and looks at one receiver section on top of the tower at a height  $H$  above the ground. The measurands of interest for opto-thermal characterization are the surface temperature map  $T_{surf}\{x,y\}$  and the surface band emittance map  $\epsilon_{surf,band}\{x,y\}$ .

The radiometric chain consists of three main atmospheric paths, assuming an equivalent heliostat, which is representative for the heliostat field:

- i) Path 1: Sun to heliostat (slant distance  $d_1$ , function of Air Mass  $AM$ )
- ii) Path 2: Heliostat to receiver (slant distance  $d_2$ )
- iii) Path 3: Receiver to IR camera (slant distance  $d_3$ )

A ground-based weather station give access to parameters such as atmospheric pressure  $p_{atm}$ , ambient temperature  $T_{amb}$  and relative humidity  $RH$ . This information is used to parametrise the atmospheric model, in particular water vapor content. One relevant unit is absolute humidity  $AH$  [ $\text{g}/\text{m}^3$ ] at ground level, computed using humidity conversion formulas [65].

The ground-based IR camera detects a radiometric signal  $S$ , which sums three contributions:

- i) Term A: Thermal radiation emitted by the diffuse receiver surface
- ii) Term B: Reflected concentrated solar radiation
- iii) Term C: Thermal radiation emitted by the atmosphere

The IR camera detector may also detect its own thermal radiation, reflected by the optics [66].

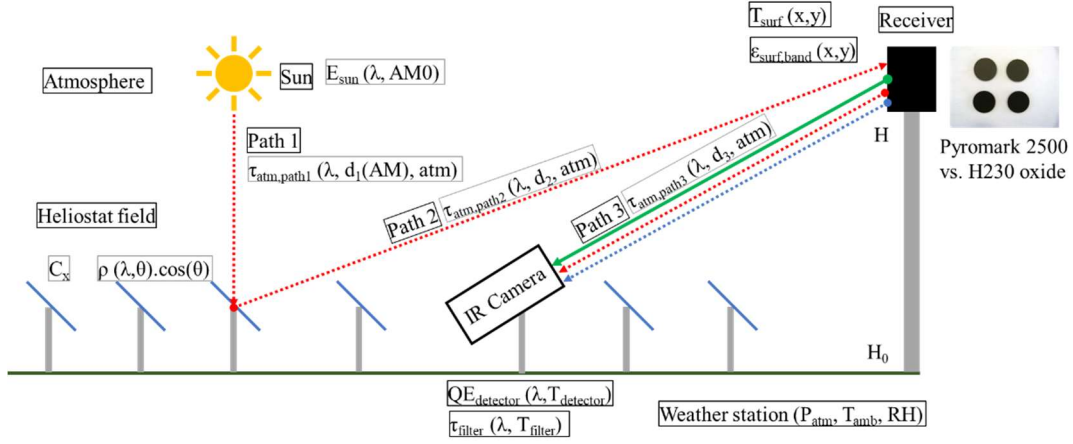


Figure 6.3: Radiometric chain for ground-based thermography of central receiver systems.

A radiometric equation is formulated for the detected spectral irradiance  $I_{\{x,y\}}(\lambda)$  (Eq.6.1), for any pixel  $\{x,y\}$  and wavelength  $\lambda$ . This radiometric equation can be further integrated bandwise (Eq.6.2) for any given NB filter over the spectral range  $[\lambda_{start}, \lambda_{stop}]$  to yield a camera signal  $S_{\{x,y\}}(filter)$ .

$$I_{\{x,y\}}(\lambda) = A_{\{x,y\}}(\lambda) + B_{\{x,y\}}(\lambda) + C_{\{x,y\}}(\lambda) + D_{\{x,y\}}(\lambda) \quad (6.1)$$

$$S_{\{x,y\}}(filter) = \int_{\lambda_{start}}^{\lambda_{stop}} I_{\{x,y\}}(\lambda) d\lambda \quad (6.2)$$

Terms A,B,C and D are explicated further in (Eq. 6.3-6.6). The pixel notation is omitted for the sake of readability:

$$A(\lambda) = \varepsilon_{surf}(\lambda) \tau_{atm,path3}(\lambda, d_3, atm) E_{bb}(\lambda, T_{surf}) SRF_{cam}(\lambda, T_{cam}) \quad (6.3)$$

$$B(\lambda) = C_x [1 - \varepsilon_{surf}(\lambda)] \left[ \prod_{i=1}^3 \tau_{atm,path(i)}(\lambda, d_i, atm) \right] \rho_{mirror}(\lambda) \cos(\theta) E_{sun}(\lambda, AM0) SRF_{cam}(\lambda, T_{cam}) \quad (6.4)$$

$$C(\lambda) = [1 - \tau_{atm,path3}(\lambda, d_3, atm)] \cdot E_{bb}(\lambda, T_{atm}) \cdot SRF_{cam}(\lambda, T_{cam}) \quad (6.5)$$

$$D(\lambda) = [1 - \tau_{filter}(\lambda, T_{filter})] \cdot E_{bb}(\lambda, T_{sensor}) \cdot QE_{sensor}(\lambda, T_{sensor}) \quad (6.6)$$

The function  $E_{bb}(\lambda, T)$  is defined by Planck's law of blackbody radiation (Eq.6.7).

$$E_{bb}(\lambda, T) = \frac{2\pi h c_0^2}{\lambda^5 [\exp(\frac{hc_0}{\lambda k T}) - 1]} \quad (6.7)$$

The camera spectral response function  $f_{cam}(\lambda, T_{cam})$  is defined by (Eq.6.8).

$$SRF_{cam}(\lambda, T_{cam}) = \tau_{window}(\lambda, T_{window}) \tau_{lens}(\lambda, T_{lens}) \tau_{filter}(\lambda, T_{filter}) QE_{sensor}(\lambda, T_{sensor}) \quad (6.8)$$

The extraterrestrial solar spectrum  $E_{sun}(\lambda, AM0)$  and atmospheric transmissivity spectra  $\tau_{atm,path(i)}$  are generated with MODTRAN6 radiative transfer code [67,68]. For simulations, a reference mirror spectrum  $\rho_{mirror}(\lambda, \theta)$  is considered for a near normal incidence angle, assuming there is no soiling or degradation. Although the heliostat field deflects solar radiation on the receiver, the cosine effect ( $\cos(\theta)$ ) is here assumed negligible for simplification.

The measurands of interest, i.e.  $T_{surf}$  and  $\epsilon_{surf}$  are embedded in term A (Eq.6.3). The surface emissivity  $\epsilon_{surf}$  is also embedded in term B (Eq.6.4). To extract  $T_{surf}$  and  $\epsilon_{surf}$  measurands, it is necessary to isolate term A (Eq.6.3). The radiometric equation (Eq.1) simplifies considerably if terms B, C and D could be considered negligible.

Term B (Eq.6.4) is negligible only under near or true solar blind conditions. This can be achieved in practice by selecting NB filters centered around atmospheric water absorption bands, for instance 1.4  $\mu\text{m}$  and 1.9  $\mu\text{m}$ . In this case, the aim is to cancel  $\tau_{atm,path1}$ , by finding suitable atmospheric conditions (AH,AM) and operating conditions  $\{C_x; T_{surf}\}$  which minimise the expected temperature error. Nonetheless, atmospheric water vapor also affects path 3, i.e. the atmospheric attenuation  $\tau_{atm,path3}$  between the receiver and the camera [69,70]. Another strategy is to work off-sun ( $C_x = 0$ ), when heliostats are defocused and the receiver cools down at dusk. NB filters centered in atmospheric windows, for instance 1.64  $\mu\text{m}$  and 2.09  $\mu\text{m}$  are significantly less affected by atmospheric conditions.

Term C (Eq.6.5) is generally negligible, as long as the atmosphere temperature  $T_{atm}$  is significantly lower than the receiver surface temperature  $T_{surf}$ . Term D is camera specific, generating a signal offset. It can become negligible, depending on the spectral range and the camera sensor temperature. This may be a potential issue for LWIR cameras (8...14  $\mu\text{m}$ ) using an uncooled microbolometer with inadequate athermalisation [66]. For a SWIR camera, this is not critical as the sensor can be cooled down below ambient temperature using thermoelectric cooling, to reduce dark current noise.

### 6.3.2 Ratio thermometry

Assuming the object thermal emission can be expressed (Eq.6.9) for a given NB filter:

$$S(filter) \approx \int_{\lambda_{start}}^{\lambda_{stop}} \epsilon_{surf}(\lambda) \tau_{atm,path3}(\lambda, d_3, atm) E_{bb}(\lambda, T_{surf}) SRF_{cam}(\lambda, T_{cam}) d\lambda \quad (6.9)$$

This equation can be expressed in lumped form after integration (Eq.6.10):

$$S(filter) \approx \epsilon_{surf}(filter) \tau_{atm,path3}(filter) BF(filter, T_{surf}) \quad (6.10)$$

Where the band surface emittance  $\epsilon_{surf}(filter)$ , band atmospheric transmittance  $\tau_{atm,path3}(filter)$  and the NB filter blackbody calibration function  $BF$  are respectively defined in (Eq.6.11-6.13).

$$\epsilon_{surf}(filter) = \frac{\int_{\lambda_{start}}^{\lambda_{stop}} \epsilon_{surf}(\lambda) E_{bb}(\lambda, T_{surf}) SRF_{cam}(\lambda, T_{cam}) d\lambda}{BF(filter, T_{surf})} \quad (6.11)$$

$$\tau_{atm,path3}(filter) = \frac{\int_{\lambda_{start}}^{\lambda_{stop}} \tau_{atm,path3}(\lambda, d_3, atm) E_{bb}(\lambda, T_{surf}) SRF_{cam}(\lambda, T_{cam}) d\lambda}{BF(filter, T_{surf})} \quad (6.12)$$

$$BF(filter, T_{surf}) = \int_{\lambda_{start}}^{\lambda_{stop}} E_{bb}(\lambda, T_{surf}) SRF_{cam}(\lambda, T_{cam}) d\lambda \quad (6.13)$$

The blackbody calibration function  $BF$  (Eq.6.13) can be simulated knowing the camera spectral response  $SRF_{cam}$  or measured in laboratory with a reference blackbody ( $\epsilon > 0.99$ ), assuming the effect of atmospheric transmittance is properly considered for the calibration path. The  $BF$  function can be further inverted, preferably in analytical form, to obtain the reciprocal function

$BF^1$  between the temperature  $T$  and the sensor signal  $S$  ( $T = BF^1(S)$ ). Various equations were proposed by Sakuma and Hattori [71].

For a single band thermometer, a priori knowledge of  $\epsilon_{surf,band}$  and  $\tau_{atm,band}$  is required to infer the surface temperature  $T_{surf}$ . While  $\tau_{atm,path3,band}$  could be derived from model-based correlations [41] using atmospheric radiative transfer codes such as MODTRAN [67,68],  $\epsilon_{surf,band}$  may be derived from laboratory measurements performed at high temperature [40], if this knowledge is available.

A ratio thermometer requires a pair of NB filters {filter 1; filter 2}. The signal ratio SR is defined as the ratio of signals obtained for each NB filter (Eq.6.14):

$$SR = \frac{S(filter\ 2)}{S(filter\ 1)} \approx \frac{\epsilon_{surf}(filter\ 2)}{\epsilon_{surf}(filter\ 1)} \frac{\tau_{atm,path3}(filter\ 2)}{\tau_{atm,path3}(filter\ 1)} \frac{BF(filter\ 2, T_{surf})}{BF(filter\ 1, T_{surf})} \quad (6.14)$$

Using a pair of NB filters provides two independent band measurements for three unknowns, i.e. the  $\epsilon_{surf}\tau_{atm,path3}$  product for each NB filter and the surface temperature  $T_{surf}$ . The equation system is thus underdetermined, without any a priori knowledge. While the atmospheric band transmittance ratio can be estimated using a radiative transfer code, a further assumption is required for the surface band emittance ratio.

The principle of ratio thermometry [47-51] relies on the greybody assumption (Eq.15). This requires selecting a pair of NB filters with central wavelengths (CWLs) chosen as close as possible to consider valid the greybody assumption, but not too close, otherwise redundant signals are measured and the equation system remains underdetermined.

$$\frac{\epsilon_{surf}(filter\ 2)}{\epsilon_{surf}(filter\ 1)} \sim 1; \epsilon_{surf,band} = \epsilon_{surf}(filter\ 1) = \epsilon_{surf}(filter\ 2) \quad (15)$$

From Chapter 5, the greybody approximation is considered relevant for the selected spectral range and for the materials of interest, i.e. Pyromark 2500 black coating or oxidised Haynes 230 (H230) metal substrate, as illustrated in Figure 6.4. Both materials also have a high spectral emissivity, near or above 90%.

On the other hand, the greybody approximation is not necessarily valid for the atmosphere. A model based atmospheric  $NGCF_{atm}$  is introduced for correction (Eq.6.16).

$$NGCF_{atm} = \frac{\tau_{atm,path3}(filter\ 2)}{\tau_{atm,path3}(filter\ 1)}; NGCF_{atm} \neq 1 \quad (6.16)$$

The ratio of blackbody calibration functions [ $BF(filter\ 2, T_{surf})/BF(filter\ 1, T_{surf})$ ] defines an ancillary greybody calibration function  $GF(T_{surf})$  (Eq.6.17):

$$GF(T_{surf}) = \frac{BF(filter\ 2, T_{surf})}{BF(filter\ 1, T_{surf})} \quad (6.17)$$

In practice, the retrieval of the surface temperature  $T_{surf}$  and band emittance  $\epsilon_{surf,band}$  occurs stepwise.  $NGCF_{atm}$  is estimated based on available weather data at ground level. Assuming a greybody receiver surface, the measured signal ratio SR is divided by  $NGCF_{atm}$ . The greybody calibration function  $GF(T_{surf})$  is then inverted to infer the surface temperature  $T_{surf}$ . Knowing this temperature, the measured signal for each NB filter is divided by the corresponding blackbody

temperature signal ( $BF(filter, T_{surf})$ ) to obtain first the  $\epsilon_{surf} \tau_{atm,path3}$  product for each NB filter, then the surface band emittance  $\epsilon_{surf,bandi}$  as  $\tau_{atm,path3}$  is already estimated for  $NGCF_{atm}$ .

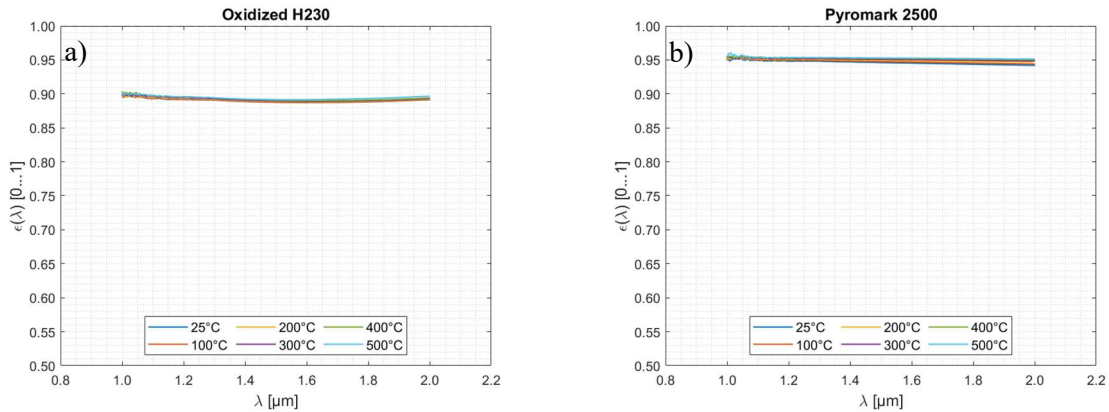


Figure 6.4: SWIR spectral measurements of reference materials from ambient temperature up to 500 °C. a) H230, pre-oxidised at 800 °C for 100 hours. b) Pyromark 2500 applied on H230 substrate.

### 6.3.3 Camera configuration

The prototype SWIR camera system consists of the following components:

- i) An InGaAs image sensor (Hamamatsu Photonics, G14673-0808W) [72]
- ii) A motorised filter wheel with six filter positions
- iii) A set of stock available NB filters supplied by Spectrogon [73]
- iv) A SWIR objective lens with a 300 mm focal length [74]

The camera system is mounted inside an outdoor protection housing with a Gorilla glass window of 2 mm thickness. Four positions of the filter wheel are used for NB filters of 1 mm thickness, while two filter positions are used for a shutter and a broadband window. The shutter and broadband window can be used for Non-Uniformity Correction (NUC). The broadband window also allows focusing the camera system on remote objects at ambient temperature.

Selected NB filters are listed in Table 6.2. Two pairs of NB filters are considered as SWIR ratio thermometers. The first SWIR ratio thermometer is sensitive to water vapor and should allow near solar blind measurements, while the second SWIR ratio thermometer is minimally sensitive to atmosphere, but definitely not solar blind.

Table 6.2: Specifications of NB filters for SWIR ratio thermography.

Filter ID	Central Wavelength (CWL)	Full Width at Half Maximum (FWHM)	Ratio thermometer
NB 1386-10	1386 ± 5 nm	10±3 nm	Pair 1; Filter 1 (Water absorption)
NB 1912-10	1912 ± 5 nm	10±3 nm	Pair 1; Filter 2 (Water absorption)
NB 1640-25	1640 ± 10 nm	25±10 nm	Pair 2; Filter 1 (Atmosphere window)
NB 2090-25	2090 ± 10 nm	25±10 nm	Pair 2; Filter 2 (Atmosphere window)

The spectral response of each relevant optical component (sensor, objective lens, NB filters, protective window) is shown in Figure 6.5. The image sensor is cooled at -20 °C, while other components remain at ambient temperature.

Virtual blackbody calibration curves are shown for each NB filter in Figure 6.6.a, while virtual greybody calibration curves are shown for each SWIR ratio thermometer in Figure 6.6.b.

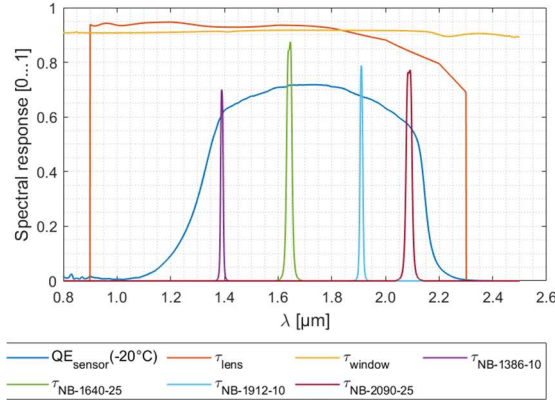


Figure 6.5: Spectral response of camera system components.

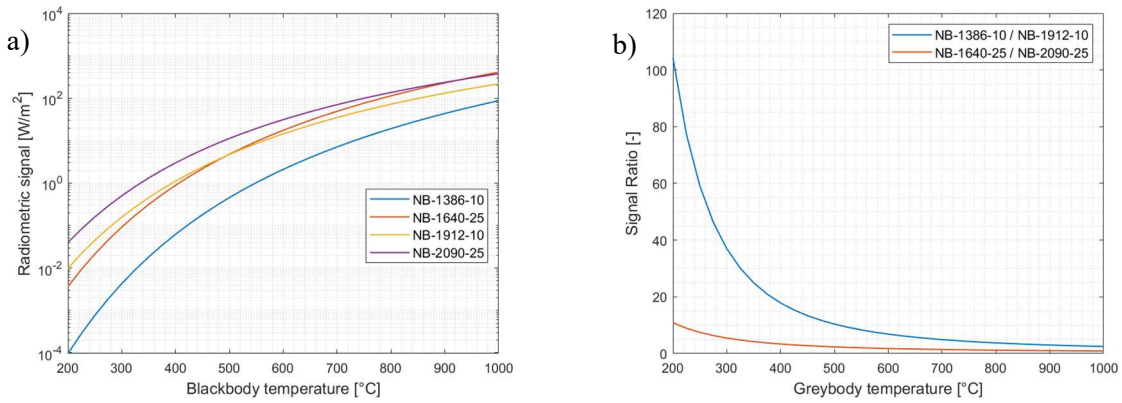


Figure 6.6: Camera system response. a) Virtual blackbody calibration for each NB filter [200-1000] °C. b) Virtual greybody calibration for each ratio thermometer [200-1000] °C.

Virtual blackbody filter calibrations (Figure 6.6.a) can be fitted with a Sakuma-Hattori (SH) Planck 1 equation [71] (Eq.6.18), while virtual greybody ratio calibrations (Figure 6.6.b) can be fitted with a log-linear model (Eq.6.19), considering the inverse of the temperature  $T$ . In both equations, the temperature must be expressed in Kelvins.

$$BF(T) = \frac{A_1}{\exp\left(\frac{A_2}{T}\right) - 1} \quad (6.18)$$

$$BF(T) = \exp\left(\frac{B_1}{T} + B_2\right) \quad (6.19)$$

Corresponding fitted calibration coefficients are respectively listed in Table 6.3 for each NB filter and in Table 6.4 for each SWIR ratio thermometer, along with their coefficient of determination  $R^2$ .

Table 6.3: Sakuma Hattori fit coefficients for virtual blackbody calibration (Eq.6.18).

Filter ID	$A_1$ [W.m <sup>-2</sup> ]	$A_2$ [K <sup>-1</sup> ]	$R^2$
NB 1386-10	2.9393 1e5	1.0344 1e4	100%
NB 1640-25	3.9924 1e5	8.7614 1e3	100%
NB 1912-10	8.0316 1e4	7.5312 1e3	100%
NB 2090-25	8.3629 1e4	6.8913 1e3	100%



Table 6.4: Fit coefficients for virtual greybody calibration (Eq.6.19).

Ratio thermometer	Filter 1	Filter 2	B <sub>1</sub> [K <sup>-1</sup> ]	B <sub>2</sub> (intercept)	R <sup>2</sup>
Pair 1	NB1386-10	NB1912-10	2.8113 1e3	-1.2946	100%
Pair 2	NB1640-25	NB2090-25	1.8673 1e3	-1.5591	100%

## 6.4 Modelling approach

A MATLAB software tool has been developed for the spectral simulation of the radiometric chain described in Section 3.1, in order to analyse ratio thermometers described in Sections 3.2 and 3.3. The software tool consists of two steps, i.e. a forward problem and an inverse problem, presented in the next subsections. The last subsection describes the batch simulation setup.

### 6.4.1 Forward problem

In the forward problem, spectral data is known and accessible for simulation (Eq.6.1-6.16). On the one hand, the user can define a set of spectra for the tower system. Extraterrestrial solar irradiation (*AM0*) and atmospheric paths are configured via MODTRAN6 [67,68]. Reference spectra for mirror reflectivity and surface emissivity are also defined from laboratory measurements. On the other hand, the user can define a camera system spectral response (Figure 6.5) and derive corresponding virtual calibration curves (Figure 6.6).

Some excerpt visualizations are illustrated here. Figure 6.7 displays simulated spectra for the three relevant atmospheric paths shown in Figure 6.3. It is worth observing that suitable atmospheric water vapor absorption, around 1.4 μm and 1.9 μm, allows blocking most of solar irradiation on path 1, but also induces significant attenuation on path 3. Figure 6.8.a shows the input spectral data for the calculation of  $\epsilon_{surf}(filter)$  and  $\tau_{atm,path3}(filter)$  (Eq.11,12) (Figure 6.8.b).

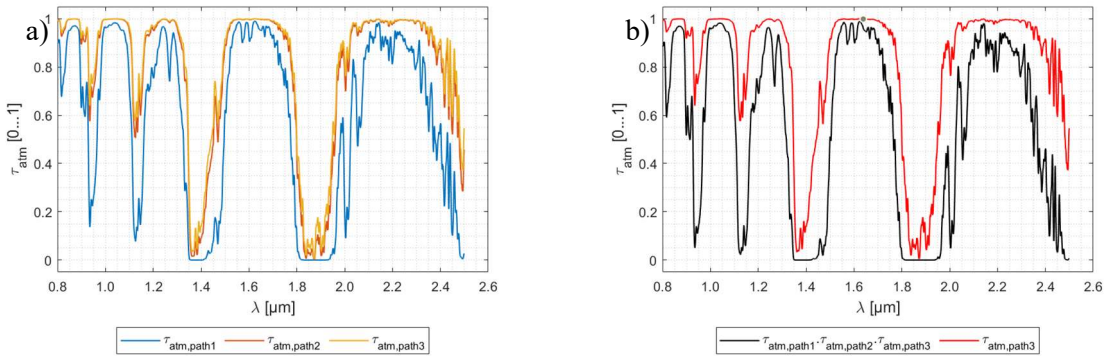


Figure 6.7: Spectral simulation of atmospheric paths. Simulation parameters:  $SZA = 60^\circ$  (*AM2*),  $d_2 = 500$  m,  $d_3 = 350$  m,  $p_{atm} = 960$  mbar,  $T_{amb} = 30$  °C,  $RH = 30\%$ . a) Atmospheric transmissivity  $\tau_{atm}$  for each path. b) Atmospheric transmissivity; path product and path 3.

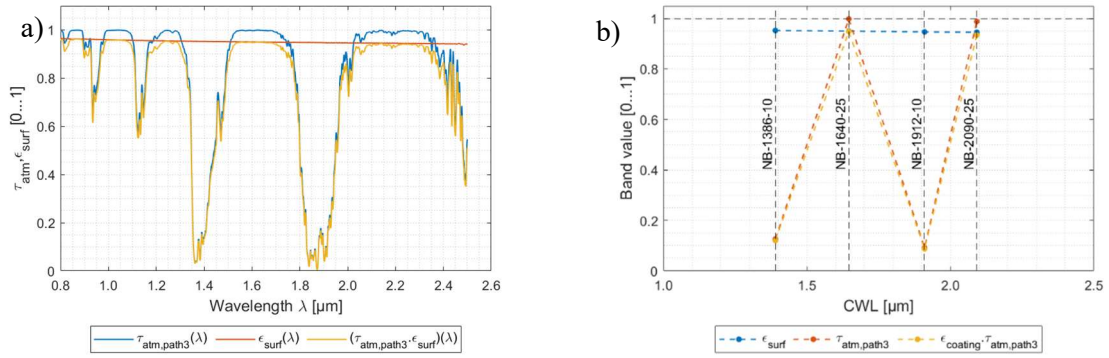


Figure 6.8: Surface emittance and atmospheric transmittance. Simulation parameters: Pyromark 2500,  $SZA = 60^\circ$  (AM2),  $d_2 = 500$  m,  $d_3 = 350$  m,  $p_{atm} = 960$  mbar,  $T_{amb} = 30$  °C,  $RH = 30\%$ . a) Spectral emissivity  $\epsilon_{surf}(\lambda)$  for Pyromark 2500 and atmospheric transmissivity for path 3  $\tau_{atm,path3}(\lambda)$ . b) Surface band emittance  $\epsilon_{surf}(filter)$  and atmospheric band transmittance  $\tau_{atm,path3}(filter)$  for each NB filter.

Figure 6.9 shows a spectral radiometric balance, before applying the camera spectral response (Eq.6.8). This figure highlights the magnitude of each signal contribution, i.e. terms A, B and C (Eq.6.3-6.5). While atmospheric thermal emission (Term C) remain negligible, near solar blindness conditions are rarely met in the SWIR spectral range, except for water absorption bands around 1.4  $\mu\text{m}$  and 1.9  $\mu\text{m}$ . Figure 6.10 shows the same radiometric balance, applying the camera spectral response for each NB filter (Eq.6.8). This visualization allows determining if the measured signal, i.e. the emitted surface thermal radiation (Term A) is dominant over the reflected concentrated solar irradiation (Term B), considered as noise.

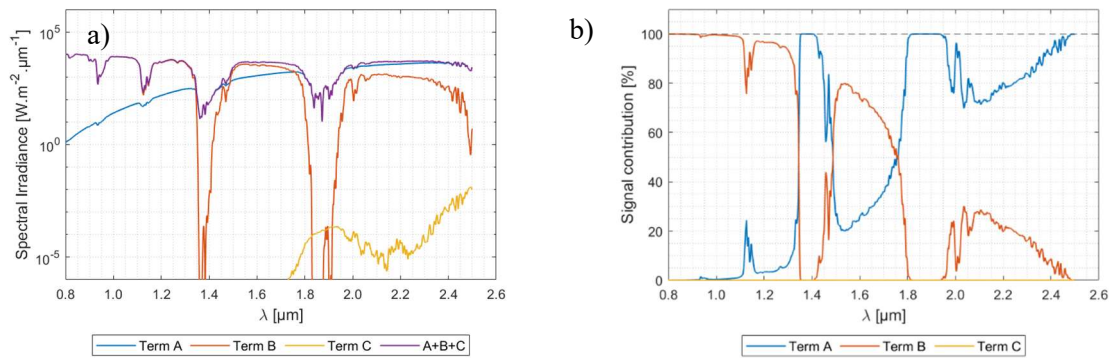


Figure 6.9: Spectral radiometric balance. Simulation parameters: Pyromark 2500:  $T_{surf} = 600$  °C,  $C_x = 300$ ,  $SZA = 60^\circ$  (AM2),  $d_2 = 500$  m,  $d_3 = 350$  m,  $p_{atm} = 960$  mbar,  $T_{amb} = 30$  °C,  $RH = 30\%$ . a) Spectral irradiance, absolute values [ $\text{W}\cdot\text{m}^{-2}\cdot\mu\text{m}^{-1}$ ]. b) Relative values [%].

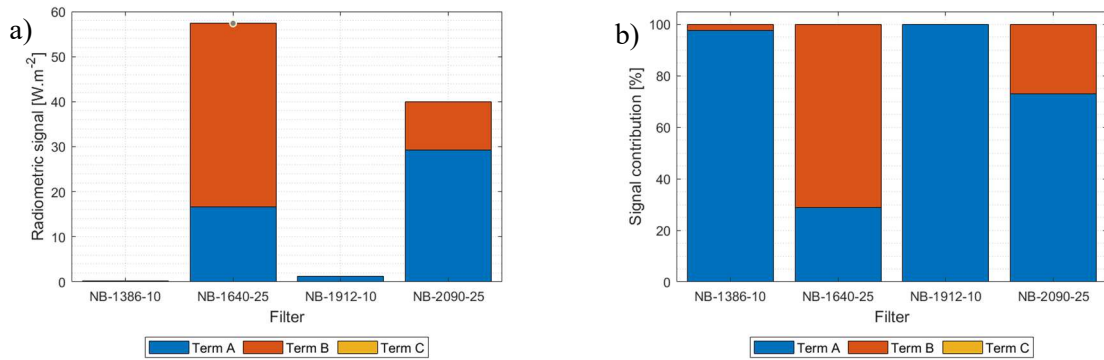


Figure 6.10: Band radiometric balance. Simulation parameters: Pyromark 2500;  $T_{surf}= 600$  °C,  $C_x= 300$ ,  $SZA= 60^\circ$  ( $AM2$ ),  $d_2= 500$  m,  $d_3= 350$  m,  $p_{atm}:= 960$  mbar,  $T_{amb}= 30$  °C,  $RH= 30\%$ ). a) Radiometric signal, absolute values [ $W.m^{-2}$ ]. b) Relative values [%].

### 6.4.2 Inverse problem

In the inverse problem, spectral data is no longer accessible, but embedded in the reference forward problem. The aim of the inverse problem is to estimate  $T_{surf}$  and  $\epsilon_{surf,band}$ , having access to the following data:

- i) Calibration functions for each NB filter and the ratio thermometer (Eq.18-19).
- ii) Measured signal ratio  $SR$  from the forward problem
- iii) Model-based  $\tau_{atm,path3}(filter)$  and  $NGCF_{atm}$  from the forward problem

Two assumptions are made a priori in order to solve the inverse problem:

- Solar blindness conditions are met, i.e. (Term B  $\ll$  Term A)
- The receiver surface behaves as a greybody ( $\epsilon_{surf}(filter\ 1) \sim \epsilon_{surf}(filter\ 2)$ )

Estimated values for  $T_{surf}$  and  $\epsilon_{surf,band}$  are then compared to the reference values defined within the reference forward problem to evaluate the accuracy of ratio thermometers. It is worth remarking that temperature and band emittance errors are negatively correlated. If the estimated temperature is over-estimated, the estimated band emittance would be under-estimated and vice versa.

### 6.4.3 Batch simulation setup

Simulation parameters are listed in Table 6.5. The virtual tower power plant is located in Tabernas, Spain. The receiver height  $H$  is set to 235 m. The equivalent heliostat is positioned at a slant range of 0.5 km. Atmospheric transmissivity spectra are generated for the three defined paths using MODTRAN6, defining three meteorological parameters at ground height:  $p_{atm}$ ,  $T_{amb}$ ,  $RH$  and assuming a Mid-Latitude Summer (MLS) profile [75], used for scaling temperature and humidity altitude profiles along the measurement path. This scaling is done internally within MODTRAN6 by solving the hydrostatic equation. The default  $CO_2$  concentration is set at 400 ppm. Clear sky conditions are assumed and aerosol scattering is assumed negligible in first approximation for SWIR calculations.

A full factorial design of experiments (DOE) is defined on the one hand for the atmosphere water vapor  $\{p_{atm}; T_{amb}; RH\}$ , converted into a synthetic variable  $AH[g/m^3]$ . This DOE is combined

with another full factorial DOE modelling variable operating conditions  $\{C_x, T_{surf}, SZA\}$ . The camera slant range  $d_3$  is also allowed to vary, with a default value set at 350 m.

The aim of this simulation is to analyze the sensitivity of the two SWIR ratio thermometers defined in Section 3.3. The first SWIR ratio thermometer is known to be sensitive to atmospheric water vapor absorption. Suitable atmospheric and operating conditions have to be identified for which the measurement process can be considered nearly solar blind, i.e. for a relative temperature error  $\Delta T/T$  less than 2%, expressing the reference temperature in Kelvins. Once these conditions are identified, ratio temperature measurements can be performed, applying the atmospheric compensation factor  $NGCF_{atm}$ . Finally, the correlation between the relative temperature error  $\Delta T/T$  and the band emittance error  $\Delta \epsilon$  can be characterised. The second SWIR ratio thermometer is insensitive to atmospheric water vapor, solar blind conditions are assumed at dusk, when heliostats are defocused ( $C_x = 0$ ) and the receiver is cooling down before molten salts drainage ( $T_{surf} > 250$  °C).

Table 6.5: Inventory of simulation parameters.

Parameter	Symbol	Category	Units	Value range
Latitude	$LAT$	Site	[°]	37.0976° North
Longitude	$LON$	Site	[°]	2.35818° West
Ground height	$H_0$	Site	m.a.s.l	500 m
Receiver height	$H$	CRS/configuration	[km]	235 m
Surface temperature	$T_{surf}$	CRS/configuration	[°C]	{200:50:800} °C
Concentration factor	$C_x$	CRS/configuration	[-]	{0:100:1000}
Receiver surface	-	CRS/configuration	-	Pyromark 2500 or H230 oxide
Solar Zenith Angle	$SZA$	Atmosphere/Path 1	[°]	{0:10:80} °
Slant range (path 2)	$d_2$	Atmosphere/Path 2	[km]	0.5 km (Equivalent heliostat)
Slant range (path 3)	$d_3$	Atmosphere/Path 3	[km]	{0.3:0.05:1} km
Atmospheric pressure	$p_{atm}(H_0)$	Atmosphere	[mbar]	960 mbar
Ambient temperature	$T_{amb}(H_0)$	Atmosphere	[°C]	{10:10:40} °C
Relative humidity	$RH(H_0)$	Atmosphere	[%]	{10:10:90} %
Atmospheric profile	-	Atmosphere	[-]	Mid Latitude Summer (MLS)

## 6.5 Results and discussion

### 6.5.1 First SWIR ratio thermometer

The first SWIR ratio thermometer (Table 6.2, Pair 1) combines two NB filters, i.e. NB1386-10 and NB1912-10, which are centered on atmospheric water absorption bands. This SWIR ratio thermometer is thus expected to be sensitive to humidity on the one hand and the atmospheric path length (Figure 6.7) on the other hand. Atmospheric water vapor here plays a role in blocking solar irradiation on Path 1 to achieve near solar blindness, while it also attenuates the thermal radiation emitted by the receiver surface on Path 3 (Figure 6.3).

Figure 6.11 shows the optical depth on path 1 ( $OD_{path1}$ ) for these two NB filters as a function of  $AH$  and  $SZA$ . For each NB filter,  $\tau_{atm,path1}(filter)$  is calculated according to (Eq.6.20).  $OD$  is here defined as the decimal logarithm of  $\tau_{atm,path1}(filter)$  (Eq.6.21). An  $OD$  value of -3 corresponds to an atmospheric transmittance of 0.1%. To achieve solar blindness,  $OD_{path1}$  has to be minimised.

$$\tau_{atm,path1}(filter) = \frac{\int_{\lambda_{start}}^{\lambda_{stop}} \tau_{atm,path1}(\lambda, d_1, atm) \cdot E_{sun}(\lambda, AM0) SRF_{cam}(\lambda, T_{cam}) \cdot d\lambda}{\int_{\lambda_{start}}^{\lambda_{stop}} E_{sun}(\lambda, AM0) SRF_{cam}(\lambda, T_{cam}) \cdot d\lambda} \quad (6.20)$$

$$OD_{path1}(filter) = \log(\tau_{atm,path1}(filter)) \quad (6.21)$$

For both NB filters,  $OD_{path1}$  decreases as  $AH$  and  $SZA$  increase, i.e. a stronger attenuation of solar radiation is achieved. A lower  $OD_{path1}$  value is observed for the NB1912-10 filter (Figure 6.11.b) in comparison to the NB1386-10 filter (Figure 6.11.a). This latter NB filter is thus more sensitive to reflected concentrated solar irradiation. The atmospheric water absorption band around  $1.4 \mu\text{m}$  is narrower in comparison to the next band around  $1.9 \mu\text{m}$ , although both absorption bands broaden as  $AH$  and  $SZA$  increase.

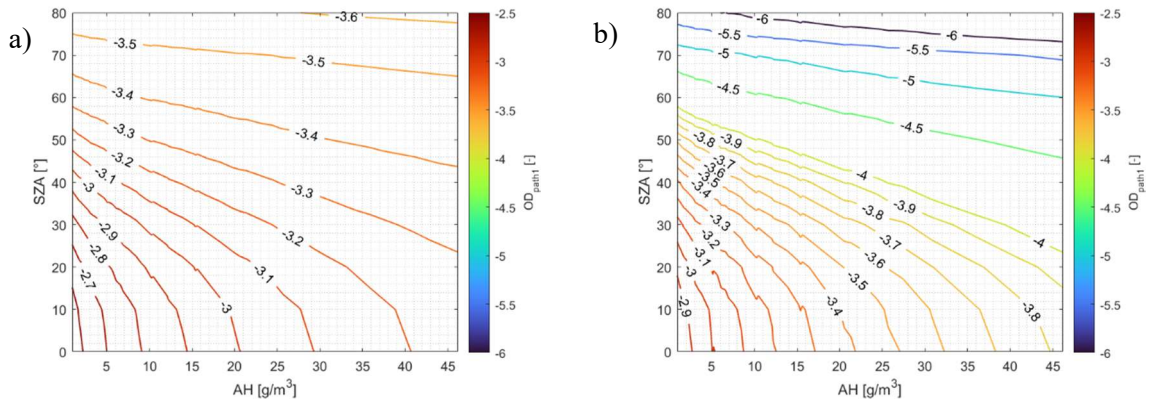


Figure 6.11: Contour plot of  $OD_{path1}$  as a function  $AH$  and  $SZA$ . a) NB1386-10 b) NB1912-10

Figure 6.12 shows the atmospheric transmittance on path 3 ( $\tau_{atm,path3}$ ) for both NB filters as a function of  $AH$  and slant range  $d_3$ . For both NB filters,  $\tau_{atm,path3}$  decreases as  $AH$  and  $d_3$  increase. A significant attenuation is observed, the maximum transmittance is about 30% for a dry atmosphere and a slant range  $d_3$  of 300 m. This is the minimal applicable slant range for a typical receiver height of 235 m.

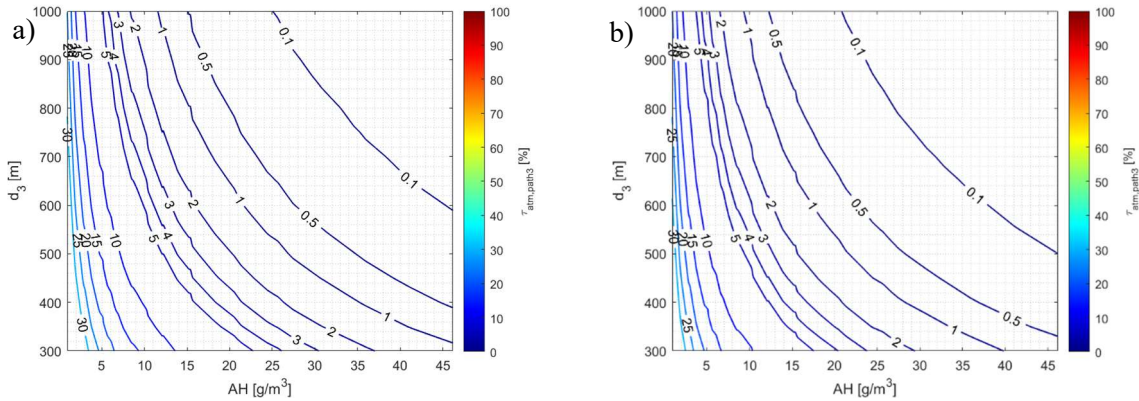
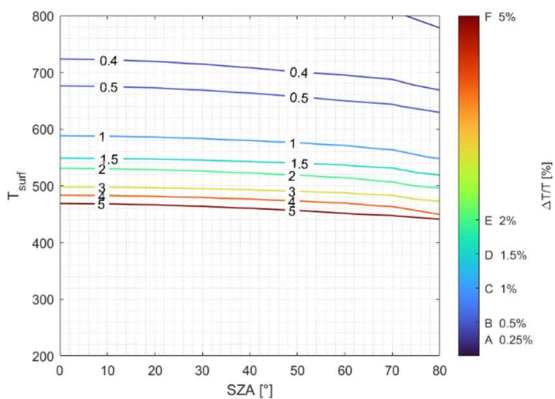


Figure 6.12: Contour plot of  $\tau_{atm,path3}$  as a function of  $AH$  and  $d_3$ . a) NB1386-10 b) NB1912-10

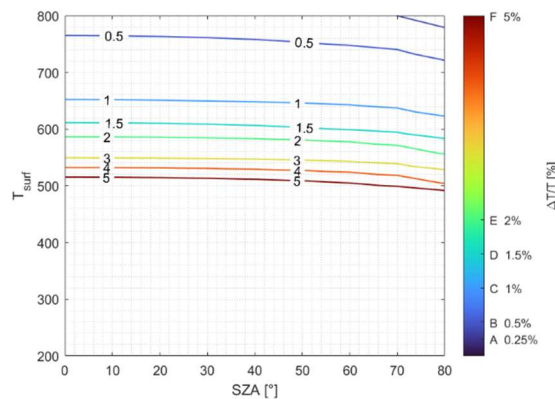
Figure 6.13 shows the expected relative error  $\Delta T/T$  (%) for the first SWIR ratio thermometer as a function of  $C_x$ ,  $T_{surf}$ ,  $SZA$  and  $AH$ . The reference surface is Pyromark 2500 and slant range  $d_3$  is set at 350 m. Four sections of the simulated hypercube are shown, i.e. for low and high absolute

humidity at ground level ( $AH \sim 6 \dots 15 \text{ g/m}^3$ ) and for low and high concentration factor ( $C_x$ : 300...1000). The relative error  $\Delta T/T$  should be less than 2% for an accurate surface temperature measurement. This criterion allows defining a minimal temperature threshold. Figure 6.13 shows that this temperature threshold is dynamic. If  $AH \sim 6 \text{ g/m}^3$ , the minimum temperature threshold is respectively 530 °C for  $C_x = 300$  and 620 °C for  $C_x = 1000$ . If  $AH \sim 15 \text{ g/m}^3$ , the minimum temperature threshold is 590 °C for  $C_x = 300$  and 690 °C for  $C_x = 1000$ . These temperature thresholds overlap or even exceed the maximum  $T_{surf}$  value allowed for molten salt receivers, i.e.  $\sim 600 \text{ °C}$ . These thresholds slightly relax by at least 10 K at higher  $SZA$  above  $45^\circ$  (winter or sunrise/sunset). This limits significantly the applicability of this first SWIR ratio thermometer for remote opto-thermal characterization.

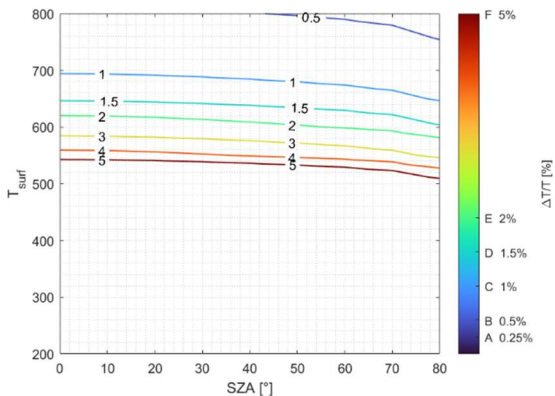
a)  $AH \sim 6 \text{ g/m}^3, C_x = 300$



b)  $AH \sim 15 \text{ g/m}^3, C_x = 300$



c)  $AH \sim 6 \text{ g/m}^3, C_x = 1000$



d)  $AH \sim 15 \text{ g/m}^3, C_x = 1000$

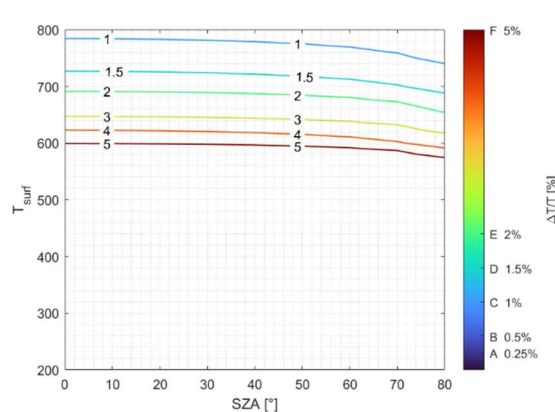


Figure 6.13: Analysis of  $\Delta T/T$  as a function of  $SZA$ ,  $AH$ ,  $T_{surf}$  and  $C_x$ . Boundary conditions:  $d_3 = 350 \text{ m}$ , Pyromark 2500.  $p_{atm} = 960 \text{ mbar}$ ,  $T_{amb} = 30 \text{ °C}$ ,  $RH: (20 \dots 50) \%$ .

Figure 6.14 shows the correlation between the absolute band emittance error  $\Delta \epsilon$  and the relative temperature error  $\Delta T/T$  for the first SWIR ratio thermometer, applying a threshold of 2%. A linear negative correlation is observed between  $\Delta \epsilon$  and  $\Delta T/T$  for Pyromark 2500 (Figure 6.14.a) and oxidised H230 (Figure 6.14.b). Reference  $\epsilon_{surf}(filter)$  values for both surfaces are given in Table 6.6. The grey hypothesis is confirmed for both surfaces, although the ratio of band emittance is slightly lower for oxidised H230. For Pyromark 2500, the correlation slope coefficient is estimated at  $-6.3 \text{ p.p. } \Delta \epsilon$  for a 1% variation of  $\Delta T/T$  (Figure 6.14.a). For oxidised H230, the correlation slope coefficient is estimated at  $-5.7 \text{ p.p. } \Delta \epsilon$  per 1%  $\Delta T/T$  (Figure 6.14.b).

Table 6.6. First SWIR ratio thermometer. Reference values  $\epsilon_{surf}(filter)$  values for Pyromark 2500 and oxidised H230.

$\epsilon_{surf}(filter)$	Filter 1: NB1386-10	Filter 2: NB1912-10	Grey hypothesis
Pyromark 2500	95.3%	94.7%	99.4%
Oxidised H230	87.8%	86.2%	98.2%
Deviation	7.5 p.p.	8.5 p.p.	-

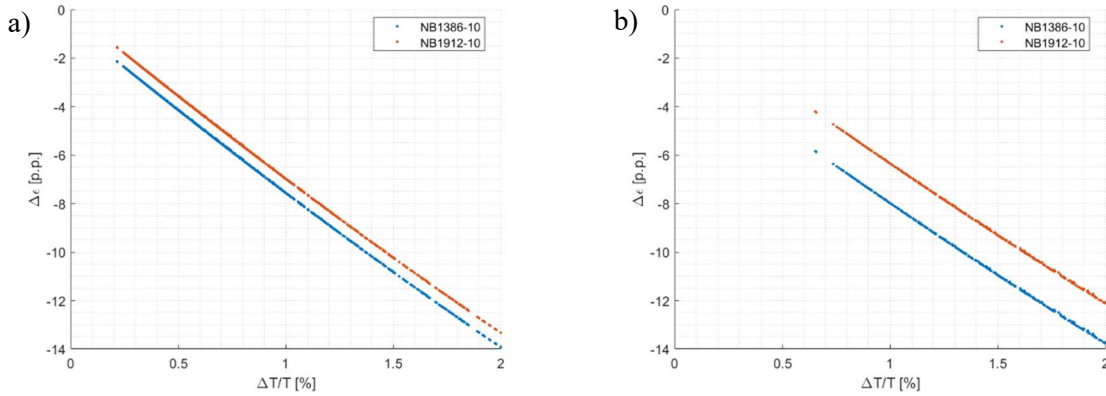


Figure 6.14. Correlation of  $\Delta\epsilon$  and  $\Delta T/T$  for the first SWIR ratio thermometer. Boundary conditions:  $\Delta T/T < 2\%$ ;  $d_3 = 350$  m. a) Pyromark 2500. b) Oxidised H230.

### 6.5.2 Second SWIR ratio thermometer

The second SWIR ratio thermometer (Table 6.2, Pair 2) combines two NB filters, i.e. NB1640-25 and NB2090-25, which are centered on atmospheric windows. This SWIR ratio thermometer is not suitable for on-sun temperature measurements. This configuration is thus analysed for off-sun ( $C_x = 0$ ) temperature measurements, with  $T_{surf} > 250$  °C (molten salts freezing point).

Figure 6.15 shows the atmospheric transmittance on path 3 ( $\tau_{atm,path3}$ ) for both NB filters as a function of  $AH$  and slant range  $d_3$ . The filter NB1640-25 is barely affected by  $AH$  and  $d_3$  parameters (Figure 6.15.a),  $\tau_{atm,path3}(filter)$  values remain above 99%. For the filter NB2090-25, a minor dependence is observed (Figure 6.15.b), although  $\tau_{atm,path3}(filter)$  values remain above 90%. Both NB filters are thus suited for remote opto-thermal characterization.

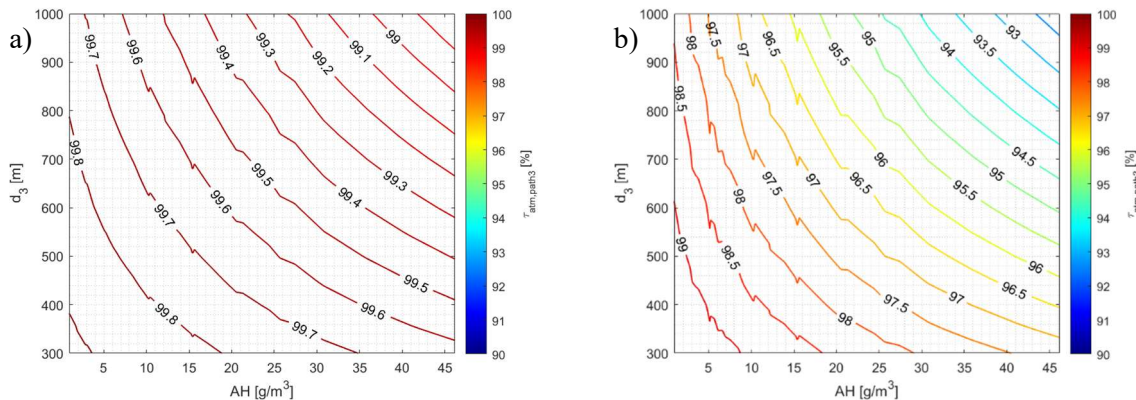


Figure 6.15: Contour plot of  $\tau_{atm,path3}$  as a function of  $AH$  and  $d_3$ . a) NB1640-25 b) NB2090-25

Figure 6.16 shows the expected relative error  $\Delta T/T$  for the second SWIR ratio thermometer as a function of  $T_{surf}$  and  $AH$  for both reference surfaces. The concentration factor  $C_x$  is set at 0 and the slant range  $d_3$  is set at 350 m. One can first observe that  $\Delta T/T$  is independent of  $AH$  and increase linearly with  $T_{surf}$ . Furthermore, the expected value for  $\Delta T/T$  is low for both surfaces:

for Pyromark 2500,  $\Delta T/T$  is bounded between 0.12% at 250 °C and 0.26% at 800 °C. For oxidised H230,  $\Delta T/T$  is bounded between 0.16% at 250 °C and 0.34% at 800 °C.

If the central receiver cannot be heated to an arbitrary temperature  $T_{surf}$  above 300 °C with a suitable heat tracing system, this SWIR ratio thermometer could only be used in practice for low receiver surface temperature levels. The central receiver must be maintained isothermal, above the molten salt freezing temperature, when the heliostat field is defocused ( $C_x = 0$ ). This would correspond to the daily cool-down operation phase before molten salt drainage, when the calibration of the reference LWIR thermographic system is typically performed.

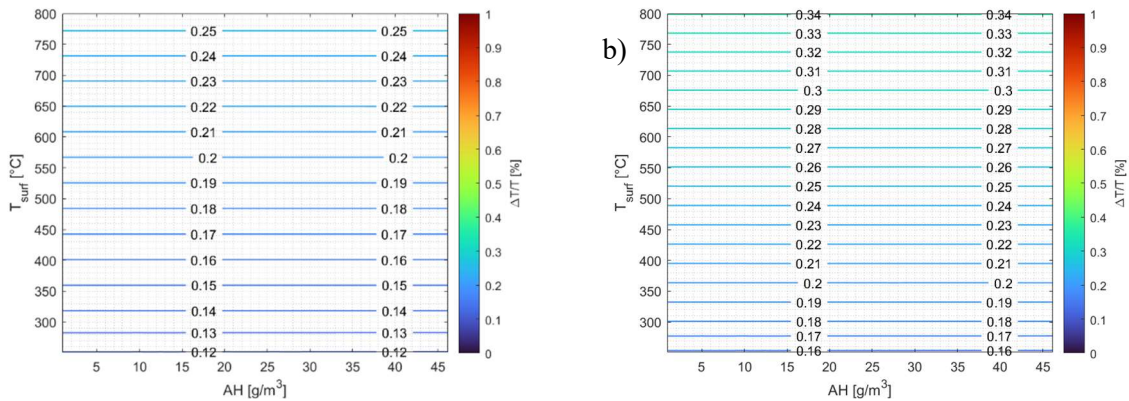


Figure 6.16: Analysis of relative temperature error  $\Delta T/T$  as a function of  $T_{surf}$ . Boundary conditions:  $d3=350$  m,  $C_x=0$ . a) Pyromark 2500. b) oxidised H230.

Figure 6.17 shows the correlation between the absolute band emittance error  $\Delta\epsilon$  and the relative temperature error  $\Delta T/T$  for the second SWIR ratio thermometer. A negative correlation is observed between  $\Delta\epsilon$  and  $\Delta T/T$  for Pyromark 2500 (Figure 6.17.a) and oxidised H230 (Figure 6.17.b). Reference  $\epsilon_{surf}(filter)$  values for both surfaces are given in Table 6.7. The grey hypothesis is confirmed for both surfaces. The estimated band emittance is systematically underestimated. For Pyromark 2500, the absolute value of  $\Delta\epsilon$  does not exceed 2 p.p., while its maximum value is about 2.5 p.p. for oxidised H230. The second SWIR ratio thermometer allows discriminating both surfaces.

Table 6.7: Second SWIR ratio thermometer. Reference  $\epsilon_{surf}(filter)$  values for Pyromark 2500 and oxidised H230.

$\epsilon_{surf}(filter)$	Filter 1: NB1640-25	Filter 2: NB2090-25	Grey hypothesis
<b>Pyromark 2500</b>	95.0%	94.6%	99.6%
<b>Oxidised H230</b>	86.7%	86.2%	99.4%
<b>Deviation</b>	8.3 p.p.	8.7 p.p.	-



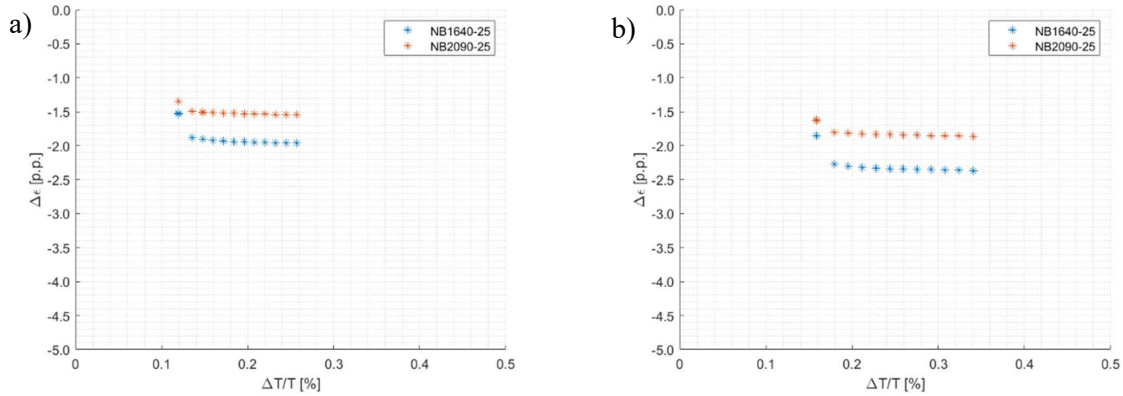


Figure 6.17: Correlation of  $\Delta\epsilon$  and  $\Delta T/T$  for the second SWIR ratio thermometer. Boundary conditions:  $C_x=0$ ,  $d_3=350$  m. a) Pyromark 2500. b) Oxidised H230.

## 6.6 Conclusion and outlook

In this chapter, a new measurement principle has been introduced and analysed for the remote opto-thermal characterization of central external cylindrical receivers in solar tower power plants. The new measurement principle relies on passive shortwave infrared (SWIR) ratio thermography. It allows a simultaneous retrieval of surface temperature and band emittance for grey surfaces such as black coatings and oxidised metals. The atmosphere does not behave a priori as a greybody. A model-based estimation of band atmospheric transmittance has been introduced to correct this hypothesis, using meteorological parameters available at ground level, i.e. ambient temperature  $T_{amb}$ , relative humidity  $RH$  and atmospheric pressure  $p_{atm}$ .

A MATLAB software tool has been developed and coupled to MODTRAN6 radiative transfer code, for the spectral simulation of radiometric chains relevant in Concentrating Solar Power. The accuracy and sensitivity of two SWIR ratio thermometers have been analysed using spectral simulations. Relevant parameters combine atmospheric conditions, in particular absolute humidity  $AH$  and Solar Zenith Angle ( $SZA$ ) and operating conditions, i.e. concentration factor  $C_x$  and surface temperature  $T_{surf}$ . The first SWIR ratio thermometer combines two narrow bandpass (NB) filters centered on two water vapor atmospheric absorption bands, respectively located at  $1.4 \mu\text{m}$  and  $1.9 \mu\text{m}$ . The second SWIR ratio thermometer combines two NB filters centered on atmospheric windows, respectively located at  $1.64 \mu\text{m}$  and  $2.09 \mu\text{m}$ .

The first SWIR ratio thermometer ( $1.4/1.9 \mu\text{m}$ ) is particularly sensitive to atmospheric water vapor, which filters extraterrestrial solar radiation on the one hand but also attenuates thermal radiation emitted by the receiver surface on the other hand, in particular for a typical receiver height above 200 m. Under realistic  $AH$  levels, this ratio thermometer can be considered nearly solar blind, but only for temperatures above  $550 \text{ }^\circ\text{C}$ . The temperature threshold for which the relative temperature error  $\Delta T/T$  is less than 2% varies with the absolute humidity  $AH$  estimated at ground level, the solar zenith angle  $SZA$  and the concentration factor  $C_x$ . This SWIR ratio thermometer, has probably a limited applicability for remote opto-thermal characterization during power plant operation, especially for a receiver height above 200 m and without detailed knowledge of temperature and humidity profiles along the measurement path. It may be applied for shorter distances on high temperature objects, if atmospheric conditions are well characterised.

The second SWIR ratio thermometer (1.64/2.09  $\mu\text{m}$ ) is not sensitive to atmospheric water vapor, however it cannot operate during daily power plant operation. It could remotely characterise the receiver surface temperature  $T_{surf}$  and surface band emittance  $\epsilon_{surf,band}$  with a good accuracy when the heliostat field is defocused ( $C_x=0$ ) and the receiver surface is maintained isothermal ( $T_{surf} \sim 300\text{ }^\circ\text{C}$ ) before molten salt drainage. The relative temperature error  $\Delta T/T$  is lower than 0.5% and the band emittance error  $\Delta\epsilon$  is less than 2.5 p.p., according to spectral simulations for Pyromark 2500 and oxidised Haynes 230. This operation phase is also often used in commercial power plants for the calibration of Longwave Infrared (LWIR) cameras. The second SWIR ratio thermometer could therefore offer an alternative method to support the LWIR system during calibration and map remotely the receiver band emittance.

A prototype SWIR multispectral camera, including both ratio thermometer configurations described above, has been assembled and tested at Plataforma Solar de Almería, Spain. The experimental validation of the measurement principle under laboratory conditions is currently on going and the camera system is being fine-tuned for future field measurements in Central Receiver Systems. Future simulation work may investigate the sensitivity of both SWIR ratio thermometers with respect to aerosols or water vapor atmospheric profiles. The software tool for spectral simulations is also capable to simulate other spectral ranges, i.e. visible wavelengths (0.4-0.8  $\mu\text{m}$ ) for flux measurement systems, as well as midwave and infrared wavelengths (MWIR: 2.5-5.5  $\mu\text{m}$ , LWIR: 8-14  $\mu\text{m}$ ) relevant for other thermographic camera configurations.

## 6.7 References: Chapter 6

- [1] M. Perez, R. Perez, Update 2022 – A fundamental look at supply side energy reserves for the planet, *Solar Energy Advances*, 2 (2022), 100014. <https://doi.org/10.1016/j.seja.2022.100014>
- [2] MIT Energy Initiative, The Future of Solar Energy (2015), available at: <https://energy.mit.edu/wp-content/uploads/2015/05/MITEI-The-Future-of-Solar-Energy.pdf>. Accessed: 01/12/23.
- [3] IRENA, Solar Energy, (2023), available at: <https://www.irena.org/Energy-Transition/Technology/Solar-energy>. Accessed: 01/12/2023.
- [4] PV magazine, World has installed 1TW of solar capacity, available at: <https://www.pv-magazine.com/2022/03/15/humans-have-installed-1-terawatt-of-solar-capacity/>. Accessed: 01/12/2023.
- [5] International Energy Agency SolarPACES, CSP projects around the world, available at: <https://www.solarpaces.org/worldwide-csp/csp-projects-around-the-world/>. Accessed: 01/12/2023.
- [6] International Energy Agency SolarPACES, China now has 30 CSP projects with thermal energy storage underway (2022), available at: <https://www.solarpaces.org/china-now-has-30-csp-projects-with-thermal-energy-storage-underway/>. Accessed: 01/12/2023.
- [7] German Aerospace Center (DLR) Institute of Solar Research, Solar thermal power plants: heat, electricity and fuels from concentrated solar power, (2021), available at: [https://www.dlr.de/sf/en/PortalData/73/Resources/dokumente/publikationen\\_medien/dlr\\_un\\_d\\_sf/Study\\_Solar\\_thermal\\_power\\_plants\\_DLR\\_2021-05.pdf](https://www.dlr.de/sf/en/PortalData/73/Resources/dokumente/publikationen_medien/dlr_un_d_sf/Study_Solar_thermal_power_plants_DLR_2021-05.pdf). Accessed: 01/12/2023.
- [8] DCSP, German Association for Concentrated Solar Power, Solar Power around the Clock, (2021), available at: [EN%20211116\\_DCSP\\_Kurzstudie\\_online\\_EN.pdf \(website-editor.net\)](EN%20211116_DCSP_Kurzstudie_online_EN.pdf). Accessed: 01/12/2023.

- [9] Solar Payback, Solar Heat for Industry, (2017), available at: <https://www.solar-payback.com/download/solar-heat-for-industry-april-2017/>. Accessed: 01/12/2023.
- [10] R. Pitz-Paal et al., Decarbonizing the German industrial thermal energy use with solar, hydrogen, and other options–Recommendations for the world, *Solar Compass*, 3-4 (2022), 100029. <https://doi.org/10.1016/j.solcom.2022.100029>
- [11] A. Fernandez-Garcia et al., Parabolic-trough solar collectors and their applications, *Renewable and Sustainable Energy Reviews*, 14 (2010) 1695–1721. <https://doi.org/10.1016/j.rser.2010.03.012>
- [12] C.K. Ho, Advances in central receivers for concentrating solar applications, *Solar Energy*, 152 (2017), 38-56. <https://doi.org/10.1016/j.solener.2017.03.048>
- [13] P. Gauche et al., System value and progress of CSP, *Solar Energy*, 152 (2017), 106-139. <https://doi.org/10.1016/j.solener.2017.03.072>
- [14] M. Zheng et al., Analysis of tubular receivers for concentrating solar tower systems with a range of working fluids, in exergy-optimised flow-path configurations, *Solar Energy*, 211 (2020), 999-1016. <https://doi.org/10.1016/j.solener.2020.09.037>
- [15] C.A. Asselineau, J. Pye, J. Coventry, Exploring efficiency limits for molten-salt and sodium external cylindrical receivers for third-generation concentrating solar power, *Solar Energy*, 240 (2022), 354-375. <https://doi.org/10.1016/j.solener.2022.05.001>
- [16] C.K. Ho et al., Characterization of Pyromark 2500 paint for high-temperature solar receivers, *Journal of Solar Energy Engineering*, 136(1) (2014), 014502. <https://doi.org/10.1115/1.4024031>
- [17] J. Coventry, P. Burge, Optical properties of Pyromark 2500 coatings of variable thicknesses on a range of materials for concentrating solar thermal applications, *AIP Conference Proceedings*, 1850 (2017), 030012. <https://doi.org/10.1063/1.4984355>
- [18] A. Ambrosini et al., Influence of application parameters on stability of Pyromark® 2500 receiver coatings, *AIP Conference Proceedings*, 2126 (2019), 030002. <https://doi.org/10.1063/1.5117514>
- [19] R. Harzallah et al., Development of high performances solar absorber coatings, *AIP Conference Proceedings*, 2126 (2019), 030026. <https://doi.org/10.1063/1.5117538>
- [20] L. Noč et al., High-solar-absorptance CSP coating characterization and reliability testing with isothermal and cyclic loads for service-life prediction, *Energy & Environmental Science*, 12 (2019),1679-1694. <https://doi.org/10.1039/C8EE03536A>
- [21] J.F. Torres et al., Highly efficient and durable solar thermal energy harvesting via scalable hierarchical coatings inspired by stony corals, *Energy & Environmental Science*, 15 (2022), 1893-1906. <https://doi.org/10.1039/D1EE03028K>
- [22] F. Sutter et al., Dynamic corrosion testing of metals in solar salt for concentrated solar power, *Solar Energy Materials and Solar Cells*, 232 (2021), 111331. <https://doi.org/10.1016/j.solmat.2021.111331>
- [23] D. Hering et al., Monitoring of service life consumption for tubular solar receivers: Review of contemporary thermomechanical and damage modeling approaches, *Solar Energy*, 226 (2021), 427-445. <https://doi.org/10.1016/j.solener.2021.08.022>
- [24] L.L. Vant-Hull, The Role of "Allowable Flux Density" in the Design and Operation of Molten-Salt Solar Central Receivers, *Journal of Solar Energy Engineering*, 124(2) (2002),165-169. <https://doi.org/10.1115/1.1464124>
- [25] R. Flesch et al., Towards an optimal aiming for molten salt power towers, *Solar Energy*, 155 (2017), 1273-1281. <https://doi.org/10.1016/j.solener.2017.07.067>

- [26] A. Sanchez-Gonzalez, M.R. Rodriguez-Sanchez, D. Santana, Aiming strategy model based on allowable flux densities for molten salt central receivers, *Solar Energy*, 157 (2017), 1130-1144. <https://doi.org/10.1016/j.solener.2015.12.055>
- [27] J.F. Torres, I. Ellis, J. Coventry, Degradation mechanisms and non-linear thermal cycling effects in a high-temperature light-absorber coating, *Solar Energy Materials and Solar Cells*, 218 (2020), 110719. <https://doi.org/10.1016/j.solmat.2020.110719>
- [28] S. Hosseini et al., Long-term thermal stability and failure mechanisms of Pyromark 2500 for high-temperature solar thermal receivers, *Solar Energy Materials and Solar Cells*, 246 (2022), 111898. <https://doi.org/10.1016/j.solmat.2022.111898>
- [29] N. Martinez et al., Influence of different thermal degradation processes on the optical property of Pyromark-2500, *Solar Energy*, 253 (2023), 58-72. <https://doi.org/10.1016/j.solener.2023.02.004>
- [30] S. Caron et al., Forty shades of black: A benchmark of high temperature sprayable black coatings applied on Haynes 230, *AIP Conference Proceedings*, 2303 (2020), 150007. <https://doi.org/10.1063/5.0028773>
- [31] S. Caron et al., A comparative analysis of opto-thermal figures of merit for high temperature solar thermal absorber coatings, *Renewable Sustainable Energy Review*, 154 (2022), 111818. <https://doi.org/10.1016/j.rser.2021.111818>
- [32] S. Caron et al., A laboratory intercomparison of solar absorptance and thermal emittance measurements at room temperature, *Solar Energy Materials and Solar Cells* 238 (2022), 111579. <https://doi.org/10.1016/j.solmat.2022.111579>
- [33] C.K. Ho, J. Pacheco, Levelized Cost of Coating (LCOC) for selective absorber materials, *Solar Energy*, 108 (2014), 315-321. <https://doi.org/10.1016/j.solener.2014.05.017>
- [34] A. Boubault et al., Levelized cost of energy (LCOE) metric to characterize solar absorber coatings for the CSP industry, *Renewable Energy*, 85 (2016), 472-483. <https://doi.org/10.1016/j.renene.2015.06.059>
- [35] InfraTec GmbH, Industrial Automation; Thermographic Monitoring of Solar Power Tower - SPTC, available at: <https://www.infratec.eu/thermography/industrial-automation/solar-power-tower-check-sptc/>. Accessed: 30/11/2023.
- [36] Surface Optics, 410-Vis-IR Portable Emissometer & Solar Reflectometer, available at: <https://surfaceoptics.com/products/reflectometers-emissometers/410-vis-ir/>. Accessed: 30/11/2023.
- [37] M. Mehos et al., Concentrating Solar Power Best Practices Study, *NREL Technical report*, NREL/TP-5500-75763 (2020), available at: <https://www.nrel.gov/docs/fy20osti/75763.pdf> Accessed: 30/11/2023.
- [38] G. Naor et al., Flux measurement system using IR camera, *SolarPACES 2010 Proceedings*, Perpignan, France, September 21-24, 2010.
- [39] A. Eitan et al., Accurate Flux Calculations Using Thermographic IR cameras in Concentrated Solar Power Fields, *Quantitative Infrared Thermography (QIRT) 2014 Conference Proceedings* (2014). <http://qirt.org/archives/qirt2014doi/papers/QIRT-2014-220.pdf>
- [40] I. González de Arrieta et al., Infrared emissivity of copper-alloyed spinel black coatings for concentrated solar power systems, *Solar Energy Materials and Solar Cells*, 200 (2019), 109961. <https://doi.org/10.1016/j.solmat.2019.109961>
- [41] W. Minkina, D. Klecha, Atmospheric transmission coefficient modelling in the infrared for thermovision measurements, *Journal of Sensors and Sensors Systems*, 5 (2016) 17-23. <https://doi.org/10.5194/jsss-5-17-2016>

- [42] D. Hernandez et al., Analysis and Experimental Results of Solar-Blind Temperature Measurements in Solar Furnaces, *Journal of Solar Energy Engineering*, 126(1) (2004), 645-653. <https://doi.org/10.1115/1.1636191>
- [43] J. Ballestrin et al., Testing a solar-blind pyrometer, *Metrologia*, 47 (2010), 646. doi: 10.1088/0026-1394/47/6/003
- [44] A. Marzo et al., Solar blind pyrometry not relying on atmospheric absorption bands, *Solar Energy*, 107 (2014), 415-422. <https://doi.org/10.1016/j.solener.2014.04.031>
- [45] M. Pfänder, E. Lüpfert, P. Heller, Pyrometric Temperature Measurements on Solar Thermal High Temperature Receivers, *Journal of Solar Energy Engineering*, 128(3) (2006), 285-292. <https://doi.org/10.1115/1.2210499>
- [46] M. Pfänder, E. Lüpfert, P. Pistor, Infrared temperature measurements on solar trough absorber tubes, *Solar Energy*, 81(5) (2007), 629-635. <https://doi.org/10.1016/j.solener.2006.08.016>
- [47] M. Musto et al., Error analysis on measurement temperature by means dual-color thermography technique, *Measurement*, 90(2016), 265-277. <https://doi.org/10.1016/j.measurement.2016.04.024>
- [48] L. Savino et al., Free emissivity temperature investigations by dual color applied physics methodology in the mid- and long-infrared ranges, *International Journal of Thermal Sciences*, 117 (2017), 328-341. <https://doi.org/10.1016/j.ijthermalsci.2017.03.028>
- [49] F. Di Carolo et al., Standard thermography vs free emissivity dual color novel CIRA physics technique in the near-mid IR ranges: Studies for different emissivity class materials from low to high temperatures typical of aerospace re-entry, *International Journal of Thermal Sciences*, 147 (2020), 106123. <https://doi.org/10.1016/j.ijthermalsci.2019.106123>
- [50] A. Hijazi et al., A calibrated dual-wavelength infrared thermometry approach with non-grey body compensation for machining temperature measurements, *Measurement Science and Technology*, 22 (2011), 025106. doi:10.1088/0957-0233/22/2/025106
- [51] A. Araujo, Multi-spectral pyrometry – a review, *Measurement Science and Technology*, 28 (2017), 082002. <https://doi.org/10.1088/1361-6501/aa7b4b>
- [52] J.-C. Krapez, Measurements without contact in heat transfer: multiwavelength radiation thermometry. Principle, implementation and pitfalls, *Metti 7 Advanced School: Thermal Measurements and Inverse Techniques*, (2019) Porquerolles, France.
- [53] D. Hernandez, J.L. Sans, M. Pfänder, Pyroreflectometry to determine the true temperature and optical properties of surfaces, *Journal of Solar Energy Engineering*, 130(3) (2008), 031003. <https://doi.org/10.1115/1.2840575>
- [54] D. Hernandez, A. Netchaieff, A. Stein, True temperature measurement on metallic surfaces using a two-color pyroreflectometer method, *Review of Scientific Instruments*, 80 (2009) 094903. <https://doi.org/10.1063/1.3208011>
- [55] D. Hernandez et al., Experimental validation of a pyroreflectometric method to determine the true temperature on opaque surface without hampering reflections, *Measurement*, 42(6) (2009), 836-843. <https://doi.org/10.1016/j.measurement.2009.01.012>
- [56] H.R Tschudi, M. Schubnell, Measuring temperatures in the presence of external radiation by flash assisted multiwavelength pyrometry, *Review of Scientific Instruments*, 70 (1999), 2719-2727. <https://doi.org/10.1063/1.1149835>
- [57] H.R. Tschudi, G. Morian, Pyrometric Temperature Measurements in Solar Furnaces, *Journal of Solar Energy Engineering*, 123(2) (2001), 164-170. <https://doi.org/10.1115/1.1355035>

- [58] I. Alxneit, Measuring temperatures in a high concentration solar simulator – Demonstration of the principle, *Solar Energy*, 83(3) (2011),516-522. <https://doi.org/10.1016/j.solener.2010.12.016>
- [59] D. Potamias, I. Alxneit, A. Wokaun, Double modulation pyrometry: A radiometric method to measure surface temperatures of directly irradiated samples, *Review of Scientific Instruments*, 88 (2017) 095112. <https://doi.org/10.1063/1.4987129>
- [60] D. Potamias et al., Double modulation pyrometry applied to radiatively heated surfaces with dynamic optical properties, *Journal of Solar Energy Engineering*, 141(1) (2018), 011003. <https://doi.org/10.1115/1.4040842>
- [61] D. Potamias et al., Assessment of Double Modulation Pyrometry as a diagnostic tool for use in concentrated solar facilities, *Solar Energy*, 174 (2018), 660-668. <https://doi.org/10.1016/j.solener.2018.09.028>
- [62] T. Sentenac et al., Bi-color near infrared thermo-reflectometry: A method for true temperature field measurement, *Review of Scientific Instruments*, 83 (2012), 124902. <https://doi.org/10.1063/1.4769802>
- [63] R. Gilblas et al., Quantitative temperature field measurements on a non-gray multi-materials scene by thermoreflectometry, *Infrared Physics & Technology*, 66 (2014), 70-77. <https://doi.org/10.1016/j.infrared.2014.05.014>
- [64] B. Jahne, Practical Handbook on Image Processing for Scientific and Technical Applications, Second Edition, CRC Press (2004). ISBN 9780849390302.
- [65] Vaisala, Humidity conversions: Formulas and methods for calculating humidity parameters, available at: <https://www.vaisala.com/en/lp/make-your-job-easier-humidity-conversion-formulas>. Accessed: 01/12/2023.
- [66] B.D. Maione, C. Baldrige, M. W. Kudenov, Microbolometer with a multi-aperture polymer thin-film array for neural-network-based target identification, *Applied Optics*, 58 (27) (2019), 7285-7297. <https://doi.org/10.1364/AO.58.007285>
- [67] Spectral Sciences Inc., MODTRAN®, available at: <http://modtran.spectral.com/>. Accessed: 01/12/2023.
- [68] A. Berk et al., MODTRAN6: a major upgrade of the MODTRAN radiative transfer code, *SPIE Proceedings. Algorithms and Technologies for Multispectral, Hyperspectral, and Ultraspectral Imagery 30*, 9088 (2014), 90880H. <https://doi.org/10.1117/12.2050433>
- [69] C. Gueymard, G. Lopez, I. Rapp-Arraras, Atmospheric transmission loss in mirror-to-tower slant ranges due to water vapor, *AIP Conference Proceedings*, 1850 (2017), 140010. <https://doi.org/10.1063/1.4984518>
- [70] G. Lopez et al., Modeling water vapor impacts on the solar irradiance reaching the receiver of a solar tower plant by means of artificial neural networks, *Solar Energy*, 169 (2018), 34-39. <https://doi.org/10.1016/j.solener.2018.04.023>
- [71] F. Sakuma, M. Kobayashi, "Interpolation equations of scales of radiation thermometers", *Proceedings of TEMPMEKO 1996*, pp. 305–310 (1996).
- [72] Hamamatsu, Image sensor module C16090-03, available at: <https://www.hamamatsu.com/us/en/product/optical-sensors/image-sensor/image-sensor-modules/C16090-03.html>. Accessed: 01/12/2023.
- [73] Spectrogon, Narrow Bandpass Filters, available at: [https://www.spectrogon.com/products/optical-filters/spectrogon-ab/narrow-bandpass-filters/#of\\_target](https://www.spectrogon.com/products/optical-filters/spectrogon-ab/narrow-bandpass-filters/#of_target). Accessed: 01/12/2023.
- [74] OPTEC SRL, IR lenses, available at: <https://ir.optec.eu/index.asp>. Accessed: 01/12/2023.
- [75] A.J. Kantor, A.E. Cole, Mid-latitude atmospheres, winter and summer, *Geofisica Pura e Applicata* 53 (1962), 171–188 (1962). <https://doi.org/10.1007/BF02007120>.

## **Chapter 7. Conclusion and outlook**





## 7 Conclusion and outlook

The results of this research have materialized in four publications, three of them published in indexed scientific journals of high impact and a fourth currently under review in another high impact journal. The main contributions of this research work are presented below.

### 7.1 Publication n°1: A comparative analysis of opto-thermal figures of merit for high temperature solar thermal absorber coatings

In this chapter, opto-thermal figures of merit relevant for the characterization of solar thermal absorber coatings were analysed and compared. These figures of merit were calculated on the basis of spectral measurements (0.25  $\mu\text{m}$  to 20  $\mu\text{m}$ ) made at room temperature for a near-normal angle of incidence. Reference solar thermal absorber coatings included two types of coatings, i.e. solar selective and black coatings. For each coating type, a reference coating and an ideal coating were analysed.

For the comparative analysis, a set of modelling assumptions were made for simplification, in particular a flat geometry, negligible angular effects, negligible convection and stable optical properties at operating temperature. The list of figures of merit includes two standard indicators, i.e. solar absorptance  $\alpha_{sol}$  and thermal emittance  $\varepsilon_{th}$ , spectral parameters for a solar selective coating model ( $f_{SSC}(\lambda)$ ), i.e. cut-off wavelength ( $\lambda_{cut-off}$ ), shape factor ( $f_{shape}$ ) and reflectivity asymptotes ( $\rho_{low}$  and  $\rho_{high}$ ). Further existing compound figures of merit were analysed, i.e. Selectivity ratio  $Si$ , useful heat flux  $\dot{q}_{use}''$ , opto-thermal efficiency  $\eta_{opt-th}$ , Maximum steady-state temperature  $T_{SST,max}$ , Solar reflectance index  $SRI$  and thermal efficiency  $\eta_{thermal}$ . Additional figures of merit were introduced, i.e. a normalised selectivity ratio  $Si^*$  and solar reflectance index  $SRI^*$ , a trade-off factor  $Z_{trade-off}$  and a peak efficiency temperature  $T_{peak,opt}$ . The interactions between all figures of merit were summarised in a synoptical diagram.

A first subset of figures of merit allows a finer characterization of selectivity, i.e. spectral model parameters  $\{\lambda_{cut-off}, f_{shape}, \rho_{low}$  and  $\rho_{high}\}$ , the selectivity ratio  $Si$ , the maximum steady-state temperature  $T_{SST,max}$  and the solar reflectance index  $SRI$ . The  $Si$  and  $SRI$  figures of merit have been tentatively normalised ( $Si^*$  and  $SRI^*$ ) for a better adaptation in the field of CSP. Their correlation to the absorber temperature  $T_{abs}$  and the maximum steady-state temperature  $T_{SST,max}$  has also been highlighted.

A second subset of figures of merit, i.e. useful heat flux  $\dot{q}_{use}''$ , opto-thermal efficiency  $\eta_{opt-th}$  and thermal efficiency  $\eta_{thermal}$  allow a dynamic ranking of solar thermal absorber coatings, depending on the specific operating point  $\{C_x, T_{abs}\}$  and the corresponding trade-off factor  $Z_{trade-off}$  between solar absorptance  $\alpha_{sol}$  and thermal emittance  $\varepsilon_{th}$ . The existence of a Pareto front between a reference black coating and a reference solar selective coating has been shown and a spectral evolution of cumulative opto-thermal efficiency has also been illustrated. At high concentration and low temperature, the influence of solar absorptance is dominant over thermal emittance, favoring black coatings for central receiver systems. Spectral selectivity is more important to achieve at lower concentration and higher temperature, for instance in parabolic trough applications.

The thermal efficiency  $\eta_{thermal}$  corrects a shortcoming of the opto-thermal efficiency  $\eta_{opt-th}$ , which decreases at higher temperature by definition, while a higher temperature is desired to

maximise the thermal efficiency. Thermal efficiency  $\eta_{thermal}$  offers the most comprehensive perspective: it increases up to a plateau around the peak efficiency temperature  $T_{peak,opt}$  then it decreases until the maximum steady-state temperature  $T_{SST,max}$ . The figure of merit  $T_{peak,opt}$  is deemed more relevant as the figure of merit  $T_{SST,max}$  as  $T_{peak,opt}$  indicates the optimal operating temperature range of a solar thermal absorber coating, while  $T_{SST,max}$  typically exceeds the maximal operating temperature of such coatings.

## **7.2 Publication n°2: Laboratory intercomparison of solar absorptance and thermal emittance measurements at room temperature**

In this chapter, spectral directional hemispherical reflectivity measurements have been compared at several laboratories on two flat solar thermal absorber coatings, i.e. a high absorbing black coating and a solar selective coating. Measurements have been carried out at room temperature both with benchtop spectrophotometers and portable devices.

A good agreement was found between spectrophotometer datasets. In the UV-VIS-NIR range, all datasets agree well until 2.0  $\mu\text{m}$ . Above 2.5  $\mu\text{m}$ , a minor deviation can be observed for both coatings. In the Infrared range, a good agreement is observed for the solar selective coating (SSC) until 16  $\mu\text{m}$ . For the black coating, a higher dispersion is noticeable. Spectral mismatch in the range from 2  $\mu\text{m}$  to 2.5  $\mu\text{m}$  is less than 1 p.p. for the black coating, while a slightly higher deviation is noticed for the SSC.

Applying ASTM G173-03 (*AM1.5 direct+circumsolar*), the average and standard deviation for the solar absorptance  $\alpha_{sol}$  are respectively  $96.6 \pm 0.16\%$  for the black coating and  $94.5 \pm 0.35\%$  for the SSC. The selection of the reference solar spectrum does not significantly affect the  $\alpha_{sol}$  calculation for the black coating, while the sensitivity is more pronounced for the solar selective coating. The SOC 410-Solar portable device delivers values in agreement with benchtop spectrophotometers.

For thermal emittance  $\epsilon_{th}$  calculations, a good agreement is found for the SSC (650 °C:  $\epsilon_{th,calc} = 25.0 \pm 0.5\%$ ), while a larger deviation can be noticed for the black coating (650 °C:  $\epsilon_{th,calc} = 80.8 \pm 3.8\%$ ), mainly explained by the dispersion of infrared spectra. The calculated temperature dependence of  $\epsilon_{th}$  is moderate for the black coating and more pronounced for the solar selective coating, as the overlap of the blackbody and solar spectra increases.

Extrapolating spectral data from 16  $\mu\text{m}$  to 50  $\mu\text{m}$  has a moderate impact on  $\epsilon_{th}$  calculation results. For the black coating,  $\epsilon_{th}$  values converge at higher temperature, while their dispersion decreases. For the solar selective coating, a systematic offset of 1 p.p. remains for  $\epsilon_{th}$  at higher temperature, as more weight is given to the solar selective coating high reflectivity at long wavelengths. Extrapolating spectral data beyond 16  $\mu\text{m}$  according to ISO 22975-3 may not be a suitable guideline for any coating. In the case of solar selective coating, sigmoid models or far infrared measurements provide a more realistic asymptotical reflectivity value.

The comparison of portable emissometers show that the AZ Technology Temp 2000A device agrees best with benchtop spectrophotometers. It reports however a single value at 300 K, while the SOC ET-100 can perform calculations over a broader temperature range, thanks to its multispectral configuration.

The propagation of  $\alpha_{sol}$  and  $\varepsilon_{th}$  uncertainties on the opto-thermal efficiency  $\eta_{opt-th}$  were further analysed. At low temperature and high concentration factor, the  $\alpha_{sol}$  parameter is dominant and its uncertainty defines the lower bound for the combined uncertainty  $u_c(\eta_{opt-th})$ , while the  $\varepsilon_{th}$  parameter is more dominant at high temperature and low concentration factor and its accuracy gradually affects the combined uncertainty  $u_c(\eta_{opt-th})$ .

### **7.3 Publication n°3: Intercomparison of opto-thermal spectral measurements for concentrating solar thermal receiver materials from room temperature up to 800 °C**

In this chapter, spectral measurements performed by five different European laboratories from room temperature up to 800 °C have been evaluated and compared for relevant receiver materials in Concentrating Solar Thermal applications. Two relevant receiver material substrates were considered Haynes 230 and Silicon carbide. Haynes 230 was investigated with three different surface finishes i) oxidised, ii) Pyromark 2500, iii) an industrial black coating. Two key figures of merits were analysed for all samples: solar absorptance  $\alpha_{sol}$  and thermal emittance  $\varepsilon_{th}(T)$ . Solar absorptance  $\alpha_{sol}$  was calculated for room temperature measurements over the spectral interval [0.3; 2.5]  $\mu\text{m}$ , while thermal emittance  $\varepsilon_{th}(T)$  was calculated for measurements performed at room temperature and operating temperature, over the common spectral range [2; 14]  $\mu\text{m}$ .

Oxidised Haynes 230 sample coupons reached an  $\alpha_{sol}$  value of  $90.9 \pm 1.0\%$ . Pyromark 2500 sample coupons reached an  $\alpha_{sol}$  value of  $96.3 \pm 0.5\%$  and the industrial black coating achieved an  $\alpha_{sol}$  value of  $97.0 \pm 0.4\%$ . Silicon carbide sample coupons reached an  $\alpha_{sol}$  value of  $93.5 \pm 1.1\%$ . Low standard deviations indicated reproducible measurements at room temperature for  $\alpha_{sol}$ .

For oxidised H230 sample coupons, the  $\varepsilon_{th,calc}(T)$  value derived from room temperature spectral measurements varied from 55% at 25 °C up to 85% at 1000 °C. For Pyromark 2500 and the industrial black coating, the  $\varepsilon_{th,calc}(T)$  value lied between 90% and 95%, with a weak temperature dependence. For silicon carbide sample coupons, the  $\varepsilon_{th,calc}(T)$  varied from 70% at room temperature up to 87% at 1000 °C. The typical standard deviation among participating laboratories is about 3%. Consistent  $\varepsilon_{th,calc}(T)$  values were obtained for room temperature spectral measurements, with a higher standard deviation in comparison to the solar absorptance  $\alpha_{sol}$ .

For both figures of merit  $\alpha_{sol}$  and  $\varepsilon_{th,calc}(T)$ , all absolute Z-score values were lower than 2, i.e. the intercomparison of both figures of merit at room temperature could be interpreted as statistically satisfactory according to ISO 13528.

Spectral measurements at operating temperature were performed by two laboratories (CEA and PROMES) with three different experimental setups. Thermal emittance  $\varepsilon_{th,meas}(T)$  values obtained from spectral measurements performed at operating temperature up to 800 °C were overall consistent within a few percentage points in comparison to thermal emittance  $\varepsilon_{th,calc}(T)$  values obtained from spectral measurements at room temperature, despite a few outliers.

## **7.4 Publication n°4: Simulation of shortwave infrared ratio thermometers for the remote opto-thermal characterization of central external cylindrical receivers**

In this chapter, a new measurement principle has been introduced and analysed for the remote opto-thermal characterization of central external cylindrical receivers in solar tower power plants. The new measurement principle relies on passive shortwave infrared (SWIR) ratio thermography. It allows a simultaneous retrieval of surface temperature and band emittance for grey surfaces such as black coatings and oxidised metals. The atmosphere does not behave a priori as a greybody. A model-based estimation of band atmospheric transmittance has been introduced to correct this hypothesis, using meteorological parameters available at ground level, i.e. ambient temperature  $T_{amb}$ , relative humidity  $RH$  and atmospheric pressure  $p_{atm}$ .

A MATLAB software tool has been developed and coupled to MODTRAN6 radiative transfer code, for the spectral simulation of radiometric chains relevant in Concentrating Solar Power. The accuracy and sensitivity of two SWIR ratio thermometers have been analysed using spectral simulations. Relevant parameters combine atmospheric conditions, in particular absolute humidity  $AH$  and Solar Zenith Angle ( $SZA$ ) and operating conditions, i.e. concentration factor  $C_x$  and surface temperature  $T_{surf}$ . The first SWIR ratio thermometer combines two narrow bandpass (NB) filters centered on two water vapor atmospheric absorption bands, respectively located at 1.4  $\mu\text{m}$  and 1.9  $\mu\text{m}$ . The second SWIR ratio thermometer combines two NB filters centered on atmospheric windows, respectively located at 1.64  $\mu\text{m}$  and 2.09  $\mu\text{m}$ .

The first SWIR ratio thermometer (1.4/1.9  $\mu\text{m}$ ) is particularly sensitive to atmospheric water vapor, which filters extraterrestrial solar radiation on the one hand but also attenuates thermal radiation emitted by the receiver surface on the other hand, in particular for a typical receiver height above 200 m. Under realistic  $AH$  levels, this ratio thermometer can be considered nearly solar blind, but only for temperatures above 550 °C. The temperature threshold for which the relative temperature error  $\Delta T/T$  is less than 2% varies with the absolute humidity  $AH$  estimated at ground level, the solar zenith angle  $SZA$  and the concentration factor  $C_x$ . This SWIR ratio thermometer, has probably a limited applicability for remote opto-thermal characterization during power plant operation, especially for a receiver height above 200 m and without detailed knowledge of temperature and humidity profiles along the measurement path. It may be applied for shorter distances on high temperature objects, if atmospheric conditions are well characterised.

The second SWIR ratio thermometer (1.64/2.09  $\mu\text{m}$ ) is not sensitive to atmospheric water vapor, however it cannot operate during daily power plant operation. It could remotely characterise the receiver surface temperature  $T_{surf}$  and surface band emittance  $\epsilon_{surf,band}$  with a good accuracy when the heliostat field is defocused ( $C_x = 0$ ) and the receiver surface is maintained isothermal ( $T_{surf} \sim 300$  °C) before molten salt drainage. The relative temperature error  $\Delta T/T$  is lower than 0.5% and the band emittance error  $\Delta \epsilon$  is less than 2.5 p.p., according to spectral simulations for Pyromark 2500 and oxidised Haynes 230. This operation phase is also often used in commercial power plants for the calibration of Longwave Infrared (LWIR) cameras. The second SWIR ratio thermometer could therefore offer an alternative method to support the LWIR system during calibration and map remotely the receiver band emittance.

## **7.5 General conclusion and outlook**

The opto-thermal performance of a solar thermal absorber coating for CSP applications is sensitive to the concentration factor  $C_x$  and the surface temperature  $T$ . While solar selective coatings are definitely relevant for parabolic trough collectors, high solar absorptance black coatings are more relevant for central receiver systems, due to the higher concentration factor.

Intercomparison measurement campaigns have shown that solar absorptance values derived from room temperature spectral measurements are reproducible with a low standard deviation of 1%, for solar selective coatings, black coatings, oxidized Haynes 230 and silicon carbide. For the same materials, a higher standard deviation of  $\sim 3\%$  was observed for thermal emittance values derived from room temperature spectral measurements. The comparison of thermal emittance values derived from room and operating temperature up to 800 °C show a rather consistent agreement for oxidised Haynes 230, black coatings and silicon carbide.

The remote opto-thermal characterization of grey materials such as oxidised Haynes 230 and black coatings is feasible in a Central Receiver System using shortwave infrared thermography. Two configurations were respectively analysed for on-sun and off-sun operating conditions.

A prototype shortwave infrared multispectral camera, including both ratio thermometer configurations, has been assembled and tested at Plataforma Solar de Almería, Spain. The experimental validation of the measurement principle under laboratory conditions is currently on going and the camera system is being fine-tuned for future field measurements in Central Receiver Systems.

Future research may investigate the measurement and stability of solar absorptance at operating temperature for receiver materials and solar thermal absorber coatings found in CSP applications. Accurate quantitative infrared thermography remains challenging for solar selective coatings in the context of Central Receiver Systems.

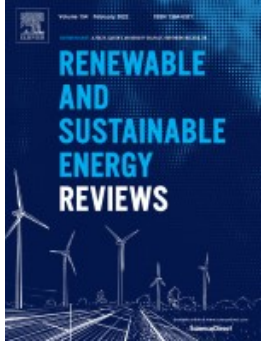


## **Appendix. Publications derived from this thesis**





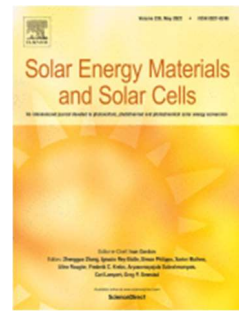
**Publication n°1: A comparative analysis of opto-thermal figures of merit for high temperature solar thermal absorber coatings**

Published article (Accepted 24 <sup>th</sup> October 2021)		
<p><i>Title:</i></p> <p><i>Journal:</i></p> <p><i>Impact factor:</i></p> <p><i>Quartile JCR:</i></p> <p><i>Authors:</i></p> <p><i>Volume:</i></p> <p><i>Pages:</i></p> <p><i>Year:</i></p> <p><i>DOI:</i></p>	<p>A comparative analysis of opto-thermal figures of merit for high temperature solar thermal absorber coatings</p> <p>Renewable and Sustainable Energy Reviews</p> <p>15.9</p> <p>Q1</p> <p>S. Caron, J. Garrido, J. Ballestrín, F. Sutter, M. Röger, F. Manzano-Agugliaro</p> <p>154</p> <p>111818 (21 pages)</p> <p>2022</p> <p><a href="https://doi.org/10.1016/j.rser.2021.111818">https://doi.org/10.1016/j.rser.2021.111818</a></p>	
<p><b>Abstract:</b></p> <p>Solar thermal absorber coatings play a key role in the thermal efficiency of receivers for applications in the field of Concentrated Solar Power (CSP). The development of stable spectral selective coatings with a high solar absorptance <math>\alpha_{sol}</math> and a low thermal emittance <math>\epsilon_{th}</math> is often desired to reduce thermal losses. However, quantitative indicators describing selectivity and the trade-off between solar absorptance and thermal emittance is seldom discussed in the literature.</p> <p>In this review, relevant opto-thermal figures of merit are analysed for the comparison of reference solar thermal absorber coatings, including real and ideal coatings, both black and spectral selective. The comparison is made for a temperature ranging from 25 °C to 1000 °C and for a concentration factor ranging from 20 to 1000, based on spectral data measured at room temperature from 0.25 <math>\mu\text{m}</math> to 20 <math>\mu\text{m}</math>.</p> <p>New figures of merit are introduced, i.e. a normalised selectivity ratio <math>Si^*</math>; a trade-off factor <math>Z_{trade-off}</math>; a normalised solar reflectance index <math>SRI^*</math> and a peak efficiency temperature <math>T_{peak,opt}</math>. These metrics are derived from existing figures of merit and adapted for CSP.</p> <p>The set of figures of merit analysed in this review offer a complementary perspective for the detailed characterization of any coating opto-thermal performance. For solar thermal absorber coatings, thermal efficiency <math>\eta_{thermal}</math> and peak efficiency temperature <math>T_{peak,opt}</math> are respectively deemed more insightful than opto-thermal efficiency <math>\eta_{opt-th}</math> and maximum steady-state temperature <math>T_{SST,max}</math>, when comparing the relative opto-thermal performance of two coating formulations.</p>		

**Publication n°2: Laboratory intercomparison of solar absorptance and thermal emittance measurements at room temperature**

Published article (Accepted 31 <sup>st</sup> December 2021)		
<p><i>Title:</i></p> <p><i>Journal:</i></p> <p><i>Impact factor:</i></p> <p><i>Quartile JCR:</i></p> <p><i>Authors:</i></p> <p><i>Volume:</i></p> <p><i>Pages:</i></p> <p><i>Year:</i></p> <p><i>DOI:</i></p>	<p>Laboratory intercomparison of solar absorptance and thermal emittance measurements at room temperature</p> <p>Solar Energy Materials and Solar Cells</p> <p>6.9</p> <p>Q1</p> <p>S. Caron, L. Herding, Y. Binyamin, M. Baidossi, Y. Vinetsky, A. Morales, C. Hildebrant, R. Reoyo-Prats, O. Faugoux, A. Agüero, S. Rodriguez, F. Sutter, M. Röger, F. Manzano-Agugliaro</p> <p>238</p> <p>111579 (15 pages)</p> <p>2022</p> <p><a href="https://doi.org/10.1016/j.solmat.2022.111579">https://doi.org/10.1016/j.solmat.2022.111579</a></p>	
<p><b>Abstract:</b></p> <p>Solar thermal absorber coatings play an important role in the opto-thermal efficiency of receivers in Concentrated Solar Power (CSP). Two standard figures of merit are the solar absorptance <math>\alpha_{sol}</math> and thermal emittance <math>\epsilon_{th}</math> derived from spectral directional hemispherical reflectivity measurements at room temperature. These two figures of merit allow comparing coating formulations in terms of performance and durability.</p> <p>In this study, a black coating and a solar selective coating are optically characterised by different laboratories to compare spectral datasets, solar absorptance <math>\alpha_{sol}</math> and thermal emittance <math>\epsilon_{th}</math> calculations. The comparison includes various benchtop spectrophotometers operating in the UV-VIS-NIR and Infrared spectral ranges as well as three commercial portable reflectometers/emissometers.</p> <p>A good agreement is found between the nine parties participating in this intercomparison campaign. The black coating <math>\alpha_{sol}</math> value is <math>96.6 \pm 0.2\%</math>, while the solar selective coating <math>\alpha_{sol}</math> value is <math>94.5 \pm 0.4\%</math>. For the thermal emittance, spectral data is concatenated and integrated from <math>0.3 \mu\text{m}</math> to <math>16 \mu\text{m}</math>. The black coating <math>\epsilon_{th}</math> value calculated at <math>650 \text{ }^\circ\text{C}</math> is <math>80.8 \pm 3.8\%</math>, while the solar selective coating <math>\epsilon_{th}</math> value calculated at <math>650 \text{ }^\circ\text{C}</math> is <math>25.0 \pm 0.5\%</math>.</p>		

**Publication n°3: Intercomparison of opto-thermal spectral measurements for concentrating solar thermal receiver materials from room temperature up to 800 °C**

Published article (Accepted 4 <sup>th</sup> December 2023)		
<p><i>Title:</i></p> <p><i>Journal:</i></p> <p><i>Impact factor:</i></p> <p><i>Quartile JCR:</i></p> <p><i>Authors:</i></p> <p><i>Volume:</i></p> <p><i>Pages:</i></p> <p><i>Year:</i></p> <p><i>DOI:</i></p>	<p>Intercomparison of opto-thermal spectral measurements for concentrating solar thermal receiver materials from room temperature up to 800 °C</p> <p>Solar Energy Materials and Solar Cells</p> <p>6.9</p> <p>Q1</p> <p>S. Caron, M. Farchado, G. San Vicente, A. Morales, J. Ballestrín, M. Joao Carvalho, S. Pascoa, E. Le Baron, A. Disdier, E. Guillot, C. Escape, J.-L. Sans, Y. Binyamin, M. Baidossi, F. Sutter, M. Röger, F. Manzano-Agugliaro</p> <p>266</p> <p>112677 (17 pages)</p> <p>2024</p> <p><a href="https://doi.org/10.1016/j.solmat.2023.112677">https://doi.org/10.1016/j.solmat.2023.112677</a></p>	
<p><b>Abstract:</b></p> <p>An intercomparison of opto-thermal spectral measurements has been performed for some relevant receiver materials in concentrating solar thermal applications, from room temperature up to 800 °C. Five European laboratories performed spectral measurements at room temperature, while two laboratories performed infrared spectral measurements at operating temperature up to 800 °C. Relevant materials include Haynes 230 (oxidized, Pyromark 2500 and industrial black coating) and silicon carbide. Two key figures of merit were analysed: i) solar absorptance <math>\alpha_{sol}</math> at room temperature, over the spectral range [0.3;2.5] <math>\mu\text{m}</math>, ii) thermal emittance <math>\epsilon_{th}(T)</math>, over the common spectral range [2;14] <math>\mu\text{m}</math>, derived from spectral measurements performed from room temperature up to 800 °C.</p> <p>Oxidized Haynes 230 reached an <math>\alpha_{sol}</math> value of <math>90.9\pm 1.0\%</math>. Pyromark 2500 reached an <math>\alpha_{sol}</math> value of <math>96.3\pm 0.5\%</math>, while the industrial black coating achieved an <math>\alpha_{sol}</math> value of <math>97.0\pm 0.4\%</math>. Silicon carbide reached an <math>\alpha_{sol}</math> value of <math>93.5\pm 1.1\%</math>. Low standard deviations in <math>\alpha_{sol}</math> indicate reproducible measurements at room temperature.</p> <p>For oxidised Haynes 230, the <math>\epsilon_{th,calc}(T)</math> value derived from room temperature varied from 55% at 25 °C up to 81% at 800 °C. For Pyromark 2500 and the industrial black coating, <math>\epsilon_{th,calc}(T)</math> fluctuated between 90% and 95%, with a weak temperature dependence. For silicon carbide, <math>\epsilon_{th,calc}(T)</math> varied from 70% at room temperature up to 86% at 800 °C. The typical standard deviation among participating laboratories is about 3%. <math>\epsilon_{th,meas}(T)</math> values derived from spectral measurements at operating temperature were consistent within a few percentage points in comparison to <math>\epsilon_{th,calc}(T)</math> values derived from spectral measurements at room temperature.</p>		

**Publication n°4: Simulation of shortwave infrared ratio thermometers for the remote opto-thermal characterization of central external cylindrical receivers**

Draft manuscript (Under Review)														
<p><i>Title:</i></p> <p><i>Journal:</i></p> <p><i>Impact factor:</i></p> <p><i>Quartile JCR:</i></p> <p><i>Authors:</i></p> <p><i>Manuscript Volume:</i></p> <p><i>Pages:</i></p> <p><i>Year:</i></p> <p><i>DOI:</i></p>	<p>Simulation of shortwave infrared ratio thermometers for the remote opto-thermal characterization of central external cylindrical receivers</p> <p>Solar Energy</p> <p>6.7</p> <p>Q2</p> <p>S. Caron, R. Larue, A. Kämpgen, F. Sutter, M. Röger, F. Manzano-Agugliaro</p> <p>SEJ-D-23-03730</p> <p>-</p> <p>-</p> <p>2024</p> <p>-</p>													
<table border="1"> <thead> <tr> <th>Action</th> <th>Manuscript Number</th> <th>Title</th> <th>Initial Date Submitted</th> <th>Status Date</th> <th>Current Status</th> </tr> </thead> <tbody> <tr> <td> <a href="#">View Submission</a>  <a href="#">View Reference Checking Results</a>  <a href="#">Publishing Options</a>  <a href="#">Send E-mail</a> </td> <td>SEJ-D-23-03730</td> <td>Simulation of shortwave infrared ratio thermometers for the remote opto-thermal characterisation of central external cylindrical receivers</td> <td>Dec 06, 2023</td> <td>Jan 04, 2024</td> <td>Under Review</td> </tr> </tbody> </table>			Action	Manuscript Number	Title	Initial Date Submitted	Status Date	Current Status	<a href="#">View Submission</a> <a href="#">View Reference Checking Results</a> <a href="#">Publishing Options</a> <a href="#">Send E-mail</a>	SEJ-D-23-03730	Simulation of shortwave infrared ratio thermometers for the remote opto-thermal characterisation of central external cylindrical receivers	Dec 06, 2023	Jan 04, 2024	Under Review
Action	Manuscript Number	Title	Initial Date Submitted	Status Date	Current Status									
<a href="#">View Submission</a> <a href="#">View Reference Checking Results</a> <a href="#">Publishing Options</a> <a href="#">Send E-mail</a>	SEJ-D-23-03730	Simulation of shortwave infrared ratio thermometers for the remote opto-thermal characterisation of central external cylindrical receivers	Dec 06, 2023	Jan 04, 2024	Under Review									
<p><b>Abstract:</b></p> <p>The accurate knowledge of the receiver surface temperature <math>T_{surf}</math> is important for a safe, efficient and durable power plant operation. Its distribution is typically measured in real time using ground-based longwave infrared (LWIR) thermal cameras. Their calibration requires a priori knowledge of the receiver surface LWIR band emittance <math>\epsilon_{LWIR}</math>. This parameter can be measured with great effort, using portable reflectometers for on tower optical inspection during periodical power plant maintenance. This paper analyses a new measurement principle, based on passive shortwave infrared (SWIR) ratio thermography, for the simultaneous measurement of surface temperature <math>T_{surf}</math> and band emittance <math>\epsilon_{SWIR}</math>.</p> <p>The first SWIR ratio thermometer combines two narrow bandpass filters centered on water vapor atmospheric absorption bands (1.4/1.9 <math>\mu\text{m}</math>). This thermometer is sensitive to water vapor to block solar radiation, however thermal radiation emitted by the receiver is also attenuated. The applicability of this thermometer is limited for remote opto-thermal characterization. Under favorable operating conditions, assuming a scaling of the Mid-Latitude Summer standard atmospheric profile for the temperature and humidity along the measurement path, it could measure temperature levels above 550 °C with a relative temperature error <math>\Delta T/T &lt; 2\%</math>.</p> <p>The second SWIR ratio thermometer combines two narrow bandpass filters centered on atmospheric windows (1.64/2.09 <math>\mu\text{m}</math>). This thermometer is insensitive to water vapor and suited for remote distances, however it can only operate off-sun when the receiver surface temperature is still above 300 °C, for instance during the cool down phase, before molten salts drainage. The relative temperature error <math>\Delta T/T</math> is then less than 0.5% for Pyromark 2500 and oxidised Haynes 230, while the absolute band emittance error <math>\Delta\epsilon</math> is less than 2.5 percentage points.</p>														





El cambio climático es uno de los principales retos a los que se enfrenta la humanidad en el siglo XXI. Es imprescindible aprovechar la energía solar para descarbonizar el sistema energético mundial. Se espera que la tecnología de concentración solar térmica (CST) desempeñe un papel decisivo en el suministro de calor para procesos industriales de media y alta temperatura. Los receptores térmicos y los recubrimientos absorbentes solares térmicos son componentes críticos de los sistemas CST. La monitorización de las características opto-térmicas de dichos recubrimientos, tales como la absorbancia solar, la emitancia térmica y la temperatura de superficie, es crítica para el funcionamiento eficiente y durable de dichos sistemas.

El objetivo principal de esta tesis doctoral es desarrollar un marco para el análisis óptico-térmico de los recubrimientos absorbentes solares térmicos para CST. El análisis óptico-térmico se basa principalmente en técnicas de medición infrarroja, como la espectrofotometría y la radiometría multispectral. El análisis se desarrolla para materiales relevantes, primero en condiciones de laboratorio, tanto a temperatura ambiente como de funcionamiento, hasta 800 °C. Se introduce una nueva técnica de medición para la caracterización opto-térmica in situ de recubrimientos absorbentes solares térmicos en sistemas de receptor central.

*Climate change is one of the major challenge faced by mankind in the 21st century. Solar energy must be harnessed for decarbonising the global energy system. Concentrated Solar Thermal (CST) technology is expected to play a decisive role in supplying heat for medium to high temperature industrial processes. Thermal receivers and solar thermal absorber coatings are critical components in CST systems. The monitoring of coating opto-thermal characteristics, such as solar absorptance, thermal emittance and surface temperature, is critical for the efficient and durable operation of such systems.*

*The main objective of this doctoral thesis is to develop a framework for the opto-thermal analysis of solar thermal absorber coatings for CST. The opto-thermal analysis is mostly based on infrared measurement techniques, such as spectrophotometry and multispectral radiometry. The analysis is developed for relevant materials, first under laboratory conditions, both at ambient and operating temperature, up to 800 °C. A new measurement technique is introduced for the in-situ opto-thermal characterisation of solar thermal absorber coatings in Central Receiver Systems (CRS).*